Department of Energy

Richland Operations Office
P.O. Box 550
Richland, Washington 99352

AUG 3 1 2009

09-AMCP-0199

Ms. J. A. Hedges, Program Manager
Nuclear Waste Program
State of Washington
Department of Ecology
3100 Port of Benton
Richland, Washington 99354

Mr. D. A. Faulk, Program Manager
Office of Environmental Cleanup
Hanford Project Office
U.S. Environmental Protection Agency
309 Bradley Boulevard, Suite 115
Richland, Washington 99352

Addressees:

ELECTRICAL RESISTIVITY CORRELATION TO VADOSE ZONE SEDIMENT AND
PORE-WATER COMPOSITION FOR THE BC CRIBS AND TRENCHES AREA,
PNNL-17821

This letter formally transmits the Electrical Resistivity Correlation to Vadose Zone Sediment and
Pore-Water Composition for the BC Cribs and Trenches Area, PNNL-17821. This report
documents the results of comparing electrical resistivity characterization to geochemical
measurements on sediment obtained from four boreholes in the 200-BC Cribs and Trenches
Area.

This report was previously distributed directly by the Pacific Northwest National Laboratory on
compact disc to the distribution list indicated in the back of the report. Several paper copies were
also provided to your staff at that time. If you have any questions, please contact me, or your
staff may contact Briant Charboneau, of my staff, on (509) 373-6137.

Sincerely,

Matthew S. McCormick, Assistant Manager
for the Central Plateau

AMCP:GLS

Attachment

cc: See Page 2

RECEIVED
SEP 0 8 2009
EDMC

cc w/attach:
G. Bohnee, NPT
L. Buck, Wanapum
S. Harris, CTUIR
R. Jim, YN
S. L. Leckband, HAB
R. A. Lobos, EPA
K. Niles, ODOE
J. B. Price, Ecology
Administrative Record (200-BC-1)
Environmental Portal

cc w/o attach:
R. H. Engelmann, CHPRC
D. L. Foss, CHPRC
M. J. Hickey, FFS
M. N. Jaraysi, CHPRC
R. E. Piippo, CHPRC
J. G. Vance, FFS

Electrical Resistivity Correlation to Vadose Zone Sediment and Pore-Water Composition for the BC Cribs and Trenches Area

RJ Serne
AL Ward
W Um
BN Bjornstad

DF Rucker[1]
DC Lanigan
MW Benecke[2]

[1] HydroGEOPHYSICS, Inc., Tucson, AZ
[2] CH2M-HILL Plateau Remediation Contractor, Richland, WA

June 2009

Pacific Northwest
NATIONAL LABORATORY

Proudly Operated by **Battelle** *Since 1965*

DISCLAIMER

This report was prepared as an account of work sponsored by an agency of the United States Government. Neither the United States Government nor any agency thereof, nor Battelle Memorial Institute, nor any of their employees, makes **any warranty, express or implied, or assumes any legal liability or responsibility for the accuracy, completeness, or usefulness of any information, apparatus, product, or process disclosed, or represents that its use would not infringe privately owned rights**. Reference herein to any specific commercial product, process, or service by trade name, trademark, manufacturer, or otherwise does not necessarily constitute or imply its endorsement, recommendation, or favoring by the United States Government or any agency thereof, or Battelle Memorial Institute. The views and opinions of authors expressed herein do not necessarily state or reflect those of the United States Government or any agency thereof.

This document was printed on recycled paper.
(9/2003)

Electrical Resistivity Correlation to Vadose Zone Sediment and Pore-Water Composition for the BC Cribs and Trenches Area

RJ Serne   DF Rucker[1]
AL Ward   DC Lanigan
W Um   MW Benecke[2]
BN Bjornstad

[1] HydroGEOPHYSICS, Inc., Tucson, AZ
[2] CH2M-HILL Central Plateau Remediation Contractor, Richland, WA

June 2009

Acknowledgments

measurements, such as sediment hydraulic conductivity, as function of moisture content. Wayne Martin and Dawn Wellman (at PNNL) are our liaisons and advocates with EM-22 to keep the collaborative efforts active. Their efforts are greatly appreciated.

Abstract

This technical report documents the results of comparing electrical-resistivity characterization (ERC) to geochemical measurement on sediment obtained from four boreholes (C4191, C5923, C5924, and C5925) drilled in the BC Cribs and Trench area. The geochemical characterization was conducted to determine the efficacy of ERC methodology for use at the Hanford Site and was focused on addressing three data quality objectives specified in Sampling and Analysis Plan DOE/RL-2007-13. As a whole, the ERC data do correlate with the presence of high-concentration sodium nitrate salt plumes as determined by extensive sediment sampling. The surface-based ERC data were sufficient to indicate the lateral, and to some extent, vertical, distribution of mobile contaminants. The surface-based geophysical survey data seemed to suffer from a sort of "myopia," where looking down from the ground surface, the maximum pore-water salt concentration depths were difficult to resolve. Further, ERC measures bulk resistivity, which is related to dissolved electrolyte content and not individual chemical species. Further, because technetium-99 has transport attributes that are very similar to nitrate, the ERC measurements correlate to technetium-99 in the vadose zone fortuitously. The concentrations of elevated technetium-99 range from 90 to 146 pCi/g sediment (C5923), 34 to 51 pCi/g sediment (C5924), and 64 to 107 pCi/g sediment (C4191). Again we stress that ERC cannot directly distinguish individual chemical or radionuclide species themselves.

One specific outcome of the BC Cribs and Trenches area ground-truthing exercise was confirmation that separate contaminant plumes exist for the cribs and nearby trenches. Finally, because ERC data were used to select the borehole locations for three of the new boreholes outside the footprints of BC Cribs and Trenches, and contaminants were found (or not found) as expected, ERC is a very useful guide for selecting vadose zone sampling locations, particularly when the targeted subsurface plumes exhibit high ionic strength.

Laboratory-scale resistivity measurements conducted on grab and core samples from Well C5923 (A) directly verify the presence of anomalously low-resistivity zones observed by the surface-based resistivity survey. Based on this correlation alone, the surface-based ERC approach can map the probable lateral extent of high-ionic-strength subsurface plumes and thus is applicable at Hanford as long as the sites are not significantly impacted by sub-surface low-resistivity infrastructure (e.g., metallic tanks and pipelines). The leading edge of the salt plume at three boreholes (C5924, C4191, and C5923) reached depths of 130, 160, and 260 ft, respectively. Borehole C5925 showed no significant indications of any contamination. The leading edge of each salt plume is shallower than the regional water table, which is present at ~340 to 350 ft bgs. The fact that the salt plumes at each borehole did not reach the water table despite millions of liters being disposed of is likely because of the thin, fine-grained lenses in the Hanford H2 unit, which provide several capillary breaks that promote horizontal spreading in the upper portion of the Hanford formation.

A second goal of the sediment characterization was to measure the total and water-leachable concentrations of key contaminants of concern as a function of depth and distance from the footprints of inactive disposal facilities. The total and water-leachable concentrations of key contaminants will be used to update contaminant-distribution conceptual models and to provide more data for improving baseline risk predictions and remedial alternative selections. None of the borehole sediments show significantly elevated acid-extractable Resource Conservation and Recovery Act (RCRA) metals. As expected, based

on their known immobility, no detectable amount of mercury, strontium-90 or nickel-63 was found in the sediments obtained from boreholes C5923, C5924, or C5925. Thus, outside the facility footprints, the vadose zone sediments do not appear to contain concentrations of RCRA metals significantly different from natural background. Elevated acid-extractable (likely precipitated) uranium appears to exist only right at the bottoms of the inactive cribs and trenches as was found at borehole C4191 (drilled right through the 216-B-26 trench footprint). In conclusion, outside the facility footprints and also deep below (e.g., more than 20 meters) the facility footprints, the vadose zone sediments do not appear to contain chemical or radionuclide contaminants, **except sodium, nitrate, sulfate, and technetium-99**, at concentrations significantly above natural background levels.

Executive Summary

This technical report documents the results of comparing electrical resistivity characterization (ERC) to geochemical measurement on sediment obtained from four boreholes (C4191, C5923, C5924, and C5925) drilled in the BC Cribs and Trench area. The data used in this study were derived from 1) subsurface electrical-resistivity models constructed from surface-based resistivity surveys, 2) geochemical measurements of water extracts of sediments from the four boreholes, and 3) laboratory-scale resistivity measurements conducted on vadose sediment grab and core samples from borehole C5923. Vadose zone sediment samples were obtained at a frequency of about every 2.5 ft from approximately 5 ft bgs to borehole total depth. In total, 505 grab samples and thirty-nine 6-in.-long cores were obtained for characterization. This sediment suite represents the largest data set ever collected at the Hanford site for correlating with surface-based soil electrical-resistivity field measurements.

The geochemical characterization was conducted to determine the efficacy of ERC methodology for use at the Hanford Site and focused on addressing three data quality objectives (DQOs) specified in Sampling and Analysis Plan DOE/RL-2007-13.

The DQO process led to the following three key questions that needed to be answered:

#1   Do ERC data generally correlate with vadose zone contaminant of concern (COC) plumes that are established by analyzing borehole sediment samples?

#2   Is the correlation of ERC and laboratory analytical data sufficient to use ERC to assist in updating the existing conceptual site models (CSMs) and evaluating remedial alternatives?

#3   Is ERC data interpretation useful for guiding vadose zone sediment sampling for targeted COCs?

As a whole, the ERC data do correlate with the presence of high-concentration (>0.3 M) sodium nitrate salt plumes as determined by extensive sediment sampling (DQO #1). For the BC Cribs and Trenches area waste sites, the surface-based ERC data were sufficient to indicate the extent of contamination, particularly on a lateral scale. This groundtruthing exercise has improved our ability to interpret field electrical resistivity surveys in a more quantitative fashion and has provided valuable data on determining the capability of surface-based ERC to delineate the bounds of lateral and vertical distances so that the technique can identify low resistivity (high electrical conductivity) sub-surface plumes. However, ERC techniques measure bulk resistivity (or its reciprocal electrical conductivity, which is related to dissolved electrolyte content) and not individual chemical species. At the BC Cribs and Trenches area (and at most Hanford sites surrounding inactive disposal units), the dominant electrolytes in the vadose zone pore water are nitrate and sodium. The ERC measurements correlate to the total electrolyte concentrations and because nitrate and sodium dominate the electrolyte composition, correlations with these two individual species are good. Further, because technetium-99 has transport attributes that are very similar to nitrate, the ERC measurements correlate to technetium-99 in the vadose zone fortuitously. ERC cannot distinguish individual chemical or radionuclide species themselves, especially contaminants that are present at low mass concentrations in the subsurface. The ERC technique can aid in delineating the lateral and, to some extent, vertical distribution of mobile contaminants that have transport attributes similar to the nitrate and thus can aid in improving mobile CSMs. One specific outcome of the BC Cribs and Trench area ground-truthing exercise was confirmation that separate contaminant plumes exist for the cribs and nearby trenches (DQO #2). Finally, because

ERC data were used to select the borehole locations for the three new boreholes outside the foot prints of BC Cribs and Trenches, and contaminants were found (or not found) as expected, ERC is a very useful guide to selecting vadose zone sampling locations, particularly when the targeted subsurface plumes exhibit high ionic strength (DQO #3).

Laboratory-scale resistivity measurements conducted on grab and core samples from Well C5923 (A) directly verify the presence of anomalously low-resistivity zones observed by the surface resistivity survey. In this case, sedimentary intervals with relatively high ionic-strength pore-water have a corresponding laboratory-measured soil-resistivity that is well below natural variations in uncontaminated sediments. Based on this correlation alone, a target-based approach using surface-based electrical-resistivity to map the probable lateral extent of high-ionic-strength subsurface plumes or zones is applicable at the Hanford Site as long as the sites are not significantly impacted by the presence of sub-surface low resistivity infrastructure (e.g., metallic tanks and pipelines). The infrastructure complications can be mitigated by using other complementary geophysical measurements and historical knowledge (used judiciously). The lower limit of pore-water ionic strength that is necessary to yield definitive detection of low-resistivity sub-surface zones was not quantitatively determined, but pore-water ionic strength above 0.3 M appears to yield adequate low-resistivity signals that are readily detected.

The pore-water chemical composition data, laboratory-scale soil resistivity, and other ancillary physical and hydrologic measurements and analyses described in this report are designed to provide a crucial link between direct measurements on sediments and the surface-based electrical-resistivity information obtained via field surveys. A second goal of the sediment characterization was to measure the total and water-leachable concentrations of key contaminants of concern as a function of depth and distance from the footprints of inactive disposal facilities. The total and water-leachable concentrations of key contaminants will be used to update contaminant-distribution conceptual models and to provide more data for improving baseline risk predictions and remedial alternative selections.

The ERC ground-truthing exercise for the individual boreholes, as quantified by regression analysis of soil resistivity values versus vadose zone pore-water constituent concentrations, showed mixed results. The regression correlations, as quantified by the R^2 coefficient, varied between 0.01 and 0.73, dependent on borehole and whether the correlation was based on a linear or logarithm relationship with a pore-water parameter. In general, the best correlations were for a logarithm relationship. These correlation coefficients are not as high as might be desired; the low-correlation results from the different scales of investigations between the coarser-scale surface-based resistivity data and the finer-scale borehole sediment based data. Despite the differences in measurement scales, high concentrations of dissolved salts in the pore waters of sediments from C5923, C5924, and C4191 generally produced a low-resistivity "target" in the processed resistivity field surveys, and variability could be seen in the resistivity data that relates to the variability in pore-water concentrations.

In all boreholes except C5925 (C), where the geochemical characterization was conducted at a much lower rate (because it was discovered early that there was little or no contamination present), the inverted (processed) ERC profiles, which were based on a much coarser volume (scale), were not capable of producing high correlation coefficients with the smaller-scale pore-water measurements. The resolution of the ERC surveys is less than the scale at which the geochemical sampling was conducted. The large variation in pore-water composition in the thin, fine-grained sediments in comparison to the composition of the bulk sand sediments is impossible for the surfaced-based geophysics to replicate, and the geophysical measurements act as a low-pass filter. That is, high-frequency components are not observed

in the raw apparent-resistivity (field survey) measurements. Then during inversion, the same smooth apparent-resistivity data used as input to the inversion model produce a smooth estimate of the true soil resistivity. The inversion cannot recreate the high-frequency components (highly varying pore-water chemistry over small depth increments) that were removed during the original field measurements. That being said, the best correlation was at borehole C4191 where the fine-scale variability in pore-water chemistry as a function of depth showed two nearly equally concentrated salt plumes separated by only a few 10s of feet. The correlation coefficients for the inverted (processed) field geophysical profiles with the actual pore-water major chemical constituents ranged from 0.4 to 0.7 where a value of 1 is perfect correlation.

The surface-based geophysical survey data also seemed to suffer from a sort of "myopia," where looking down from the ground surface, the target's (e.g., each of the maximum pore-water salt concentration) depths were difficult to resolve. This was certainly the case with the ERC comparison made with Borehole C5923 (A), which exhibited at least a tri-modal depth distribution in pore-water salt concentrations. Some improvement in correlating the field-resistivity profile with the pore-water profiles was shown by shifting the geophysical response either downwards for the 2D inversion or upwards for the 3D inversion. The required shift was slight (3 to 5 m, dependent on borehole) and was on the order of the thickness of an individual layer used in the finite difference numerical model used to process the field survey data. The apparent depth shift in the geophysics is likely a consequence of the smoothing constraints and stabilization function implemented in the commercial inversion codes used to perform the modeling. To combat this problem, academic and industry researchers are currently studying methods to sharpen images and form more realistic geologic interpretations of geophysical data. It will be some time, however, before these new methods are routinely applied.

The best correlations between the field electrical-resistivity surveys and borehole pore-water data sets were obtained when focusing on the areal extent of the salt plume. Lateral resolution of the geophysical field data is best conducted by comparing an aggregated set of geophysical data on all boreholes together. When assembling the pore-water data for all four boreholes in an areal view, the surface-based field ERC data in the author's judgment produced a reasonable distribution (physically plausible) of low-resistivity values that were indicative of the high-concentration salt plumes that exist below the BC Cribs and Trenches area. To estimate the lateral extent of contamination from historical disposal in the BC Cribs and Trenches area, the resistivity data were converted to ionic strength using the least squares regression formula obtained using inversion results from the 3D resistivity. The 3D inverted results were chosen for this exercise based on their reasonable reconciliation of the resistivity in the northeast corner between the cribs and trenches (near borehole C). The lateral extent of the subsurface salt plume from this exercise is shown in Figure S.1. The 3D inversion results were composed of four individual models that encompass overlapping domains. Figure S.1 was created by merging the results of the four models. The figure shows the areal rendering (plan view) of calculated ionic strength equal to or above 0.3 M. The 0.3-M isopleth covers the area of the footprints of the individual liquid disposal trenches as well as the area between each of the trenches, suggesting that liquids from each trench mixed in the sediments below each trench and coalesced into one larger plume in each north-south row of trenches. In the middle of the trenches near the location of borehole B (C5924), the 0.3-M isopleth is continuous between the two westernmost rows of trenches. The total volume of waste and total mass of salt disposed of into each of the five cribs closest to this region with continuous salt plume (216-B-33, 216-B-34, 216-B-52, 216-B23, and 216-B-24) averages over 5-million liters and 1.5-million kg of nitrate. Another trench region with lateral continuity of the salt plume is between the northern diagonal trenches (216-B-22, 216-B-21, and
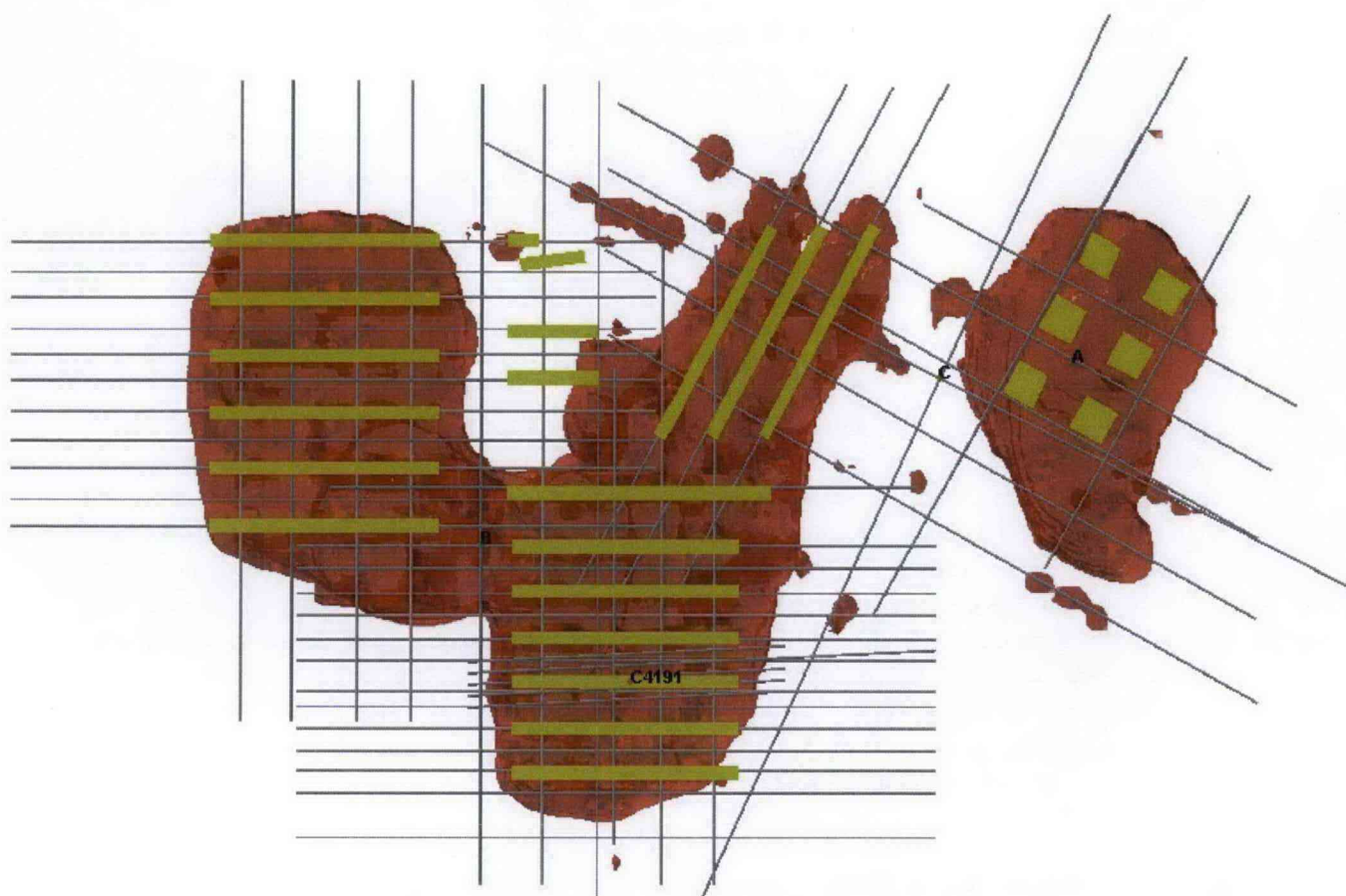
Figure S.1. Field Survey Estimate of the Lateral Extent of the Subsurface Salt Plume at BC Cribs and Trenches Area (0.3-M pore-water ionic strength calculated from 3D inverted soil resistivity data)

216-B-20) and 216-B-52. The total area that encompasses the 0.3-M isopleths in the region of the BC trenches is 11.3 hectares.

In the northeast corner of the BC Cribs and Trenches area, where the six cribs are located, the subsurface salt plume is continuous and much larger than the footprint of the individual cribs. The 0.3-M ionic strength isopleths extend approximately 90 m south of crib B-18 (southeastern corner of BC Crib complex). The total area encompassed by the 0.3-M isopleths in the BC cribs region is 2.7 hectares. The lateral extent of the salt plumes analysis shown in Figure S.1 predicts that at the location of borehole C (C5925), there is no contamination with salt at or above 0.3 M. This is corroborated by the actual sediment analyses (see Section 8) that shows pore-water ionic strengths throughout the depth profile (20 to 203 ft bgs) range from 0.02 to 0.12 M. We conclude that the surface-based ERC survey at the BC Cribs and Trenches area provides a good estimate of the lateral extent of sub-surface contamination where the pore-water ionic strength is near to or above 0.3 M.

Future work that relies on more laboratory soil resistivity and the incorporation of other types of field data (spectral gamma, neutron moisture, and soil density logs) and physical and hydraulic measurements

could be used to develop a more detailed petrophysical model of the sediments below the BC Cribs and Trenches. This more detailed petrophysical model can be used as a more realistic "earth model" in the inversion process to better manipulate the raw field survey data. It is also recommended that one more borehole be drilled after a thorough vetting of the current data with geophysics experts and other Hanford stakeholders to optimize where to place the borehole, what electrical and other geophysical surveys should be conducted, where to take sediment samples, and what parameters should be measured on the sediments to attempt one more "ground-truthing" exercise. The rest of this executive summary describes 1) details of the borehole sediment characterization activities and 2) findings on the second objective of determining the distribution of potential contaminants of concern.

As part of the vadose zone sediment characterization, experienced geologists examined the samples and all available geophysical logging data for the new boreholes and then generated very detailed information on the local stratigraphy in the BC Cribs and Trenches area. The geologic framework of the vadose zone sediments controls the migration of the liquid waste and dissolved contaminants as they travel towards the unconfined aquifer. A key geological finding is the presence of several (5 to 7) thin (< 1-m thick), finer-grained relatively wet lenses within the upper 130 ft of Hanford formation H2 unit at all four boreholes. These thin, relatively moist sediments can act as horizontal spreading zones for slowly percolating liquid wastes or natural recharge waters.

The most important geochemical parameters that were measured to "ground truth" the surface-based field-resistivity surveys at the BC Cribs and Trenches region were major dissolved salts in the vadose zone pore waters. Pore-water electrical conductivity (EC), and the major ions sodium and nitrate are especially relevant. Theoretically, the pore-water parameter having the highest correlation with electrical response should be total ionic strength, which accounts for the total electrical conductivity of the pore water.

As part of the second objective, gamma energy analysis, de-ionized water, and strong acid extractions were performed on selected grab samples to identify the distribution of key contaminants. Contaminants of potential concern included Resource Conservation and Recovery Act (RCRA) metals and radionuclides, with an emphasis on mercury and chromium and technetium-99, uranium, strontium-90, nickel-63, and gamma-emitting fission products, respectively. Gross-beta and gross-alpha analyses of the acid extracts were used to assess whether we had overlooked any radionuclides of potential concern. The gross-alpha and beta results for the acid extracts did not show any signs of unaccounted radioactivity beyond that found in the specific analyses.

The vadose zone sediments at three of the boreholes (C5923, C5924, and C4191) contained high concentrations (>0.3 M) of dissolved salts (mainly sodium nitrate) with either bi- or tri-modal distributions with depth. The vertical distribution of the salt plume at C5923 was the most irregular and tri-modal and extended at least 246 ft below ground surface. The highest pore-water EC at C5923 was 293 mS/cm. The vertical distribution of the salt plume at boreholes C5924 and C4191 were bi-modal with the shallower lobe being slightly more concentrated than the deeper lobe. At C4191, the highest pore-water EC was 176 mS/cm and at C5924 was 92.7 mS/cm. The two maxima (bi-modal) salt concentrations in both of these boreholes occurred at about the similar depths (~70 and 123 ft bgs) and (~90 and 133 ft bgs), respectively. The pore-water–corrected EC data for C5925 ranged from 1.2 to 8.8 mS/cm, which in comparison to the other three boreholes are very low, which is consistent with the hypothesis that no waste percolated through these sediments. The total ionic strengths of the pore waters in the borehole's maximum salt plume regions ranged as follows: 2.4 to 3.5 M (C5923), 0.7 to 1.3 M

(C5924), and 0.4 to 2.3 M (C4191). The total ionic strength distribution in C5925 pore waters ranges from 0.019 to 0.12 M, which is within the range of uncontaminated Hanford formation pore-water values.

The leading edge of the salt plume at two boreholes (C5924 and C4191) near to or within trenches reached depths of 130 and 160 ft, respectively. The leading edge of each salt plume is shallower than the regional water table, which is present at ~340 to 350 ft bgs. The fact that the salt plumes at each borehole did not reach the water table despite millions of liters being disposed of is likely because of the thin, fine-grained lenses in the Hanford H2 unit, which provide several capillary breaks (contrasts between fine sand and coarse sand) that promote horizontal spreading in the upper portion of the Hanford formation. On an areal basis, the BC cribs received much larger volumes of liquid waste than the BC trenches so that the deeper penetration of the salt plume at C5923 makes sense. Further, the sediments underlying C5923 appear to exhibit fewer (5 vs 7) finer-grained lenses that promote horizontal spreading of wastes.

The vadose zone pH profiles in C5923 and C4191 show elevated values (maximum >9.2), indicative of caustic waste in the depth region of 8 to 18 ft bgs and 17.5 to 37.5 ft bgs, respectively. At C5924, the highest pH observed was 8.8, and two zones appeared to show weak signs of caustic waste interaction (18 to 35 and 53 to 57 ft bgs). At borehole C5925, there was no elevated pH in the water extracts and no other chemical signatures indicating the presence of waste. For the three boreholes where elevated pH was found in the shallow sediments, a few of the major elements (Al, Fe, and Mn) show elevated acid-extractable concentrations. This suggests that the sediments interact with the caustic-waste fluids through dissolution and precipitation/neutralization reactions that likely form more leachable amorphous solid phases and metal hydroxides/oxides in contrast with more stable alumino-silicate and crystalline metal oxides. The shallow sediments at these three boreholes also show signs of elevated acid-extractable phosphorous indicative of phosphate precipitates from the waste interacting with native sediments. None of the borehole sediments show significantly elevated acid-extractable RCRA metals, and only borehole C4191 shows signs of elevated acid-extractable uranium (>5 μg/g).

The water-extractable concentrations of major cations in the C5923 vadose zone sediments do not show depletions in the divalent cations in the shallowest ion exchange front (which also is the thickest lobe and highest concentration of pore-water sodium). This may indicate that waste fluids migrated horizontally into the sediments in the shallow portion of borehole C5923 as opposed to vertically. At boreholes C5924 and C4191, two ion exchange fronts (where the monovalent cation concentrations are low and divalent cation concentrations are high relative to each other) were found at the depths where the bi-modal salt peaks reside, suggesting a significant vertical flow pattern for disposed waste liquids. The two ion exchange fronts at borehole C5924 and C4191 are readily discernable in contrast to the water-extract cation distribution at borehole C5923 that does not show distinct separation between the mono- and divalent cations in the borehole profile with depth. Thus, the vertical distribution of water-extractable cations observed at borehole C5923 is not easily interpreted as being caused by one or a few separate ion exchange fronts.

The water-extract data for technetium-99 in boreholes C5923, C5924, and C4191 show elevated technetium-99 concentrations occurring at the same locations as elevated nitrate and EC. The deepest penetration of significant technetium-99 contamination also occurs at the same place as the significantly elevated nitrate because they are mobile contaminants and distribute in the vadose zone in a similar pattern. The concentrations of elevated technetium-99 at these three boreholes range from 90 to 146 pCi/g sediment (C5923), 34 to 51 pCi/g sediment (C5924), and 64 to 107 pCi/g sediment (C4191).

In contrast to the shallow sediments at borehole C4191, which was emplaced directly through the footprint of the 216-B-26 trench, no detectable strontium-90 or nickel-63 was found in the sediments obtained from boreholes C5923 or C5924. Because these radionuclides are quite immobile in the geochemical environment in Hanford's subsurface, given the nature of the waste stream disposed of at BC Cribs and Trenches, and the fact that the boreholes are several 10s of feet from facility footprints, finding no detectable nickel-63 or strontium-90 was expected. The sediment samples from C5923, C5924, and C5925 also did not contain detectable concentrations of mercury, and the concentrations of other RCRA metals were low and within the range of natural background. Thus, outside the facility footprints, the vadose zone sediments do not appear to contain concentrations of RCRA metals significantly different from natural background. Elevated acid-extractable (likely precipitated) uranium appears to exist only right at the bottoms of the inactive cribs and trenches as was found at borehole C4191 (drilled right through the 216-B-26 trench footprint).

The sediment from borehole C4191 contains some manmade gamma radioactivity in some of the shallow grab samples. Essentially, the only significant gamma activity observed was in C4191 where cesium-137 was detected in the first few samples from 13 and 27.5 ft bgs. The samples at 13 to 14 ft bgs contain between $5 \times 10^{+5}$ to $1 \times 10^{+6}$ pCi/g cesium-137, and sediments deeper down to 27.5 ft bgs contain about 10 pCi/g or less. In addition, a few pCi/g of shorter-lived antimony-125 and europium-155 were detected in isolated samples. Sub-pCi/g activities of cobalt-60 were also detected in a few samples with no consistent depth profile. At the three boreholes outside facility footprints, manmade gamma activities (cesium-137) were at most a few tenths pCi/g in the shallow sediments. In conclusion, outside the facility footprints and also deep below (e.g., more than 20 meters) the facility footprints, the vadose zone sediments do not appear to contain chemical or radionuclide contaminants, **except sodium, nitrate, sulfate, and technetium-99** at concentrations significantly above natural background levels.

Based on historical groundwater monitoring records and the highly elevated deep vadose zone nitrate concentrations at C5923 (A), we hypothesize that low concentrations of nitrate exist, and perhaps other mobile contaminants from the mid 1950s disposal of scavenged bismuth phosphate waste, in the groundwater below the BC cribs. The groundwater concentration of nitrate (10 to 20 mg/L) currently is below the drinking water standard of 45 mg/L. There was no detectable technetium-99 in the groundwater at the bottom of borehole C5923 (A). Based on groundwater results at borehole C4191, the vadose zone sediment distribution of nitrate and technetium-99 (deepest descent found more that 180 ft above the water table) and the historical records reviewed in Appendix C, we hypothesize that groundwater below most of the BC trenches is not contaminated with residual scavenged bismuth phosphate wastes today nor was the groundwater below the BC trenches contaminated significantly in the past during and within a decade after the active disposal in the mid 1950s.

Acronyms and Abbreviations

BET	Brunauer-Emmett-Teller—method used to measure specific surface area of solid
bgs	below ground surface
CCU	Cold Creek Unit
CEC	Cation Exchange Capacity
COC	contaminant(s) of concern
CSM	Conceptual Site Model
DETW	Deep electrode to well electrode configuration of field electrical resistivity electrodes
DIC	depth of investigation characteristics
DOE	U.S. Department of Energy
DQO	Data Quality Objectives
EC	electrical conductivity—measure of salt content in fluid
EPA	Environmental Protection Agency
EM	electromagnetic induction
ERC	Electrical Resistivity Characterization
ERDF	Environmental Restoration Disposal Facility
ESL	Environmental Sciences Laboratory
FFS	focused feasibility studies
FHI	Fluor Hanford, Inc.
GD	gravel-dominated
GEA	Gamma Energy Analysis
GPS	global positioning survey
GW	groundwater
HASQARD	*Hanford Analytical Services Quality Assurance Requirements Document* (DOE/RL-96-68)
HEIS	Hanford Environmental Information System
HGI	HydroGEOPHYSICS, Inc.
HRR	High Resolution Resistivity
IC	Ion Chromatograph—used to measure anions concentrations
IC	inorganic carbon
ICP-MS	Inductively Coupled Plasma Mass Spectroscopy
ICP-OES	Inductively Coupled Plasma Optical Emission Spectroscopy
ID	identification
IDF	Integrated Disposal Facility
IP	induced polarization
ISSD	Interbedded sand- and silt-dominated

LDS	Laser Diffraction Spectrometry
NIST	National Institute of Standards and Technology
NM	neutron moisture
PNNL	Pacific Northwest National Laboratory
PSD	Particle size distribution
RL	(DOE's) Richland Operations Office
RTK	real-time kinematic
SD	sand-dominated
SG	spectral gamma
SGE	Surface Geophysical Exploration
SSA	specific surface area
STW	Ground surface to well electrode configuration of field electrical resistivity electrodes
TDR	time domain reflectrometry
TG	Total gamma
UFA	Unsaturated Flow Apparatus –used to extract pore fluids out of moist sediments
USGS	United States Geological Society
WSCF	Waste Sampling and Characterization Facility
WTDE	Well to deep electrode configuration of field electrical resistivity electrodes
WTS	Well to ground surface configuration of field electrical resistivity electrodes
WTW	Well to well configuration of field electrical resistivity electrodes

Contents

Contents

Contents

Contents

Contents

Figures

Figures

Figures

Figures

Figures

Figures

Figures

Tables

Tables

Tables

1.0 Introduction

1.1 Goals

The overall goal of this report is to provide data and analyses to quantify the resolution limits of surface-based, electrical-resistivity surveys conducted at the BC-Cribs and Trenches area in terms of the capability to accurately image the subsurface electrical distribution and detect geo-electrical effects resulting from past liquid waste discharges. The data and analyses described in this report are designed to provide a crucial link between direct measurements of geochemical, hydraulic, and soil resistivity of subsurface material and the surface-based electrical-resistivity information obtained via field surveys. This borehole sediment-to-surface–based linkage is otherwise known as "ground truthing" and is accomplished by directly measuring resistivity and other hydraulic properties of sediment samples taken from boreholes placed in the region of study. Water extracts should also be taken from the sediments with subsequent measurement of pore-water composition. Pore-water parameters measured include specific electrical conductivity (EC), common cation and anion concentrations, pH, and alkalinity. From all these laboratory measurements on sediments and water extracts, pore water ionic strength and petrophysics relationships are generated that can be compared with the field (or laboratory) electrical resistivity data, both directly and after the field data are processed using petrophysics-based algorithms.

Secondary goals of the work described in this report are to measure the total and/or water-leachable concentrations of key contaminants of concern (COCs) in the sediments as a function of depth and distance from inactive disposal facilities in a region called the BC Cribs and Trenches area. All the data collected on the sediments from the boreholes are used to generate conceptual models of the contaminants' distribution in the subsurface and future potential mobility. From these conceptual models and the available sediment characterization, data baseline risk assessments and guidance on choosing remedial-action alternatives are possible. Finally, the newly acquired data and analyses can aid in the future decisions that must be made by the U.S. Department of Energy (DOE) regarding the near-term operations, future waste site remediation, and final closure activities for the inactive disposal facilities.

1.2 Scope

Specifically, this report contains all the geologic, geochemical, hydrological, geophysical, and selected physical characterization data collected on vadose zone sediment recovered from four boreholes placed within the BC Crib and trenches area [C4191, C5923, C5924, and C5925]. Also provided is interpretation of the data in the context of determining the appropriate lithologic model, the vertical extent of contamination, the migration potential of the contaminants that still reside in the vadose zone, and the correspondence of the contaminant distribution in the borehole sediment to groundwater plumes in the unconfined aquifer proximate and downgradient from the BC Cribs and Trenches area.

1.3 Report Organization

This report covers the recently acquired data for the noted four boreholes; up to two additional boreholes may be emplaced in the future to allow more "ground truthing" of the field electrical resistivity data. If additional boreholes are emplaced, the results would be documented in a revision of this technical report. Additional hydraulic characterization testing (e.g., hydraulic conductivity both saturated and

unsaturated) is also being collected on intact cores from borehole C5923 to augment information on vadose zone water transport and allow correlation between sediment hydraulic, physical, electrical, and geochemical parameters. The correlation exercises relate to a new concept called pedotransfer functions wherein one develops correlations between more readily measured (i.e., less expensive or less time consuming) and more difficult-to-measure parameters. These additional studies and pedotransfer functions derived from adding the new data to existing Hanford data will likely be documented in a separate report.

This document describes the laboratory characterization data collected by Pacific Northwest National Laboratory (PNNL) and field data collected by hydroGEOPHYSICS, Inc [HGI] located in Tucson, AZ. Data were interpreted in concert by both organizations and were ably reviewed by Fluor Hanford, Inc. (FHI) staff, their consultants, and U.S. Department of Energy Richland Operations (DOE-RL).

This report is divided into sections that describe the geology, geochemical characterization methods, field and laboratory geophysical methods and materials, and geochemical and geophysical results by borehole, as well as summary and conclusions, references, and Appendices A and B with additional details including borehole driller's logs and sediment grab-sample photographs.

1.4 BC Cribs and Trenches Field Electrical Resistivity Characterization (ERC) "Ground Truthing"

A diverse group of Hanford stakeholders agreed upon activities required to ground truth the field electrical resistivity data with the Data Quality Objectives (DQO) process. A consensus document (Benecke 2008), entitled "Data Quality Objectives Summary Report for the BC Cribs and Trenches Area – High-Resolution Resistivity (HRR) Correlation (DQO)" was prepared after several meetings of a diverse group of Hanford stakeholders and technical experts. Other details such as sampling and parameter analysis requirements were documented in DOE/RL-2007-13, Rev. 0, *Sampling and Analysis Plan for Electrical Resistivity Correlation for the BC Cribs and Trenches Area Waste Site.*

The DQO process led to the following three key questions that needed to be answered:

1. **Do ERC data generally correlate with vadose zone COC plumes that are established by analyses of borehole sediment samples?**

2. **Is the correlation of ERC and laboratory analytical data sufficient to use ERC to assist in updating the existing conceptual site models [CSM] and evaluating remedial alternatives?**

3. **Is ERC data interpretation useful for guiding vadose zone sediment sampling for targeted COCs?**

To answer these three questions, the following actions were needed:

1. Estimate the degree of correlation between ERC data and the distribution (i.e., concentration and location) of targeted COCs in the vadose zone.

2. Determine whether ERC and analytical data correlate sufficiently to use ERC data to assist in updating the existing CSM and evaluating remedial alternatives.

3. Determine whether ERC data interpretations are useful for guiding vadose zone sediment sampling for targeted COCs.

Tables 3-1 and 3-4 in the DQO document list the information required to resolve the decision statements identified above. Table 3-1 lists the important physical and geochemical data that could be collected on the sediment samples obtained from the proposed boreholes. Table 3-4 lists the key COCs at the BC Cribs and Trenches that should be measured in the sediment samples obtained from the boreholes. Additional physical and geochemical data are listed in Table 3-2 of the DQO document for parameters that are not required for ERC evaluation, but are useful for updating and further developing the conceptual site model (CSM). Table 3-3 in the DQO indicates whether the data already exist, and when they do exist, source references are provided for data that already exist. In general, Table 3-3 in the DQO shows that for many parameters, there are no data or only data of low quality and quantity. Thus, they are insufficient to resolve the associated decision statements.

Therefore, a drilling and sampling program was developed with a potential for five new boreholes in the vadose zone of the BC Cribs and Trenches Area. Accommodations were also made to collect additional data on key contaminants of potential concern (COPCs) and sediment hydraulic properties to augment future focused feasibility studies (FFSs) of remedial alternatives. Furthermore, the boreholes could be deepened and converted to groundwater monitoring wells if necessary to collect saturated zone data, or the boreholes could be converted into vadose zone injection wells wherein dry air is pumped in to desiccate the sediments to lower the transport of contaminants through the vadose zone.

The key focus of the ERC ground-truthing efforts were 1) to gather and characterize vadose zone sediment samples from the boreholes that were strategically located where apparent resistivity anomalies of varying intensity were found with the ERC ground-surface geophysical surveys and 2) to measure the concentrations of COCs and develop the distribution of mobile risk-based COCs in sediment samples from the boreholes. The DQO document explains the process for evaluating ERC geophysical interpretations by comparing the vertical and lateral extent of the ERC anomalies to the vadose zone pore-water concentrations of major cations and anions and mobile COCs in the vadose zone of the BC Cribs and Trenches Area. Analyses of sediment samples from outside the ERC anomaly are intended to assess the potential for ERC data interpretations to produce a "false negative."

Sediment analytical data from the new boreholes were compared to corresponding ERC data. The proposed new borehole locations are shown in Figure 1.1. The purpose of each borehole is described below. The planned total depth of each borehole depends on its location, but no borehole was planned to extend beyond the water table. For boreholes that are not planned to intercept the water table, drilling was continued below the ERC anomaly until field-screening and/or "quick turnaround" laboratory analyses indicated that sediment electrical conductivity, and water-extractable nitrate and technetium-99 has returned to background values.

Borehole A (C5923) is located between the cribs and trenches near an area where FY06 ERC data were interpreted as a "pantleg effect" (i.e., a "false positive" image showing diagonally downwarded target's edges) at a depth of approximately 70 meters below ground surface (bgs). Drilling for Borehole C5923 (A) reached a depth of 110 m (361 ft) bgs and reached the water table at 106.9 m (350.6 ft) bgs. One groundwater sample was taken before the deeper portion of the borehole was decommissioned. Borehole B (C5924) and proposed borehole D (C5926) are located where ERC data indicate lower or no COC concentrations in the deeper vadose zone. The total depth for Borehole C5924 (B) was 248 ft bgs (75.6 m bgs), which is approximately 10 meters (32.8 ft.) deeper than the base of the ERC apparent resistivity anomaly at that location. Borehole D (C5926) (if drilled) would be located east of Trenches 216-B-25 and 216-B-26, outside the lateral perimeter of the ERC apparent resistivity anomaly. The total

required depth for ERC evaluation in Borehole D is approximately 196.9 ft. (60 meters) bgs because the nearby ERC apparent resistivity anomaly extends to approximately 50 meters bgs. Borehole C (C5925) and Borehole E (C5927) if it is drilled are located where ERC data indicate relatively higher COC concentrations at deeper depths in the vadose zone. The total depth for Borehole C was approximately 62.2 meters (204 ft) bgs. Drilling at Borehole E might be continued until the water table is encountered should a decision be made to drill this borehole. However, in fiscal year (FY) 2008, only three wells (C5923, C5924, and C5925) were drilled, and subsequent sediments samples were collected. The first vadose zone sediment samples were taken at a depth of 1.5 m (5 ft) bgs in each borehole, near the bottom of the shallower waste sites in the BC Cribs and Trenches Area. Subsequent sediment samples were taken at depth intervals of 0.76 meters (2.5 ft) until the total depth of each borehole was reached. Selected sediment samples were analyzed for ERC evaluation and/or CSM updating. Other sediment samples were archived. Groundwater samples were collected from the two boreholes that encountered the water table (C5923 and C4191). Summary information on all four boreholes is given in Table 1.1.

1.5 Early Efforts to "Ground Truth" the ERC Method

In late 2003, vadose zone sediment samples were collected at 0.76-meter (2.5-foot) intervals from Borehole C4191 that was drilled in the approximate center of Trench 216-B-26 (see Figure 1.1 for the location). The EC of pore-water extracts from 39 of the sediment samples from depths of 5.3 to 104 meters (17.3 to 341 ft) bgs was compared to concentrations of technetium-99, uranium-238, sodium, calcium, potassium, magnesium, fluoride, chloride, nitrate, and sulfate. The comparison was based on waste inventory data in DOE (1996). After borehole C4191 was drilled, HGI was subcontracted to perform a surface-based soil resistivity survey of the BC Cribs and Trenches area so that this ERC technique could be compared with the laboratory data obtained from the sediment samples from C4191. The details on the surface-based ERC are found in several internal contractor reports and nicely summarized in Rucker and Benecke (2006). HGI compared their apparent soil resistivity (HRR) field data with the laboratory-calculated pore-water concentrations of individual constituents using linear regression and found correlation coefficients of 0.85 to 0.89 for technetium-99, sodium, calcium, magnesium, chloride, and nitrate. Correlation coefficients for potassium and sulfate were positive, but less than 0.65. Negative correlation coefficients of -0.12 and -0.24 were calculated for uranium-238 and fluoride, respectively. A correlation coefficient of 0.9 was calculated between EC and the total ionic strength. HGI indicated that nitrate and sodium provided most of the total ionic strength of pore water. The ERC correlation results for Borehole C4191 represent a comparison in a single relatively high concentration area directly under a waste disposal site. A key conclusion of this early analysis was that the correlation of ERC and sediment analytical data should be further evaluated in other portions of the vadose zone in the BC Cribs and Trenches Area. Thus, the activities documented in the DQO and additional tasks described in this report were performed. Additional details on the preliminary correlation of ERC data with sediment pore water from borehole C4191 can be found in Rucker and Benecke (2006).

2008/DCL/BC Crib/001 (07/13)

Figure 1.1. Location of the Boreholes Either Drilled in 2003 and 2007-2008 or Proposed for Future Years

Table 1.1. Summary of BC Cribs and Trenches Drilling Information

Borehole and Well ID	Start Date	Finish Date for Drilling	Northing (m)	Easting (m)	Ground Surface (m)	Total Drill Depth (m)	Comments
A (C5923) 299-E13-62	2/19/08	7/2/08	134,361.44	573,588.14	227.43	107.29	Tagged water table at 350.6 ft bgs & sampled groundwater at 359.9 ft bgs.
B (C5924) 299-E13-63	1/30/08	2/21/08	134,69.53	573,192.36	226.20	75.59	
C (C5925) 299-E13-64	2/28/08	3/13/08	134,350.79	573,500.38	226.91	62.03	
C4191 No well # assigned	12/9/03	1/13/04	134,146.02	573,286.84	224.11	104.02	Tagged water table at 337.8 ft bgs & sampled at 338 to 340 ft bgs.

All locations are Washington State Plane Coordinates (South Zone) using NAD83(91) Horizontal Datum and NAVD88 Vertical Datum.

2.0 Geology

2.1 Regional Geologic Setting

2.1.1 Stratigraphy and Lithology

Strata within the Pasco Basin and Hanford Site can be divided into five stratigraphic units: 1) Recent deposits, 2) Hanford formation, 3) Cold Creek unit, 4) Ringold Formation, and 5) Columbia River Basalt Group. More detailed descriptions on the regional geology are provided in a number of other reports (Tallman et al. 1979; DOE 1988, 2002; Lindsey et al. 1992; Lindsey 1995; Reidel et al. 1994; Williams et al. 2000, Reidel and Chamness 2007). A regional geologic cross section showing the general stratigraphic relationships of the suprabasalt sediments within the vadose zone is presented in Figure 2.1.
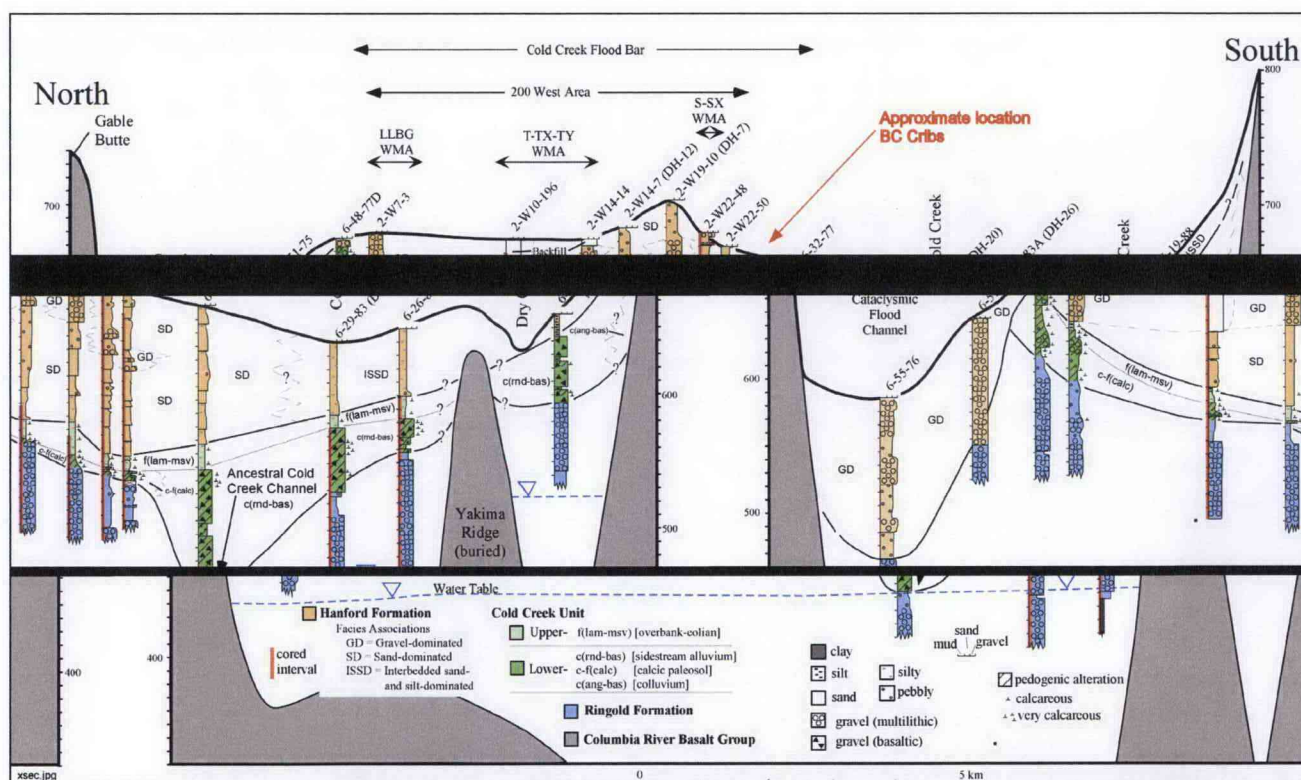
Figure 2.1. North-South Geologic Cross Section Across the Western Hanford Site (after DOE 2002). See Figure 2.2 for location. Strata at BC Cribs are comparable to those illustrated about midway and ~4 miles out of line with this cross section.

2.1.1.1 Columbia River Basalt Group

Miocene Columbia River basalt forms the basement rock over most of eastern Washington, derived from north-south trending volcanic vents in southeast Washington, northeast Oregon, and west-central Idaho (DOE 1988; Reidel and Hooper 1989). Up to 300 separate basaltic lava flows accumulated to

15,000 ft thick within the Pasco Basin. The earliest flows of Columbia River basalt reached the Pasco Basin about 17 million years ago and the last about 8.5 million years ago. During and since their eruption, flows of Columbia River basalt have been folded into a series of east-west trending anticlines and synclines, referred to as the Yakima Fold Belt.

2.1.1.2 Ringold Formation

The Ringold Formation blankets Columbia River basalt over most of the Pasco Basin. The Ringold Formation records fluvial-lacustrine deposition associated with the ancestral Columbia River drainage system, following the last eruption of basalt at the Hanford Site about 8.5 m.y. ago (DOE 1988, Lindsey 1995). Deformation of the Yakima folds, which began in the middle Miocene Epoch, concurrent with the Columbia River basalt volcanism, continued into Ringold time so the centers of down-warped basins received more sediments than the margins. The Ringold Formation is up to 600 ft (185 m) thick in the center of the basin and pinches out against the basin-bounding basalt ridges.

The Ringold Formation consists of semi-indurated clay, silt, fine- to coarse-grained sand, and variably cemented granule to cobble gravel. Ringold Formation sediments have been classified into five sediment facies associations: 1) fluvial gravel, 2) fluvial sand, 3) overbank deposits, 4) lacustrine deposits, and 5) alluvial fan deposits. More detailed descriptions of these facies are presented in Lindsey (1995). Most of the unconfined aquifer in the Pasco Basin lies within the member of Wooded Island (Unit E) of the Ringold Formation.

2.1.1.3 Cold Creek Unit (CCU)

The Cold Creek unit represents deposits that accumulated within the central Pasco Basin from about 2 to 3 million years ago, which brackets two significant geologic events. The older event is a regional base-level drop and subsequent incision of the Ringold Formation (DOE 1988). The younger event is the initiation of Ice Age cataclysmic flooding, which began at the beginning of the Pleistocene, about 1.5 to 2.5 million years ago (Bjornstad et al. 2001; Bjornstad 2006).

The accumulation of the Ringold Formation ceased abruptly beginning about 3.4 million years ago, during a period of rapid downcutting and incision by the ancestral Columbia-Snake River system (Fecht et al. 1987; DOE 1988; Reidel et al. 1994). Incision resulted in the removal of up to 600 ft of Ringold Formation sediments from the central portion of the Pasco Basin. Following incision, a new local base level was established at approximately the 100-m (300-ft) elevation at Wallula Gap. At this point, significant fluvial erosion and incision of the Ringold Formation ceased, once again permitting aggradation and backfilling to occur locally on the post-Ringold Formation landscape.

After this period of post-Ringold incision, the eroded surface of the Ringold Formation was locally weathered and/or covered with accretionary deposits of the CCU. These deposits consist of fluvial, eolian, and/or colluvial sediment, often pedogenically altered (DOE 2002). The CCU includes those deposits formerly referred to as the "Plio-Pleistocene unit" and "pre-Missoula Gravels," as well as the "early Palouse soil" and "caliche layer" within the 200 West Area. The new name, Cold Creek unit, was given to these deposits because more-recent studies suggest this unit is mostly or all of late Pliocene age (DOE 2002).

Five CCU lithofacies can be differentiated on the basis of grain size, sedimentary structure, sorting, roundness, fabric, and mineralogic composition. The five facies, along with interpreted depositional environment, are listed in Table 2.1.

Table 2.1. Lithofacies of the Cold Creek Unit (after DOE 2002)

Lithofacies	Symbol	Environment of Deposition
Fine-grained, laminated to massive	CCUf(lam-msv)	Fluvial-overbank and/or eolian
Fine- to coarse-grained, calcium-carbonate cemented	CCUf-c(calc)	Calcic paleosol
Coarse-grained, multilithic	CCUc(mL)	Mainstream alluvium
Coarse-grained, angular, basaltic	CCUc(ang-bas)	Colluvium
Coarse-grained, rounded, basaltic	CCUc(rnd-bas)	Sidestream alluvium

Some Cold Creek unit deposits appear to be present beneath most of the central Pasco Basin, except where it was locally stripped away during subsequent Pleistocene cataclysmic flooding. Ice Age flooding locally removed older sediments and scoured into basalt bedrock, particularly through the central Pasco Basin where the floodwaters were the most active. Around the margins of the basin, however, little or no erosion of the Cold Creek unit occurred during flooding.

2.1.1.4   Hanford Formation

The Hanford formation is an informal name assigned to Pleistocene cataclysmic flood deposits within the Pasco Basin (Tallman et al. 1979; DOE 1988, 2002). Ice-Age floods originated from periodic outbursts from glacial Lake Missoula and other Pleistocene water bodies (Bjornstad 2006). The Hanford formation consists predominantly of unconsolidated sediments that cover a wide range in grain size and sorting, from poorly sorted boulder-size gravel to better-sorted sand, silty sand, and silt. The sorting ranges from poorly sorted for coarse-grained to well sorted for fine-grained flood deposits. In general, the Hanford formation is subdivided into three principal facies: 1) gravel-dominated (GD), 2) sand-dominated (SD), and 3) interbedded sand- and silt-dominated (ISSD). These facies may grade into one another, both laterally as well as vertically.

GD flood deposits formed toward the center of the basin where currents and energy were the strongest. Here smaller particles were kept in suspension by the fast moving, highly turbulent flood waters. As flood energy decreased toward the margins of the basin, flood deposits transitioned laterally to the SD and ISSD facies (Figure 2.1). Because of the widely different and complex flow dynamics during Ice Age flooding, Hanford formation strata are extremely heterogeneous and anisotropic (DOE 2002; Bjornstad 2006). The bulk of the vadose zone within the Pasco Basin and the Hanford Site lies within sediments of the Hanford formation.

During Ice Age flooding, sediments accumulated onto the huge Cold Creek Bar (Figure 2.2), which makes up the 200 Area Plateau. Cold Creek Bar is a major floods' landform, up to 12 miles long and several miles wide, that grew during repeated Ice Age floods that expanded into the basin and dropped their sedimentary load. Cold Creek Bar grew as sediments were episodically laid down in series of

perhaps hundreds of floods spanning a million years or more (Pluhar et al. 2006). The north edge of the bar received mostly coarse-grained gravel and sand (GD facies) while the central and southern portions of the bar received thick blankets of sand intercalated with thin beds of silt (SD facies). Further to the south, ISSD facies were deposited in areas of increased slack-water sedimentation (Figure 2.1).
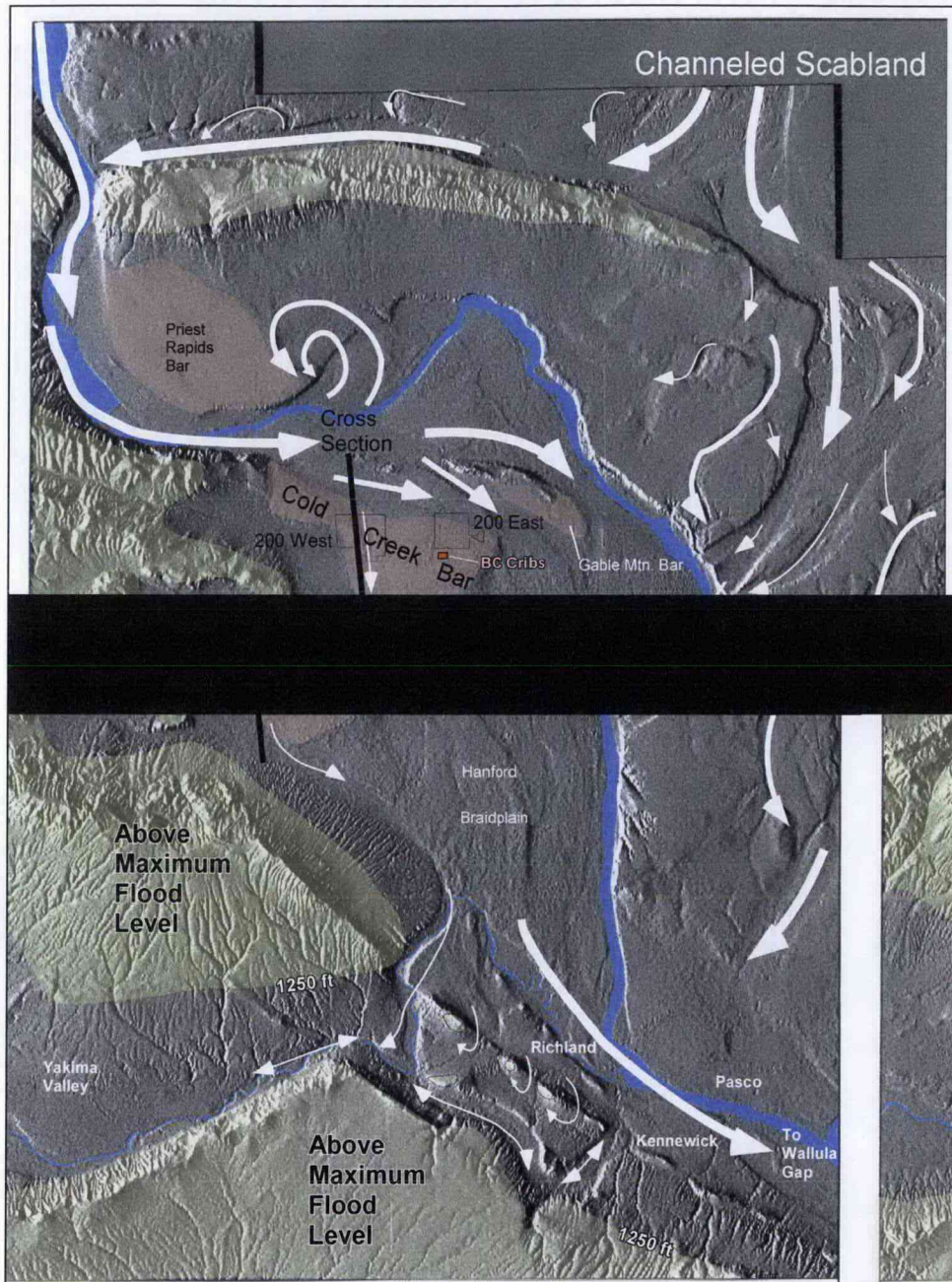
Figure 2.2. BC Cribs and Trenches Area in Relation to Ice Age Flood Features Within the Central Pasco Basin. The BC Cribs and Trenches Area lies atop the 12-mile-long and 300-ft-thick Cold Creek flood bar. See Figure 2.1 for a geologic profile across the bar.

Along the northern 200 Area Plateau, two sequence of coarser, GD facies are separated by SD facies. In some studies (e.g., Reidel and Chamness 2007) the SD facies has been assigned the Hanford formation H2 unit, while the upper and lower GD facies are designated H1 and H3, respectively. However, along the southern margin of the 200 Area Plateau, the GD facies grade laterally into a single thick sequence of SD facies, like that at BC Cribs.

Unlike other stratigraphic units, the stratigraphy of the Hanford formation is extremely complex. This is primarily due a dynamic, constantly changing environment of deposition and erosion that took place with each Ice Age flood. With evidence for up to hundreds of separate Ice Age flood events, and the variable sedimentation that occurred during each flood, the variability is understandable. The end result is a diverse assemblage of layered, heterogeneous strata, especially within the SD and ISSD facies of the Hanford formation, which behave anisotropically with respect to movement of vadose-zone moisture and contaminants.

2.1.1.5 Recent Deposits

Recent deposits within the Pasco Basin include Holocene-age eolian deposits of sand and loess (windblown sand and silt), alluvium, and mass-wastage deposits (i.e., slopewash and talus). Other recent deposits are anthropogenic (e.g., backfill) deposits laid down on the surface over waste-management areas.

2.1.2 Structure

The Pasco Basin is defined by uplifted basalt ridges (Rattlesnake Mountain and Saddle Mountains) of the Yakima Fold Belt. The Yakima Fold belt is characterized by a series of segmented, narrow, asymmetric east-west trending anticlines. The northern limbs of these anticlines generally dip steeply to the north and are vertical or even overturned; thrust or high-angle reverse faults with fault planes that generally parallel fold axial trends occur on the north sides of these anticlines. The southern limbs of Yakima folds dip gently to the south. The anticlinal ridges are separated by broad synclines or basins that, in many cases, contain thick accumulations of Neogene- to Quaternary-age sediments.

Clastic dikes are vertical to subvertical sedimentary structures that crosscut normal sedimentary layering that are common to ice-age flood deposits, especially in the SD and ISSD facies of the Hanford formation (Fecht et al. 1999). Clastic dikes are much less common in the GD facies of the Hanford formation.

Where clastic dikes intersect the ground surface and are not covered with younger deposits, a feature known as patterned ground can be observed (Fecht et al. 1999). Clastic dikes occur in swarms with 4- to 8-sided polygons that range from 3 cm to 1 m in width, from 2 m to greater than 20 m in depth, and from 1.5 to 100 m along strike. Smaller dikelets, sills, and small-scale faults and shears are commonly associated with master dikes that form the polygons.

In general, a clastic dike has an outer skin of clay with coarser infilling material. Clay linings are commonly 0.03 mm to 1.0 mm in thickness, but linings up to about 10 mm are known. The width of individual infilling layers ranges from as little as 0.01 mm to more than 30 cm, and their length can vary from about 0.2 m to more than 20 m. Infilling sediments are typically poor- to well-sorted sand, but may contain clay, silt, and gravel.

2.2 Geologic Setting of the BC Cribs

2.2.1 Stratigraphy and Lithology

The stratigraphy and lithology in the vicinity of the BC Cribs and Trenches is illustrated in two hydrogeologic cross sections (Figure 2.3). Cross section A-A' (Figure 2.4) is a north-south profile over a larger area, compared to cross section B-B' (Figure 2.5), an east-west profile in the immediate vicinity of the BC Cribs and Trenches. A more detailed location map for BC Cribs and Trenches and cross section B-B' is presented in Figure 2.6. Background information on the boreholes used to construct these cross sections is presented in Table 2.2.
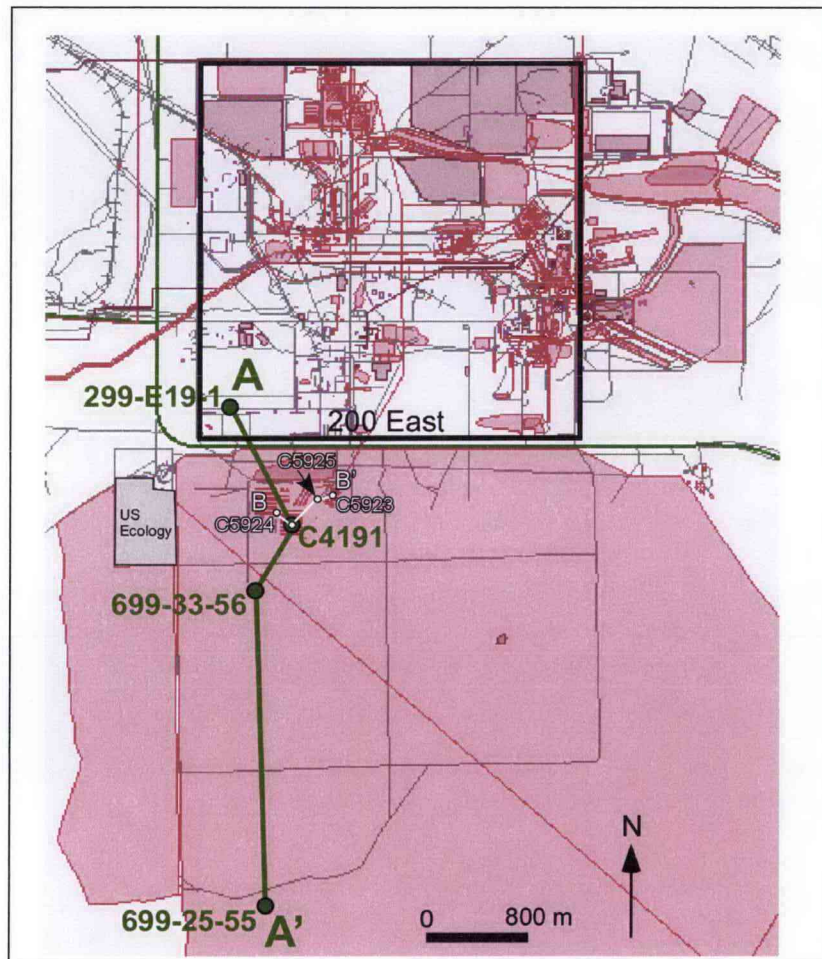
Figure 2.3. Location of Hydrogeologic Cross Sections. See Figure 2.6 for more detailed location of cross section B-B'.
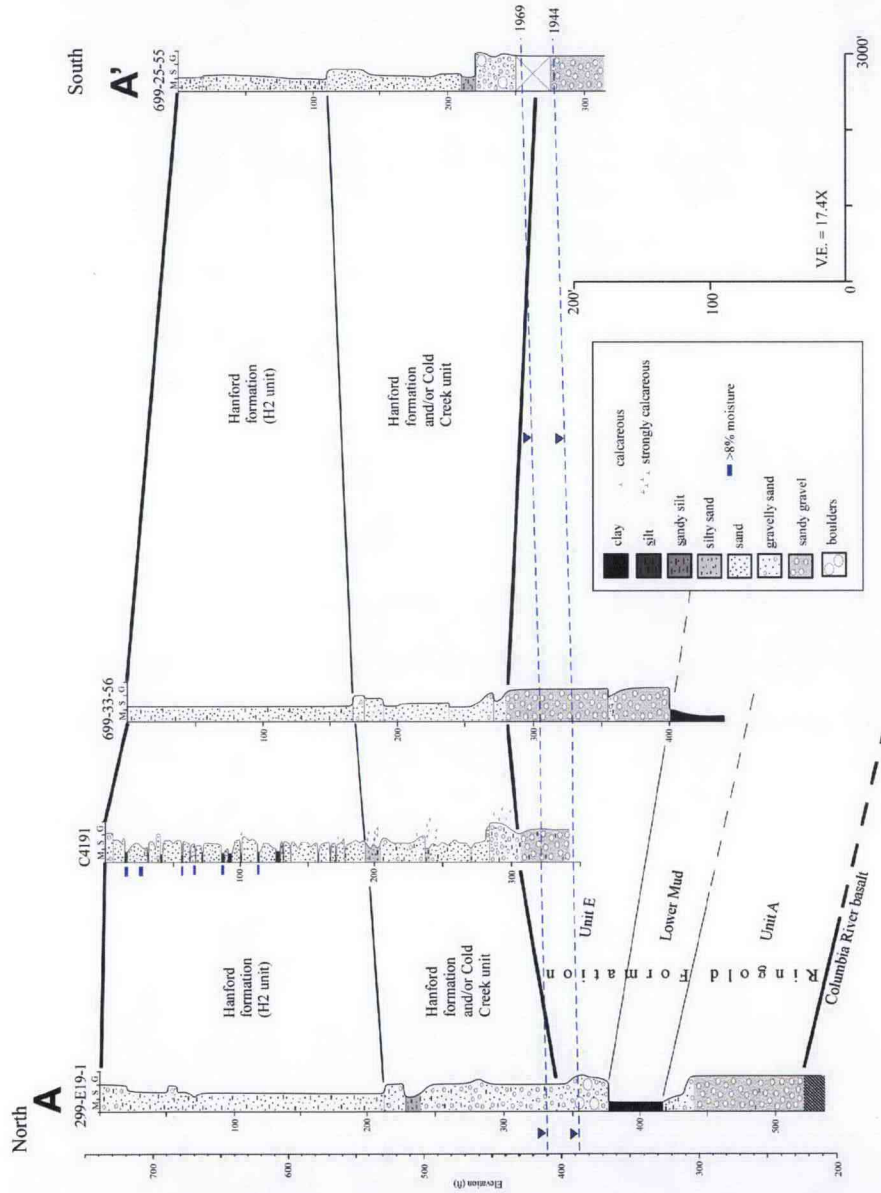
Figure 2.4. Hydrogeologic Cross Section A-A'
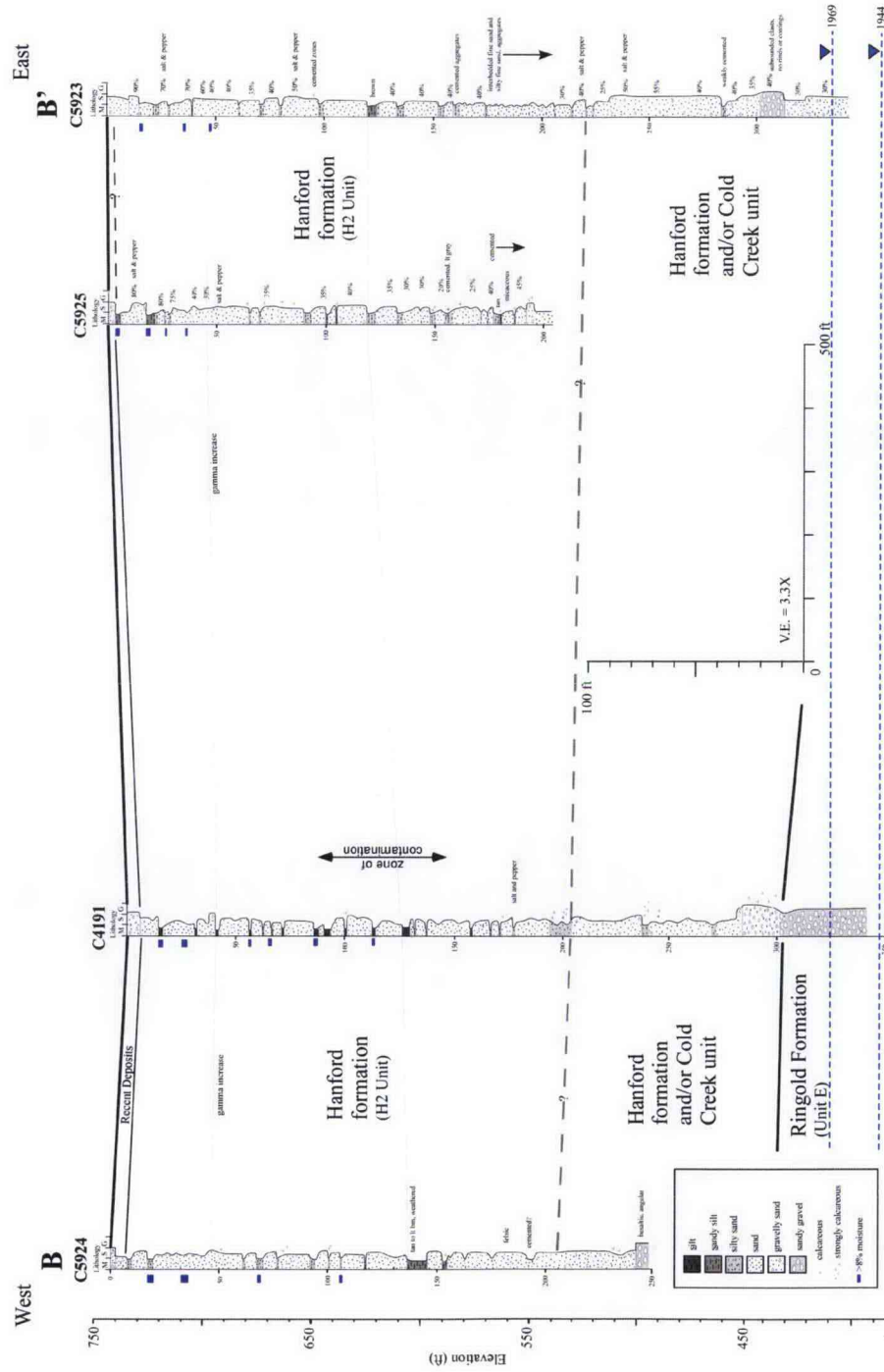
Figure 2.5. Hydrogeologic Cross Section B-B'. See Figure 2.6 for location.
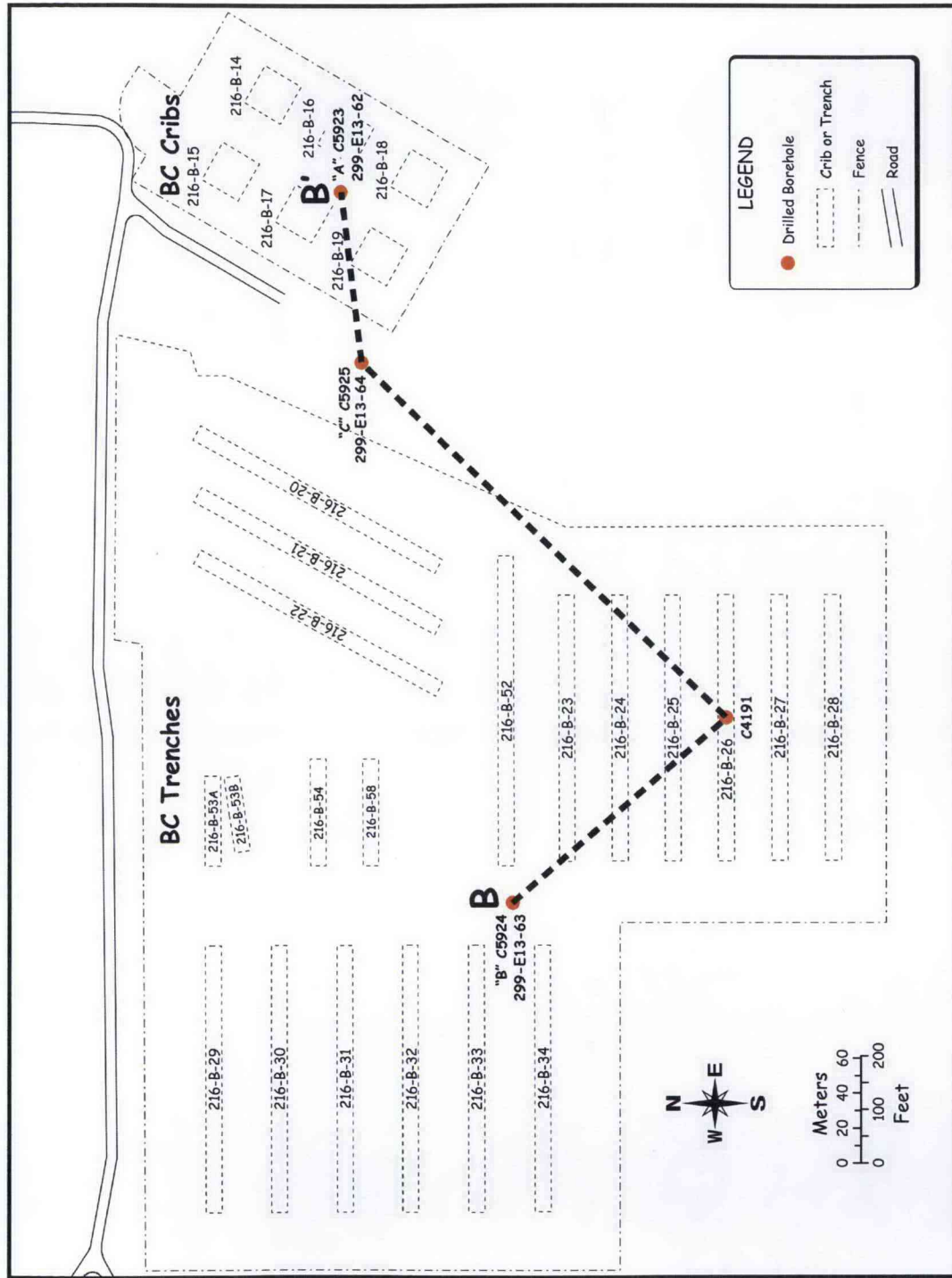
Figure 2.6. BC Cribs and Trenches Area Location Map. Heavy dashed line is location for cross section B-B' (Figure 2.5).

2008/DCL/BC Crib/002 (07/23)

2.

Table 2.2. Boreholes in Vicinity of BC Cribs and Trenches Area Used in Hydrogeologic Cross Sections

Borehole ID	Borehole Name	Cross Section	Drilling completed	Surface Elevation	Total Depth (ft)	Drill Method	Geophysical Logs[a]	Comments
New Wells								
C4191		A, B	1/04	735	341	Cable tool	TG, SG, NM	Groundwater sample taken before Decommissioning; 14 split spoon samples
C5923	299-E13-62	B	7/08	746	352	Cable tool	TG, SG, NM	Groundwater sample taken ; 19 split-spoon cores that yielded 39 "intact" liner samples
C5924	299-E13-63	B	2/08	742	248	Cable tool	TG, SG, NM	
C5925	299-E13-64	B	3/08	744.5	203.5	Cable tool	TG, SG, NM	
Older Wells								
A5889	299-E19-1	A	12/57	739	368/536	Cable tool/ diamond rotary core		Core from 368-536 ft in 1977
A5133	699-33-56	A	10/58	720	440	Cable tool		
A5098	699-25-55	A	7/48	680	315	Cable tool		

(a) TG = total gamma; SG = spectral gamma; NM = neutron moisture

The strata beneath the BC Cribs and Trenches Area are divided into five units: 1) Recent deposits, 2) Hanford formation, 3) Hanford formation/Cold Creek unit (undifferentiated), 4) Ringold formation, and 5) Columbia River basalt. The following is a description of these strata, from oldest to youngest.

2.2.1.1 Columbia River Basalt Group

Bedrock beneath the BC Cribs and Trenches area consists of black, volcanic rock belonging to the Miocene-age Columbia River Basalt Group. The youngest basalt flow beneath the BC Cribs and Trenches area belongs to the Elephant Mountain Member, dated at 10.5 million years before present. None of the new borings were drilled deep enough to reach basalt; however, the depth and attitude of the basalt is generally known from deep wells drilled to the north within the 200 East Area (see cross section A-A' in Figure 2.4).

2.2.1.2 Ringold Formation

Only one of the four new boreholes (C4191) at the BC Cribs and Trenches area penetrated deep enough to intersect the Ringold Formation. Older, nearby boreholes (Figure 2.4), on the other hand, penetrate deeper into the Ringold Formation. These wells show that the top of basalt and the Ringold Formation dip southward toward the axis of the Cold Creek Syncline. Beneath the BC Cribs and Trenches, two sequences of fluvial Ringold Formation gravel (Unit A and Unit E) are separated by a thick sequence of fluvial-lacustrine silt and clay, known as the Ringold Formation lower mud unit (Lindsey 1995).

Within the BC Trenches, only one of the boreholes (C4191) encountered the Ringold Formation (i.e., sandy gravel facies of the Ringold Formation [Unit E]) at a depth of about 300 ft bgs. One of the grab samples from this unit is shown in Figure 2.7.

Figure 2.7. Silty Sandy Gravel of the Ringold Formation Unit E in borehole C4191, 321 ft Depth. The combination of unbroken clasts that are well rounded and have low basalt content, overall brown color, and cementation characterize this sediment as Ringold Formation.

Characteristics used to identify the Ringold Formation Unit E are 1) bimodal pebble-cobble gravel in a well-sorted fine- to medium-grained sand matrix, 2) well rounded and polished gravel clasts, 3) weathering rinds and clay skins around gravel clasts, 4) quartzo-feldspathic matrix with normally <20% mafic grains, 5) pervasive, rusty orange stain on sand and gravel, and 6) slight-to-moderate consolidation or cementation. Sand grains in fluvial facies of the Ringold Formation are predominantly quartz and feldspar, derived from erosion of older, silicic and felsic basement rocks around the perimeter of the Columbia Plateau.

2.2.1.3 Hanford Formation/Cold Creek Unit (Undifferentiated)

Above the sandy gravel facies of Ringold Formation Unit E is a sedimentary sequence, up to 33 m (100 ft) thick, of sand to gravelly sand with occasional layers of fine-grained silty sand. The basalt (i.e., mafic) content of the sand fraction is generally ~20 to 40 volume %, which is typically greater than that observed in the Ringold Formation, but less than typical for the Hanford formation. Furthermore, these deposits are overall less weathered and generally lack the pervasive iron-stained coatings, weathering rinds, and clay skins that are typical of the Ringold Formation. There are some calcic zones, especially in C4191, which are atypical of the Ringold Formation. In summary, this sequence is distinctly different from the underlying Ringold Formation and lacks regular graded bedding, which is characteristic of the overlying Hanford formation. Therefore, the coarser gravelly strata are believed to be all or part of the mainstream alluvial facies of the Cold Creek unit (CCUc[mL]), formerly referred to as pre-Missoula gravels (Table 2.2).

The upper portion of this sequence may be all or in part equivalent to a coarser-grained facies of the Hanford formation, deposited early in the history of Ice Age flooding before the Cold Creek flood bar had grown appreciably (Figure 2.8). With the information available, it is unclear where the CCU alluvium

ends and the Ice Age flood deposits of the Hanford formation begin. Thus this sequence, for the time being, is referred to as Hanford formation/CCU (undifferentiated). A higher basalt content, subrounded

Figure 2.8. Gravelly Sand of the Hanford Formation/Cold Creek Unit (Undifferentiated) Sequence from Borehole C5923, 303 ft Depth

to subangular gravel clasts and less weathering, indicates that these sediments are younger and separate from the Ringold Formation (Figure 2.9).

Figure 2.9. Moderately Sorted, Medium- to Coarse-Grained Sand of the Hanford Formation/CCU (Undifferentiated) from Borehole C4191, 266 ft Depth. The moderate number of basalt grains (~20 volume %) in this sample distinguishes this from almost pure, light-colored quartzo-feldspathic sand of the Ringold Formation and the more-concentrated basaltic sand of the Hanford formation.

2.2.1.4　Hanford Formation

Several excavations exposing the Hanford formation are located near the BC Cribs and Trenches (Figure 2.10). These include Hanford's Integrated Disposal Facility (IDF) to the northeast, the U.S. Ecology disposal trenches (Smith 1993) immediately to the west, and the Environmental Restoration Disposal Facility (ERDF) farther to the west. These excavations have produced excellent exposures for evaluating the stratigraphy of the uppermost 50 ft of the Hanford formation. Since these sites all lie near the same elevation along the Cold Creek flood bar (Figure 2.2) and within a similar depositional environment with respect to the Ice Age floods, they should be very similar to the sediments deposited in the uppermost 50 ft at the BC Cribs and Trenches area.
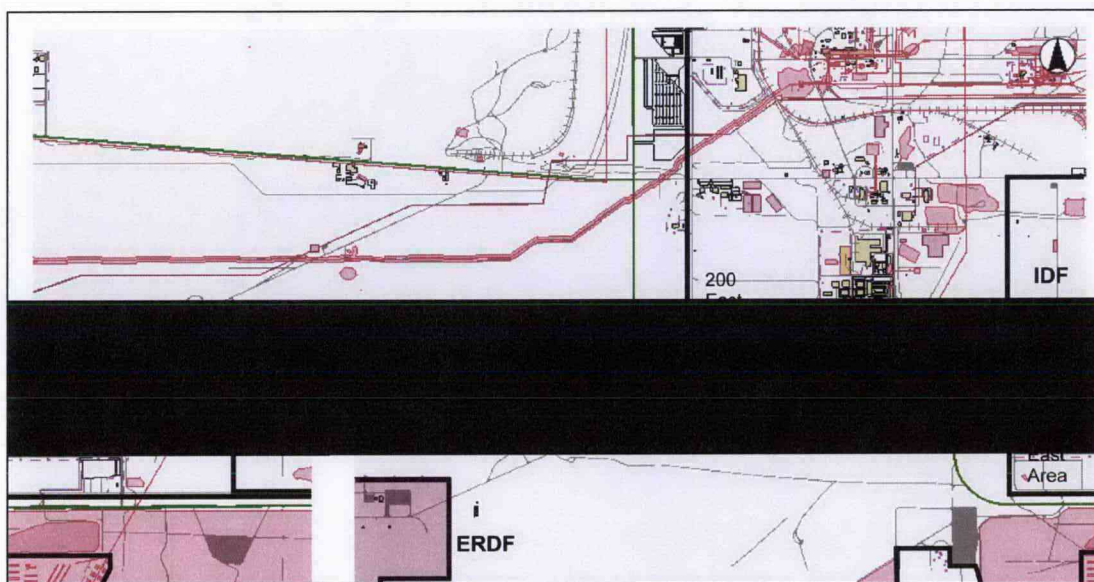
Figure 2.10.　Nearby Excavations and Analog Sites for the Hanford Formation Near the BC Cribs and Trenches. ERDF = Environmental Restoration Disposal Facility, IDF = Integrated Disposal Facility

A thick sand-dominated sequence of the Hanford formation (H2 unit), dominates the vadose zone beneath the BC Cribs and Trenches area. Internally, this sequence appears to contain multiple beds of fine- to coarse-grained sand up to several meters thick. Typically, sand-dominated facies average about 50% mafic (i.e., basalt) and 50% quartz-feldspar (Tallman et al. 1979). The coarser sands typically have a higher basalt content and are commonly referred to as "salt-and-pepper" sands and are generally shades of gray. This is a direct result of the coarser units being derived from the extensive erosion of the Columbia River basalt, which underlies the Channeled Scabland, by the Ice Age floods. Sand-dominated deposits of the Hanford formation typically display horizontal-to-ripple laminations in outcrops (Figure 2.11). Normal and reverse grading between different sand sizes is common, adding to the heterogeneity and anisotropy of this facies type. Reverse grading is common between strata in the SD facies and may represent pulsations or surges during flooding.

The thick beds of sand may grade back and forth between coarse sand to fine sand multiple times before finally grading up into a silty fine sand to silt textured cap (Figure 2.12 and Figure 2.11). The finer-grained layers typically contain a higher proportion of quartz, feldspar, and mica, resulting in a more brown color (Figure 2.11). Finer-grained materials present in the Hanford formation H2 unit produce

higher moisture retention (10 to 15 wt%) due to naturally higher capillary forces present in these types of sediments. Fine-grained flood deposits, however, are derived principally from reworked quartzo-feldspathic deposits of Palouse loess, and/or other older fluvial or glaciofluvial deposits eroded along the flood path. During flooding, these finer-grained materials remained suspended within the floodwaters, some of which settled out of suspension in slack-water environments during the waning stages of flooding.

The texture and thickness of graded beds in the area appear to decrease upward within the Hanford formation H2 unit. This is apparent in cross section B-B' (Figure 2.5) and clearly visible at the U.S. Ecology excavation (Figure 2.13). The overall fining and thinning of beds is probably related to Ice Age floods that became progressively smaller at the end of the Ice Age (Waitt 1980). This is significant to moisture and contaminant migration since there is an increased likelihood for lateral spreading in the upper Hanford formation H2 unit. This is due to a higher frequency of fine-grained, silty, slack-water beds in the upper part of the Hanford formation. Flood beds that are thicker and coarser downsection have proportionately less fine-grained beds to cause lateral spreading.

In continuous outcrops, such as that exposed at U.S. Ecology (Figure 2.13), fine-grained facies appear to be laterally continuous and can be traced laterally for hundreds of feet. However, using borehole information, it is difficult to correlate individual beds with confidence from one borehole to another. One exception at the BC Cribs and Trenches area is a relatively thick (up to 15 ft) of fine silty sand to sandy silt, which lies at a depth of ~120 to 130 ft bgs (Figure 2.5) and may be correlative across the site. This thick fine-grained layer lies within the zone of elevated ^{99}Tc and electrical conductivity observed in borehole C4191. Another correlative boundary within the Hanford formation is a sudden increase in TG activity at 40 to 50 ft. There is no evidence for a distinct lithologic boundary at this depth, but it may conform to a mineralogical change from more to less basaltic sand starting at this depth.
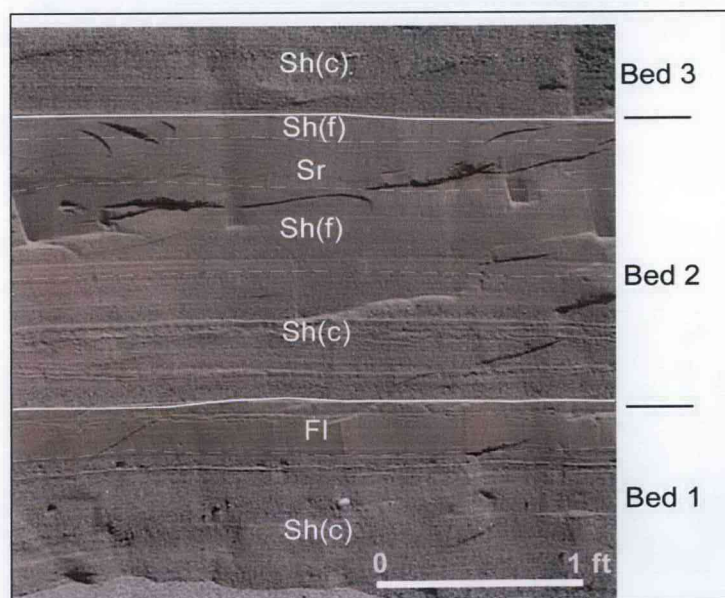
Figure 2.11. Close-up of Heterogeneous, Anisotropic Sedimentary Strata Typical of the Hanford Formation H2 Unit at ~50 ft Depth in the ERDF Excavation

Each of the three graded beds may represent as many separate Ice-Age flood events: Sh(c) = horizontally laminated medium to coarse sand deposited during initial flood pulse followed by, Sh(f) = horizontally laminated fine to medium sand, Sr = ripple-laminated fine sand, and/or finally Fl = laminated fine sand to silt, laid down during final slackwater phase of flooding. Vadose-zone moisture tends to concentrate along interfaces between strongly contrasting beds or within finer-grained strata, which have an affinity for moisture that may spread laterally.
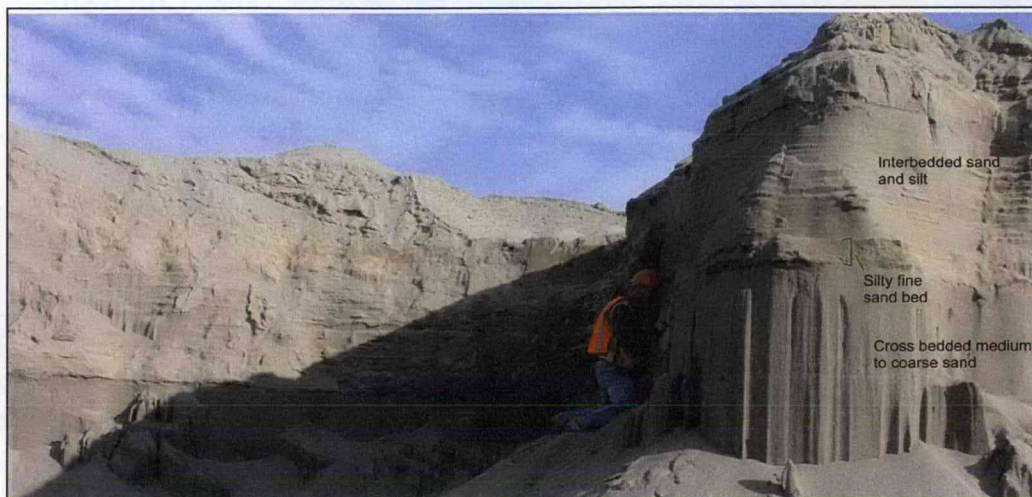
Figure 2.12. Hanford Formation H2 Unit Exposed in the IDF Excavation. Several feet of uniform medium- to coarse-grained sand are capped by a thin bed of slackwater silty fine sand. Above the worker's head are multiple layers of complexly interstratifed sandy and silty beds. These deposits are from about 30 to 40 ft depth in the excavation.
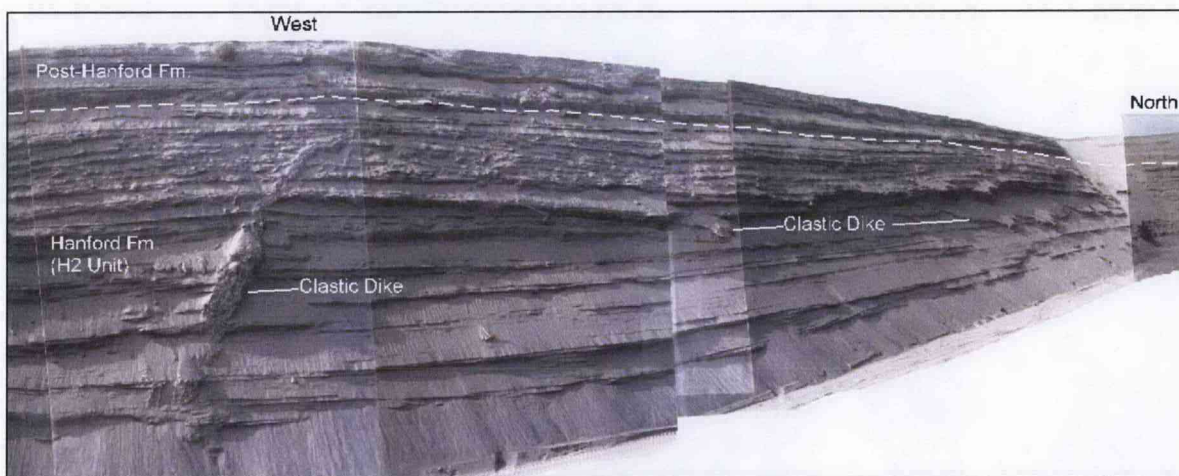
Figure 2.13. U.S. Ecology Excavation, Located Just West of BC Trenches and Cribs. Excavation is about 50 ft deep. Note lateral continuity of finer-grained beds, which are more cohesive and thus stand out with more relief along bluff face. Note that the overall thickness of the rhythmic, graded beds decreases upsection. Discordant clastic dikes cut across the bedding.

Examples of grab samples collected during drilling of the Hanford formation at BC Cribs and Trenches are shown in the photographs below. Figure 2.14 is from a bed of coarse sand especially concentrated in basalt rock fragments (~90%). This highly basaltic layer, located ~12 ft bgs, may correlate with a near-surface layer of highly basaltic sand reported at the IDF excavation (Qb layer of Reidel and Fecht 2005).

Figure 2.14. Hanford Formation (H2 Unit) from Borehole C5923, 13 ft Depth

This sample consists of predominantly coarse-grained sand, composed of up to 90% basalt rock fragments.

Figure 2.15 shows a loose, poorly sorted, gravelly, fine-to-coarse–grained sand. About 40 to 50% of sand grains are basalt rock fragments, more typical of the Hanford formation than that represented in Figure 2.14.

Figure 2.15. Gravelly, Basaltic Sand from the Hanford Formation (H2 Unit) in Borehole C5925, 78 ft Depth

Figure 2.16 shows a poorly sorted, sandy mixture of sand with abundant silty aggregates. Silty sediment is more compact and cohesive and therefore does not totally disaggregate during the process of drilling and sampling. Apparently during the drilling of this sample, multiple beds were sampled, including a layer of loose sand, along with a more cohesive silty bed resulting in the mixture of different sediment types.

Figure 2.16. Hanford Formation (H2 Unit) from Borehole C4191, 86 ft Depth. This grab sample is a mixture of sand and finer-grained aggregates derived from drilling into a silty interbed.

Figure 2.17 shows characteristic loose, moderately sorted, "salt and pepper" sands, which are the dominant lithofacies beneath the BC Cribs and Trenches area.

2.2.1.5   Recent Deposits

A few feet of anthropogenic backfill, composed of a mixture of sand and gravel, often blankets the surface of the BC Cribs and Trenches area.

2.3   Summary of Recent Characterization Activities at BC Cribs and Trenches Area

Hydrogeologic characterization of the four new boreholes at the BC Cribs and Trenches area (Figure 2.6) included the drilling of over 1,100 ft of hole via the cable-tool drill method. These holes were geologically logged in the field and also logged via down-hole spectral gamma (SG) and neutron-moisture geophysical tools. During drilling, over 480 grab sediment samples were collected in air-tight containers and transported to PNNL's Environmental Sciences Laboratory (ESL) for laboratory analysis. In the laboratory, subsamples were collected for moisture content immediately upon opening the grab samples, and high-resolution, color photographs were obtained of each sample (Appendix B). Next, standard descriptions of grain size, sorting, color, consolidation, visible moisture, mineralogy, and reaction with hydrochloric acid were entered onto geologic logs (Appendix A). Cores were archived in refrigerators until analyses of grab samples were available to guide further laboratory characterization of physical, hydraulic, and chemical properties. A listing of all the samples collected for each of the four holes is presented below.

Figure 2.17. Hanford Formation (H2 Unit) from Borehole C5923, 103 ft Depth

Note medium- to coarse-grained, salt-and-pepper sand, composed of about equal amounts of dark basalt rock fragments vs. light-colored quartz, feldspar, and mica.

The composite summary logs (Figure 2.18 to Figure 2.21), compiled from all available field and laboratory data, are also presented for each borehole. The sediment sampling frequency and efforts to examine and describe the sediments from these four boreholes greatly improved the data set for the BC Cribs and Trenches area. Before these four boreholes were drilled, very little detailed information was

available of the local stratigraphy. These logs show there is a good correlation between fine-grained, silty, slack-water beds and moisture measured both in neutron-moisture geophysical logs and moisture measured in the laboratory on the grab samples. The composite logs also show relatively large volumes of sand-dominated sediment vs. finer-grained silty beds. Even though slack-water beds make up a relatively small volume of the total Hanford formation sequence, they appear to have a large impact on the distribution and lateral movement of moisture within the vadose zone.

2.3.1   Borehole C4191

Drilling grab samples collected for physical and chemical characterization from borehole C4191 are listed in Table 2.3.

A summary hydrogeologic log, which shows an integration of all the geologic, geophysical, and moisture data collected for borehole C4191, is presented in Figure 2.18.

Table 2.3. Grab Samples Collected, Described, and Photographed from Borehole C4191

Type	Lab #	Depth	Lithology	Stratigraphic Unit
Grab	C4191-13	13	md-crs sand	Hanford fm (H2 unit)
Grab	C4191-17.5	17.5	silty fn-crs sand	Hanford fm (H2 unit)
Grab	C4191-22.5	22.5	silty fn-crs sand	Hanford fm (H2 unit)
Grab	C4191-27.5	27.5	fn sand	Hanford fm (H2 unit)
Grab	C4191-37.5	37.5	sl pebbly md-crs sand	Hanford fm (H2 unit)
Grab	C4191-41	41	silty fn sand	Hanford fm (H2 unit)
Grab	C4191-43.5	43.5	md-crs sand	Hanford fm (H2 unit)
Grab	C4191-46	46	md-crs sand	Hanford fm (H2 unit)
Grab	C4191-48.5	48.5	md sand	Hanford fm (H2 unit)
Grab	C4191-51	51	md sand	Hanford fm (H2 unit)
Grab	C4191-53.5	53.5	md-crs sand	Hanford fm (H2 unit)
Grab	C4191-56	56	md-crs sand	Hanford fm (H2 unit)
Grab	C4191-58.5	58.5	md-crs sand	Hanford fm (H2 unit)
Grab	C4191-61	61	fn-md sand	Hanford fm (H2 unit)
Grab	C4191-63.5	63.5	fn-crs sand	Hanford fm (H2 unit)
Grab	C4191-66	66	md-crs sand	Hanford fm (H2 unit)
Grab	C4191-68.5	68.5	fn-md sand	Hanford fm (H2 unit)
Grab	C4191-71	71	fn-md sand	Hanford fm (H2 unit)
Grab	C4191-73.5	73.5	md-crs sand	Hanford fm (H2 unit)
Grab	C4191-76	76	md-crs sand	Hanford fm (H2 unit)
Grab	C4191-78.5	78.5	md-crs sand	Hanford fm (H2 unit)
Grab	C4191-81	81	fn-md sand	Hanford fm (H2 unit)
Grab	C4191-83.5	83.5	md sand	Hanford fm (H2 unit)
Grab	C4191-86	86	silty fn-md sand	Hanford fm (H2 unit)
Grab	C4191-88.5	88.5	fn-md sand	Hanford fm (H2 unit)
Grab	C4191-91	91	silty fn-md sand	Hanford fm (H2 unit)
Grab	C4191-93.5	93.5	fn-md sand	Hanford fm (H2 unit)
Grab	C4191-96	96	md-crs sand	Hanford fm (H2 unit)
Grab	C4191-98.5	98.5	md-crs sand	Hanford fm (H2 unit)
Grab	C4191-101	101	md-crs sand	Hanford fm (H2 unit)
Grab	C4191-103.5	103.5	md sand	Hanford fm (H2 unit)
Grab	C4191-106	106	md-crs sand	Hanford fm (H2 unit)
Grab	C4191-108.5	108.5	md-crs sand	Hanford fm (H2 unit)
Grab	C4191-111	111	md sand	Hanford fm (H2 unit)
Grab	C4191-113.5	113.5	fn-md sand	Hanford fm (H2 unit)
Grab	C4191-116	116	md-crs sand	Hanford fm (H2 unit)
Grab	C4191-118.5	118.5	md-crs sand	Hanford fm (H2 unit)
Grab	C4191-121	121	fn-md sand	Hanford fm (H2 unit)
Grab	C4191-123.5	123.5	fn-md sand	Hanford fm (H2 unit)
Grab	C4191-126	126	silty fn sand	Hanford fm (H2 unit)
Grab	C4191-128.5	128.5	md-crs sand	Hanford fm (H2 unit)
Grab	C4191-131	131	md-crs sand	Hanford fm (H2 unit)
Grab	C4191-133.5	133.5	fn-md sand	Hanford fm (H2 unit)
Grab	C4191-136	136	silty fn sand	Hanford fm (H2 unit)

Table 2.3. Grab Samples Collected, Described, and Photographed from Borehole C4191

Type	Lab #	Depth	Lithology	Stratigraphic Unit
Grab	C4191-138.5	138.5	md-crs sand	Hanford fm (H2 unit)
Grab	C4191-141	141	silty fn sand	Hanford fm (H2 unit)
Grab	C4191-143.5	143.5	fn-md sand	Hanford fm (H2 unit)
Grab	C4191-146	146	md-crs sand	Hanford fm (H2 unit)
Grab	C4191-148.5	148.5	md-crs sand	Hanford fm (H2 unit)
Grab	C4191-151	151	fn-md sand	Hanford fm (H2 unit)
Grab	C4191-153.5	153.5	md sand	Hanford fm (H2 unit)
Grab	C4191-156	156	md sand	Hanford fm (H2 unit)
Grab	C4191-158.5	158.5	silty fn sand	Hanford fm (H2 unit)
Grab	C4191-161	161	md sand	Hanford fm (H2 unit)
Grab	C4191-163.5	163.5	md sand	Hanford fm (H2 unit)
Grab	C4191-166	166	silty fn-md sand	Hanford fm (H2 unit)
Grab	C4191-168.5	168.5	silty fn-md sand	Hanford fm (H2 unit)
Grab	C4191-171	171	silty fn-md sand	Hanford fm (H2 unit)
Grab	C4191-173.5	173.5	md-crs sand	Hanford fm (H2 unit)
Grab	C4191-176	176	md sand	Hanford fm (H2 unit)
Grab	C4191-178.5	178.5	fn-md sand	Hanford fm (H2 unit)
Grab	C4191-181	181	fn-md sand	Hanford fm (H2 unit)
Grab	C4191-183.5	183.5	md sand	Hanford fm (H2 unit)
Grab	C4191-186	186	fn-md sand	Hanford fm (H2 unit)
Grab	C4191-188.5	188.5	md sand	Hanford fm (H2 unit)
Grab	C4191-191	191	fn-md sand	Hanford fm (H2 unit)
Grab	C4191-193.5	193.5	fn-md sand	Hanford fm or Cold Creek unit
Grab	C4191-196	196	silty fn sand	Hanford fm or Cold Creek unit
Grab	C4191-198.5	198.5	fn-md sand	Hanford fm or Cold Creek unit
Grab	C4191-201	201	silty fn-md sand	Hanford fm or Cold Creek unit
Grab	C4191-203.5	203.5	sandy gravel	Hanford fm or Cold Creek unit
Grab	C4191-206	206	silty sandy gravel	Hanford fm or Cold Creek unit
Grab	C4191-208.5	208.5	pebbly md-crs sand	Hanford fm or Cold Creek unit
Grab	C4191-211	211	sandy gravel	Hanford fm or Cold Creek unit
Grab	C4191-213.5	213.5	pebbly fn-crs sand	Hanford fm or Cold Creek unit
Grab	C4191-216	216	pebbly fn-crs sand	Hanford fm or Cold Creek unit
Grab	C4191-218.5	218.5	pebbly fn-crs sand	Hanford fm or Cold Creek unit
Grab	C4191-221	221	fn-crs sand	Hanford fm or Cold Creek unit
Grab	C4191-223.5	223.5	sl pebbly sand	Hanford fm or Cold Creek unit
Grab	C4191-226	226	sandy gravel	Hanford fm or Cold Creek unit
Grab	C4191-228.5	228.5	pebbly fn-crs sand	Hanford fm or Cold Creek unit
Grab	C4191-231	231	pebbly fn-crs sand	Hanford fm or Cold Creek unit
Grab	C4191-233.5	233.5	pebbly fn-crs sand	Hanford fm or Cold Creek unit
Grab	C4191-236	236	pebbly fn-crs sand	Hanford fm or Cold Creek unit
Grab	C4191-238.5	238.5	silty fn-md sand	Hanford fm or Cold Creek unit
Grab	C4191-241	241	sl pebbly fn-crs sand	Hanford fm or Cold Creek unit
Grab	C4191-243.5	243.5	fn-md sand	Hanford fm or Cold Creek unit
Grab	C4191-246	246	md-crs sand	Hanford fm or Cold Creek unit

Table 2.3. Grab Samples Collected, Described, and Photographed from Borehole C4191

Type	Lab #	Depth	Lithology	Stratigraphic Unit
Grab	C4191-248.5	248.5	fn-crs sand	Hanford fm or Cold Creek unit
Grab	C4191-251	251	silty fn-crs sand	Hanford fm or Cold Creek unit
Grab	C4191-253.5	253.5	fn-md sand	Hanford fm or Cold Creek unit
Grab	C4191-256	256	fn-crs sand	Hanford fm or Cold Creek unit
Grab	C4191-258.5	258.5	fn-md sand	Hanford fm or Cold Creek unit
Grab	C4191-261	261	fn-md sand	Hanford fm or Cold Creek unit
Grab	C4191-263.5	263.5	md sand	Hanford fm or Cold Creek unit
Grab	C4191-266	266	md-crs sand	Hanford fm or Cold Creek unit
Grab	C4191-268.5	268.5	fn-md sand	Hanford fm or Cold Creek unit
Grab	C4191-271	271	fn-md sand	Hanford fm or Cold Creek unit
Grab	C4191-273.5	273.5	fn-md sand	Hanford fm or Cold Creek unit
Grab	C4191-276	276	fn-md sand	Hanford fm or Cold Creek unit
Grab	C4191-278.5	278.5	fn-crs sand	Hanford fm or Cold Creek unit
Grab	C4191-281	281	fn-md sand	Hanford fm or Cold Creek unit
Grab	C4191-283.5	283.5	pebbly fn-md sand	Hanford fm or Cold Creek unit
Grab	C4191-286	286	silty pebbly fn-crs sand	Hanford fm or Cold Creek unit
Grab	C4191-288.5	288.5	silty sandy gravel	Hanford fm or Cold Creek unit
Grab	C4191-291	291	silty sandy gravel	Hanford fm or Cold Creek unit
Grab	C4191-293.5	293.5	silty sandy gravel	Hanford fm or Cold Creek unit
Grab	C4191-296	296	sl gravelly sandy silt	Hanford fm or Cold Creek unit
Grab	C4191-298.5	298.5	silty fn-crs sand	Hanford fm or Cold Creek unit
Grab	C4191-301	301	sandy silty gravel	Ringold Formation (Unit E)
Grab	C4191-303.5	303.5	sandy gravelly silt	Ringold Formation (Unit E)
Grab	C4191-306	306	sandy gravelly silt	Ringold Formation (Unit E)
Grab	C4191-308.5	308.5	sandy gravelly silt	Ringold Formation (Unit E)
Grab	C4191-311	311	sandy gravelly silt	Ringold Formation (Unit E)
Grab	C4191-313.5	313.5	sandy silty gravel	Ringold Formation (Unit E)
Grab	C4191-316	316	sandy gravelly silt	Ringold Formation (Unit E)
Grab	C4191-318.5	318.5	sandy gravelly silt	Ringold Formation (Unit E)
Grab	C4191-321	321	sl silty sl sandy gravel	Ringold Formation (Unit E)
Grab	C4191-323.5	323.5	silty sandy gravel	Ringold Formation (Unit E)
Grab	C4191-326	326	sandy gravelly silt	Ringold Formation (Unit E)
Grab	C4191-328.5	328.5	sandy silty gravel	Ringold Formation (Unit E)
Grab	C4191-331	331	sl sandy sl silty gravel	Ringold Formation (Unit E)
Grab	C4191-333.5	333.5	silty gravelly sand	Ringold Formation (Unit E)
Grab	C4191-336	336	silty sandy gravel	Ringold Formation (Unit E)
Grab	C4191-338.5	338.5	silty gravelly sand	Ringold Formation (Unit E)
Grab	C4191-341	341	silty sandy gravel	Ringold Formation (Unit E)

Crs = coarse; fn = fine; md = medium; sl = slightly; v = very
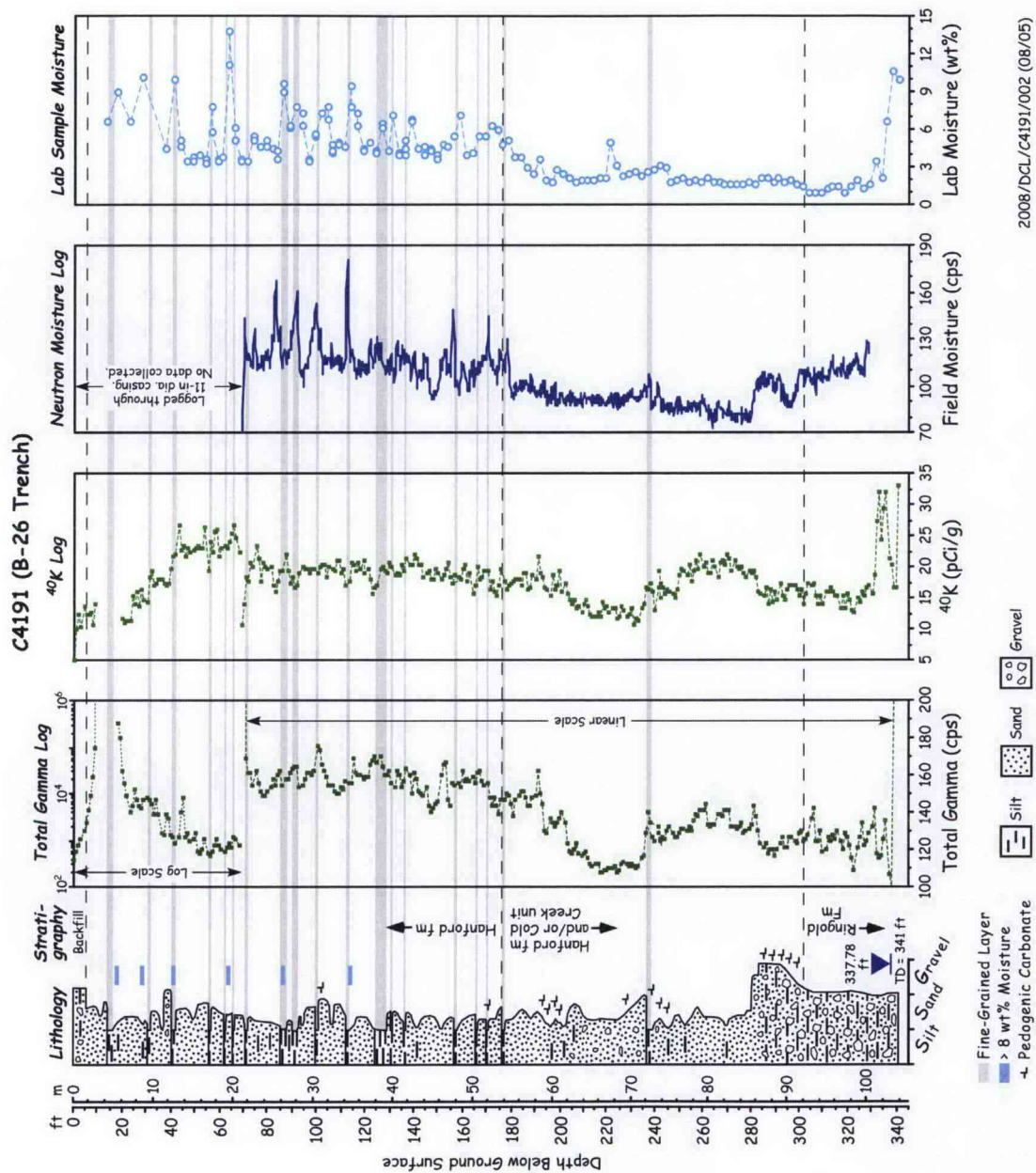
Figure 2.18. Composite Summary Log for Borehole C4191

2.3.2   Borehole C5923 (299-E13-62)

Drilling grab samples collected for physical and chemical characterization from borehole C5923 (BC Crib and Trenches borehole A) are listed in Table 2.4.

Table 2.4.   Vadose Zone Samples Collected, Described, and Photographed from Borehole C5923

Type	HEIS #	Depth (ft)	Lithology	Stratigraphic Unit
Grab	B1T740	5 -6	sl pebbly fn sand	Hanford fm (H2 unit)
Grab	B1T741	7.5-8.5	sl pebbly fn-crs sand	Hanford fm (H2 unit)
Grab	B1T742	10 -11	sl pebbly crs sand	Hanford fm (H2 unit)
Grab	B1T743	12.5-13.5	sl pebbly crs sand	Hanford fm (H2 unit)
Grab	B1T744	15-16	fn-crs sand	Hanford fm (H2 unit)
Grab	B1T745	17.5-18.5	fn-md sand	Hanford fm (H2 unit)
Grab	B1T746	20-21	fn-md sand	Hanford fm (H2 unit)
Grab	B1T816	20-21	fn-md sand	Hanford fm (H2 unit)
Grab	B1T747	22.5-23.5	md sand	Hanford fm (H2 unit)
Grab	B1T748	25-26	md sand	Hanford fm (H2 unit)
Grab	B1T749	27.5-28.5	md sand	Hanford fm (H2 unit)
Grab	B1T750	30-31	md sand	Hanford fm (H2 unit)
Grab	B1T751	32.5-33.5	md sand	Hanford fm (H2 unit)
Grab	B1T825	36.5-37.0	md sand	Hanford fm (H2 unit)
Core	B1T7J4-2	38.0 38.5		Hanford fm (H2 unit)
Core	B1T7J3-3	38.0-38.5		Hanford fm (H2 unit)
Core	B1T7J3-2	38.5-39.0		Hanford fm (H2 unit)
Grab	B1T826	39.0-39.5	md-crs sand	Hanford fm (H2 unit)
Core	B1T7J5-3	40.5-41.0		Hanford fm (H2 unit)
Core	B1T7J5-2	41.0-41.5		Hanford fm (H2 unit)
Grab	B1T827	41.5-42.0	crs sand	Hanford fm (H2 unit)
Core	B1T7J6-3	43.0-43.5		Hanford fm (H2 unit)
Core	B1T7J6-2	43.5-44.0		Hanford fm (H2 unit)
Grab	B1T828	44.0-44.5	sl pebbly crs sand	Hanford fm (H2 unit)
Grab	B1T752	45-46	sl pebbly crs sand	Hanford fm (H2 unit)
Grab	B1T753	47.5-48.5	md-crs sand	Hanford fm (H2 unit)
Grab	B1T754	50-51	md-crs sand	Hanford fm (H2 unit)
Grab	B1T755	52.5-53.5	sl pebbly crs sand	Hanford fm (H2 unit)
Grab	B1T756	55-56	md sand	Hanford fm (H2 unit)
Grab	B1T757	57.5-58.5	md sand	Hanford fm (H2 unit)
Grab	B1T758	60-61	md sand	Hanford fm (H2 unit)

Table 2.4 (contd)

Type	HEIS #	Depth (ft)	Lithology	Stratigraphic Unit
Grab	B1T759	62.5-63.5	sl pebbly md-crs sand	Hanford fm (H2 unit)
Grab	B1T760	65-66	sl pebbly md sand	Hanford fm (H2 unit)
Grab	B1T761	67.5-68.5	md sand	Hanford fm (H2 unit)
Grab	B1T762	70-71	md-crs sand	Hanford fm (H2 unit)
Grab	B1T763	72.5-73.5	crs sand	Hanford fm (H2 unit)
Grab	B1T764	75-76	crs sand	Hanford fm (H2 unit)
Grab	B1T765	77.5-78.5	md sand	Hanford fm (H2 unit)
Grab	B1T766	80-81	md-crs sand	Hanford fm (H2 unit)
Grab	B1T767	82.5-83.5	sl pebbly md-crs sand	Hanford fm (H2 unit)
Field Dup	B1T817	82.5-83.5	sl pebbly md-crs sand	Hanford fm (H2 unit)
Core	B1T7J7-3	85.5-86.0		Hanford fm (H2 unit)
Core	B1T7J7-2	86.0-86.5		Hanford fm (H2 unit)
Grab	B1T829	86.5-87.0	md-v.crs sand	Hanford fm (H2 unit)
Core	B1T7J8-3	88.0-88.5		Hanford fm (H2 unit)
Core	B1T7J8-2	88.5-89.0		Hanford fm (H2 unit)
Grab	B1T985	89.0-89.5	md sand	Hanford fm (H2 unit)
Grab	B1T768	90-91	md sand	Hanford fm (H2 unit)
Grab	B1T769	92.5-93.5	md sand	Hanford fm (H2 unit)
Grab	B1T770	95-96	md sand	Hanford fm (H2 unit)
Grab	B1T771	97.5-98.5	md sand	Hanford fm (H2 unit)
Grab	B1T772	100-101	sl pebbly md-crs sand	Hanford fm (H2 unit)
Grab	B1T773	102.5-103.5	sl pebbly md-crs sand	Hanford fm (H2 unit)
Core	B1T7J9-3	105.5-106.0		Hanford fm (H2 unit)
Core	B1T7J9-2	106.0-106.5		Hanford fm (H2 unit)
Grab	B1T9K9	106.5-107.0	md sand	Hanford fm (H2 unit)
Core	B1T7K0-3	108.0-108.5		Hanford fm (H2 unit)
Core	B1T7K0-2	108.5-109.0		Hanford fm (H2 unit)
Grab	B1T9L0	109.0-109.5	md sand	Hanford fm (H2 unit)
Core	B1T7L3-3	113.0-113.5		Hanford fm (H2 unit)
Core	B1T7L3-2	113.5-114.0		Hanford fm (H2 unit)
Grab	B1T9L1	114.0-114.5	md sand	Hanford fm (H2 unit)
Grab	B1T774	115-116	fn-md sand	Hanford fm (H2 unit)
Grab	B1T775	117.5-118.5	fn-md sand	Hanford fm (H2 unit)
Grab	B1T776	120-121	fn-md sand	Hanford fm (H2 unit)
Grab	B1T777	122.5-123.5	fn-md sand	Hanford fm (H2 unit)
Field Dup	B1T818	122.5-123.5	fn-md sand	Hanford fm (H2 unit)
Core	B1T7K1-3	125.5-126.0		Hanford fm (H2 unit)
Core	B1T7K1-2	126.0-126.5		Hanford fm (H2 unit)
Grab	B1T9L2	126.5-127.0	fn-md sand	Hanford fm (H2 unit)

Table 2.4 (contd)

Type	HEIS #	Depth (ft)	Lithology	Stratigraphic Unit
Core	B1T7K2-3	128.5-129.0		Hanford fm (H2 unit)
Core	B1T7K2-2	129.0-129.5		Hanford fm (H2 unit)
Grab	B1T9L3	129.0-129.5	fn-md sand	Hanford fm (H2 unit)
Core	B1T7K3-3	130.5-131.0		Hanford fm (H2 unit)
Core	B1T7K3-2	131.0-131.5		Hanford fm (H2 unit)
Grab	B1T9L4	131.5-132.0	fn-md sand	Hanford fm (H2 unit)
Core	B1T7K4-3	133.0-133.5		Hanford fm (H2 unit)
Core	B1T7K4-2	133.5-134.0		Hanford fm (H2 unit)
Grab	B1T9L5	134.0-134.5	silty fn sand	Hanford fm (H2 unit)
Grab	B1T778	135-136	silty fn sand	Hanford fm (H2 unit)
Grab	B1T779	137.5-138.5	md sand	Hanford fm (H2 unit)
Grab	B1T780	140-141	md-crs sand	Hanford fm (H2 unit)
Grab	B1T781	142.5-143.5	silty fn-md sand	Hanford fm (H2 unit)
Grab	B1T782	145-146	md sand	Hanford fm (H2 unit)
Grab	B1T783	147.5-148.5	md sand	Hanford fm (H2 unit)
Grab	B1T784	150-151	silty md sand	Hanford fm (H2 unit)
Grab	B1T785	152.5-153.5	md-crs sand	Hanford fm (H2 unit)
Grab	B1T786	155-156	md sand	Hanford fm (H2 unit)
Grab	B1T787	157.5-158.5	md sand	Hanford fm (H2 unit)
Grab	B1T788	160-161	md sand	Hanford fm (H2 unit)
Grab	B1T789	162.5-163.5	md sand	Hanford fm (H2 unit)
Grab	B1T790	165-166	silty md sand	Hanford fm (H2 unit)
Grab	B1T791	167.5-168.5	md sand	Hanford fm (H2 unit)
Grab	B1T792	170-171	md sand	Hanford fm (H2 unit)
Grab	B1T793	172.5-173.5	md sand	Hanford fm (H2 unit)
Core	B1T7K5-3	175.5-176.0		Hanford fm (H2 unit)
Core	B1T7K5-2	176.0-176.5		Hanford fm (H2 unit)
Grab	B1T9L6	176.5-177.0	md sand	Hanford fm (H2 unit)
Core	B1T7K6-3	178.0-178.5		Hanford fm (H2 unit)
Core	B1T7K6-2	178.5-179.0		Hanford fm (H2 unit)
Grab	B1T9L7	179.0-179.5	md sand	Hanford fm (H2 unit)
Core	B1T7K7-3	180.5-181.0		Hanford fm (H2 unit)
Core	B1T7K7-2	181.0-181.5		Hanford fm (H2 unit)
Grab	B1T9L8	181.5-182.0	md sand	Hanford fm (H2 unit)
Core	B1T7K8-3	183.0-183.5		Hanford fm (H2 unit)
Core	B1T7K8-2	183.5-184.0		Hanford fm (H2 unit)
Grab	B1T9L9	184.0-184.5	md sand	Hanford fm (H2 unit)
Grab	B1T794	185-186	md sand	Hanford fm (H2 unit)

Table 2.4 (contd)

Type	HEIS #	Depth (ft)	Lithology	Stratigraphic Unit
Grab	B1T795	187.5-188.5	md sand	Hanford fm (H2 unit)
Grab	B1T796	190-191	md sand	Hanford fm (H2 unit)
Grab	B1T819	190-191	md sand	Hanford fm (H2 unit)
Grab	B1T797	192.5-193.5	md sand	Hanford fm (H2 unit)
Grab	B1T798	195-196	sl pebbly md sand	Hanford fm (H2 unit)
Grab	B1T799	197.5-198.5	md sand	Hanford fm (H2 unit)
Grab	B1T7B0	200-201	md sand	Hanford fm (H2 unit)
Grab	B1T7B1	202.5-203.5	md sand	Hanford fm (H2 unit)
Grab	B1T7B2	205-206	md-crs sand	Hanford fm (H2 unit)
Grab	B1T820	205-206	md sand	Hanford fm (H2 unit)
Grab	B1T7B3	207.5-208.5	md sand	Hanford fm (H2 unit)
Grab	B1T7B4	210-211	md sand	Hanford fm (H2 unit)
Grab	B1T7B5	212.5-213.5	md sand	Hanford fm (H2 unit)
Grab	B1T7B6	215-216	fn-md sand	Hanford fm (H2 unit)
Grab	B1T7B7	217.5-218.5	md-crs sand	Hanford fm (H2 unit)
Grab	B1T7B8	220-221	fn-md sand	Hanford fm or Cold Creek unit
Grab	B1T7B9	222.5-223.5	fn-md sand	Hanford fm or Cold Creek unit
Grab	B1T821	222.5-223.5	fn-md sand	Hanford fm or Cold Creek unit
Grab	B1T7C0	225-226	fn-md sand	Hanford fm or Cold Creek unit
Grab	B1T7C1	227.5-228.5	sl pebbly md sand	Hanford fm or Cold Creek unit
Grab	B1T7C2	230-231	sl pebbly md sand	Hanford fm or Cold Creek unit
Grab	B1T7C3	232.5-233.5	sl pebbly md sand	Hanford fm or Cold Creek unit
Core	B1T7K9-3	235.5-236.0		Hanford fm or Cold Creek unit
Core	B1T7K9-2	236.0-236.5		Hanford fm or Cold Creek unit
Grab	B1T9K6	236.5-237.0	sl pebbly md-crs sand	Hanford fm or Cold Creek unit
Core	B1T7L0-3	238.0-238.5		Hanford fm or Cold Creek unit
Core	B1T7L0-2	238.5-239.0		Hanford fm or Cold Creek unit
Grab	B1T9K7	239.0-239.5	sl pebbly md-crs sand	Hanford fm or Cold Creek unit
Core	B1T7L1-3	240.5-241.0		Hanford fm or Cold Creek unit
Core	B1T7L1-2	241.0-241.5		Hanford fm or Cold Creek unit
Grab	B1T9K8	241.5-242.0	sl pebbly md-crs sand	Hanford fm or Cold Creek unit
Core	B1T7L2-3	243.0-243.5		Hanford fm or Cold Creek unit
Core	B1T7L2-2	243.5-244.0		Hanford fm or Cold Creek unit
Grab	B1T824	244.0-244.5	gravelly sand	Hanford fm or Cold Creek unit
Grab	B1T7C4	245-246	gravelly sand	Hanford fm or Cold Creek unit
Grab	B1T7C5	247.5-248.5	gravelly sand	Hanford fm or Cold Creek unit
Grab	B1T7C6	250-251	gravelly sand	Hanford fm or Cold Creek unit
Grab	B1T7C8	252.5-253.5	gravelly sand	Hanford fm or Cold Creek unit
Grab	B1T7C7	255-256	md sand	Hanford fm or Cold Creek unit

Table 2.4 (contd)

Type	HEIS #	Depth (ft)	Lithology	Stratigraphic Unit
Grab	B1T7C9	257.5-258.5	sl pebbly md sand	Hanford fm or Cold Creek unit
Grab	B1T7D0	260-261	sl pebbly md sand	Hanford fm or Cold Creek unit
Grab	B1T822	260-261	sl pebbly md sand	Hanford fm or Cold Creek unit
Grab	B1T7D1	262.5-263.5	sl pebbly md sand	Hanford fm or Cold Creek unit
Grab	B1T7D2	265-266	sl pebbly md sand	Hanford fm or Cold Creek unit
Grab	B1T7D3	267.5-268.5	sl pebbly md sand	Hanford fm or Cold Creek unit
Grab	B1T7D4	270-271	sl pebbly md sand	Hanford fm or Cold Creek unit
Grab	B1T7D5	272.5-273.5	sl pebbly md sand	Hanford fm or Cold Creek unit
Grab	B1T7D6	275-276	gravelly sand	Hanford fm or Cold Creek unit
Grab	B1T7D7	277.5-278.5	gravelly sand	Hanford fm or Cold Creek unit
Grab	B1T7D8	280-281	gravelly sand	Hanford fm or Cold Creek unit
Grab	B1T7D9	282.5-283.5	sl pebbly md sand	Hanford fm or Cold Creek unit
Grab	B1T7F0	285-286	sl pebbly md sand	Hanford fm or Cold Creek unit
Grab	B1T7F1	287.5-288.5	sl pebbly md-crs sand	Hanford fm or Cold Creek unit
Grab	B1T7F2	290-291	sl pebbly md sand	Hanford fm or Cold Creek unit
Grab	B1T7F3	292.5-293.5	gravelly fn-md san	Hanford fm or Cold Creek unit
Grab	B1T7F4	295-296	silty gravel	Hanford fm or Cold Creek unit
Grab	B1T7F5	297.5-298.5	gravelly fn-md sand	Hanford fm or Cold Creek unit
Grab	B1T7F6	300-301	gravelly sandy silt	Hanford fm or Cold Creek unit
Grab	B1T7F7	302.5-303.5	silty sandy gravel	Hanford fm or Cold Creek unit
Grab	B1T7F8	305-306	sl silty sl gravelly fn sand	Hanford fm or Cold Creek unit
Grab	B1T7F9	307.5-308.5	gravelly sandy silt	Hanford fm or Cold Creek unit
Grab	B1T7H0	310-311	gravelly sandy silt	Hanford fm or Cold Creek unit
Grab	B1T7H1	312.5-313.5	sl gravelly fn-md sand	Hanford fm or Cold Creek unit
Grab	B1T7H2	315-316	sl gravelly md sand	Hanford fm or Cold Creek unit
Grab	B1T7H3	317.5-318.5	sl gravelly md sand	Hanford fm or Cold Creek unit
Grab	B1T7H4	320-321	sl gravelly fn-md sand	Hanford fm or Cold Creek unit
Grab	B1T7H5	322.5-323.5	gravelly fn sand	Hanford fm or Cold Creek unit
Grab	B1T7H6	325-326	gravelly sandy silt	Hanford fm or Cold Creek unit
Grab	B1T7H7	327.5-328.5	gravelly sandy silt	Hanford fm or Cold Creek unit
Grab	B1T7H8	330-331	gravelly sandy silt	Hanford fm or Cold Creek unit
Grab	B1T823	330-331	gravelly sandy silt	Hanford fm or Cold Creek unit
Grab	B1T7H9	332.5-333.5	gravelly sandy silt	Hanford fm or Cold Creek unit
Grab	B1T7J0	335-336	silty sandy gravel	Hanford fm or Cold Creek unit
Grab	B1T7J1	337.5-338.5	sl gravelly sandy silt	Hanford fm or Cold Creek unit
Grab	B1T7J2	340-341	gravelly sandy silt	Hanford fm or Cold Creek unit
Grab	B1T984	341-342	gravelly sandy silt	Hanford fm or Cold Creek unit
Grab	B1V530	343.5-344.5	Not processed	Not processed
Grab	B1V531	346-347	Not processed	Not processed

Table 2.4 (contd)

Type	HEIS #	Depth (ft)	Lithology	Stratigraphic Unit
Grab	B1V532	348.5-349.5	Not processed	Not processed
Grab	B1V533	351-352	Not processed	Not processed

Crs = coarse; fn = fine; md = medium; sl = slightly; v = very; pink highlight represents core liners

A summary hydrogeologic log, which shows an integration of all the geologic, geophysical, and moisture data collected for borehole C5923, is presented in Figure 2.19.
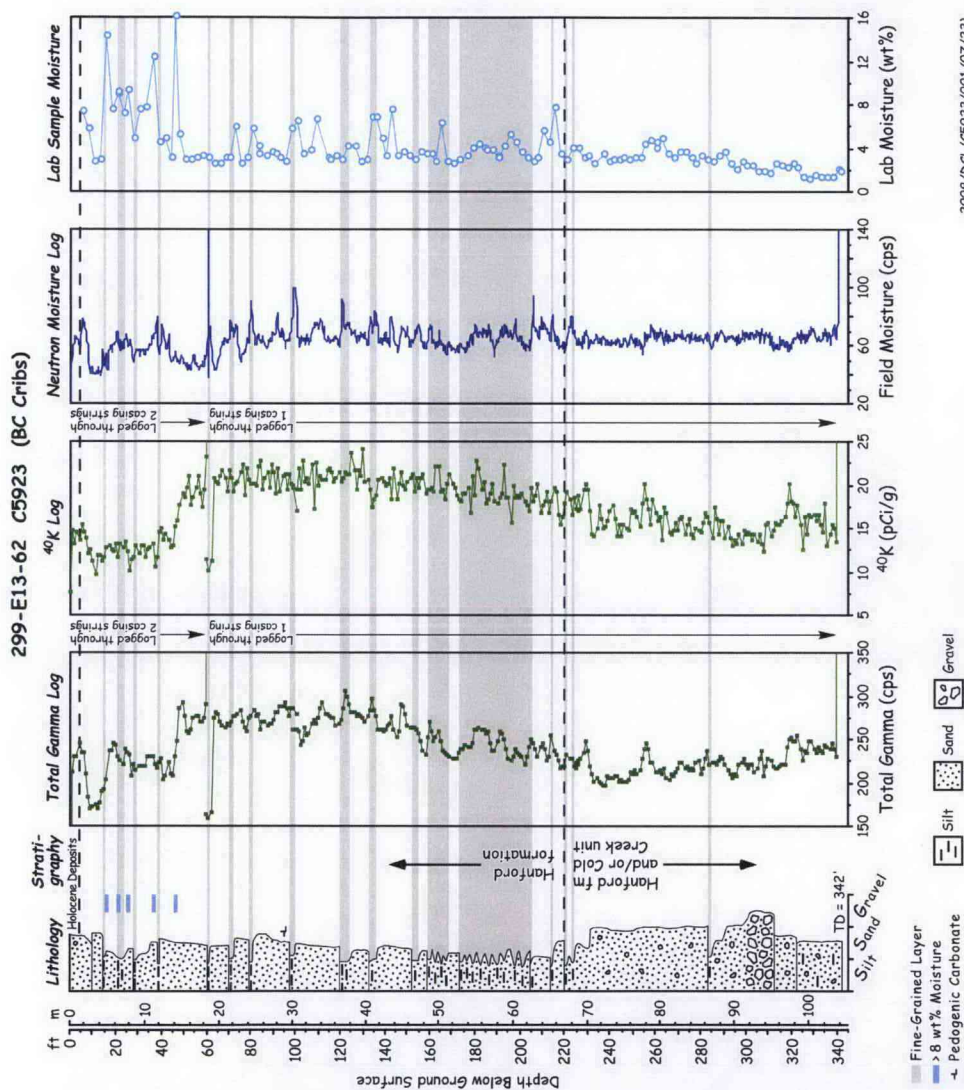
Figure 2.19. Composite Summary Log for Borehole C5923

2.3.3 Borehole C5924 (299-E13-63)

Grab samples collected for physical and chemical characterization from borehole C5924 (BC Cribs and Trenches area borehole B) are listed in Table 2.5.

Table 2.5. Grab Samples Collected, Described, and Photographed from Borehole C5924

Sample Type	HEIS #	Depth (ft)	Lithology	Stratigraphic Unit
Grab	B1T677	5.0-5.5	fn-md sand	Hanford fm (H2 unit)
Grab	B1T678	7.5-8.0	sl pebbly fn-crs sand	Hanford fm (H2 unit)
Grab	B1T679	9.5-10.0	sl pebbly fn-crs sand	Hanford fm (H2 unit)
Grab	B1T680	12.0-12.5	md-crs sand	Hanford fm (H2 unit)
Grab	B1T681	14.5-15.0	md sand	Hanford fm (H2 unit)
Grab	B1T682	17.5-18.0	fn sand	Hanford fm (H2 unit)
Grab	B1T683	19.5-20.0	fn sand	Hanford fm (H2 unit)
Grab	B1T730	19.5-20.0	fn sand	Hanford fm (H2 unit)
Grab	B1T684	22.5-23.0	md-crs sand	Hanford fm (H2 unit)
Grab	B1T685	25.0-25.5	md sand	Hanford fm (H2 unit)
Grab	B1T686	27.0-27.5	md-crs sand	Hanford fm (H2 unit)
Grab	B1T687	29.5-30.0	md sand	Hanford fm (H2 unit)
Grab	B1T688	32.0-32.5	fn-md sand	Hanford fm (H2 unit)
Grab	B1T689	34.5-35.0	fn sand	Hanford fm (H2 unit)
Grab	B1T690	37.0-37.5	fn-md sand	Hanford fm (H2 unit)
Grab	B1T691	40.0-40.5	fn-md sand	Hanford fm (H2 unit)
Grab	B1T692	42.5-43.0	fn-md sand	Hanford fm (H2 unit)
Grab	B1T693	44.5-45.0	md-crs sand	Hanford fm (H2 unit)
Grab	B1T694	47.0-47.5	md-crs sand	Hanford fm (H2 unit)
Grab	B1T695	50.5-51.0	fn-md sand	Hanford fm (H2 unit)
Grab	B1T696	52.5-53.0	md sand	Hanford fm (H2 unit)
Grab	B1T697	54.5-55.0	md sand	Hanford fm (H2 unit)
Grab	B1T698	57.0-57.5	md sand	Hanford fm (H2 unit)
Grab	B1T699	60.0-60.5	md sand	Hanford fm (H2 unit)
Grab	B1T6B0	62.0-62.5	fn-md sand	Hanford fm (H2 unit)
Grab	B1T6B1	65.0-65.5	md sand	Hanford fm (H2 unit)
Grab	B1T731	65.0-65.5	md sand	Hanford fm (H2 unit)
Grab	B1T6B2	67.5-68.0	md sand	Hanford fm (H2 unit)
Grab	B1T6B3	70.0-70.5	fn sand	Hanford fm (H2 unit)
Grab	B1T6B4	72.5-73.0	fn-md sand	Hanford fm (H2 unit)
Grab	B1T6B5	75.0-75.5	md-crs sand	Hanford fm (H2 unit)
Grab	B1T6B6	77.0-77.5	fn sand	Hanford fm (H2 unit)
Grab	B1T6B7	79.5-80.0	md sand	Hanford fm (H2 unit)
Grab	B1T6B8	82.5-83.0	md sand	Hanford fm (H2 unit)
Grab	B1T6B9	85.5-86.0	fn-md sand	Hanford fm (H2 unit)
Grab	B1T6C0	87.5-88.0	fn-md sand	Hanford fm (H2 unit)
Grab	B1T6C1	90.0-90.5	fn-md sand	Hanford fm (H2 unit)
Grab	B1T6C2	92.0-92.5	fn-md sand	Hanford fm (H2 unit)
Grab	B1T6C3	95.0-95.5	fn-md sand	Hanford fm (H2 unit)
Grab	B1T6C4	97.5-98.0	md-crs sand	Hanford fm (H2 unit)
Grab	B1T6C5	100.0-100.5	md sand	Hanford fm (H2 unit)

Table 2.5 (contd)

Sample Type	HEIS #	Depth (ft)	Lithology	Stratigraphic Unit
Grab	B1T6C6	102.5-103.0	md sand	Hanford fm (H2 unit)
Grab	B1T6C7	105.0-105.5	fn-md sand	Hanford fm (H2 unit)
Grab	B1T732	105.0-105.5	fn-md sand	Hanford fm (H2 unit)
Grab	B1T6C8	107.0-107.5	fn-md sand	Hanford fm (H2 unit)
Grab	B1T6C9	110.0-110.5	fn-md sand	Hanford fm (H2 unit)
Grab	B1T6D0	112.0-112.5	fn-md sand	Hanford fm (H2 unit)
Grab	B1T6D1	115.0-115.5	fn-md sand	Hanford fm (H2 unit)
Grab	B1T6D2	117.5-118.0	fn sand	Hanford fm (H2 unit)
Grab	B1T6D3	120.0-120.5	md sand	Hanford fm (H2 unit)
Grab	B1T6D4	122.5-123.0	md sand	Hanford fm (H2 unit)
Grab	B1T6D5	125.0-125.5	md sand	Hanford fm (H2 unit)
Grab	B1T6D6	127.0-127.5	fn-md sand	Hanford fm (H2 unit)
Grab	B1T6D7	130.0-130.5	fn sand	Hanford fm (H2 unit)
Grab	B1T6D8	132.5-133.0	fn sand	Hanford fm (H2 unit)
Grab	B1T6D9	135.0-135.5	fn-md sand	Hanford fm (H2 unit)
Grab	B1T6F0	137.5-138.0	fn-md sand	Hanford fm (H2 unit)
Grab	B1T6F1	139.5-140.0	fn-md sand	Hanford fm (H2 unit)
Grab	B1T6F2	142.0-142.5	fn sand	Hanford fm (H2 unit)
Grab	B1T6F3	144.5-145.0	fn sand	Hanford fm (H2 unit)
Grab	B1T6F4	147.0-147.5	md sand	Hanford fm (H2 unit)
Grab	B1T6F5	150.0-150.5	md sand	Hanford fm (H2 unit)
Grab	B1T733	150.0-150.5	md sand	Hanford fm (H2 unit)
Grab	B1T6F6	153.0-153.5	fn-md sand	Hanford fm (H2 unit)
Grab	B1T6F7	155.0-155.5	fn-md sand	Hanford fm (H2 unit)
Grab	B1T6F8	157.5-158.0	fn-md sand	Hanford fm (H2 unit)
Grab	B1T6F9	160.0-160.5	md sand	Hanford fm (H2 unit)
Grab	B1T6H0	162.5-163.5	fn-md sand	Hanford fm (H2 unit)
Grab	B1T6H1	165.0-165.5	md sand	Hanford fm (H2 unit)
Grab	B1T6H2	167.5-168.0	md sand	Hanford fm (H2 unit)
Grab	B1T6H3	170.0-170.5	md sand	Hanford fm (H2 unit)
Grab	B1T6H4	172.5-173.0	md sand	Hanford fm (H2 unit)
Grab	B1T6H5	175.0-175.5	fn-md sand	Hanford fm (H2 unit)
Grab	B1T6H6	178.0-178.5	fn sand	Hanford fm (H2 unit)
Grab	B1T6H7	181.0-181.5	md sand	Hanford fm (H2 unit)
Grab	B1T6H8	182.5-183.0	md sand	Hanford fm (H2 unit)
Grab	B1T6H9	184.5-185.0	md sand	Hanford fm (H2 unit)
Grab	B1T6J0	187.5-188.0	fn sand	Hanford fm (H2 unit)
Grab	B1T6J1	190.5-191.0	md sand	Hanford fm (H2 unit)
Grab	B1T6J2	192.0-192.5	fn-md sand	Hanford fm (H2 unit)
Grab	B1T6J3	195.0-195.5	fn-md sand	Hanford fm (H2 unit)
Grab	B1T6J4	197.5-198.0	fn-md sand	Hanford fm (H2 unit)
Grab	B1T6J5	201.0-201.5	md-crs sand	Hanford fm (H2 unit)
Grab	B1T6J6	202.5-203.0	fn-md sand	Hanford fm (H2 unit)
Grab	B1T6J7	205.0-205.5	fn-md sand	Hanford fm (H2 unit)
Grab	B1T6J8	207.5-208.0	sl gravelly fn-md sand	Hanford fm or Cold Creek unit
Grab	B1T6J9	210.5-211.0	gravelly md-crs sand	Hanford fm or Cold Creek unit
Grab	B1T6K0	212.0-212.5	sl gravelly md-crs sand	Hanford fm or Cold Creek unit
Grab	B1T6K1	215.0-215.5	sl gravelly md-crs sand	Hanford fm or Cold Creek unit

Table 2.5 (contd)

Sample Type	HEIS #	Depth (ft)	Lithology	Stratigraphic Unit
Grab	B1T734	215.0-215.5	sl gravelly md-crs sand	Hanford fm or Cold Creek unit
Grab	B1T6K2	217.0-217.5	sl gravelly md sand	Hanford fm or Cold Creek unit
Grab	B1T6K3	220.0-220.5	sl gravelly fn sand	Hanford fm or Cold Creek unit
Grab	B1T6K4	222.5-223.0	sl gravelly fn-md sand	Hanford fm or Cold Creek unit
Grab	B1T6K5	225.0-225.5	sl gravelly fn-md sand	Hanford fm or Cold Creek unit
Grab	B1T6K6	227.0-227.5	md sand	Hanford fm or Cold Creek unit
Grab	B1T6K7	230.0-230.5	md sand	Hanford fm or Cold Creek unit
Grab	B1T6K8	232.5-233.0	fn sand	Hanford fm or Cold Creek unit
Grab	B1T6K9	235.0-235.5	fn sand	Hanford fm or Cold Creek unit
Grab	B1T6L0	237.5-238.0	fn sand	Hanford fm or Cold Creek unit
Grab	B1T6L1	240.0-240.5	md-crs sand	Hanford fm or Cold Creek unit
Grab	B1T6L2	243.0-243.5	sl gravelly md-crs sand	Hanford fm or Cold Creek unit
Grab	B1T6L3	245.0-245.5	sl gravelly md-crs sand	Hanford fm or Cold Creek unit
Grab	B1T6L4	247.5-248.0	sl gravelly md-crs sand	Hanford fm or Cold Creek unit

Crs = coarse; fn = fine; md = medium; sl = slightly; v = very

A summary hydrogeologic log, which shows an integration of all the geologic, geophysical, and moisture data collected for borehole C5924, is presented in Figure 2.20.
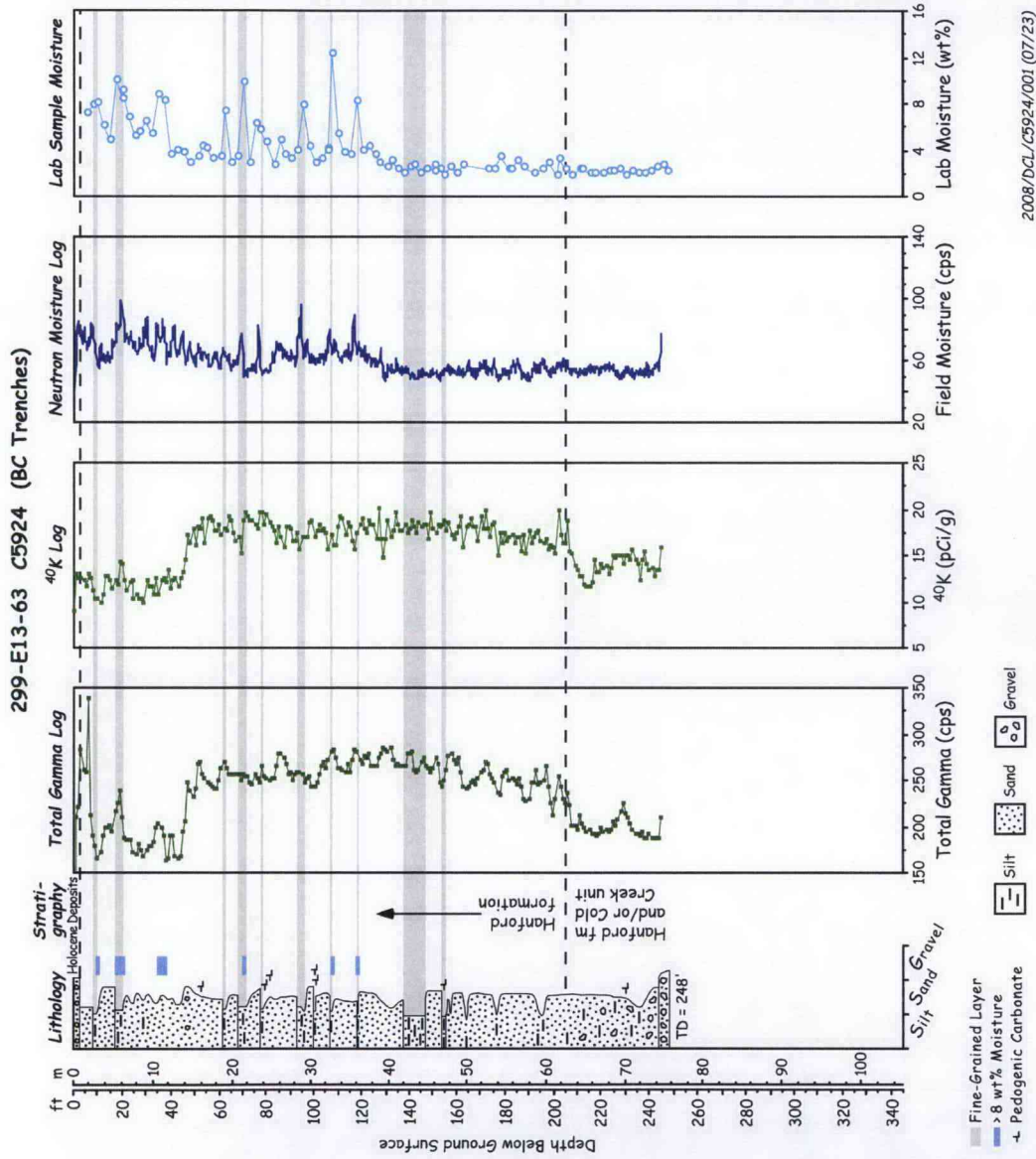
Figure 2.20. Composite Summary Log for Borehole C5924

2.3.4 Borehole C5925 (299-E13-64)

Drilling grab samples collected for physical and chemical characterization from borehole C5925 (BC Cribs and Trenches Area borehole C) are listed in Table 2.6.

Table 2.6. Grab Samples Collected, Described, and Photographed from Borehole C5925

Type	HEIS #	Depth (ft)	Lithology	Stratigraphic Unit
Grab	B1T884	5-5.5	fn sand	Hanford fm (H2 unit)
Grab	B1T885	7.5-8.0	fn sand	Hanford fm (H2 unit)
Grab	B1T886	10-10.5	sl gravelly md-crs sand	Hanford fm (H2 unit)
Grab	B1T887	12.5-13.0	sl gravelly md-crs sand	Hanford fm (H2 unit)
Grab	B1T888	16-16.5	sl gravelly crs sand	Hanford fm (H2 unit)
Grab	B1T889	18-18.5	crs sand	Hanford fm (H2 unit)
Grab	B1T890	20-20.5	sandy silt	Hanford fm (H2 unit)
Grab	B1T891	23-23.5	silty fn-md sand	Hanford fm (H2 unit)
Grab	B1T892	24.5-25	md sand	Hanford fm (H2 unit)
Grab	B1T893	28-28.5	sl silty fn sand	Hanford fm (H2 unit)
Grab	B1T894	30-30.5	sl gravelly crs sand	Hanford fm (H2 unit)
Grab	B1T895	32.5-33	md sand	Hanford fm (H2 unit)
Grab	B1T896	35-35.5	md sand	Hanford fm (H2 unit)
Grab	B1T897	37.5-38	fn-md sand	Hanford fm (H2 unit)
Grab	B1T898	40-40.5	crs sand	Hanford fm (H2 unit)
Grab	B1T899	42.5-43	md sand	Hanford fm (H2 unit)
Grab	B1T8B0	45-45.5	md sand	Hanford fm (H2 unit)
Grab	B1T8B1	47.5-48	md-crs sand	Hanford fm (H2 unit)
Grab	B1T8B2	50-50.5	md-crs sand	Hanford fm (H2 unit)
Grab	B1T8B3	52-53	md sand	Hanford fm (H2 unit)
Grab	B1T8B4	55-55.5	md-crs sand	Hanford fm (H2 unit)
Grab	B1T8B5	57-57.5	md-crs sand	Hanford fm (H2 unit)
Grab	B1T8B6	60-61	md-crs sand	Hanford fm (H2 unit)
Grab	B1T8B7	62.5-63	md-crs sand	Hanford fm (H2 unit)
Grab	B1T8B8	65.5-66	sl gravelly md sand	Hanford fm (H2 unit)
Grab	B1T8B9	65.5-66	sl silty sand	Hanford fm (H2 unit)
Grab	B1T8C0	67.5-68	md sand	Hanford fm (H2 unit)
Grab	B1T8C1	70-70.5	fn-crs sand	Hanford fm (H2 unit)
Grab	B1T8C2	73-73.5	md-crs sand	Hanford fm (H2 unit)
Grab	B1T8C3	75.5-76	md-crs sand	Hanford fm (H2 unit)
Grab	B1T8C4	77.5-80	sl gravelly md-crs sand	Hanford fm (H2 unit)
Grab	B1T8C5	80-80.5	sl gravelly md-crs sand	Hanford fm (H2 unit)
Grab	B1T8C6	82.5-83	md-crs sand	Hanford fm (H2 unit)
Grab	B1T8C7	85.5-86	md sand	Hanford fm (H2 unit)

Table 2.6 (contd)

Type	HEIS #	Depth (ft)	Lithology	Stratigraphic Unit
Grab	B1T8C8	87.5-88	md sand	Hanford fm (H2 unit)
Grab	B1T8C9	90.5-91	sl silty md sand	Hanford fm (H2 unit)
Grab	B1T8D0	93-93.5	sl silty md sand	Hanford fm (H2 unit)
Grab	B1T8D1	95-95.5	sl silty md sand	Hanford fm (H2 unit)
Grab	B1T8D2	97.5-98	md sand	Hanford fm (H2 unit)
Grab	B1T8D3	100-100.5	silty fn sand	Hanford fm (H2 unit)
Grab	B1T8D4	102.5-103	md sand	Hanford fm (H2 unit)
Grab	B1T8D5	105-105.5	md sand	Hanford fm (H2 unit)
Grab	B1T8D6	108-108.5	md sand	Hanford fm (H2 unit)
Grab	B1T8D7	110.5-111	md sand	Hanford fm (H2 unit)
Grab	B1T8D8	110.5-111	md sand	Hanford fm (H2 unit)
Grab	B1T8D9	112.5-113	md-crs sand	Hanford fm (H2 unit)
Grab	B1T8F0	115-115.5	md-crs sand	Hanford fm (H2 unit)
Grab	B1T8F1	117.5-118	md sand	Hanford fm (H2 unit)
Grab	B1T8F2	120-120.5	md sand	Hanford fm (H2 unit)
Grab	B1T8F3	123-123.5	md sand	Hanford fm (H2 unit)
Grab	B1T8F4	125.5-126	md-crs sand	Hanford fm (H2 unit)
Grab	B1T8F5	127.5-128	md sand	Hanford fm (H2 unit)
Grab	B1T8F6	130.5-131	md-crs sand	Hanford fm (H2 unit)
Grab	B1T8F7	132.5-133	silty fn sand	Hanford fm (H2 unit)
Grab	B1T8F8	135-135.5	fn sand	Hanford fm (H2 unit)
Grab	B1T8F9	137.5-138	md-crs sand	Hanford fm (H2 unit)
Grab	B1T8H0	140-140.5	md-crs sand	Hanford fm (H2 unit)
Grab	B1T8H1	142.5-143	fn-md sand	Hanford fm (H2 unit)
Grab	B1T8H2	145.5-146	md sand	Hanford fm (H2 unit)
Grab	B1T8H3	148-148.5	fn-md sand	Hanford fm (H2 unit)
Grab	B1T8H4	150-150.5	md sand	Hanford fm (H2 unit)
Grab	B1T8H5	153-153.5	md sand	Hanford fm (H2 unit)
Grab	B1T8H6	155-155.5	fn-md sand	Hanford fm (H2 unit)
Grab	B1T8H7	158-158.5	fn-md sand	Hanford fm (H2 unit)
Grab	B1T8H8	160-160.5	md-crs sand	Hanford fm (H2 unit)
Grab	B1T8H9	162.5-163	md-crs sand	Hanford fm (H2 unit)
Grab	B1T8J0	162.5-163	md-crs sand	Hanford fm (H2 unit)
Grab	B1T8J1	165.5-166	md-crs sand	Hanford fm (H2 unit)
Grab	B1T8J2	167.5-168	md sand	Hanford fm (H2 unit)
Grab	B1T8J3	170-170.5	md sand	Hanford fm (H2 unit)
Grab	B1T8J4	172.5-173	md sand	Hanford fm (H2 unit)
Grab	B1T8J5	175-175.5	md sand	Hanford fm (H2 unit)
Grab	B1T8J6	177.5-178	fn-md sand	Hanford fm (H2 unit)
Grab	B1T8J7	180-181	md sand	Hanford fm (H2 unit)

Table 2.6 (contd)

Type	HEIS #	Depth (ft)	Lithology	Stratigraphic Unit
Grab	B1T8J8	182.5-183	md sand	Hanford fm (H2 unit)
Grab	B1T8J9	185-185.5	md sand	Hanford fm (H2 unit)
Grab	B1T8K0	187.5-188	fn-md sand	Hanford fm (H2 unit)
Grab	B1T8K1	190-190.5	md-crs sand	Hanford fm (H2 unit)
Grab	B1T8K2	192.5-193	md sand	Hanford fm (H2 unit)
Grab	B1T8K3	195-195.5	md sand	Hanford fm (H2 unit)
Grab	B1T8K4	197.5-198	md-crs sand	Hanford fm (H2 unit)
Grab	B1T8K5	200-200.5	md sand	Hanford fm (H2 unit)
Grab	B1T8K6	200-200.5	md sand	Hanford fm (H2 unit)
Grab	B1T8K7	203-203.5	md sand	Hanford fm (H2 unit)

Crs = coarse; fn = fine; md = medium; sl = slightly; v = very

A summary hydrogeologic log, which shows an integration of all the geologic, geophysical, and moisture data collected for borehole C5925, is presented in Figure 2.21.
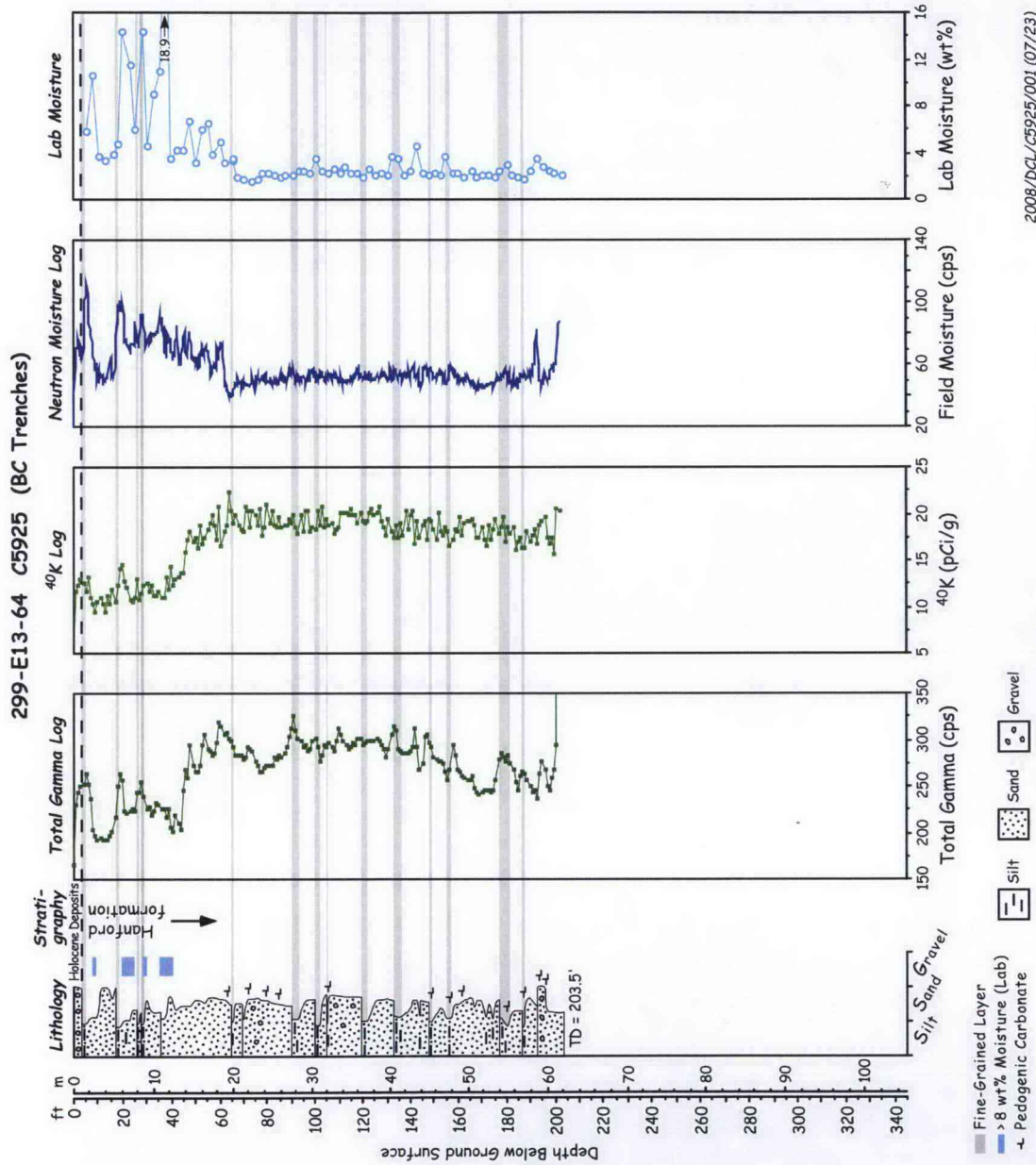
Figure 2.21. Composite Summary Log for Borehole C5925

2.4 Historical Water Levels

Hydrographs of wells in the BC Cribs and Trenches area show historical changes in groundwater levels going back to 1957. Water levels rose steadily through the 1950s, reaching a peak ~1969–1971, and then decreased slowly until 1982. Then the water level increased sharply again, reaching a secondary peak in 1988–1991, which about equaled the 1969 level. Since then the water table has been steadily decreasing as shown in Figure 2.22. These changes in water level appear to be related to fluctuations in artificial recharge at waste-disposal facilities that occurred in the 200 East Area during this time. At the time that C4191 was completed in January 2004, the water table was tagged at 397.49 ft elevation, which is about 3 ft lower than for the hydrograph for well 299-E13-14. In July 2008, the water table was tagged at 395.4 ft elevation for C5923, suggesting that the water table is still declining since 2004.
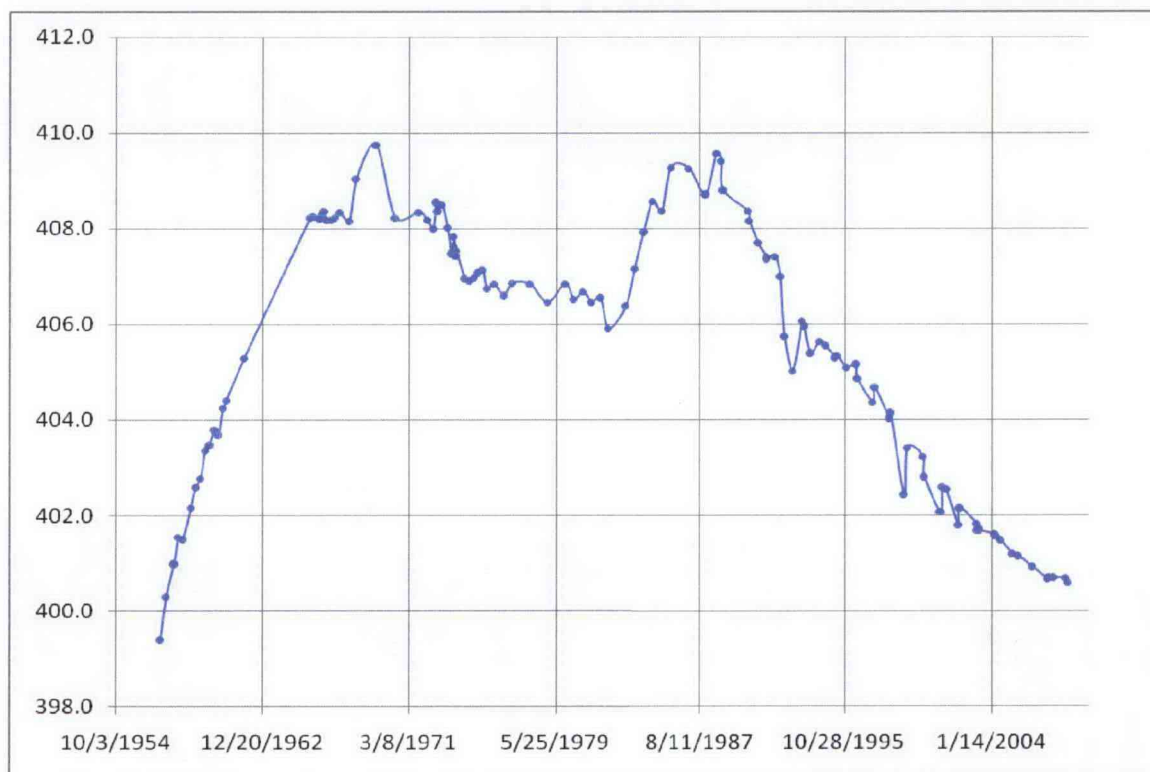
Figure 2.22. Hydrograph for Well 299-E13-14. Y-axis is elevation (ft).

The total difference in water level between 1957 and 2004 has been ~10 ft, and by 2008 the water table may have dropped a total of 12 ft since the two highest elevations. However, the pre-Hanford water table in the vicinity of the BC Cribs and Trenches lays at about 388 ft elevation (Gephart et al. 1979). Thus, the total difference in water levels may have ranged 20 ft or more since the beginning of liquid-waste disposal activities on the Hanford Site, suggesting that the water table may drop another ~7.5 ft to return to pre-Hanford conditions. These water-table elevation changes can be used to study whether any sediment samples obtained within these depths show signs of residual water or contaminants from groundwater when it was at its highest elevation.

3.0 Geochemical/Geohydrological Methods and Materials

This chapter discusses the methods and philosophy used to characterize the sediments collected from the BC Cribs and Trenches Area boreholes and the parameters that were measured and analyzed in the laboratory. It also describes the materials and methods used to conduct analyses of the geochemical, radio-analytical, and physical properties of the sediments.

3.1 Sample Inventory

Samples were numbered using Hanford Environmental Information System (HEIS)–specific sample names. The core samples from the split-spoon sampling at C5923 were further identified by the numbers 1, 2, 3, or 4, where the number 1 liner was always in the deeper position closest to the drive shoe. Four 0.5-ft Lexan liners were emplaced within the split-spoon coring device. After discarding liner 4 (top liner) as slough and using liner 1 and the core barrel drive shoe to generate a composite grab sample, liners 2 and 3 were generally sent to the PNNL ESL laboratory in an intact condition. Both core liners (total 39) and grab (total 147 including duplicates) were received from borehole C5923 (A). Additional laboratory duplicate samples were generated during sub-sampling and designated by DUP so that Hanford Analytical Services Quality Assurance Requirements Documents (HASQARD) QA/QC protocols could be met. The PNNL document for implementing HASQARD is *Conducting Analytical Work in Support of Regulatory Programs*, located at http://etd.pnl.gov/docs/conducting-work/index.stm. Details about the core and grab samples received from borehole A (C5923) are listed in Table 2.4. Only grab samples were received from Borehole C5924 (B) (total 105), C (total 84), and C4191 (total 126). More details and a listing of the grab samples received from boreholes C5924 (B), C5925 (C), and C4191 are found in the previous section (see Table 2.5, Table 2.6, and Table 2.3, respectively).

3.2 Approach

From past borehole characterization investigations on Hanford sediments, it was found that changes in sediment type and contaminant concentrations often occurred within a distance of a few inches within a given liner (Serne et al. 2002b). It was concluded that a more methodical scoping approach would be necessary to provide the technical justification for selecting samples for detailed characterization as defined in data quality objectives processes (see, for example, DOE 1999). Subsequently, a method was developed to select samples that considered depth, geology (e.g., lithology, grain-size composition, and carbonate content), individual sediment sample contaminant concentration (e.g., radionuclides, nitrate), moisture content, and overall sample quality. Extraction/leaching procedures were performed and certain key parameters (i.e., moisture content, gamma energy analysis [GEA]) were measured on each sediment sample. During the geologic examination of the grab samples, the sediment contents were sub-sampled for moisture content, gamma-emission radiocounting, 1:1 water extractions (which provide soil pH, alkalinity, [EC, cation and anion data, and ionic strength calculation), cation exchange capacity (CEC), and surface area measurement. Sampling preference was always biased towards the finer-grained and/or wetter material contained in each grab sample. The remaining sediment from each grab sample was then sealed and placed in cold storage. To date, only grab samples from boreholes C5923, C5924, C5925, and C4191 were used for geochemical characterization. Core samples received from borehole C5923 (A) were used solely for laboratory geophysical resistivity and other hydraulic measurements described in sections 4.2 and 3.3-11 to 3.3-15, respectively.

3.3 Materials and Methods

During sub-sampling, every effort was made to minimize moisture loss and prevent cross contamination between samples. Depending on the sample matrix, very coarse pebbles and larger material (i.e., >32 mm) were removed during sub-sampling. Larger substrate was excluded to provide moisture contents representative of GEA and 1:1 sediment: water-extraction samples. Therefore, the results from the sub-sample measurements may contain a possible bias toward higher concentrations for some analytes that would be preferentially associated with the smaller sized sediment fractions.

Procedures ASTM D2488-93 (1993) and PNL-MA-567-DO-1 (PNL 1990) were followed for visual descriptions and geological descriptions of all samples. The sediment classification scheme used for geologic identification of the sediment types (used solely for graphing purposes in this report) was based on the modified Folk/Wentworth classification scheme (Folk 1968 and Wentworth 1922).

This section also describes the laboratory methods used to characterize the geo-hydrologic properties of soil samples collected from Borehole C5923 (A) during the recent drilling campaign. Laboratory measurements were performed on intact cores and grab samples to characterize geo-hydrologic properties. Measured properties included particle-size distribution (PSD), particle density (ρ_s), specific surface area (SSA), porosity (ϕ), hydraulic conductivity (K_w), air permeability (K_a), and water retention, $\theta(\psi)$, which relates volumetric water content, θ, to the matric potential, ψ. A total 20 grab samples from Borehole C5923 (A) and 10 from Borehole C5924 (B) were selected for particle-size analysis and surface area measurements. In addition, 12 samples from Borehole C5923 (A) were selected for analysis of pneumatic and hydraulic properties. In general, samples were selected from fine textured lenses and the first coarse-textured layer occurring beneath each fine layer, i.e., layer sequences that might constitute a capillary break.

3.3.1 Moisture Content

Gravimetric water contents of the sediment samples were determined using PNNL procedure PNNL-AGG-WC-001 (PNNL 2005). This procedure is based on the American Society for Testing and Materials procedure "Test Method for Laboratory Determination of Water (Moisture) Content of Soil and Rock by Mass" (ASTM D2216-98 [ASTM 1998]). One representative sub-sample of at least 15 to 70 g was used. Sediment aliquots were placed in tared containers, weighed, and dried in an oven at 105°C until constant weight was achieved, which took at least 24 hours. The containers were removed from the oven, sealed, cooled, and weighed. At least two weighings, each after a 24-hour heating period, were performed to verify that all moisture was removed. All weighings were performed using a calibrated balance. A calibrated weight set was used to verify balance performance before weighing the samples. The gravimetric water content was computed as the percentage change in soil weight before and after oven drying.

3.3.2 1:1 Sediment: Water Extracts

Water-soluble inorganic constituents were determined using a 1:1 sediment:de-ionized-water extract method. The extracts were prepared by adding an exact weight of de-ionized water to approximately 60 to 80 g of sediment (post air-drying and sieving). The weight of de-ionized water needed was calculated based on the weight of the air-dried samples (residual moisture in the air-dried samples was considered

negligible). An appropriate amount of de-ionized water was added to screw-cap jars containing the sediment samples. The jars were sealed and briefly shaken by hand and then placed on a mechanical orbital shaker for 1 hour. The samples were allowed to settle overnight until the supernatant liquid was fairly clear. The supernatant was carefully decanted, filtered (passed through 0.45-μm membranes) and analyzed for conductivity, pH, anions, cations, alkalinity, and radionuclide analyses. More details can be found in Rhoades (1996) and within Methods of Soils Analysis - Part 3 (ASA 1996).

3.3.2.1   pH and Conductivity

Two aliquots of approximately 3-mL volume of the 1:1 sediment:water extract supernatants were used for pH and conductivity measurements. The pH of the extracts was measured with a solid-state pH electrode and a pH meter calibrated with buffers 7 and 10. The EC was measured using a Pharmacia Biotech Conductivity Monitor. Approximately 2 to 3 milliliters of filtered sample were measured in the conductivity meter and compared to potassium chloride standards with a range of 0.001 to 1.0 M.

3.3.2.2   Anions

The 1:1 sediment:water extracts were analyzed for anions using ion chromatography (IC). Fluoride, chloride, nitrite, bromide, nitrate, phosphate, and sulfate were separated on a Dionex AS17 column with a gradient elution of 1 mM to 35 mM sodium hydroxide and measured using a conductivity detector. This methodology is based on U.S. Environmental Protection Agency (EPA) Method 300.0A (EPA 1984) with the exception of using the gradient elution of sodium hydroxide.

3.3.2.3   Cations and Trace Metals

Major cation analysis was performed using an inductively coupled plasma-optical emission spectroscopy (ICP-OES) unit using high-purity calibration standards to generate calibration curves and verify continuing calibration during the analysis run. Dilutions of 100×, 50×, 10×, and 5× were made of each 1:1 water extraction for analysis to investigate and correct for matrix interferences. Details of this method are found in EPA Method 6010B (EPA 2000b). The second instrument used to analyze trace metals, including technetium-99 and uranium-238, was an inductively coupled plasma-mass spectrometer (ICP-MS) using the PNNL-AGG-415 method (PNNL 1998). This method is quite similar to EPA Method 6020 (EPA 2000c).

3.3.2.4   Alkalinity

Alkalinity was measured using a standard titration with acid method. The alkalinity procedure is equivalent to the U.S. Geological survey method in the National Field Manual for the Collection of Water-Quality Data (USGS 2004). Measured alkalinity (mg/L as $CaCO_3$) was converted to determine CO_3^{2-} concentration in solution.

3.3.3   8 M Nitric Acid Extracts and Elemental Analysis

Approximately 20 g of oven-dried sediment was contacted with 8-M nitric acid at a ratio of approximately five parts acid to one part sediment. The slurries were heated to about $80^\circ C$ for several hours, and then the fluid was separated by filtration through 0.2-μm membranes. The acid extractions

were analyzed for major cations and trace metals using ICP-OES and ICP-MS techniques, respectively, to determine the elemental composition of the bulk sediment samples. The acid digestion procedure is based on EPA SW-846 Method 3050B (EPA 2000a).

3.3.4 Radioanalytical Analysis

The GEA was performed on selected grab sediments from the four boreholes. All samples for GEA were analyzed using 60% efficient intrinsic germanium gamma detectors. All germanium counters were efficiency calibrated for distinct geometries using mixed gamma standards traceable to the National Institute of Standards and Technology (NIST). Field-moist samples were placed in 150-cm^3 counting containers and analyzed for 100 minutes in a fixed geometry. All spectra were background-subtracted. Spectral analysis was conducted using libraries containing most mixed fission products, activation products, and natural decay products. Control samples were run throughout the analysis to verify correct operation of the detectors. The controls contained isotopes with photo peaks spanning the full detector range and were monitored for peak position, counting rate, and full-width half-maximum. Details are found in Gamma Energy Analysis, Operation, and Instrument Verification using Genie2000™ Support Software (PNNL 1997).

Aliquots of sediment used for strontium-90 analysis were weighed and spiked with strontium-85. Samples were then leached overnight with concentrated nitric acid after which an aliquot of the leachate was diluted 50% with de-ionized water. The resulting solutions were passed through SrSpec columns obtained from Eichrom (Darien, IL) with 8 M nitric acid to capture strontium. The resin column was then washed with 10 column volumes of 8 M nitric acid. The strontium was eluted from the SrSpec column using de-ionized water. The de-ionized water eluent was evaporated to dryness in a liquid scintillation vial and was ready for counting after adding the cocktail. The purified strontium samples were analyzed first by gamma spectroscopy to determine chemical yield from the added strontium-85 tracer and to quantify any contamination from other gamma emitters such as cesium-137 that might have been present in the sediment. De-ionized eluents were then analyzed by liquid scintillation counting to determine the amount of strontium-90. A matrix spike, a blank spike, a duplicate, and procedure blanks were run with each batch of samples (generally 20 samples) to determine the efficiency of the separation procedure as well as the purity of reagents. Chemical yields were generally good with some explainable exceptions. Matrix and blank spike yields were good, bias was consistent, and blanks were below detection limits.

The nickel-63 procedure recovers all the nickel (both radioactive and stable) from the BC Cribs and Trench area sediments with very high decontamination of other beta emitters. No yield monitor was used other than the nickel-63 spike used in matrix and blank spikes. An aliquot of the acid extract sample (same acid extract as strontium-90; see above) was placed in a beaker, and 0.1 mg of stable nickel and 2 mg of stable iron (both as 10,000 ppm solutions) were added to the acid extract. Additionally, 200 μL of 5000 dpm nickel-63 was used for the blank spike and matrix spike. The treated acid-extract aliquots were evaporated to dryness and then wet-ashed with concentrated nitric acid to eliminate halides, cyanide, organics, and other species that could complex with the nickel. The dry residue was dissolved in dilute nitric acid and then transferred to a centrifuge tube. Strong sodium hydroxide solution was added to precipitate the iron, as $Fe(OH)_3$, which co-precipitates the nickel from solution. This step separates the nickel from the bulk of the treated acid extract. The iron-nickel hydroxide precipitate was dissolved in a small amount of hydrochloric acid, and 5 mg of strontium carrier was added. The solution was made basic with concentrated ammonium hydroxide (NH_4OH), and then ammonium carbonate ($NH_4)_2CO_3$ was

added and reacted for 10 minutes to form $Fe(OH)_3$ and $SrCO_3$ precipitates. During this step, the nickel stayed in solution as an ammonium complex. Most other elements, including strontium, yttrium, the rare earth, and iron, precipitated. The sample slurry then was centrifuged, and the separated supernatant was transferred to a clean container.

The precipitate was dissolved in a small amount of hydrochloric acid as before, and the precipitation was repeated as before to recover the small amount of nickel that might have been entrained in the precipitate. The second supernatant was combined with the first supernatant and evaporated to dryness. The dry residue was dissolved in dilute (1:10) ammonium hydroxide and transferred to a centrifuge tube. Dimethylglyoxime was added to precipitate the nickel as a dimethylglyoxime complex. After the precipitate was completely formed, methylene chloride (10 mL) was added, and the sample was shaken thoroughly. After centrifugation, the upper layer was washed twice with dilute ammonium hydroxide. Nickel was stripped back out of the methylene chloride solution by shaking it with dilute hydrochloric acid. The hydrochloric acid was evaporated off, and the remaining nickel in solution was counted for nickel-63 by liquid scintillation count (LSC) after adding cocktail solution (15 mL).

3.3.5 Unsaturated Flow Apparatus (UFA) Analysis

Several field-moist sediments were packed in drainable cells that were inserted into an UFA. The samples were centrifuged for up to 8 hours at several thousand g's to squeeze the pore water out of the sediment. The pore waters were characterized for pH, EC, cation, trace metals, selected radionuclides, and anions with the same techniques as used for the 1:1 sediment-to-water extracts.

3.3.6 Pore Water Composition Analysis

Major cations (Na^+, Ca^{2+}, K^+, Mg^{2+}, and Ba^{2+}) and anions (NO_3^-, PO_4^{3-}, CO_3^{2-}, SO_4^{2-}, Cl^-, F^-, and when present NO_2^-) concentration measured from both 1:1 water extracts and UFA solution were used to determine the total inorganic salt concentration and the ionic strength (moles/L). The total ionic strength (M) of the pore water was calculated by the molar concentration of each ionic species multiplied by its charge squared:

$$I = \frac{1}{2} \sum_i C_i Z_i^2 \tag{3.1}$$

where C_i is the molar concentration (mole/L) of each ionic species, and Z is the charge valence of each ionic species.

Equivalents of both cations and anions were also determined by the measured molar concentration multiplied by its charge valence. Equivalents of total cation and anion species were used to calculate charge balance of measured ionic species in pore water by:

$$ABS\left[\frac{(cations - anions)}{(cations + anions)}\right] \tag{3.2}$$

where ABS is the absolute value; cations and anions are total cation and anion concentrations with respect to equivalents.

3.3.7   Carbon Content on Sediment

The total carbon concentration in aliquots of sediment from the core liners was measured with a Shimadzu TOC-V CSN instrument with a SSM-5000A Total Organic Carbon Analyzer by combustion at approximately 900°C based on the ASTM Method, "Standard Test Methods for Analysis of Metal Bearing Ores and Related Materials by Combustion Infrared Absorption Spectrometry" (ASTM 2001). Samples were placed into pre-combusted, tared, ceramic combustion sample holders and weighed on a calibrated balance. After the combustion sample holders were placed into the furnace introduction tube, an approximately 2-minute waiting period was allowed for the ultra-pure oxygen carrier gas to remove any carbon dioxide (CO_2) introduced to the system from the atmosphere during sample placement. After this sparging process, the sample was moved into the combustion furnace, and the combustion was begun. The carrier gas then delivered the sample combustion products to the cell of a non-dispersive infrared (NDIR) gas analyzer where the CO_2 was detected and measured. The amount of CO_2 measured is proportional to the total carbon content of the sample. Adequate system performance was confirmed by analyzing known quantities of a calcium carbonate standard.

Sediment/solid samples were analyzed for inorganic carbon content by placing a small aliquot of oven-dry sediment into a ceramic combustion boat. The combustion boat was placed into the sample introduction tube where it was sparged with ultra-pure oxygen for 2 minutes to remove atmospheric CO_2. A small amount (usually 0.6 mL) of 3 M phosphoric acid was then added to the sample in the combustion boat. The boat was moved into the combustion furnace where it was heated to 200°C. Samples were completely covered by the acid to allow a full reaction to occur. Ultra-pure oxygen swept the resulting CO_2 through a dehumidifier and scrubber into the cell of an NDIR gas analyzer where the CO_2 was detected and measured. The amount of CO_2 measured is proportional to the inorganic carbon content of the sample.

The organic carbon content was determined by the difference between the inorganic carbon and total carbon concentration.

3.3.8   Particle Size Distribution

T he PSD of rocks and soils is important in understanding their hydrogeophysical and geochemical properties. Two methods were used to determine PSD: 1) mechanical analysis by dry sieving, and 2) laser diffraction spectrometry (LDS). Soil samples were separated into four grain-size fractions, namely, gravel, sand, silt, and clay, and sub classes were based on the logarithmic Udden-Wentworth grade scale (Wentworth 1922).

Dry sieving was used to separate the sediments above 62 μm into the very coarse, coarse, medium, fine, and very fine subclasses of the gravel and sand fractions. All sieving was performed in a fume hood using a Gilson SS-15 Sieve Shaker with two stacks of 8-in. sieves, one for the gravel fraction and one for the sand fraction. The gravel sieve stack included the 2½ in., 1¼ in., ⁵/₈ in., and ⁵/₁₆ in., # 5 sieves and a pan. The sand sieve stack consisted of the #10, #18, #35, #60, #120, and #230 sieves and a pan. Approximately 500 grams of each sample of interest was placed on a sheet of brown shipping paper laid out on wire racks to air dry over a 48-hr period. Each sample was first sieved through the gravel sieve stack and sieved for about 30 minutes at 3,000 oscillations/min, and the mass of soil was retained on each sieve recorded. The soil collected in the pan was then placed on the sand sieve stack and sieved for 30 minutes, and the mass was retained on each sieve and in the pan recorded. The soil collected in the

pan consisted of particles with a mean diameter < 63 μm (< #230 sieve). The percentage of each size fraction was used to determine texture according to the USDA classification. Grain-size statistics were calculated from the grain-size distributions using the methods described by Ward et al. (2006a).

The LDS measurements of PSD were performed with a Mastersizer 2000 (Malvern Instruments, Inc., Southborough, MA). The LDS method requires that the particles be in a dispersed state, either in liquid (suspension) or in air (aerosol). The former is commonly referred to as the "wet" method (LDS-W) while the latter is termed the "dry" method (LDS-D). For these analyses, the LDS-W method was used with a dispersion accessory. The dispersion accessory consists of a 20-mL sample flow cell with a continuous variable and independent pump and ultrasound. The ultrasonic processor is used for particle-size reduction and disintegration of aggregates, a process known as sonication. Both flow and sonication can be controlled and altered. For these measurements, PSD was determined before, during, and after sonication to allow the influence of sonication energy stage on the sample's PSD to be determined. Samples were dispersed in "quartz water" that was free of dispersing agents.

The particle suspensions were placed in a stirred tank and were circulated through the cell, which was placed in the path of the laser beam. A pump speed of 3,000 RPM was used. The laser beam (He-Ne laser, wavelength 633 nm) was collimated to 18 mm. The focal length was 1,000 mm, and the cell depth was 14.2 mm. The scattered light was received on a detector consisting of 32 photosensitive rings that detected particle diameters in the range from 19 to 1,880 μm. PSDs were measured before and during sonication. For each condition, three successive 12-second measurements of PSD were taken. An average of these measurements was then generated by the analyzer software (Mastersizer 2000 software, Version 5.4). Once measurements were complete, the sonic power for the next condition was set, the sample was given 30 to 60 seconds to equilibrate, and the next set of measurements was taken. Volumetric PSDs were calculated from the distribution of the light energy on the detector using the Fraunhofer diffraction theory for spherical particles (Weiner 1984; Allen 1997). The analysis employed a particle refractive index and absorption of 1.544 and 0, respectively, and a suspending phase-particle refractive index of 1.33 (for water). Volume PSDs corresponding to coarse (31 to 62.5 μm), medium (16 to 31 μm), fine (8 to 16 μm), and very fine (4 to 8 μm) silt and to coarse (2 to 4 μm) and fine (1 to 2 μm) clay were determined and scaled to the total mass of sample passing through the #230 sieve. These data were combined with the dry sieve data to generate a complete PSD curve. Particle-size statistics were calculated from the grain-size distributions using the methods described by Ward et al. (2006a).

3.3.9 Particle Density

Particle density, ρ_s, is widely used for establishing the density-volume relationship of soil materials. It is used to calculate porosity and estimate optimum moisture in compaction tests. Particle density is defined as the mass of solids in a sample divided by the volume of the solids. Particle density is commonly assumed to be 2.65 Mg/m^3, which corresponds to the specific gravity of quartz. However, many silicate and non-silicate minerals, such as feldspars, granites, micas, and kaolinite, exhibit densities from 2.3 to 3.0 whereas the density of iron-containing minerals like hematite and goethite often exceeds 3.3. The mean particle density of a soil therefore depends on the mineral composition and is calculated using a weighted mean. Particle density, ρ_s, measurements were performed on three replicates of each size fraction less than 2 mm using the pycnometer method (Blake and Hartge 1986; ASA 1996). The mean particle density of each sample was then calculated from the n weight fractions, $x_1, x_2, \ldots, x_n$ and the associated particle densities, $\rho_{s_1}, \rho_{s_2}, \ldots, \rho_{s_n}$, of each fraction as:

$$\rho_s = \left(\frac{x_1}{\rho_{s_1}} + \frac{x_2}{\rho_{s_2}} + \ldots + \frac{x_n}{\rho_{s_n}} \right)^{-1}$$

(3.3)

3.3.10 Porosity and Bulk Density

Porosities were determined on 12 undisturbed cores from Borehole C5923 (A) by measuring the water content at saturation using time domain electrometric (TDR) techniques. These measurements were made after saturating the cores for saturated hydraulic conductivity measurements. Bulk density was calculated as the ratio of the dry weight of sediment in the packed core to the volume of the core.

3.3.11 Specific Surface Area

The SSA is a measure of the exposed surface of a solid sample on the molecular scale and is important for the calculation of sorption properties, surface conductance of the different lithofacies, and description of the retention of water at low saturations. The SSA was measured on 20 grab samples from Borehole C5923 (A) using a Micromeritics ASAP 2020 gas sorption surface-area analyzer. The Monosorb is a direct-reading dynamic-flow surface-area analyzer that uses a single-point Brunauer-Emmett-Teller (BET) method to determine the surface area (Brunauer et al. 1938). Standard surface-area reference materials were used to calibrate the instrument over the anticipated range of surface areas. Representative sediment samples from Borehole C5923 (A) were first rinsed three times for short time periods in deionized water to remove the high pore-water salt content. The washed sediments were dried overnight using a heating mantle and then weighed to an accuracy of 0.001 g. The surface analyzer measures the quantity of a gas adsorbed on a solid surface when it is cooled with liquid nitrogen by sensing the change in thermal conductivity of a flowing mixture of an adsorbate (nitrogen) and an inert (helium) carrier gas. With nitrogen and helium, the surface area can be determined down to $0.1 \ m^2$. With mixtures of krypton and helium, the limit of detection is extended down to $0.01 \ m^2$. The isotherm points are transformed with the BET equation:

$$\frac{1}{W[(P_0/P)-1]} = \frac{1}{W_m C} + \frac{(C-1)}{W_m C} \frac{P}{P_0}$$

(3.7)

where   W = weight of nitrogen adsorbed at a given P/P_0
      P = pressure at each measurement point
     P_0 = saturation pressure of the gas
    W_m = weight of gas required to give monolayer coverage
     C   constant related to the heat of adsorption.

A linear relationship between $1/W[(P_0/P)-1]$ and P/P_0 is required to obtain the quantity of nitrogen adsorbed. This linear portion of the curve is restricted to a limited portion of the isotherm, generally from 0.05 to 0.30 (P/P_0). The slope and intercept are used to determine the quantity of nitrogen adsorbed in the monolayer and used to calculate the surface area. For the single-point method, the intercept is taken as zero or a small positive value, and the slope from the BET plot is then used to calculate the surface area. The SSA is then calculated by dividing the average of the surface-area measurements obtained by the BET method by the weight of the sample.

3.3.12 Cation Exchange Capacity

The CEC of selected grab samples from borehole C5923 (A) vadose zone sediments was measured by taking 15 g of distilled water pre-rinsed (three short-duration rinses) air-dried sediment and extracting one time with 1.0 M ammonium acetate (35 mL) to prevent additional dissolution of calcium carbonate. The sediment-ammonium acetate slurries were gently shaken on a linear shaker for 24 hours and then centrifuged. Each supernatant solution was filtered through a 0.2-microm membrane. The exchangeable cations (Ba, Ca, K, Mg, Na, and Sr) in the ammonium acetate extract were analyzed by ICP-OES. Cation concentrations were converted to meq and summed to get the total CEC of the composite sediments (in meq/100 g). Our method is quite similar to the ammonium acetate method used to estimate exchangeable cations found in the chapter of ASA (1996) written by Suarez (1996; 583–584).

3.3.13 Saturated Hydraulic Conductivity

Hydraulic conductivity is known to vary with saturation and functions describing the saturation dependence are needed to interpret contaminant distributions and to predict flow and transport. The hydraulic conductivity, K, as a function of pressure head, [K = f(h)], is the proportionality factor in the Richards' water-flow equation that relates the flux density to a unit potential gradient at a specific water content. Mathematical functions are commonly used to calculate the unsaturated conductivity from the water-retention function, $\theta(h)$, with knowledge of the saturated hydraulic conductivity, K_s. Several functions are available, but the Mualem conductivity function is most commonly used (in conjunction with the van Genuchten retention function). The unsaturated hydraulic conductivity is defined as:

$$K(h) = K_s \frac{\left[1 - (\alpha h)^{mn}\left(1 + (\alpha h)^n\right)^{-m}\right]^2}{\left[1 + (\alpha h)^n\right]^{\ell m}} \tag{3.8}$$

where K_s = saturated hydraulic conductivity, the proportionality constant in the Darcy equation
that relates the flux density to a unit potential gradient
m = 1 - 1/n
α = inverse of the air entry pressure
l = pore-connectivity parameter, estimated to be about 0.5 as an average for many soils
(Mualem 1976).

However, more recent studies (e.g., Schuh and Cline 1990; Schaap and Leij 1998; Zhang et al. 2004; Ward et al. 2006b) suggest that values of ℓ (rather than 0.5) may represent the hydraulic behavior of many soils equally well or better. In layered soils, saturation-dependent anisotropy, which can lead to increased lateral flow in some layers, is best described by a pore connectivity tensor (Zhang et al. 2003; Raats et al. 2004; Ward et al. 2006b).

Saturated hydraulic conductivity measurements were made on 12 undisturbed core liners from Borehole C5923 (A) using the falling-head method (see Figure 3.1). A major advantage of the falling-head method over constant head and other methods is that it can be used for both fine-grained and coarse-grained soils, both of which are present at the BC Cribs site. For hydraulic measurements, including falling-head tests, each core liner was fitted with two machined plexiglas® collars, one at each end, to allow attachment of end plates. The end plates were attached, the core saturated and weighed, and a small-diameter reservoir attached to the bottom end of the core.
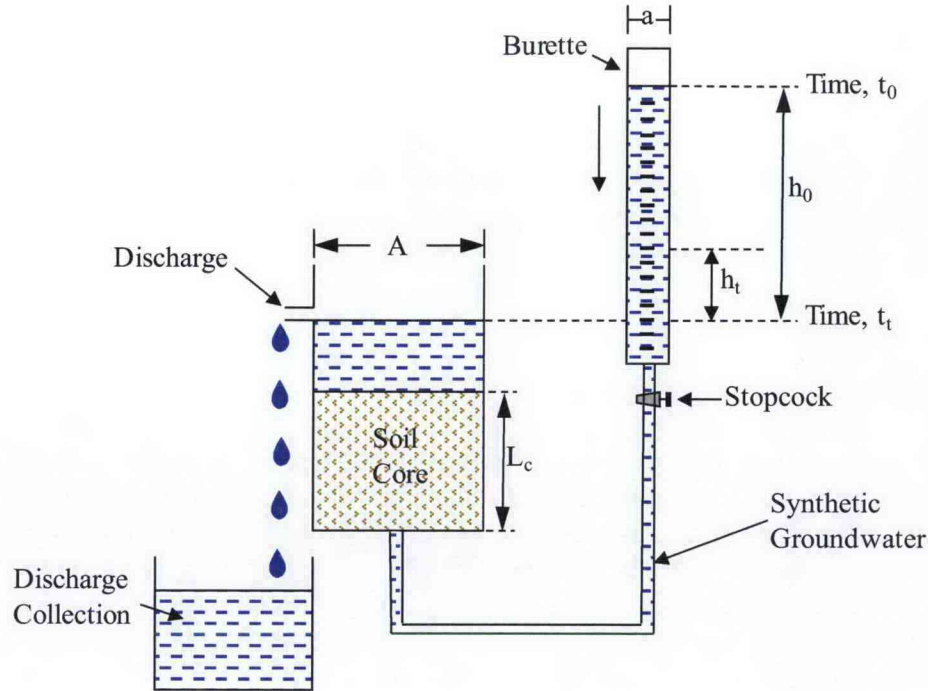
Figure 3.1. Schematic of Falling Head Apparatus to Measure Saturated Hydraulic Conductivity

For these tests, a burette was used as the small-diameter reservoir. The burette was filled with water, and the height at time zero, h_0, was recorded. The measurement was started by opening the burette stopcock, and the rate of decline of the water level in the burette was recorded over time. The hydraulic head at the upgradient end of the sample was allowed to decline from h_0, at time 0 (t_0), to h_t at some time t (t_t). The calculation of K_s is based on Darcy's Law, with K_s being defined as:

$$K_s = \left[\frac{aL_c}{A(t_t - t_0)}\right] \cdot \log\left(\frac{h_0}{h_t}\right) \tag{3.9}$$

In Eq. (3.9), a is the cross-sectional area of the small reservoir, A is the cross-sectional area of the soil core, and L_c is the length of the soil core. Equation (3.9) can be simplified to give K_s in terms of the ratio of the reservoir and core diameters, the elapsed time and head ratios, i.e.,

$$K_s = \left(\frac{d_r}{d_c}\right)^2 \cdot \left[\frac{L_c}{t_t - t_0}\right] \cdot \log\left(\frac{h_0}{h_t}\right) \tag{3.10}$$

where d_r is the diameter of the reservoir, L_c is the length of the core sample, and d_c is the diameter of the core. The head at the up-gradient end of the core is simply the height of the water level in the burette, above the datum (the level of the discharge tube), whereas the head at the down-gradient end of the core

is the height of the discharge point above the datum. Each measurement was repeated three times using different initial hydraulic gradients. A mean value of K_s was then calculated for head gradient as the average of the three replicates. The photographs in Figure 3.2 show different stages of column preparation for saturated hydraulic conductivity measurements and the soaking tank with fixed overflow used for containing the permeability cell during falling head tests. Owing to the nature and levels of contaminants in the cores, all work conducted on the cores was performed in a radiation control area.

3.3.14 Air Permeability

Air permeability is important to gas-transport studies and at the BC Cribs is needed for remediation techniques that may involve the injection of gas-phase reactants and heated dehumidified air for desiccation. Air permeability is relatively easy to measure and can be used as an indicator of soil hydraulic conductivity.

Air-permeability measurements were made on 36 undisturbed core liners from Borehole C5923 (A) using an automated gas mini-permeameter (Tidwell and Wilson 1997). The mini-permeameter consists of four electronic mass-flow meters (0 to 50, 0 to 500, 0 to 2000, and 0 to 20,000 cm^3/min. at standard conditions), a pressure transducer (0 to 100 kPa gauge), a barometer, and a gas temperature sensor that are all connected to a regulated source of air, generated by an automated piston. Measurements were made by pressing a molded silicone rubber tip seal against the soil surface (core end) while injecting gas at a constant pressure. We used a tip seal with an inner radius of 0.31 cm and an outer radius measuring twice the inner diameter. An inner spring-driven guide and an immobile outer guide maintained a consistent seal geometry under compressed conditions. The ring-shaped seal imposed a strongly divergent flow field resulting in a roughly hemispherical sample support (i.e., sample volume). Gas flow was directed into the soil via the tip seal affixed to a rigid brass housing (Tidwell and Wilson 1997; 1999).

(a)

(b)

(c)
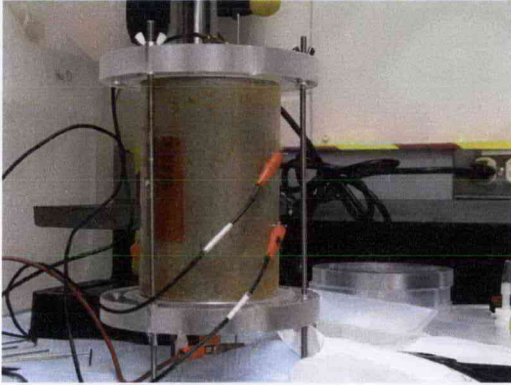
(d)

Figure 3.2. Stages of Core Preparation for Falling Head Conductivity Measurements, (a) Soil Core Just After Removal of End Caps, (b) Core After Attachment of the Collar Needed to Connect End Caps, (c) Fully Assembled Core with Collars and End Caps, and (d) Soaking Tank with Fixed Overflow Used for Containing the Core During Falling Head Tests

Using information on the seal geometry, gas flow rate, gas injection pressure, and barometric pressure, the permeability was calculated using a modified form of Darcy's Law (Goggin et al. 1988):

$$k_a = \frac{Q_1 P_1 \mu_a(T)}{0.5 r_i G_0 \left(\frac{r_0}{r_i}\right)\left[P_1^2 - P_0^2\right]} \tag{3.11}$$

where k_a = air permeability

Q_1 = gas flow rate

P_0 = atmospheric pressure

P_1 = gas injection pressure

$\mu_a(T)$ gas viscosity as a function of temperature T

$G_0(r_0/r_i)$ a geometric factor that varies according to the ratio of the outer tip seal radius r_0 to the inner tip seal radius r_i.

For the permeameter used for these measurements, $G_0(r_0/r_i) = G_0(2) = 5.03$. Vertical k_a measurements were made on three randomly selected locations on each end of the intact sediment core, and the results were averaged to compute the mean vertical air permeability for each sample.

4.0   Field Geophysical Methods and Materials

Geophysics is a science of measuring intrinsic physical properties of the earth (or subsurface) and associating observed changes in the measured properties with geologically, hydrologically, and/or anthropologically significant features. Geophysics, for example, can be used to map changes in hydrogeological properties, to locate buried utilities, and to extend borehole-derived information laterally away from the well point. Geophysical surveys are often used as a first-order target recognition tool or as a tool to map stratigraphic sequences. In the target recognition mode, the physical properties of the feature of interest must be sufficiently different from background conditions to distinguish the entirety of the target and confirm the extent of its edges. A target will not be identified if the variations in properties of the background material are similar in contrast and scale to those associated with the target. Assuming the target can be identified, the next order of interpretation is the relative degree of target size and intensity, referred to as the resolution limit and sensitivity, respectively.

Electrical-resistivity surveys have been conducted at the BC-Cribs and Trenches area (Rucker and Benecke 2006) in an attempt to identify anomalous regions (targets) that are likely associated with past liquid waste discharges. The working hypothesis is that the introduction of liquid waste (primarily of high sodium and nitrate concentrations) has locally altered the electrical properties within the subsurface to a degree measureable (and interpretable) using surface-based soil-resistivity surveys. Thus, the performance of these electrical-resistivity surveys is examined in this report, and the discussion that follows focuses on this technique.

Low electrical-resistivity regions may have discernable features that identify relative concentrations of salt and moisture within the target. If data are of exceptionally high quality, i.e., the data are free from significant noise and have been acquired properly, they may be correlated to specific observed phenomena to develop relationships that convert directly geophysical data to hydrogeological (i.e., moisture content or texture) or geochemical data (i.e., total dissolved solids or ionic strength) . This scenario requires that empirical models be developed from observed, co-located geophysical and geochemical data. The empirical models are then used to translate and extrapolate the geophysical data to obtain geochemical values over the site.

Electrical-resistivity surveys have been completed over the entire BC Cribs and Trenches area and documented in Rucker and Benecke (2006). The field-data acquisition campaign included 55 pole-pole resistivity transects separately collected along parallel and orthogonal lines (two-dimensional [2D] acquisition methodology as compared with true three-dimensional [3D] acquisition, where data are collected simultaneously over a surface areal grid). The resulting data sets were compiled for 3D analysis by 1) compositing 2D profile models into a 3D volume and 2) true 3D inversion. A few of the resistivity lines were acquired approximately one kilometer away from the BC Cribs and Trenches site in areas where no historical waste disposal is understood to have occurred to provide a control for understanding the effects of natural variability of soil types and moisture. It is believed that the interpretation of the geophysical data over the BC Cribs and Trenches waste disposal area have gone through sufficient steps to move beyond the simple target recognition and into the development of empirical models for direct comparison with co-located geochemical data from boreholes C5923 (A), C5924 (B), C5925 (C), and C4191. The following sections will help provide justification for the development of empirical models by describing the field-acquisition methods, data quality, and processing methodology. In addition to field-measured electrical resistivity, soil electrical resistivity was measured in the laboratory to supplement the

field-acquired data and help explain the occurrence of geophysical anomalies at the BC Cribs and Trenches area.

4.1 Electrical-Resistivity Field Acquisition

The primary objective of the BC Cribs and Trenches geophysical investigation was to characterize the subsurface beneath the BC Cribs and Trenches site using electrical resistivity to estimate the lateral (and to some degree, vertical) extent of ground surface that would need to be covered with a surface barrier or cap to minimize future water infiltration via natural recharge. The field investigation was performed to help extend the value of the sediment characterization information obtained from borehole C4191 and to help understand the extent to which the electrolytic components of the disposed waste may have migrated. To help augment the electrical-resistivity survey and to map subsurface infrastructure that may interfere with the interpretation of the resistivity, magnetometry and electromagnetic induction (EM) surveys were completed over the area. Interpretations of the magnetic survey identified several ferrous pipelines and suspected ferrous metallic debris. The EM data identified localized areas of conductive soil associated with liquid-waste disposal, pipelines, suspected metallic debris (ferrous and non-ferrous), and areas where disposal and mitigation efforts likely have impacted the soil.

The resistivity surveying was conducted over several field campaigns during the summers of 2004 (FY04), 2005 (FY05), and 2006 (FY06). The details of all field campaigns and results can be found in Rucker and Benecke (2006). In FY04, a 10-line exploratory survey was conducted to test the effectiveness of electrical resistivity as a mapping tool at BC Cribs and Trenches. Five lines were run parallel to trench 216-B-26 with a line spacing of 15 m. Two additional lines were run, with a line over (parallel) trench 216-B-52 and the second perpendicular to trenches 216-B-52 to 216-B-28. The last three lines of the initial campaign were run near the cribs in the northeast corner of the site.

The FY05 campaign included a full-site characterization with 42 lines of acquisition. Two of the lines were run south of BC Cribs in areas of no waste. The remaining 40 lines were distributed orthogonally to the waste sites that received liquid waste, with a focus mainly on the BC trenches. The lines were extended approximately 125 m off ends of the trenches to sufficiently characterize the background for target identification. For this effort, approximately 20 line kilometers of data were acquired.

The last campaign in FY06 included three additional lines in the cribs area to answer the question about a deep anomaly between the trenches and cribs. The anomaly was identified by both HRR and 2D inversion processing. It was suspected that the anomaly was a false positive, and the three lines were strategically placed over the area to incorporate the data into a 3D inversion model.

Figure 4.1 shows the line layout immediately over the site. For reference, the trenches, cribs, roads, and monitoring wells have been included. In total, approximately 24 line kilometers of pole-pole resistivity data have been acquired at the site.

4.1.1 Method of Acquisition

The electrical-resistivity method is based on the capacity of earth materials to conduct electrical current where zones with the lowest electrical-conductance correspond to the most electrically resistive

zones. Earth resistivity is an intrinsic material property that is a function of soil type, porosity, moisture, and electrical-properties of pore-fluids. The concept behind applying the resistivity method is to detect and map changes or distortions in an imposed electrical field due to heterogeneities in the subsurface.

In the field, the electric current may be generated by battery or motor-generator–driven equipment, depending on the particular application and the amount of power required. Current is introduced into the ground through electrodes (metal rods). Earth-to-electrode coupling is typically enhanced by pouring small volumes water around the electrodes. The electrodes are placed along linear transects and provide points for both current-transmission and voltage-potential measurements.

Estimating resistivity is not a direct process. When current (I) is applied and voltage (V) is measured, Ohms law is assumed. The transfer resistance (R) in units of ohms can be calculated:

$$R = \frac{V}{I}$$

(4.1)

Resistivity and transfer resistance are then related through a geometric factor over which the measurement is made. The simplest example is a solid cylinder with a cross sectional area of A and length, L:

$$\rho = R \frac{A}{L}$$

(4.2)
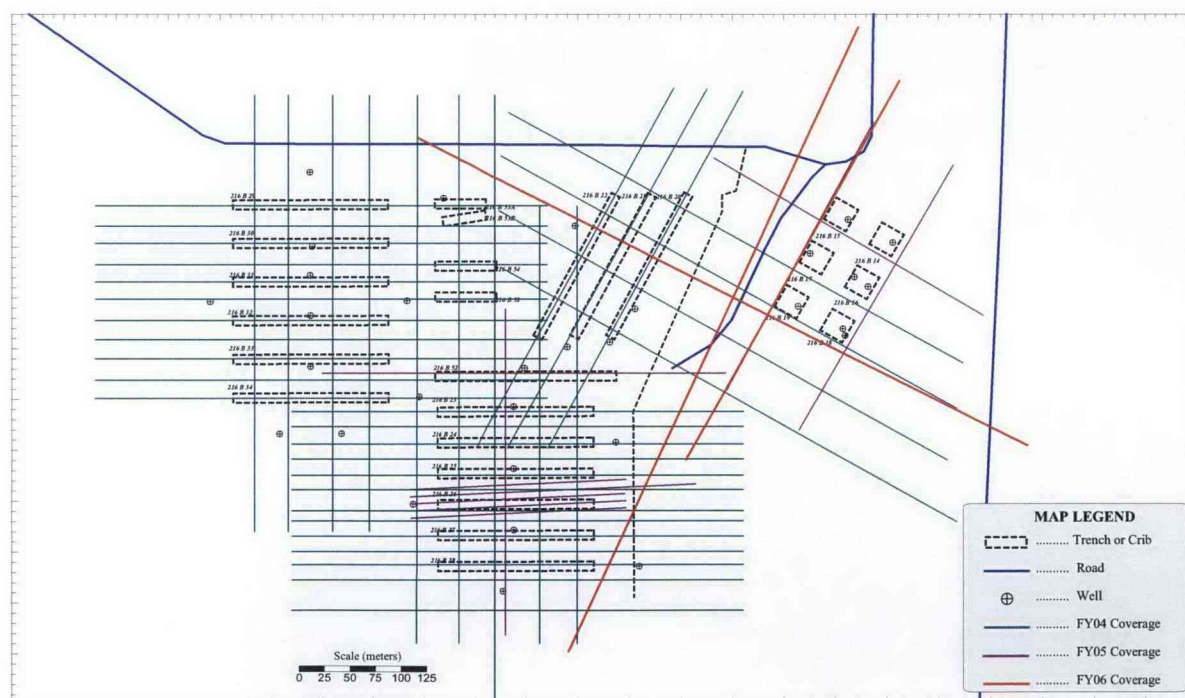
Figure 4.1. Electrical-Resistivity Line Layout over the BC Cribs and Trenches Site. North is to the top of the figure.

PNNL-17821

Hence, resistivity can be calculated by knowing the voltage, current, and geometry over which the measurement is made. In the earth, a hemispherical geometry exists and is referred to as a half-space because all current applied at the surface travels into the ground; above the ground, air has an infinite resistivity.

Field data are acquired using an electrode array. A four-electrode array employs electric current injected into the earth through one pair of electrodes (transmitting dipole, C1 and C2) and the resultant voltage potential is measured by the other pair (receiving dipole, P1 and P2). The most common configurations are dipole-dipole, Wenner and Schlumberger arrays. Their use depends upon site conditions and the information desired. For the four-electrode array, the geometric factor, K, is

$$K = 2\pi \frac{1}{\left(\dfrac{1}{r_1} - \dfrac{1}{r_2}\right) - \left(\dfrac{1}{r_3} - \dfrac{1}{r_4}\right)}$$ (4.3)

where r_1 through r_4 are defined in Figure 4.2.
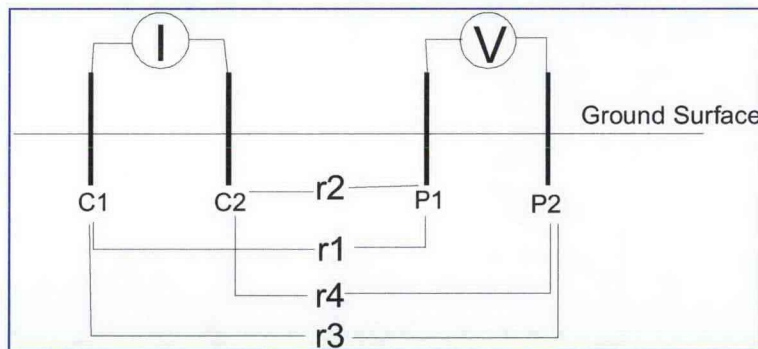
Figure 4.2. Geometry Factor for the Four Electrode Array

The earth property of resistivity is the desired product for interpretation and correlation. Thus, the measured voltage, the injected current strength, and the electrode geometry factor are used to compute a value of resistivity following Equation 4-2, substituting the area and length terms with the geometric factor, K, as defined by 4-3. The resulting resistivity value is termed an apparent resistivity (ρ_a) because the calculation assumes a homogenous earth through the region covered by the geometric factor calculation is needed to convert the measured voltage potential to resistivity. For the apparent resistivity (ρ_a) calculation, the inverse calculation assumes that each measurement of potential was a result of a homogeneous earth:

$$\rho_a = 2\pi \frac{V}{I} K$$ (4.4)

Other assumptions used in Equation (4-4) are isotropy (i.e., no directional dependence of resistivity), no displacement currents (using a DC or low-frequency current application), and constant resistivity throughout, such that Laplace's equation can be assumed. Since the degree of heterogeneity is not known

4.4

a priori, a true resistivity is not calculated in the apparent-resistivity equation. To obtain a true resistivity, tomography is required, which generates a model of true resistivity given the measurements of apparent resistivity, electrode arrangement, and other boundary conditions. The tomographic inversion is nonlinear, thus requiring multiple forward solutions developed from educated guesses of the resistivity distribution.

Resistivity data were acquired using an Advanced Geosciences, Inc. (AGI) Super Sting R8 resistivity instrument in the pole-pole array configuration. A pole-pole array was chosen based on its capability to resolve deeper targets with shorter lines compared to other array types. The resistivity meter is a DC-powered, battery operated, low voltage, low amperage, automatic, eight-channel resistivity and induced polarization (IP) system. This system employs the SuperSting Swift general-purpose cables that can be attached in series. Each cable segment contains four smart electrodes. Each electrode has the capability of acting as either a low-amperage current transmitter or as a potential measuring receiver.

The Super Sting R-8 has the capability of automatically switching between electrodes without having to physically move the electrode connections after initial set-up. Automatic switching decreases physical labor, cuts down on human transcription and tracking errors, better allows the operator to control array logistics, and increases the rate and density of data acquired. Hydrogeologic Inc. (HGI) personnel took advantage of this capability and programmed the Super Sting R-8 to use a survey line spread of 72 smart electrodes with an inter-electrode spacing ranging from 2 to 150 meters. The survey line was moved forward incrementally by removing a 12-electrode segment from the trailing end of the survey line spread and placing it at the front of the spread between measurements.

The location of the endpoints of each resistivity line was initially established using a Javad real-time kinematic (RTK) global positioning survey (GPS) unit. Rebar stakes were placed in the ground as survey orientation guides at regular intervals along each line. After data acquisition, the same GPS was used for horizontal and vertical control of regular electrode locations. The Javad unit has ± 0.03-m spherical accuracy. The elevation data were additionally quality checked against topographic contours on U.S. Geological Survey (USGS) 7.5-minute quadrangle maps.

Resistivity-data acquisition at BC Cribs and Trenches did not include making reciprocal measurements. For each pair of electrodes in the pole-pole acquisition, one electrode was the transmitter, and the other acted as the receiver. For reciprocal measurements, the pair is reversed, and the difference in voltage measurements between the forward and reverse readings is used to assess data-measurement error. Reciprocal measurements were not acquired because the acquisition time would have been doubled, making the cost of the survey prohibitively expensive. Repeat measurements are used to assess error for non-reciprocal data sets. Repeat measurements are conducted by acquiring two voltage measurements for the same transmitter-receiver pair in the same orientation. The error is computed to determine machine-level noise. It is customary to remove those data with an error above 2%. Figure 4.3 shows an example data set of error values for FY05-line 4. For reference, Borehole C5923 (A) is located at position 153 m along Line 4. The pseudo distance is calculated by averaging the positions of the transmitter and receiver along the line. Many electrode pairs may have the same pseudo distance. Error values are computed internally in the Super Sting R-8 and are recorded to the nearest tenth.

Measurement error also tends to increase with lower resistivity values. This phenomenon is easily explained when considering hardware, which has data-acquisition cards with a finite dynamic measurement range. From experience using the Super Sting R-8 (i.e., unpublished or referenced in the

user manual), data reliability is high when the transfer resistance is above 0.01 ohms. Two factors will make the transfer resistance low, high EC and large electrode separations. Therefore, when removing data of low quality, the process of data rejection tends to remove those data that represent the deepest information in a profile and those data nearest the water table.
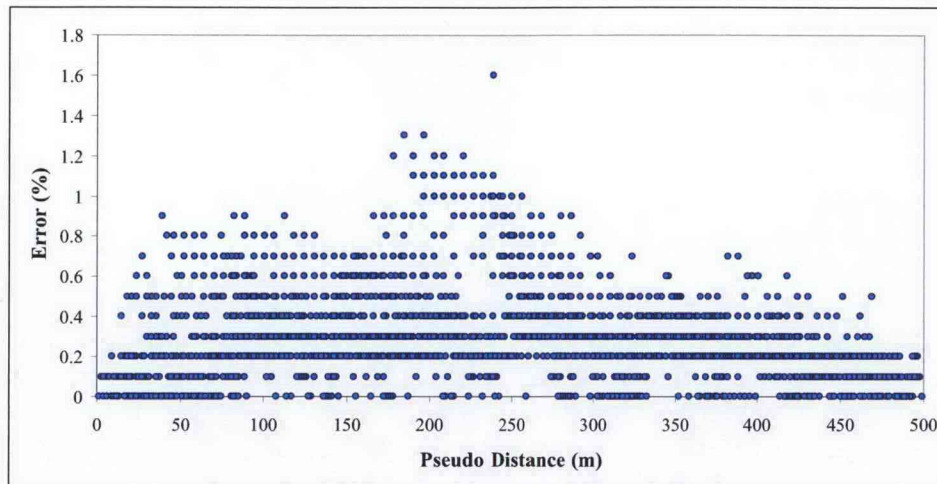
Figure 4.3. Example Error Values for FY05-Line 4

After data rejection based on measurement noise, data are evaluated for physical impossibilities based on potential field theory. This step requires that the transfer resistance (V/I) for each transmitter electrode be plotted with all of the receiver electrodes. The plot should show a smoothly varying function as the separation of the transmitter and receiver electrode increases. Large spikes in the function are physical impossibilities in natural media, and those data are removed from the data set. Figure 4.4 demonstrates an example of a data spike that is targeted for removal. The processing of data for spike rejection also includes the plotting of each receiver electrode individually with its associated transmitter electrode set.

4.1.2 HRR Processing (ERC Processing)

For the pole-pole array, one electrode from each of the current and potential pairs is fixed effectively at infinity, while the other current and potential electrodes act as "rover" electrodes. Practically, the infinite electrodes are spaced approximately 2 to 10 times the distance of the farthest separation of the rover electrodes, which can be up to 200 meters apart. The pole-pole array provides higher data density and increased signal-to-noise ratio, and it requires less transmitted energy. Roy and Apparao (1971) discuss the superiority of the pole-pole method when conducting shallow (near-surface) surveys. Rucker and Fink (2007) showed how the data from the pole-pole array can be used directly to interpret discrete conductive targets.
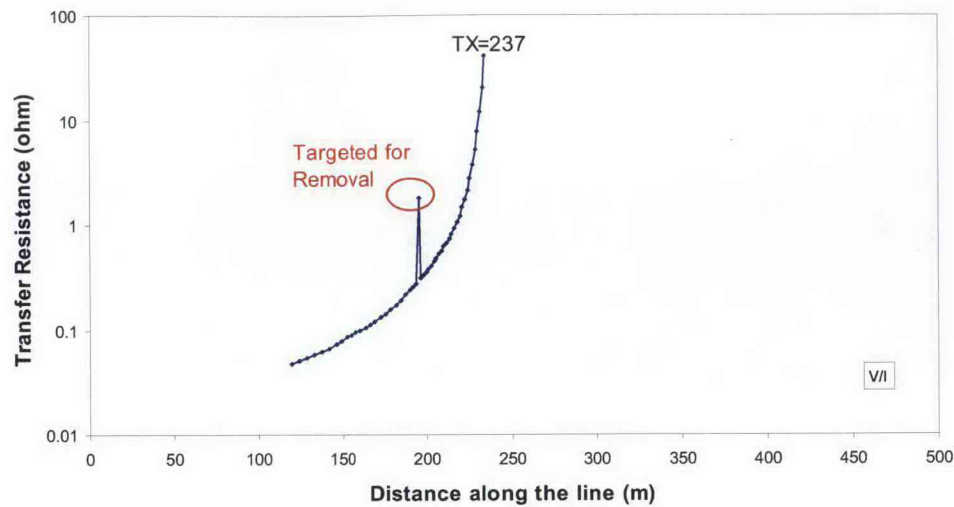
Figure 4.4. Example Data Removal Procedure

The calculation of apparent resistivity is simplified in the pole-pole array:

$$\rho_a = 2\pi \frac{V}{I}(n*a)$$

(4.5)

where a is the basic electrode spacing, and n is the integer multiplier as the current and potential electrodes incrementally separate. The schematic below demonstrates the idea of a linear transect of electrodes on the surface with the a-spacing being the separation between each electrode and the n spacing increasing as the potential electrode moves away from the current electrode. The geophysical survey at the BC Cribs site included a fixed a-spacing of 3 meters and n increased from 1 to 27. For a complete survey, each electrode has one turn at transmission while potential measurements occur at all other electrodes in the array.

The linear transect arrangement produces a 2D data set of resistivity as a function of x and z, where z is the dimension into the earth, and x is along the surface. Although resistivity is a function of the volume over which the measurement is made, its location is typically plotted as a point for ease of representation. The location of the point is a function of n and is referred to as the depth of investigation. Hallof (1957) demonstrated that the intersection of two 45^0 lines (with respect to the surface) extending downward from each of the transmission and receiving electrodes would produce a suitable pseudosection for interpretation. In this fashion, the pole-pole array has depths plotted at:

$$z = 0.5na$$

(4.6)

which is a linear plotting method. Figure 4.5 demonstrates this plotting methodology.
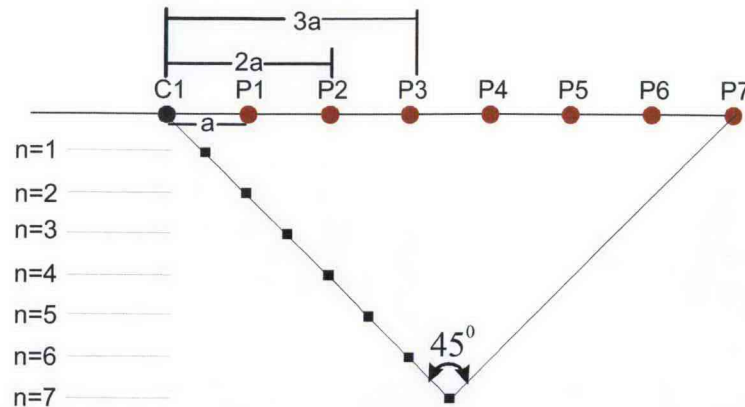
Figure 4.5. Linear Pseudosection Plotting of Apparent Resistivity Data

The traditional linear pseudo-section of Hallof (1957) has limitations with respect to a physical meaning of the earth. Therefore, many researchers have more closely examined the plotting method to allow for a more reasonable geological interpretation. The most widely accepted depth of investigation studies are those presented by Roy and Apparao (1971), Roy (1972), and Koefoed (1972), who defined a depth of investigation characteristics (DIC) model for determining the depth of a measurement. The DIC was determined by finding the depth at which a thin horizontal layer within a homogeneous background makes the maximum contribution to the total measured signal at the surface. The results were consistent in that the depth of investigation is a nearly logarithmic function of electrode spacing, regardless of how the depth of investigation is defined. This suggests a modification of the linear pseudo-section (Edwards 1977; Fink 1980).

To facilitate the nonlinear depth plotting of apparent-resistivity data, Rucker and Fink (2007) demonstrated that a function of the logarithm of the n-spacing value can be used. The logarithmic plotting algorithm of apparent-resistivity data is called high resolution resistivity (HRR). The coefficients of the function are determined by using collocated borehole data. The consequences of a nonlinear pseudo-section is shown in Figure 4.6, where the resistivity values near the surface are pushed deeper relative to the linear pseudo-section, and the deeper resistivity is pulled up relative to the linear pseudo-section. At one point, the two plotting strategies have the same depth location for a given electrode separation.
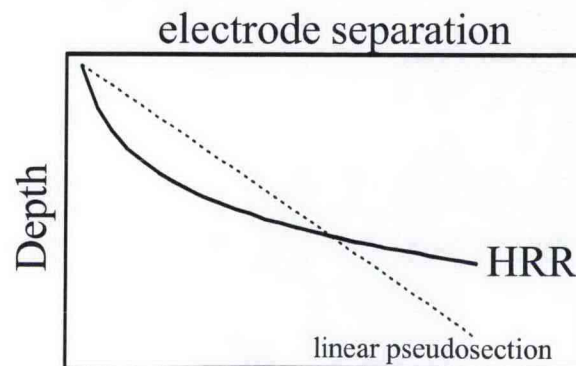
Figure 4.6.   Depth Plotting of Apparent Resistivity Data Using the HRR Algorithm and Linear Pseudosection

The depth of investigation and pseudo section plotting of data stem from a need to relate a measurement made at the surface to some particular depth so survey parameters can be optimized for target identification (Barker 1989). Before tomographic inversion was common practice among geophysicists to estimate the true resistivity from measured apparent resistivity, apparent-resistivity pseudo sections were used primarily to interpret subsurface electrical anomalies. Field practitioners became quite efficient at locating the depth to specific targets, such as ore bodies. The presentation of the pseudo-section is important in this regard. Additionally, the pole-pole array, above all others, provides the weakest edge effects, thereby facilitating the direct interpretation of these data more reliably (Robain et al. 1999).

To facilitate the nonlinear depth plotting of apparent-resistivity data, Rucker and Fink (2007) used the logarithm of the n-spacing value in a 2nd-order polynomial:

$$-z_{log} = u_1 \log(n)^2 + u_2 \log(n) + u_3 \qquad (4.7)$$

where z_{log} is the new interpreted depth location of the apparent-resistivity value, and $u_1 \ldots u_3$ are coefficients to be determined by using collocated target resistivity values. For this analysis, we are assuming that target data come from a borehole. The coefficients in Equation (4-7) can be determined using a nonlinear least-squares optimization procedure. An example of HRR plotting can be seen in Figure 4.7. The data represent lines acquired during the FY04 acquisition campaign over trench 216-B-26. For reference, borehole C4191 is located approximately 93 meters along Line 1.

The depth locations of the nonlinear pseudosection were optimized based on the C4191 borehole data of EC, with coefficients of u= (3.97, 22.4, 3.97). The apparent-resistivity data show that the low-resistivity contours for transects 1-5 are primarily from 25 to 44 m bgs. The low-resistivity areas extend laterally out to the edges of the trench where the electrical resistivity increases to approximately 400 ohm-m. For Line 7, which runs perpendicular over several trenches, the low-resistivity contours are again located at the expected depth of high EC measured in borehole C4191. However, the low-resistivity values extend from the surface beneath each of the trench locations in a triangular shape. In particular, trench 216-B-52 appears to have a much larger low-resistivity response, likely because it received the most liquid waste of any trench, approximately 8500 m^3. Other HRR plots of specific lines can be seen in Rucker and Benecke (2006).

One major disadvantage of HRR processing is the superposition of potential fields from discrete targets to form false low-resistivity anomalies. The anomalies are generated mathematically through constructive interference. This was the case of several resistivity lines over BC Cribs, where the line crossed both trenches and cribs. A false anomaly was observed between the trenches and cribs at depth, which promoted the location of borehole C5925 (borehole C). The same superposition problem can be noticed with different types of conductive targets, including the water table and pipes.

Figure 4.7. HRR plotting of data at BC Cribs. The data are from FY04 acquisition campaign.

Potential field theory describes the ideal flow of steady currents (or heat or fluid) in a homogeneous media. Laplace's equation is the mathematical differential function that is used to help formulate aspects of the theory. One main aspect of the theory that we will use to describe apparent resistivity is superposition. Superposition allows individual solutions of the voltage potential to be summed to obtain a final voltage potential field describing the subsurface. An example would be to consider a discrete body, say a plume or pipe, which is more electrically conductive than the host material. The total potential, as a function of space (x_i, i=1, 2, or 3 dimensions) is:

$$\Psi_T(x_i) = \Psi_B(x_i) + \Psi_P(x_i)$$

(4.8)

where Ψ_T is the total potential, Ψ_B is the background potential, and Ψ_P is the potential of the conductive body (which is negative). If the conductive body did not exist, then the total potential would equal the background potential. Wait (1982) showed that the voltage potential from a single current source (i.e., pole-pole array) is:

$$\Psi_T = \Psi_B = \frac{I\rho_B}{2\pi r} \tag{4.9}$$

where I is the current (amps), ρ_B is the background resistivity (ohm-m), and r is the distance between the current source and voltage potential measurement location (meters). The solution was obtained by solving Laplace's equation with a Neumann boundary condition at the surface (no current flux from the ground to the air, also referred to as a half-space), and Dirichlet boundary condition on the other three sides, where voltage potential was equal to zero at infinity.

Using this same concept, a numerical model was employed to calculate the potential field from a heterogeneous subsurface. For the examples below, the voltage potential will be converted to apparent resistivity using Equation 4-5 so that it can be directly compared to data collected at the BC Cribs. EarthImager2D (developed by AGI, Austin, TX) was used for the potential field modeling. For the first example, a plume of 10 ohm-m was placed in a background soil of 1000 ohm-m. Figure 4.8 shows the results of the apparent resistivity from this geometry using the HRR plotting methodology. The blue outlined box shows the original location of the low-resistivity plume, whereas the black contour of apparent resistivity is approximately the 333-ohm-m value. The apparent resistivity shows a low-resistivity anomaly that matches the original location of the modeled 10-ohm-m feature quite well. The exception is on the edges of the plume where it appears to have a decreased resistivity protruding downward. These protrusions are referred to as pantlegs and are inherent in the volumetric averaging of surface-resistivity measurements. As will be shown later, these pantlegs can cause some difficulties when interpreting HRR data.

The second example is of a water table only, located approximately 72 meters bgs. The water table has an apparent resistivity of 100 ohm-m, and the background soil again is 1000 ohm-m. This model for the water table is a simple two-layer geometry with a discrete decrease in electrical resistivity at the water table depth. Figure 4.9 shows the results of the apparent resistivity using this geometry. The blue horizontal line across the bottom of the color contour plot is the original location of the water table used for modeling.
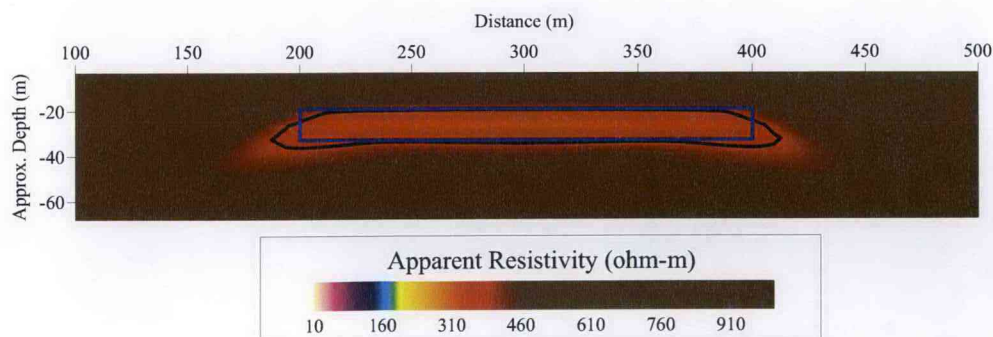
Figure 4.8. Numerical Simulation and HRR Plotting of a Low-Resistivity Anomaly in a Homogeneous Soil

The apparent-resistivity plot shows that the water table, even at 72 meters, can be detected with the resistivity method. However, due to the volumetric averaging by the method, the water table can have an effect at a much more shallow location than anticipated. The apparent resistivity is also a smooth function, whereas the initial-resistivity model was discontinuous.
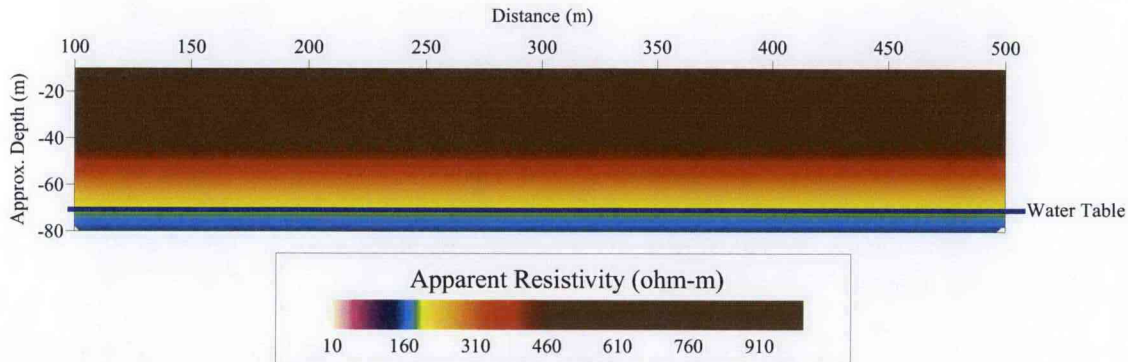
Figure 4.9. HRR Apparent-Resistivity Processing of a Water Table (100 ohm-m) in a Background Soil (1000 ohm-m).

The last example shows a combination of a low electrical-resistivity plume and a mid-value electrical-resistivity water table in a background homogeneous soil of high electrical resistivity. Figure 4.10 shows the results of the modeling with the top plot showing the starting conceptual model for the numerical algorithm. The middle plot shows the apparent resistivity with the HRR processing model. The plot shows that the edges of the plume have a more pronounced effect than shown in Figure 4.8. This is due to the additive effects of water table and plume to the total potential field solution. A cross section at 210 meters, showing depth vs apparent resistivity, reveals how the different components affect the final solution of apparent resistivity. Although apparent-resistivity functions are not directly additive, the plot does demonstrate the different effects.
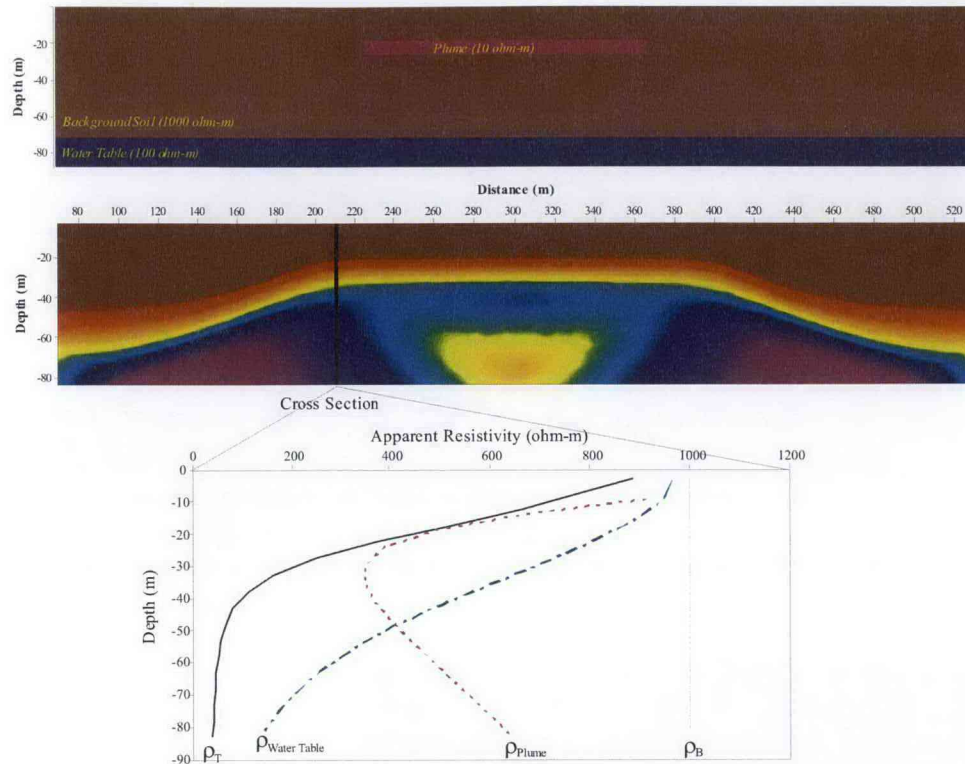
Figure 4.10. Forward Modeling of a Low-Resistivity (10 ohm-m target zone) And Water
Table (100 ohm-m) in a Background Soil (1000 ohm-m)

The top image is the conceptual model, the middle image is the HRR apparent resistivity, and the
bottom plot is a cross section at 210 meters from the edge showing the different components of
the apparent resistivity used in formulating the total value plotted in the middle plot: ρ_t = total
combined resistivity, $\rho_{water\ table}$ = resistivity from water table only, ρ_{plume} = resistivity from the
plume only, ρ_b is background resistivity.

4.1.3   2D Inversion

Rucker and Fink (2007) have shown that the spatial distribution of the raw (i.e., apparent) resistivity
can be used to distinguish discrete targets. The accuracy of both spatial position and resistivity values can
be improved by processing the raw data to account for surface topography and subsurface structure or
layering. The process of calculating an estimate of the true resistivity model based on raw apparent-
resistivity values is called inversion. The goal of resistivity inversion is to automatically calculate the
distribution of electrical resistivity of the subsurface so that the predicted voltage of the model is
equivalent to the field-measured voltage data. Conversely, forward modeling is defined as the process of
calculating the voltage data on the basis of the known values of input current, electrode configuration, and
an assumed subsurface resistivity.

An experienced geophysicist can manually invert the raw data by trial-and-error forward numerical
modeling using codes based on either finite-element or finite-difference methods. However, the
trial-and-error approach inherently presents operator bias by introducing the unique experiences of the

operator. To avoid biased results as well as to speed the process of modeling, automated inverse modeling techniques are used. Automated inverse-resistivity codes use a non-linear optimization algorithm that iteratively solves for the best-fit model of subsurface structure. A least-squares objective function is commonly used in the optimization algorithm and is commercially available in the codes: RES2DINV, RES3DINV, EarthImager 2D, and EarthImager 3D (see Daily et al. 2004a; Daily et al. 2004b; deGroot-Hedlin and Constable 1990; LaBrecque et al. 1996; LaBrecque and Yang 2001; Loke et al. 2003; Loke and Barker 1995a; Loke and Barker 1995b; Loke and Barker 1996b; Oldenburg and Li 1999; Oldenburg et al. 1998; Smith and Vozoff 1984; Stummer et al. 2004; and Tripp et al. 1984). The general form of the objective function (S) for the resistivity inversion is primarily based on the weighted least squares:

$$S = (d_{calc} - d_{meas})^T W_d (d_{calc} - d_{meas}) \qquad (4.10)$$

where d_{calc} is the calculated voltage data from the numerical modeling at coincident locations with d_{meas}, which represents the measured voltage, W_d is a weighted function based on the measurement errors and is equal to the inverse of the error covariance matrix, and T is the matrix transpose operator.

The objective function has been updated many times to include other terms, such as smooth model constraints (i.e., a smooth model based on minimizing the second spatial derivative of the resistivity). The final objective function for smooth model inversion is represented by:

$$S(m) = (d_{calc} - d_{meas})^T W_d (d_{calc} - d_{meas}) + \lambda(m - m_0)^T R(m - m_0) \qquad (4.11)$$

where   second term   =   model smoothness
λ =   dampening factor
m   =   model parameter of resistivity at every cell
m_0 =   *a priori* information and/or initial starting guess
R   =   difference operator for estimating model smoothness
T   =   transpose operator.

In general, the automated inversion routine proceeds as follows, which is shown graphically in Figure 4.11.

1. The Earth's voltage data have been measured and are discretized into grid nodes using a finite-difference or finite-element mesh. The meshing parameters depend on electrode spacing. The inversion will set out to estimate the true resistivity at every grid node.

2. The subsurface properties are initially estimated based on the literal translation of the pseudo-section to a true resistivity, a constant value, or some other distribution from *a priori* information. The forward model runs with this initial estimate to obtain the distribution of voltages in the subsurface. The root mean square (RMS) error is calculated between the measured voltage and the calculated voltage.

3. Based on the degree of match between simulated and measured voltage, the initial estimate of resistivity is changed and the forward model is rerun. The iterative method is linearizing a highly

non-linear problem using Newton's method. Essentially, the program solves the linearized problem to obtain the change in modeled resistivity (Δm) for the next iteration.

4. The resistivity model is updated using the general formula $m_{i+1} = m_i + \Delta m$, where m_{i+1} is the resistivity in a model cell at the next iteration, and the m_i is the current value.
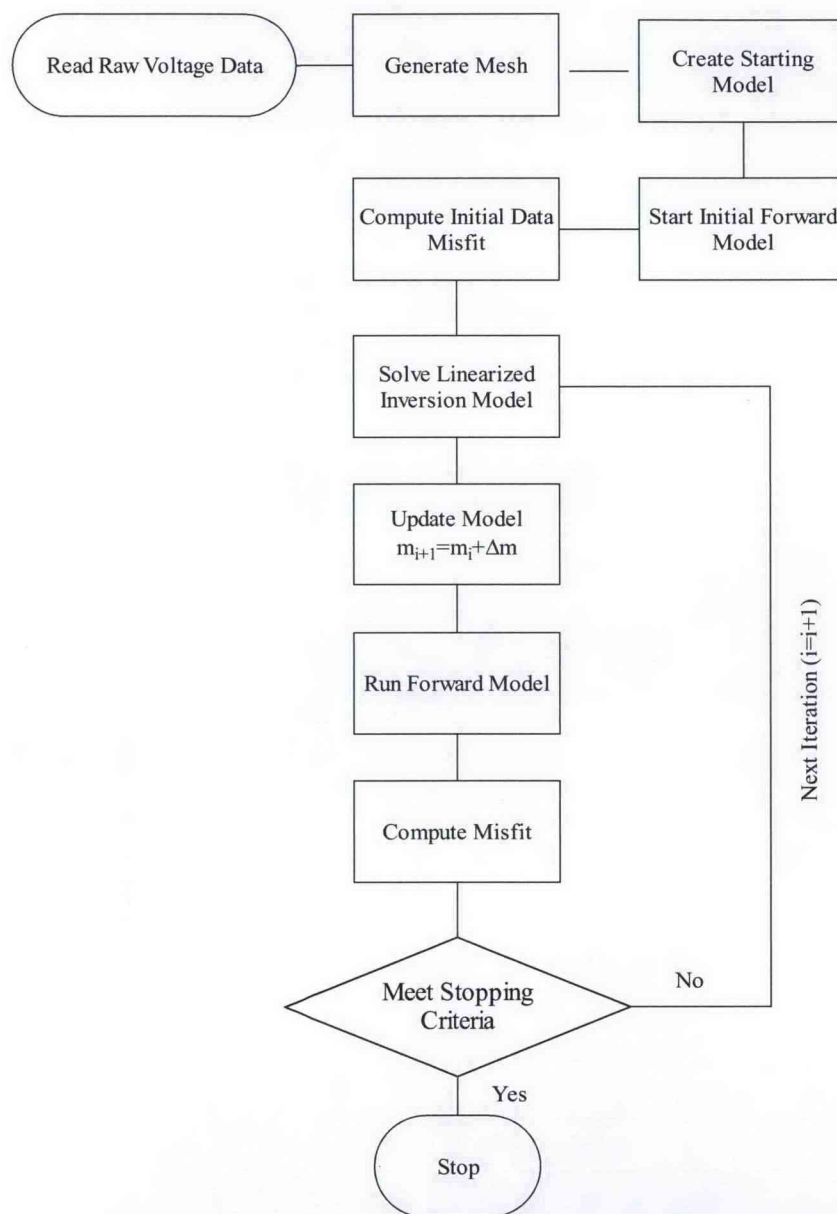
Figure 4.11. Flowchart of the Resistivity Inversion Process

1. Steps 3 and 4 are repeated until the RMS error change between successive iterations is less than 10 percent.

The six resistivity lines shown in Figure 4.7 were inverted using EarthImager2D to demonstrate the outcome of an inversion. The initial estimate for the distribution of electrical resistivity within each resistivity line was the linear pseudosection. Other parameters include using a dampening and stabilization factor of 10.0, estimated error of 5% (for the covariance weighting matrix), and maximum and minimum resistivity of 10000 and 1 ohm-m, respectively. The goodness-of-fit as well as other statistics relevant to the study are shown in Table 4.1. The inverted resistivity lines of Figure 4.12 show a similar result as the logarithmic HRR pseudosection of Figure 4.7, i.e., that a low-resistivity plume exists beneath the site likely due to the disposal activities 50 years prior. The inverted resistivity also shows the bottom edge of the plume to be less sharp than the borehole data suggest, which is a general consequence of inversion.
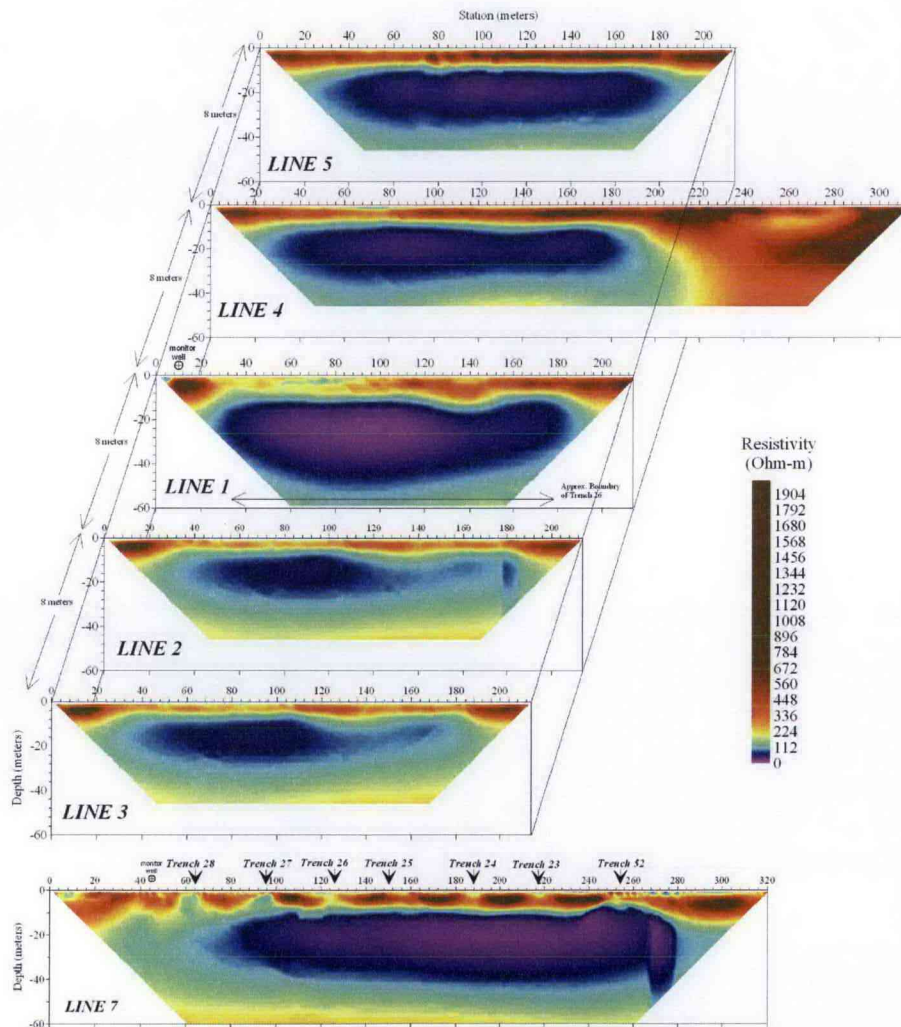
Figure 4.12. Inversion Results for the Resistivity Data Presented in Figure 4.7

Table 4.1. Resistivity Data and 2D Inversion Statistics

Statistic	Line 1	Line 2	Line 3	Line 4	Line 5	Line 6
Data Statistics						
Line Length (m)	214	214	214	314	214	321
# Electrodes	108	108	108	208	108	108
Elect. Separation (m)	2	2	2	2	2	3
Raw data count	5371	1372	1372	1909	1372	1372
Filtered data count[a]	4307	1273	1270	1800	1280	1289
Min ρ_a (ohm-m)	127	125	125	131	123	124

(a) Filtering data eliminates those measurements with high error, negative values, and data spikes.

Inversion Statistics						
Inversion Iterations	3	2	2	3	3	3
Minimum Calc. ρ (ohm-m)	18.9	46.6	45.9	38.8	34.3	8.56
RMS (%)	3.81	3.50	4.56	3.46	3.53	3.23
L_2-Norm	0.58	0.49	0.83	0.48	0.50	0.42

Other contour plots of inverted resistivity lines can be seen in Rucker and Benecke (2006).

4.1.4   3D Inversion

Numerous authors have noted the problems inherent with resolving geophysical targets with 2D data acquisition techniques over a 3D earth (Dahlin et al. 2002; Bentley and Gharibi 2004; Gunther et al., 2006). However, the dimensional complexity of the target depends on the scale. In some cases, such as a simple layered earth, arbitrarily choosing a 3D imaging technique may not significantly improve the target resolution, and one can minimize the time spent acquiring data by being mindful of the problem's dimensionality. A class of targets that would likely benefit from a 3D inversion is a contaminant plume (Slater et al. 2000; 2002). These hydrogeologic targets are typically on the order of a few 10s of meters on a side and reside within the top 20 meters of the surface. The goal of imaging these targets is to understand the source and extent of the plume as well as any time-dependent dynamics that define the fate and transport of the contaminants (e.g., Singha and Gorelick 2006; Oldenborger et al. 2007).

Acquiring true 3D electrical resistivity data is time consuming and costly when compared to 2D methods. For 3D acquisition, the metal electrodes used to pass current and measure voltage can be distributed randomly in space, but are commonly placed in a grid pattern on the surface or at multiple depths in several boreholes. Two-dimensional acquisition is conducted along a line of evenly spaced electrodes. Several suggestions have been made to help migrate 2D techniques to 3D acquisition, including the serpentine roll-along (Loke and Barker 1996a) and the leap-frog roll-along (Dahlin and Berstone 1997; Dahlin et al. 2002). These enhanced 3D acquisition techniques are an improvement over the traditional methods of running individual wires to the electrodes because they use multi-electrode cables and multi-channeled meters.

The practicality of the 3D roll-along has proven itself to be limited to small problems, as a large number of cables and multiplexors are needed to upscale to larger 3D data acquisition. A technique that

does appear suitable for the larger problems is the quasi-3D acquisition, where 2D data are collected but processed using a 3D code. The quasi-3D techniques include a series of closely spaced parallel lines (Ogilvy et al., 2002), a series of parallel and orthogonal lines within a grid (Freidel et al. 2006; Mansoor et al. 2007), radial lines around a common centroid (Nyquist et al. 2005), or concentric circles of increasing diameter (Brunner et al. 1999). Less time and equipment are needed to acquire 2D data, equating to a cheaper methodology that still provides a form of 3D interpretation of the subsurface. Gharibi and Bentley (2005) show that data acquired in a quasi-3D manner are suitable for processing and interpretation when using the proper geometric constraints, such as line and electrode spacing.

The 3D resistivity problem has also been limited by computer software and hardware constraints. Resistivity inversion is needed to reconstruct the electrical properties of the subsurface that give rise to the voltage measurements observed in the field. The resistivity inversion problem is non-linear, forcing the solution methodology to be conducted in an iterative procedure (Daily and Owen 1991; LaBrecque et al. 1996) that solves the forward model many times while changing the subsurface electrical properties. The software and hardware constraint is manifest in the large-computer-memory requirements needed to store the Jacobian matrix (J) of partial derivatives. The (NxM) J matrix contains the derivative of the simulated data measurements (N) with respect to the model parameters (M) (Gunther et al. 2006). Even on moderately sized problems, computing the J matrix can be the most time-consuming step during inversion (Loke and Dahlin 2002).

Three-dimensional inversion was applied to the BC Cribs and Trenches data set using the inversion code EarthImager3DCL (v. 1.0.1). Due to the size of the problem, the inversion was broken up into smaller domains to reduce computer-memory requirements. Figure 4.13 shows the domain boundaries and the results of the individual inversion trials; Table 4.2 lists the inversion statistics for the different models. The results are presented as a plan view of contoured data at a depth of 30 m bgs. For reference, the waste sites, resistivity lines, and boreholes used for "ground truthing" are plotted as well.

Table 4.2. Resistivity Data and 3D Inversion Statistics

Inversion Model Domain	1	2	3	4
Data Count	51,099	44,622	22,297	29,084
Inversion Iterations	4	4	3	4
Minimum Calc. ρ (ohm-m)	9.47	3.60	12.97	6.94
RMS (%)	4.26	4.99	6.98	4.75
L_2-Norm	0.56	0.81	0.57	0.90

The inversion results show zones of low electrical resistivity that are conterminous with each of the waste sites, suggesting a causal relationship between the observed resistivity anomalies and past waste discharge. The mismatch of model results from smaller overlapping domains was also noted by Rucker et al. (2008). However, the model boundaries were designed to have the borehole locations near the center where more reliable inversion data could be used to correlate with geochemistry data.
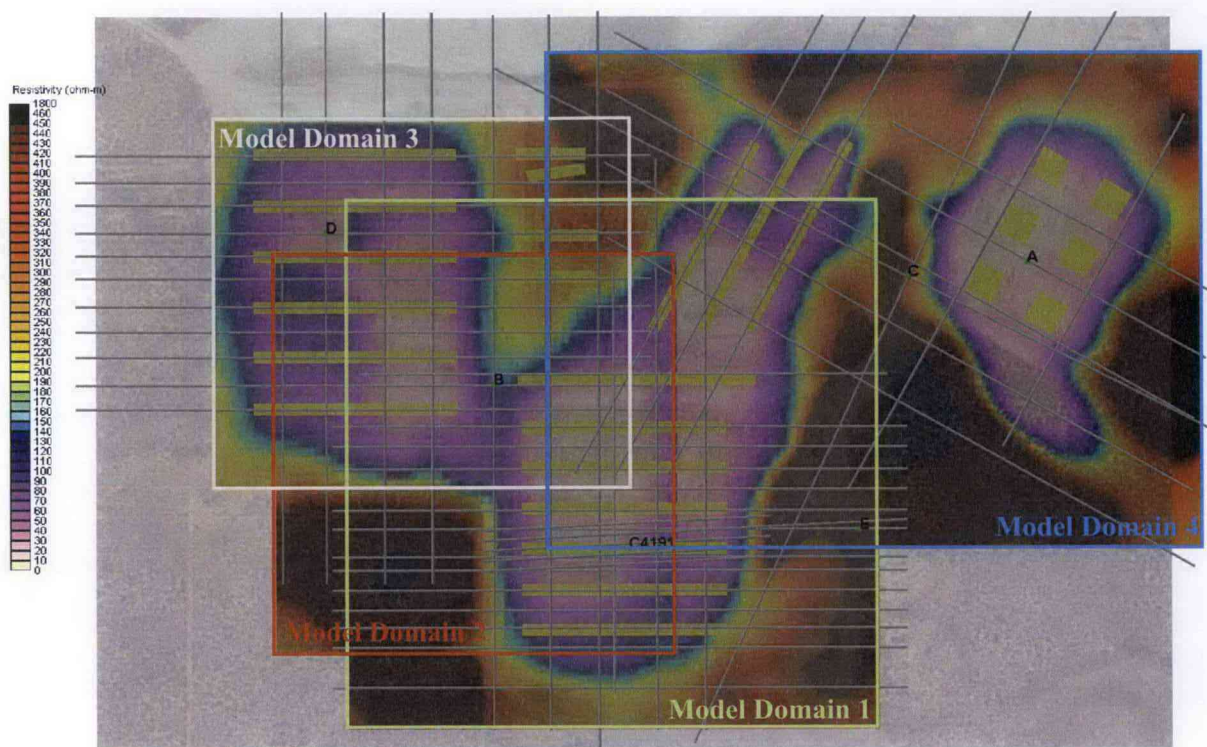
Figure 4.13. Results of the 3D inversion at BC Cribs—Slice at 30 m bgs

4.2 Electrical-Resistivity Laboratory Acquisition

The electrical properties of soils are sensitive to a number of factors, including temperature, fluid composition (especially dissolved salt content) and conductivity, clay content, porosity, and other micro-structural parameters. This sensitivity can be used to obtain information about basic physical properties that control water flow and contaminant transport. Electrical properties, including electrical resistivity and dielectric permittivity, are often used to infer water content in partially saturated rocks and soils based on field geophysical measurements. The relationships between the electrical properties, texture, and structural parameters are critical to the inversion and interpretation of field geophysical measurements. This section describes laboratory measurements of the electrical properties of saturated and partially saturated samples from Borehole C5923 (A) at room temperature. These measurements are used to provide a basis for estimating the dependence of ionic surface EC and bulk EC on lithology and the relation to ionic contaminant concentrations.

Laboratory measurements were performed on 175 samples from Borehole C5923 (A). The samples included 41 cores collected via split spoon sampling and 134 grab samples. Of the 39 cores, 20 were selected for measurements of PSD, SSA, and CEC to allow verification of ionic surface EC. Of these 20 cores, 12 were selected to measure the electrical properties as a function of saturation at room temperature.

4.2.1 Sample Preparation

In general, samples were selected from fine-textured lenses and the next underlying coarse-textured layer; i.e. layer sequences that might constitute a capillary break. To perform measurements, samples were removed from the refrigerator and allowed to stand overnight on the counter top to equilibrate to room temperature.

Each core sample was fitted with two machined Plexiglas® collars, one at each end of the core liner. An end cap fitted with stainless steel electrodes was then attached to each collar. Each electrode was 3.99 ± 0.01 inches in diameter and 0.039 inch thick and was constructed from 316 stainless steel (Mott Corporation, Farmington CT, part number 4300-3.99DIA-.039-0.2-A) to create a porous plate with a mean pore size of 0.2 μm. A 2-inch long 3/33 stainless steel wire was welded to each electrode, about 1 inch from the outer edge, to allow connection to the instruments. The end caps had two openings, one for the introduction or extraction of fluid using a syringe pump and one through which the welded wire from the electrode exited for connection to the instrumentation. The electrode connections and pump tubing exited the end cap through ferruled compression fittings. For two electrode measurements, only the stainless steel electrodes in the endcaps were used. For 4-electrode measurements, an additional two electrodes were installed through the Lexan liner sidewall such that the spacing between the four electrodes was 3 cm. The two additional electrodes were constructed of ¼-inch diameter 316 stainless steel and were 2 inches in length. Photographs in Figure 4.14 show different stages of column preparation for electrical measurements. For saturated sediment measurements, the cores were saturated with synthetic groundwater prepared to mimic uncontaminated Hanford formation pore water (specifically characterized at the 200-E Area's Integrated Disposal Facility [IDF]—see Um and Serne [2005] for details). Owing to the nature and levels of contaminants in the BC borehole C5923 cores, all work conducted on the cores was performed in a radiation control area.
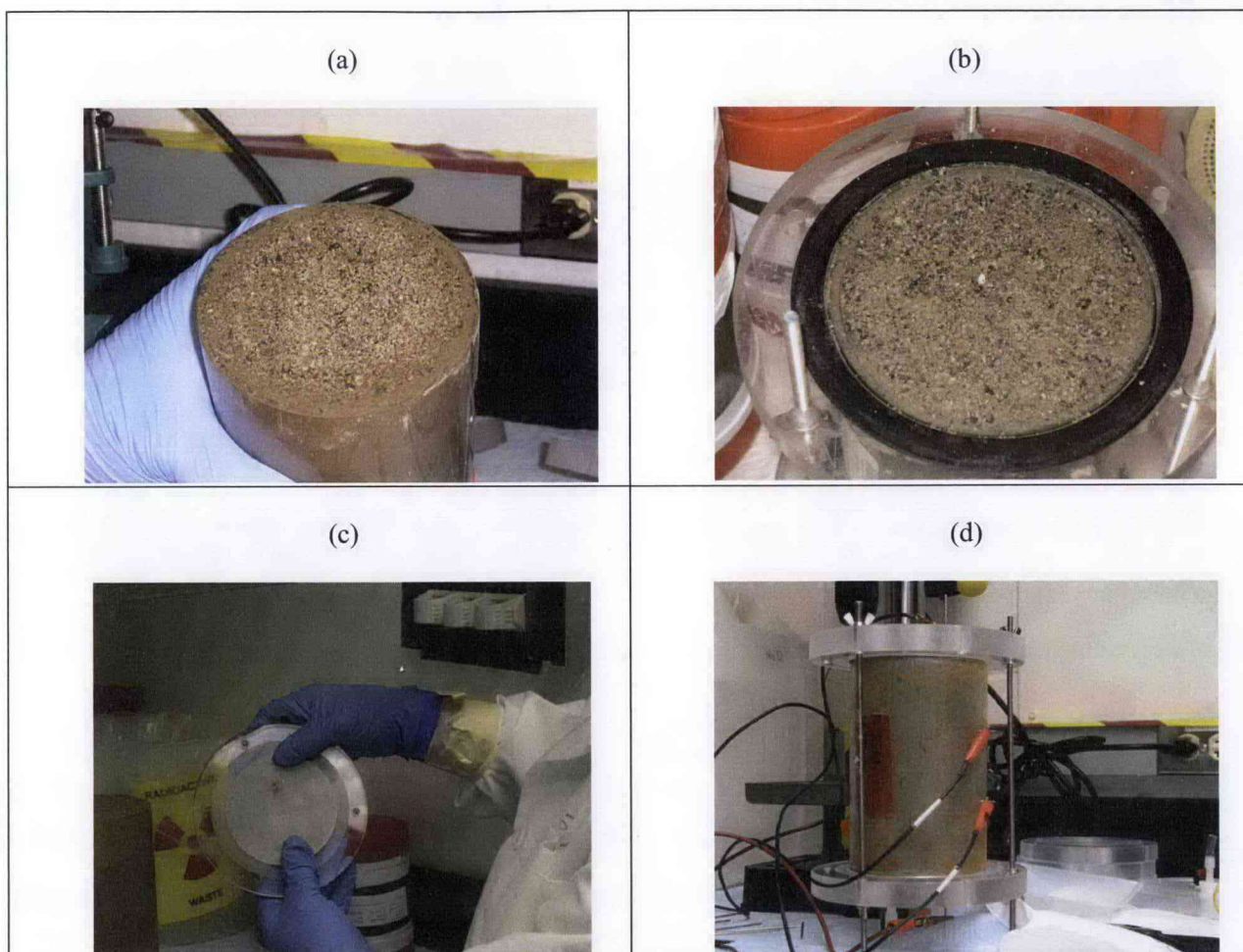
Figure 4.14. Stages of Core Preparation for Electrical Measurements, (a) Soil Core Just After Removal of End Caps, (b) Core After Attachment of the Collar Needed to Connect End Caps, (c) Porous Stainless Steel Electrode in End Cap, and (d) Fully Assembled Core with Collars and End Caps with Electrodes. Column shown is configured for 4-electrode measurements using a Wenner array.

4.2.2   Electrical-Resistivity Measurements

Electrical-resistivity and induced-polarization measurements were made using a Mini-Sting automatic earth resistivity and induced polarization system (AGI Geophysics). The Mini-Sting is a low-cost resistivity and IP meter especially designed for laboratory-scale resistivity surveys and is similar in operation to the Super Sting 8 instrument used in the field studies. Resistivity and induced polarization measurements were collected both on intact cores (within 4-inch diameter by 6-inch long Lexan liners) and grab samples of sediment using a four-electrode configuration based on a Wenner array. Figure 4.15 shows a schematic of the arrangement of the current and potential electrodes.

C1   P1   P2   C2

Figure 4.15. A Schematic of a Conventional Four-Electrode Array Used to Measure Subsurface
Resistivity. C1 and C2 are current electrodes whereas P1 and P2 are potential electrodes
used to measure voltage.

Measurements made at the scale used by the Mini-sting system represent a close approximation to the
true bulk resistivity and chargeability of the sediment, assuming that small-scale heterogeneities are either
not present or not significant within the sediment core and that such heterogeneities have been minimized
by re-packing disaggregated grab-sample sediment into the measurement cell.

Resistivity measurements were made by applying a DC voltage over two current electrodes (C1, C2)
and subsequently measuring the voltage across the other two electrodes, the potential electrodes (P1, P2).
For multi-core measurements, the Mini-Sting was connected to a Swift Interface and multiplexor with 28
channels. This automatic switching afforded by the multiplexor allowed multiple measurements to be
made simultaneously across multiple cores or re-packed grab samples.

Induced polarization (IP), like resistivity, measures parameters associated with voltages induced in
the soil by direct application of an electrical current. While resistivity gives information on bulk soil
resistivity, IP provides the capacitance or chargeability of the sediment by measuring the variation of
voltage with time. Induced polarization is observed when a steady current through two electrodes is shut
off: the voltage does not return to zero instantaneously, but rather decays slowly, indicating that electric
charge has been stored in the soil or rock. These IP data are used to determine the ground capacitance or
chargeability, which is related to soil texture, particularly through the surface conductance, CEC, and
SSA. This effect can be measured in either the time domain by observing the rate of decay of voltage or
in the frequency domain by measuring phase shifts between sinusoidal currents and voltages. The Mini-
Sting was used to make time-domain measurements at time constants of 1, 2, 4, and 8 seconds.

To verify good data quality, significant effort was expended to verify good electrode-sediment
contact. Any cavities observed after core opening were filled with glass beads of a similar grain size to
the soil sample. Anomalously high-resistivity values (e.g., > than 10s to 100s of kΩ) were indicative of
poor electrode contact, in which case, the end electrodes were sprayed with a small amount of water.
Data were stored in the internal memory of the resistivity meter and downloaded to a computer for further
processing. Data were collected from both standard and reciprocal electrode configurations.
Measurements on the BC Crib borehole grab samples were done manually, packing sediment into a core
and collecting the electrical data before processing the next sample. For the saturation-dependent
measurements, data acquisition was fully automated and involved the sequential selection of two current
electrodes and two potential electrodes on a core and the measurement of voltage and current across the
electrode pairs. The Mini-Sting and the computer communicated with the AGI administrator software.

5.0   Borehole A (C5923) Results and Discussion

This section presents the geochemical and physical characterization data collected on sediment (grab samples) from borehole C5923 (BC Cribs borehole A) recently emplaced directly south of the southeast corner of 216-B-17 Crib and directly west of the southwest corner of 216-B-16 crib (see Figure 1.1 for a location map). Besides the grab samples shown in Table 5.1, numerous 4-in.-diameter by 6-in.-long cores were obtained from select depths in borehole C5923. Many of these cores are being investigated in detail for soil resistivity and other geophysical and hydraulic properties that are discussed in Section 5.3. A listing of the cores is provided in Table 5.2. Once we discovered that the sediments in this borehole were quite contaminated with sodium nitrate salt, we decided to emphasize comparing the geochemical results with those from sediments fro borehole C4191 that was drilled right through the footprint of the 216-B-26 trench.

The first activities included tests that were inexpensive or that were key to determining the vertical distribution of mobile contaminants and moisture and major solutes in the vadose zone pore water. The latter two parameters directly relate to the soil resistivity and are key to performing the "ground-truthing" exercise. Information on the borehole sediments presented in this section includes moisture content, pH, and EC of 1:1 sediment to water extracts, and measurements of major cations, anions, trace metals, and radionuclides in both the sediment and 1:1 sediment-to-water extracts. A GEA on selected grab samples was also performed to search for any detectable man-made gamma-emitting radionuclides. The PSD was determined on selected samples and the total chemical composition of selected sediment samples were measured by strong acid extracts. COPCs specifically measured in acid extracts of selected grab samples included RCRA metals and nickel-63. The particle-size measurements and strong acid extractable constituents performed in the tier 2 phase aid in selecting contacts between major geologic units. They also help assess whether immobile COCs were present that would require consideration in predicting baseline risk and selecting appropriate remedial alternatives for final site clean up.

5.1   Geochemical Results from Borehole A (C5923)

5.1.1   Moisture Content

The gravimetric moisture content of the sediment from the grab samples from C5923, which was emplaced via cable-tool drilling with grab samples taken approximately every 2.5 ft from about 5 to 352 ft bgs, is listed in Table 5.1 and presented as a graph in Figure 5.1. The sample IDs are the sample unique HEIS numbers assigned by FHI staff. The second column in each set shows the mid depth of the grab sample, and the final column is gravimetric moisture content. Interestingly, the only sediments with moisture contents equal to or greater than 8% wt are found in the upper 46 ft of the profile. Six grab samples, representing five thin lens of less than 2.5-ft thickness, are highlighted in the upper 46 ft as being wetter than 8% wt in Figure 5.1. Specific values are shown in Table 5.1. Other relatively finer-grained lenses are found at deeper depths (see gray shading in Figure 5.1) but at moisture contents less than 8 wt%.
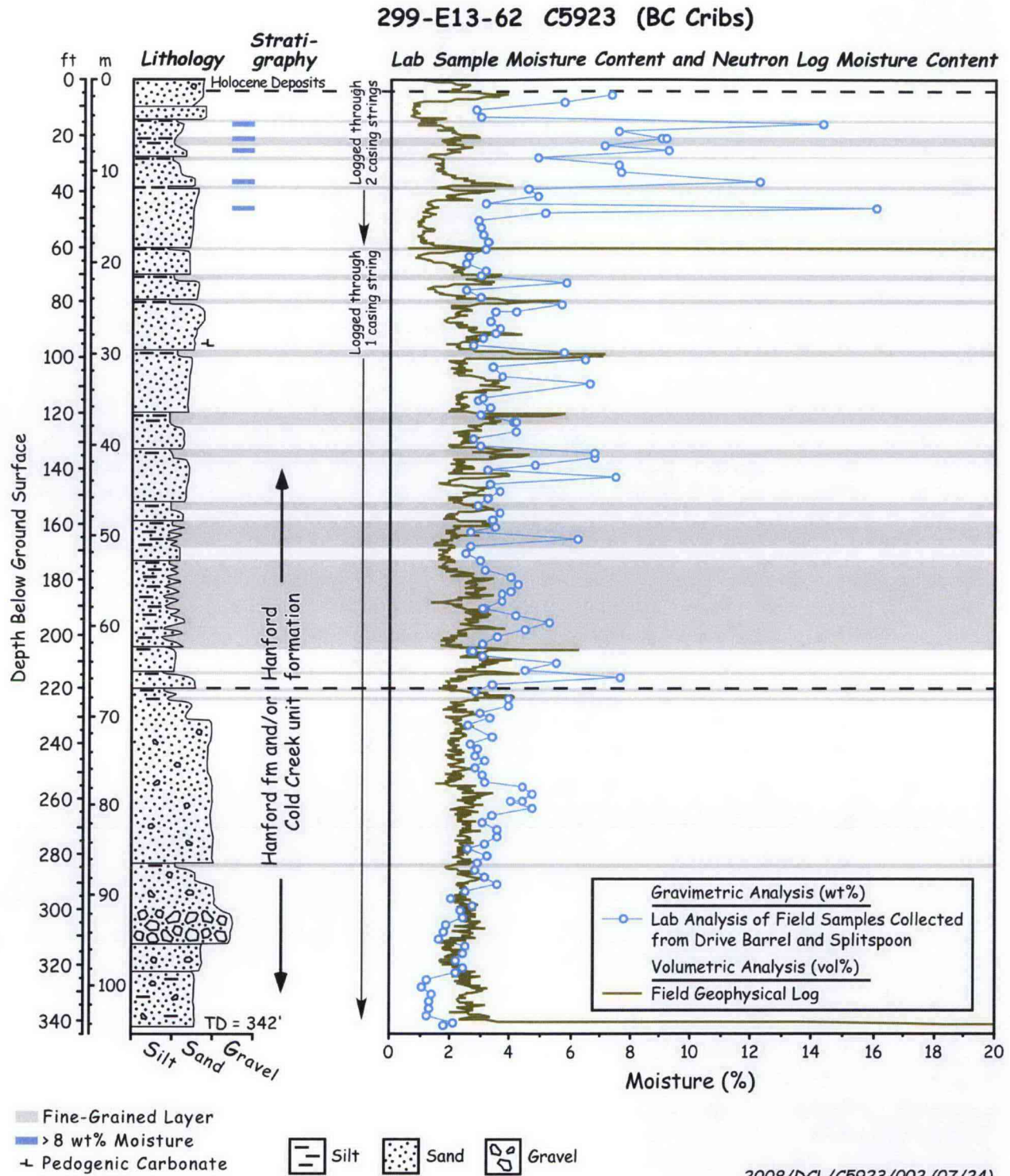
Figure 5.1. Moisture Content of Grab Samples from C5923 Compared to Field Neutron Moisture Log

Borehole C5923 contains fewer thin zones with higher moisture in the upper 110 ft of the Hanford formation (H2 unit) than borehole C4191. As stated in the Geology section (2.0), the vadose zone beneath BC Cribs is dominated by a thick sand-dominated sequence of the Hanford formation (H2 unit), but internally, this sequence contains multiple beds of fine- to coarse-grained sand up to several meters thick that grade back and forth between coarse sand to fine sand multiple times before finally grading up into a silty fine sand to silt-textured cap. The texture and thickness of graded beds in the area appears to decrease upward within the Hanford formation H2 unit. The overall fining and thinning of beds in the shallower depths is probably related to Ice Age floods that became progressively smaller at the end of the Ice Age. This is significant to moisture and contaminant migration since there is an increased likelihood for lateral spreading in the upper Hanford formation. This is due to a higher frequency of fine-grained, silty, slackwater beds in the upper part of the Hanford formation. Flood beds that are thicker and coarser deeper in the profile as evidenced by the lack of any zones with moisture contents greater than 8% wt below 46 ft bgs. Additional discussion on the field moisture logging and a comparison to the laboratory gravimetric moisture contents and their correlation to the lithology are found in Section 2.2.1.4 and Figure 2.17. There is a larger volume of liquid waste disposed of per square foot of disposal facility footprint to the BC Cribs than any individual trench, excepting trench 216-B-52, and borehole C5923 appears to contain fewer thin relatively wet fine-grained lens (based on the field neutron logs and geologist's descriptions in Section 2.2.1.4). Therefore, one might expect the vertical distribution of mobile contaminants, which migrate coincident with the waste water, to have reached deeper depths than at borehole C4191. As shown below, this expectation of deeper mobile contaminant travel at C5923 is in fact observed.

Table 5.1. Gravimetric Moisture Content of Grab Samples Obtained from Borehole C5923

ID	Mid Depth ft bgs	% Moisture wt %	ID	Mid Depth ft bgs	% Moisture wt %	ID	Mid Depth ft bgs	% Moisture wt %
B1T740	5.5	7.29	B1T818	123	4.11	B1T9K7	239.3	2.65
B1T741	8	5.69	B1T9L2	126.8	4.11	B1T9K8	241.8	2.87
B1T742	10.5	2.77	B1T9L3	129.3	2.68	B1T824	244.3	2.82
B1T743	13	2.94	B1T9L4	131.8	2.95	B1T7C4	245.5	3.09
B1T744	15.5	14.3	B1T9L5	134.3	6.74	B1T7C5	248	2.81
B1T745	18	7.56	B1T778	135.5	6.77	B1T7C6	250.5	3.05
B1T746	20.5	8.94	B1T779	138	4.75	B1T7C8	253	3.12
B1T816	20.5	9.11	B1T780	140.5	3.15	B1T7C7	255.5	4.36
B1T747	23	7.1	B1T781	143	7.47	B1T7C9	258	4.68
B1T748	25.5	9.25	B1T782	145.5	3.3	B1T7D0	260.5	4.38
B1T749	28	4.81	B1T783	148	3.55	B1T822	260	4.01
B1T750	30.5	7.51	B1T784	150.5	3.21	B1T7D1	263	4.73
B1T751	33	7.59	B1T785	153	2.83	B1T7D2	265.5	3.38
B1T825	36.8	12.2	B1T786	155.5	3.57	B1T7D3	268	3.03
B1T826	39.3	4.54	B1T787	158	3.38	B1T7D4	270.5	3.5
B1T827	41.8	4.82	B1T788	160.5	3.43	B1T7D5	273	3.53
B1T828	44.3	3.12	B1T789	163	2.6	B1T7D6	275.5	3.09
B1T752	45.5	16	B1T790	165.5	6.23	B1T7D7	278	2.54

Table 5.1 (Contd)

ID	Mid Depth ft bgs	% Moisture wt %	ID	Mid Depth ft bgs	% Moisture wt %	ID	Mid Depth ft bgs	% Moisture wt %
B1T753	48	5.12	B1T791	168	2.64	B1T7D8	280.5	3.2
B1T754	50.5	2.85	B1T792	170.5	2.46	B1T7D9	283	2.83
B1T755	53	2.95	B1T793	173	2.95	B1T7F0	285.5	2.76
B1T756	55.5	3.02	B1T9L6	176.8	3.14	B1T7F1	288	3.13
B1T757	58	3.2	B1T9L7	179.3	3.96	B1T7F2	290.5	3.53
B1T758	60.5	3.11	B1T9L8	181.8	4.21	B1T7F3	293	2.45
B1T759	63	2.55	B1T9L9	184.3	3.94	B1T7F4	295.5	1.98
B1T760	65.5	2.48	B1T794	185.5	3.67	B1T7F5	298	2.68
B1T761	68	3.11	B1T795	188	3.67	B1T7F6	300.5	2.27
B1T762	70.5	2.96	B1T796	190.5	3.14	B1T7F7	303	2.37
B1T763	73	5.8	B1T819	190.5	2.99	B1T7F8	305.5	1.82
B1T764	75.5	2.45	B1T797	193	4.16	B1T7F9	308	1.75
B1T765	78	2.98	B1T798	195.5	5.21	B1T7H0	310.5	1.57
B1T766	80.5	5.62	B1T799	198	4.49	B1T7H1	313	2.45
B1T767	83	4.11	B1T7B0	200.5	3.53	B1T7H2	315.5	2.38
B1T817	83	3.42	B1T7B1	203	3.06	B1T7H3	318	2.17
B1T829	86.8	3.28	B1T7B2	205.5	2.66	B1T7H4	320.5	2.42
B1T985	89.3	3.55	B1T820	205.5	2.72	B1T7H5	323	2.12
B1T768	90.5	3.43	B1T7B3	208	3	B1T7H6	325.5	1.21
B1T769	93	3.06	B1T7B4	210.5	5.49	B1T7H7	328	1.04
B1T770	95.5	2.7	B1T7B5	213	4.43	B1T7H8	330.5	1.36
B1T771	98	5.72	B1T7B6	215.5	7.65	B1T823	330.5	1.38
B1T772	100.5	6.47	B1T7B7	218	3.35	B1T7H9	333	1.26
B1T773	103	3.35	B1T7B8	220.5	2.8	B1T7J0	335.5	1.26
B1T9K9	106.8	3.67	B1T7B9	223	3.88	B1T7J1	338	1.2
B1T9L0	109.3	6.58	B1T821	223	3.92	B1T7J2	340.5	2.06
B1T9L1	114.3	2.99	B1T7C0	225.5	3.93	B1T984	341.5	1.73
B1T774	115.5	2.89	B1T7C1	228	2.96	B1V530	344	1.23
B1T775	118	3.24	B1T7C2	230.5	3.24	B1V531	346.5	2.99
B1T776	120.5	2.91	B1T7C3	233	2.55	B1V532	349	5.38
B1T777	123	4.09	B1T9K6	236.8	3.33	B1V533	351.5	13.2

5.1.2 1:1 Sediment-to-Water Extracts

As described in Section 3, selected grab samples were processed by adding known amounts of de-ionized water to aid in separating the native pore water in the relatively dry sediments. In this section, the water extract data are reported in both units of pore water concentration (most useful for comparing with soil-resistivity data) and units of mass per gram of dry sediment (useful for estimating vertical distribution of each species).

Table 5.2. Core Liners Obtained from Borehole C5923

C5923 Core Liner ID	Split-spoon Sampler top (ft bgs)	bottom (ft bgs)	Liner Mid Depth (ft bgs)	C5923 Core Liner ID	Split-spoon Sampler top (ft bgs)	bottom (ft bgs)	Liner Mid Depth (ft bgs)
B1T7J4-2	38.0	38.5	38.25	B1T7K3-3	130.5	131.0	130.75
B1T7J3-3	38.0	38.5	38.25	B1T7K3-2	131.0	131.5	131.25
B1T7J3-2	38.5	39.0	38.75	B1T7K4-3	133.0	133.5	133.25
B1T7J5-3	40.5	41.0	40.75	B1T7K4-2	133.5	134.0	133.75
B1T7J5-2	41.0	41.5	41.25	B1T7K5-3	175.5	176.0	175.75
B1T7J6-3	43.0	43.5	43.25	B1T7K5-2	176.0	176.5	176.25
B1T7J6-2	43.5	44.0	43.75	B1T7K6-3	178.0	178.5	178.25
B1T7J7-3	85.5	86.0	85.75	B1T7K6-2	178.5	179.0	178.75
B1T7J7-2	86.0	86.5	86.25	B1T7K7-3	180.5	181.0	180.75
B1T7J8-3	88.0	88.5	88.25	B1T7K7-2	181.0	181.5	181.25
B1T7J8-2	88.5	89.0	88.75	B1T7K8-3	183.0	183.5	183.25
B1T7J9-3	105.5	106.0	105.75	B1T7K8-2	183.5	184.0	183.75
B1T7J9-2	106.0	106.5	106.25	B1T7K9-3	235.5	236.0	235.75
B1T7K0-3	108.0	108.5	108.25	B1T7K9-2	236.0	236.5	236.25
B1T7K0-2	108.5	109.0	108.75	B1T7L0-3	238.0	238.5	238.25
B1T7L3-3	113.0	113.5	113.25	B1T7L0-2	238.5	239.0	238.75
B1T7L3-2	113.5	114.0	113.75	B1T7L1-3	240.5	241.0	240.75
B1T7K1-3	125.5	126.0	125.75	B1T7L1-2	241.0	241.5	241.25
B1T7K1-2	126.0	126.5	126.25	B1T7L2-3	243.0	243.5	243.25
B1T7K2-3	128.5	129.0	128.75	B1T7L2-2	243.5	244.0.	243.75
B1T7K2-2	129.0	129.5	129.25				

The pH and EC for the water extracts are shown in Table 5.3. Figure 5.2 shows the pore-water EC, pore-water total ionic strength, and pore-water major dissolved constituents. The pH profile shows a few samples with elevated values indicative of caustic waste in the depth region 8 to 13 ft bgs and perhaps as deep as 18 ft bgs. The crib bottoms were from 11 to 15 ft bgs at the time of their use. We are not sure whether the current ground-surface elevation is the same as during the operations of the BC Cribs. If so, some of the shallow sediments near 8 ft bgs with elevated pH are shallower than the bottom of the adjacent cribs, suggesting that caustic waste must have ponded in the cribs and also migrated horizontally up to a few hundred feet. The deepest sample analyzed to date at 340.5 ft bgs also exhibits a higher than naturally occurring pH value at 8.78, but this might be an erroneous measurement. We have never observed impacts of caustic waste on vadose zone or aquifer sediments this deep in sediments. Because there are no signs of pH values above the upper range of naturally occurring values (up to 8.5) anywhere else below 18 ft bgs, we doubt that the pH value for sample B1T7J2 is correct. At the 216-B-26 trench, high pH values (above 9) were found from 17.5 to 37.5 ft bgs. pH values above 9 but below 10 are observed below and adjacent to single-shell tanks that have leaked highly caustic waste but at more

Table 5.3. pH and EC Values for 1:1 Sediment to Water Extracts from C5923

HEIS # ID	Mid Depth ft bgs	1:1 Extract pH	1:1 Extract Conductivity mS/cm	Conductivity Dilution Corrected (in Pore Water) (mS/cm)	HEIS # ID	Mid Depth ft bgs	1:1 Extract pH	1:1 Extract Conductivity mS/cm	Conductivity Dilution Corrected (in Pore Water) (mS/cm)
B1T740	5.5	8.02	0.128	1.75	B1T818	123.0	8.0	7.127	**173.46**
B1T741	8.0	**9.24**	0.239	4.20	B1T9L2	126.8	7.68	7.717	**188.69**
B1T743	13.0	**8.88**	0.223	7.59	B1T9L3	129.3	7.9	5.013	**187.06**
B1T744	15.5	8.32	0.26	1.81	B1T9L4	131.8	7.6	5.979	**202.68**
B1T745	18.0	**8.55**	0.183	2.40	B1T9L5	134.3	7.3	12.1	**179.68**
B1T746	20.5	8.44	0.243	2.72	B1T781	143.0	7.17	8.66	115.72
B1T816	20.5	8.2	0.242	2.65	B1T790	165.5	7.95	0.348	5.58
B1T747	23.0	8.32	0.205	2.88	B1T793	173.0	8.05	0.201	6.82
B1T748	25.5	8.07	0.249	2.69	B1T9L6	176.8	8.13	0.195	6.24
B1T749	28.0	7.31	1.8	39.52	B1T9L7	179.3	8.04	0.212	5.35
B1T750	30.5	7.63	1.65	21.90	B1T9L8	181.8	7.97	0.23	5.44
B1T751	33.0	7.83	0.426	5.62	B1T9L9	184.3	8.14	0.205	5.22
B1T825	36.8	8.2	10.5	85.89	B1T798	195.5	7.74	0.381	7.33
B1T826	39.3	8.0	3.47	76.42	B1T7B4	210.5	7.51	9.58	**173.94**
B1T828	44.3	7.41	6.202	**198.80**	B1T7B6	215.5	7.73	15.54	**203.13**
B1T752	45.5	7.3	26.4	**179.66**	B1T7C2	230.5	7.14	7.48	**232.07**
B1T753	48.0	7.41	12.6	**247.03**	B1T9K6	236.8	7.28	5.5	**165.21**
B1T755	53.0	7.3	6.02	**204.10**	B1T9K7	239.3	7.26	3.868	145.97
B1T757	58.0	7.53	7.22	**227.10**	B1T9K8	241.8	7.35	3.088	107.63
B1T763	73.0	7.22	15	**258.42**	B1T824	244.3	7.37	1.831	64.98
B1T766	80.5	7.07	15	**266.57**	B1T7C4	245.5	7.52	1.548	50.18
B1T767	83.0	7.58	9.383	**230.18**	B1T7C9	258.0	8.1	0.241	5.17
B1T817	83.0	7.9	7.886	**230.60**	B1T7D1	263.0	8.05	0.217	4.59
B1T985	89.3	8.11	10.22	**287.90**	B1T7D8	280.5	8.09	0.224	6.97
B1T768	90.5	7.46	10.04	**292.87**	B1T7F2	290.5	7.85	0.26	7.32
B1T771	98.0	7.13	7.36	129.06	B1T7H1	313.0	8.44	0.174	7.14
B1T773	103.0	7.35	4.156	126.57	B1T7J2	340.5	**8.78**	0.215	10.50
B1T9K9	106.8	7.51	4.074	111.01	B1V530	344	8.61	0.23	18.62
B1T9L0	109.3	7.15	8.93	135.65	B1V531	346.5	8.13	0.144	4.79
B1T9L1	114.3	7.41	3.264	109.21	B1V532	349	7.71	0.12	2.23
B1T777	123.0	7.86	7.44	**183.27**	B1V533	351.5	7.83	0.114	0.87

pH values in red type elevated values; pore-water EC in bold denotes high salt present
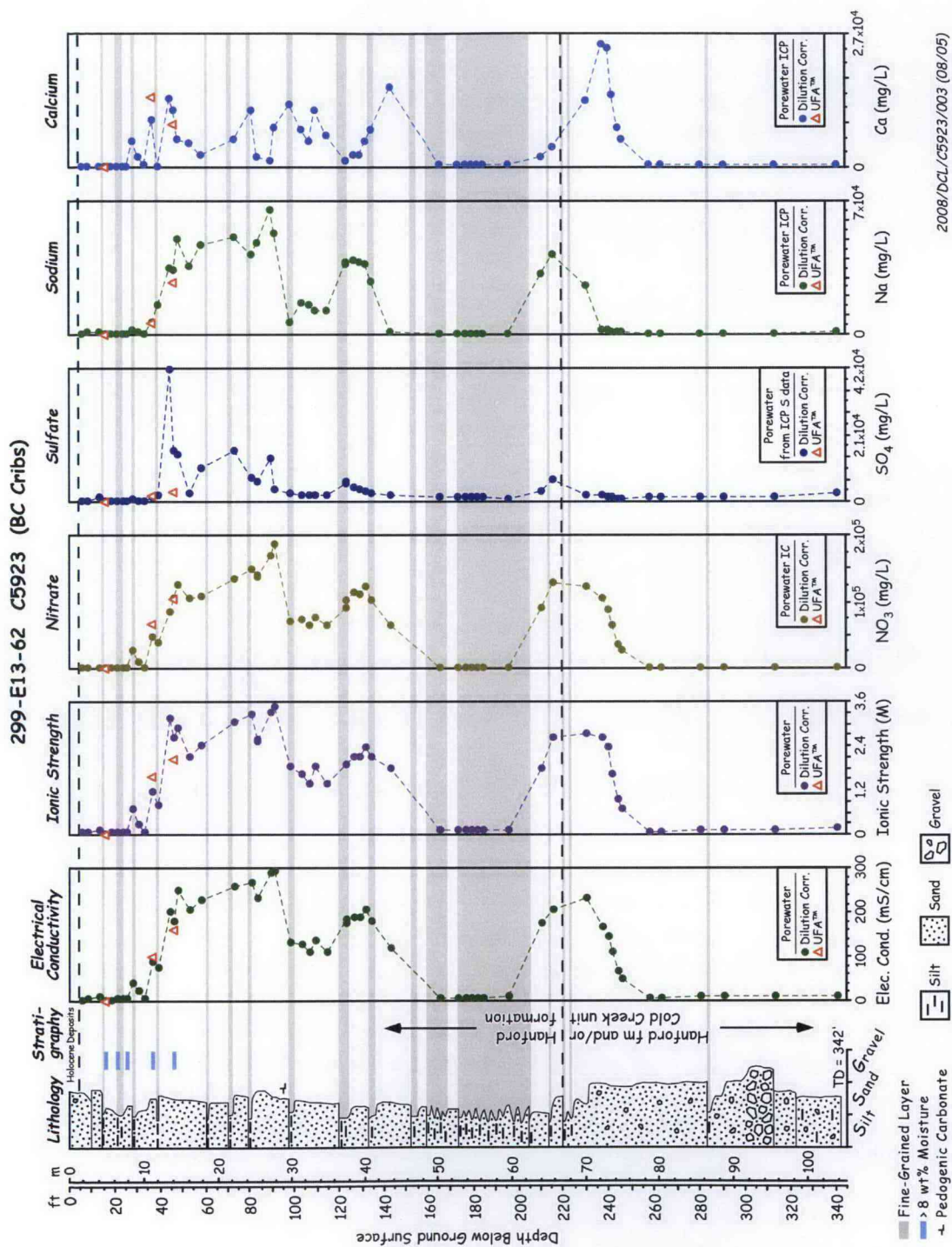
Figure 5.2. Pore-Water EC, Ionic Strength and Major Ions in Borehole C5923

limited volumes than disposed of to cribs. The vertical extent of the elevated pH at borehole C5923 (approximately 5 to at most 10 vertical ft) is a bit less than the thicknesses of impacted sediment observed below several single-shell tanks and also about half the thickness of elevated pH observed at borehole C4191 emplaced directly through the 216-B-26 trench. The thinner impact zone of elevated pH at borehole C5923 is either caused by the combination of the likely lower free-base content in the BC Crib waste stream than released from single-shell tanks or the fact that all caustic-impacted vadose zone sediments at Hanford have been buffered to pH values between ~9 and 9.8 over the 4 to 6 decades since the fluids were released. At present, almost all observations of caustic fluid attack on Hanford sediments exhibit water-extract pH values in this constrained range of approximately one pH unit, despite some of the waste streams that were projected to have pH values that ranged from 10 to greater than 14.

The sediment from C5923 (to the side but near 216-B-16 and 216-B-17) cribs appears to show a tri-modal peak in pore-water EC (i.e., exhibits the three maxima in pore-water EC). The shallowest lobe of high EC is by far the thickest lobe (~55 ft thick with maximum pore water EC of 293 mS/cm); the middle lobe of the tri-modal distribution is thin (~10 ft thick with a maximum pore water EC ~200 mS/cm), and the deepest lobe is about 30 ft thick with a maximum pore water EC of 230 mS/cm. The depths bgs for the three EC maxima are 90, 132, and 230 ft bgs, respectively. The deeper lobe of salt is considerably deeper than the bimodal salt plume at borehole C4191 drilled through 216-B-26 trench. The upper two lobes of salt maxima at C5923 occur at about the same depths as the bi-modal plume below the 216-B-26 trench. At both boreholes, C5923 and C4191, the shallowest lobe of the salt plumes has the highest electrical conductivities. The absolute value of the maximum EC at C5923 (~293 mS/cm) is about two times larger than at C4191 (152 mS/cm). The total volume of waste disposed of to 216-B-16 and 216-B-17 was 9 million liters in comparison to 4.75 million liters disposed of to the 216-B-26 trench based on estimates in Corbin et al. (2005). Thus, one might expect the observed deeper penetration of salt in borehole C5923 located near the cribs than at borehole C4191 based on the larger volume of waste disposed of near C5923.

5.1.3 Water Extract Composition of the 1:1 Sediment to Water Extracts for C5923

The 1:1 sediment-to-water extract anion composition, in units of µg/g of dry sediment and in units of mg/L for the calculated pore water, are shown in Table 5.4 and Table 5.5, respectively. Figure 5.2 shows the calculated pore-water concentrations of nitrate and sulfate, the two dominant anions. Figure 5.3 plots the nitrate concentration per gram of dry sediment as a function of depth. Values in Table 5.4 that appear to be elevated compared to the others are shown in bold type. The waste stream that was disposed of to cribs 216-B-16 and 216-B-17 was uranium recovery, and scavenging wastes from a tri-butylphosphate-based process was used to recover uranium from bismuth phosphate wastes retrieved from single-shell tanks. More details on the waste composition can be found in Corbin et al. (2005) and the appendixes to the DQO report, Benecke (2008). About 2.67 metric tons of dissolved salts consisting mainly of nitrate and sodium (combined, these represent 2.39 metric tons) and lesser amounts of sulfate, phosphate, fluoride, chloride, and potassium were disposed of in total to the 216-B-16 and 216-B-17 cribs. The vadose zone sediments in borehole C5923 outside the footprint of the BC cribs show elevated concentrations of most of the aforementioned anions with phosphate being immobilized in the upper 8 ft bgs. Elevated sulfate concentrations are found in two regions, from 28 to 143 bgs and 210 to 246 ft bgs, and elevated chloride concentrations are also found in the same two regions as the chloride. There are no

distinctly elevated fluoride regions. The most elevated nitrate concentrations are found in the same two regions as the chloride and sulfate as shown in bold in Table 5.4. These depth distributions do not show any vertical differences between sulfate, chloride, and nitrate as was found in the borehole C4191 sediments right below the 216-B-26 trench. This lack of vertical discrimination of anions in the sediments at C5923 suggests that the contamination at this borehole has migrated into the region via horizontal flow so that we are not able to discern vertical separation of anions. The bimodal vertical distribution of anions in C5923 sediments suggests at least two disposal events, or two sources distributed the wastes.

The massive quantity on nitrate disposed makes it a good tracer of the waste-fluid plume location. Figure 5.2 shows that there is no difference in the vertical distribution of the major anions sulfate and nitrate or the major cations sodium and calcium. Again, this seems to indicate that waste fluids migrated horizontally into the sediments at borehole C5923. Three sediment samples were also processed by ultracentrifugation to extract directly vadose zone pore water. The chemical composition of the three pore waters are shown in Figure 5.2 and Figure 5.3 and in general show good agreement with the values calculated by dilution correcting the 1:1 sediment to de-ionized water extracts.

Table 5.4. Anion Composition of Water Extracts of C5923 (units µg/g dry sediment)

Sample ID	Mid Depth (ft bgs)	Fluoride	Chloride	Nitrite	Nitrate	Sulfate-IC	Phosphate-IC	Alkalinity (as CaCO$_3$)
B1T740	5.5	0.787	0.631	<0.3	5.01	1.93	**9.43**	54.7
B1T741	8	1.27	0.576	<0.3	6.98	7.21	**3.54**	106.4
B1T743	13	0.756	0.629	<0.3	5.76	31.9	<2.5	65.4
B1T744	15.5	1.24	9.71	<0.3	19.02	20.1	<2.5	70.6
B1T745	18	0.84	3.69	<0.3	10.85	6.99	<2.5	64.6
B1T746	20.5	0.843	5.67	<0.3	12.82	20.8	<2.5	71.4
B1T816	20.5	0.907	5.58	<0.3	12.59	21.4	<2.5	72.9
B1T747	23	0.542	7.5	<0.3	11.94	17.1	<2.5	54
B1T748	25.5	0.604	7.08	<0.3	15.33	28.1	<2.5	63
B1T749	28	<0.4	<0.4	<323	**1.33E+03**	837.9	<2.5	32.3
B1T750	30.5	**4.19**	**50.5**	<30.3	**700.32**	90.5	<2.5	37.1
B1T751	33	0.87	**23.3**	<3.04	**104.77**	19.4	<2.5	47.8
B1T825	36.8	<0.4	**277.3**	<305	**5.73E+03**	881.9	<2.5	32.7
B1T826	39.3	<0.4	**255.1**	<304	**1.72E+03**	832.3	<2.5	81.3
B1T828	44.3	<0.4	**92.0**	<304	**2.61E+03**	1289.1	<2.5	19.8
B1T752	45.5	<0.4	**353.5**	<332	**1.68E+04**	2570	<250	34.8
B1T753	48	<0.4	**272.4**	<305	**6.43E+03**	1240.8	<2.5	29.7
B1T755	53	<0.4	**257.1**	<304	**3.05E+03**	800.3	<2.5	24.3
B1T757	58	<0.4	**258.9**	<304	**3.45E+03**	1019.7	<2.5	35.7
B1T763	73	<0.4	**280.9**	<304	**7.78E+03**	1368.4	<2.5	27.3
B1T766	80.5	<0.4	**292.8**	<304	**8.31E+03**	1065.2	<2.5	21.3
B1T767	83	<0.4	**107.9**	<307	**5.78E+03**	321.6	<2.5	31.4
B1T817	83	<0.4	**102.0**	<304	**4.69E+03**	288.0	<2.5	35.7
B1T985	89.3	<0.4	**106.0**	<304	**6.02E+03**	496.0	<2.5	38.8
B1T768	90.5	<0.4	**107.1**	<304	**6.37E+03**	233.1	<2.5	23.6
B1T771	98	<0.4	**260**	<304	**3.95E+03**	870.0	<2.5	22
B1T773	103	<0.4	**88.8**	<310	**2.48E+03**	216.3	<2.5	22.5
B1T9K9	106.8	<0.4	**90.0**	<304	**2.40E+03**	212	<2.5	25.1

Table 5.4 (contd)

Sample ID	Mid Depth (ft bgs)	Fluoride	Chloride	Nitrite	Nitrate	Sulfate-IC	Phosphate-IC	Alkalinity (as CaCO₃)
B1T9L0	109.3	<0.4	**271.9**	<304	**4.92E+03**	851.7	<2.5	22
B1T9L1	114.3	<0.4	**86.0**	<304	**1.90E+03**	207.1	<2.5	22
B1T777	123	<0.4	**257.8**	<304	**3.68E+03**	951.2	<2.5	44
B1T818	123	<0.4	**97.0**	<304	**4.14E+03**	332.1	<2.5	40.3
B1T9L2	126.8	<0.4	**99.5**	<306	**4.65E+03**	279.4	<2.5	28.3
B1T9L3	129.3	<0.4	**94.0**	<287	**2.94E+03**	230.0	<2.5	35
B1T9L4	131.8	<0.4	**105.0**	<304	**3.61E+03**	224	<2.5	25.1
B1T9L5	134.3	<0.4	**269.8**	<304	**6.77E+03**	894.3	<2.5	31.9
B1T781	143	<0.4	**264.1**	<304	**4.80E+03**	870.2	<2.5	26.6
B1T790	165.5	0.9	5.0	<3.04	35.84	70.1	<2.5	53.2
B1T793	173	0.57	1.6	<0.3	25.36	13.7	<2.5	37.3
B1T9L6	176.8	0.61	1.6	<0.31	19.42	13.7	<2.5	39.7
B1T9L7	179.3	0.61	1.7	<0.3	16.86	13.6	<2.5	39.5
B1T9L8	181.8	0.578	1.7	<0.3	8.98	49.1	<2.5	49.4
B1T9L9	184.3	0.63	1.8	<0.31	8.14	13.7	<2.5	44.2
B1T798	195.5	0.81	3.9	<3.04	**81.88**	50.2	<2.5	44.8
B1T7B4	210.5	**39.01**	263.1	<304	**4.91E+03**	922.3	<2.5	38.8
B1T7B6	215.5	<0.4	**123.0**	<304	**9.78E+03**	13829.4	<250	33.4
B1T7C2	230.5	<0.4	**258.9**	<304	**3.90E+03**	833.6	<2.5	25.1
B1T9K6	236.8	**38.98**	**91.0**	<304	**3.48E+03**	13903.8	<2.5	19
B1T9K7	239.3	<0.4	**86.0**	<304	**2.28E+03**	13910.4	<2.5	17.5
B1T9K8	241.8	<0.4	**83.0**	<304	**1.85E+03**	13913.8	<2.5	20.5
B1T824	244.3	0.8	13.4	<30.5	**1.03E+03**	1386.0	<2.5	22.1
B1T7C4	245.5	0.9	11.7	<30.5	**856.85**	1404.2	<2.5	22.1
B1T7C9	258	0.556	1.9	<0.31	10.7	52.1	<2.5	42
B1T7D1	263	0.59	1.9	<0.3	10.24	13.8	<2.5	42.6
B1T7D8	280.5	0.539	1.4	<0.3	6.54	51.4	<2.5	40.3
B1T7F2	290.5	0.57	3.2	<0.3	8.63	54.7	<2.5	50.2
B1T7H1	313	0.638	1.3	<0.3	2.83	27.8	<2.5	50.9
B1T7J2	340.5	0.753	2.9	<0.3	1.76	40.8	<2.5	47.9
B1V530	344	1.19	5.77	<1	1.32	35.9	<1.5	69.2
B1V531	346.5	1.03	2.23	<1	<1	18.6	<1.5	55.5
B1V532	349	0.842	3.48	<1	<1	13	<1.5	42
B1V533	351.5	0.562	1.99	<1	<1	11.3	<1.5	50.8

(a) Bold values are higher than others for given constituent.

Table 5.5 presents the same water-extract anion data but in units of mg/L pore-water concentrations, which are the units most related to comparing with the soil-resistivity measurements. Figure 5.2 plots some of the more important pore-water anion and cation concentrations. It should be noted that because the sediments deep in the profile are very dry, a large dilution factor exists when performing the water extracts. Therefore, when the data are plotted as pore-water concentrations, very dry sediments often exhibit elevated (biased high) calculated pore-water concentrations. The deep apparently increased fluoride concentrations are an artifact of this calculation and a mediocre detection limit constraint that adds to the positive bias.

Table 5.5. Water-Extractable Anions Converted to Pore Water Concentrations for C5923 Borehole Samples (mg/L)

HEIS #	mid depth (ft bgs)	Fluoride	Chloride	Nitrite	Nitrate	Sulfate-IC	Sulfate-ICP	Phosphate-IC	Phosphate-ICP	Alk
B1T740	5.5	10.79	8.65	<4.2	68.7	2.64E+01	2.19E+01	129.29	1.35E+02	750.2
B1T741	8.0	22.25	10.12	<5.3	122.7	1.27E+02	1.26E+02	62.19	6.31E+01	1869.9
B1T743	13.0	25.73	21.4	<10.3	195.9	1.09E+03	1.16E+03	49.1	3.96E+01	2224.1
B1T744	15.5	8.63	67.74	<2.1	132.7	1.40E+02	1.56E+02	7.38	2.65E+00	492.9
B1T745	18.0	11.04	48.46	<4.0	142.4	9.18E+01	1.14E+02	13.51	4.81E+00	848.8
B1T746	20.5	9.44	63.49	<3.4	143.4	2.33E+02	2.67E+02	11.35	5.78E+00	798.6
B1T816	20.5	9.95	61.26	<3.3	138.1	2.35E+02	2.56E+02	11.19	3.58E+00	799.8
B1T747	23.0	7.6	105.25	<4.3	167.5	2.40E+02	2.58E+02	13.34	3.38E+00	756.8
B1T748	25.5	6.53	76.47	<3.3	165.6	3.03E+02	3.19E+02	10.19	2.51E+00	680.8
B1T749	28.0	<20	5642.53	<7092	2.75E+04	1.73E+04	5.93E+02	<20	1.22E+01	667.4
B1T750	30.5	55.73	672.79	<402	9.33E+03	1.20E+03	2.79E+02	<20	6.29E+00	494.2
B1T751	33.0	11.47	307.59	<40.1	1.38E+03	2.56E+02	2.16E+02	120.37	1.91E+01	631.3
B1T825	36.8	<20	2265.95	<2495	4.69E+04	7.21E+03	1.22E+03	<20	9.11E+00	267.3
B1T826	39.3	<20	5615.72	<6695	3.78E+04	1.83E+04	1.64E+03	<20	4.45E+00	1790.9
B1T828	44.3	<20	2948.93	<9744	8.36E+04	4.13E+04	4.13E+04	<20	7.04E+01	633.4
B1T752	45.5	<20	2204.91	<2259	1.05E+05	1.61E+04	1.58E+04	<20	1.22E+01	217.2
B1T753	48.0	<20	5332.72	<5980	1.26E+05	2.43E+04	1.49E+04	<20	4.95E+01	581.1
B1T755	53.0	<20	8713.09	<10307	1.03E+05	2.71E+04	2.43E+03	<20	1.24E+01	824.5
B1T757	58.0	<20	8146.74	<9562	1.09E+05	3.21E+04	1.03E+04	<20	1.19E+01	1123.6
B1T763	73.0	<20	4841.11	<5237	1.34E+05	2.36E+04	1.58E+04	<20	1.45E+01	471.4
B1T766	80.5	<20	5207.01	<5402	1.48E+05	1.89E+04	7.57E+03	<20	2.02E+01	378.2
B1T767	83.0	<20	2624.86	<7531	1.41E+05	7.83E+03	6.16E+03	<20	2.14E+01	764.4
B1T817	83.0	<20	2982.71	<8890	1.37E+05	8.42E+03	6.00E+03	<20	1.91E+01	1044.5
B1T985	89.3	<20	2986.08	<8564	1.70E+05	1.40E+04	1.35E+04	<20	1.74E+01	1091.9
B1T768	90.5	<20	3121.22	<8868	1.86E+05	6.80E+03	3.80E+03	<20	4.32E+01	687.3
B1T771	98.0	<20	4559.1	<5331	6.92E+04	1.53E+04	2.19E+03	<20	1.73E+01	386.5
B1T773	103.0	<20	2649.52	<9441	7.40E+04	6.46E+03	2.07E+03	<20	3.26E+01	671.2
B1T9K9	106.8	<20	2452.37	<8284	6.54E+04	5.78E+03	1.81E+03	<20	2.66E+01	683.4
B1T9L0	109.3	<20	4131.65	<4618	7.48E+04	1.29E+04	1.71E+03	<20	1.61E+01	334.8
B1T9L1	114.3	<20	2877.34	<10171	6.36E+04	6.93E+03	1.79E+03	<20	3.17E+01	737.4
B1T777	123.0	<20	6355.25	<7488	9.08E+04	2.35E+04	5.52E+03	<20	8.23E+00	1085.8
B1T818	123.0	<20	2360.81	<7399	1.01E+05	8.08E+03	5.96E+03	<20	1.26E+01	980.3
B1T9L2	126.8	<20	2420.68	<7482	1.13E+05	6.80E+03	4.35E+03	<20	2.61E+01	687.6
B1T9L3	129.3	<20	3507.54	<10709	1.10E+05	8.58E+03	3.49E+03	<20	2.31E+01	1304.5
B1T9L4	131.8	<20	3559.39	<10305	1.22E+05	7.59E+03	3.20E+03	<20	3.93E+01	850.2
B1T9L5	134.3	<20	4009.43	<4514	1.01E+05	1.33E+04	2.39E+03	<20	1.99E+01	474
B1T781	143.0	<20	3527.69	<4062	6.42E+04	1.16E+04	1.69E+03	<20	1.70E+01	355.4

Table 5.5 (contd)

HEIS #	mid depth (ft bgs)	Fluoride	Chloride	Nitrite	Nitrate	Sulfate-IC	Sulfate-ICP	Phosphate-IC	Phosphate-ICP	Alk
B1T790	165.5	14.42	80.29	<48.7	574.2	1.12E+03	1.11E+03	<20	3.17E+00	852.6
B1T793	173.0	19.19	52.59	<10.3	859.5	4.63E+02	1.30E+03	13.26	3.48E+00	1262.8
B1T9L6	176.8	19.31	50.22	<9.8	618.5	4.38E+02	1.23E+03	12.84	4.13E+00	1265.6
B1T9L7	179.3	15.3	41.66	<7.7	425.7	3.44E+02	1.24E+03	10.5	5.45E+00	997.9
B1T9L8	181.8	13.67	39.02	<7.2	212.6	1.16E+03	1.21E+03	21.12	3.11E+00	1168.1
B1T9L9	184.3	15.91	45.52	<7.8	206.6	3.47E+02	1.26E+03	9.47	2.56E+00	1122.3
B1T798	195.5	15.59	75.64	<58.5	1.58E+03	9.66E+02	8.51E+02	<20	1.74E+00	863
B1T7B4	210.5	708.13	4775.31	<5520	8.91E+04	1.67E+04	2.93E+03	<20	1.01E+01	703.8
B1T7B6	215.5	<20	1607.78	<3974	1.28E+05	1.81E+05	6.62E+03	<430	2.30E+01	437.1
B1T7C2	230.5	1209.98	8035.51	<9432	1.21E+05	2.59E+04	2.02E+03	<20	3.41E+01	778.1
B1T9K6	236.8	<20	2733.48	<9132	1.05E+05	4.18E+05	1.76E+03	<20	6.67E+01	570.7
B1T9K7	239.3	<20	3245.38	<11472	8.59E+04	5.25E+05	1.54E+03	<20	6.86E+01	659.6
B1T9K8	241.8	<20	2892.79	<10595	6.45E+04	4.85E+05	1.29E+03	<20	5.77E+01	715.2
B1T824	244.3	28.39	475.52	<1082	3.65E+04	4.91E+04	9.38E+02	<20	4.24E+01	782.1
B1T7C4	245.5	29.17	379.24	<989	2.77E+04	4.54E+04	8.80E+02	<20	3.37E+01	714.4
B1T7C9	258.0	11.88	41.46	<6.5	228.6	1.11E+03	1.06E+03	19.19	2.05E+00	896.5
B1T7D1	263.0	12.56	41	<6.4	216.4	2.91E+02	1.18E+03	<20	3.39E+00	899.9
B1T7D8	280.5	16.78	43.14	<9.5	203.5	1.60E+03	1.47E+03	27.89	4.24E+00	1253.7
B1T7F2	290.5	16.04	88.62	<8.6	242.6	1.54E+03	1.49E+03	24.79	1.49E+00	1411.5
B1T7H1	313.0	26.24	53.09	<12.5	116.4	1.14E+03	1.14E+03	<20	5.47E+00	2090.9
B1T7J2	340.5	36.78	143.72	<14.9	86	1.99E+03	2.20E+03	<20	5.08E+00	2339
B1V530	344	96.36	467.22	<81	106.9	2.91E+03	3.55E+03	<120	<260	5603
B1V531	346.5	34.29	74.25	<33	<33	6.19E+02	6.95E+02	<50	<106	1848
B1V532	349	15.66	64.72	<18	<19	2.41E+02	2.81E+02	<28	<60	781
B1V533	351.5	4.29	15.19	<8	<8	8.62E+01	9.46E+01	<12	<25	388

Table 5.6 shows the water-leachable concentrations of divalent and monovalent cations, in units of μg per gram of dry sediment for the grab samples analyzed from borehole C5923. Table 5.7 shows the same water-leachable cation data in units of mg/L of pore water, which as mentioned is a better convention for comparing with the soil-resistivity data. Table 5.6 shows a complicated pattern (in comparison to C4191) of ion-exchange front dynamics that occurs when sodium-dominated liquid wastes are disposed of into native Hanford sediments that have their cation exchange surface sites naturally loaded with divalent cations such as calcium, magnesium, and strontium. When waste liquid percolates below a crib or trench bottom both vertically and horizontally into a sediment profile, the sodium in the waste replaces the native divalent cations (and to some extent native potassium) on the exchange sites and "pushes" the replaced divalent cations out in the leading edge of the waste plume. Table 5.6 shows depleted divalent cations over the depth range of 8 to 20.5 ft bgs, but below this depth, there are three zones with elevated divalent cations with no zones of depleted (in comparison to native sediments) divalent cations between the elevated zones. The deeper zones of elevated divalent cations occur from 28 to 36, 44 to 143, and 210 to 246 ft bgs. The lack of significantly depleted divalent cation zones in the depth ranges 35 to 44, 65 to 70, 83 to 88, and 115 to 122 ft bgs suggest that the predominant waste fluid flow patterns might have

been horizontal at some of these regions, especially the two shallowest zones. At borehole C5923, the water-extractable Na shows elevated values over two thick zones, from 15 to 143 bgs and from 210 to 242 ft bgs. However, thorough scrutiny of the sodium distribution shows five discrete maxima at 46 to 48, 73 to 83, 89 to 91, 123 to 134, and 211 to 216 ft bgs. Thus, the waste fluid flow was strictly in the vertical direction. We would have expected to see a different distribution for the divalent cations as just discussed. The water-extractable Na and nitrate (μg/g units) are shown in Figure 5.3.

Compared to the water-extractable major cation distribution at borehole C4191 (directly below 216-B-26 trench), the profile at borehole C5923 off to the sides of the 216-B-16 and 216-B-17 cribs is much more complicated. Undoubtedly, the effects of lateral spreading from both the east and west from the two cribs and perhaps from the north and south from the other two rows of cribs has led to a complicated mixture of lateral ion exchange fronts where the sodium in the waste is replacing/displacing the native divalent cations and pushing the divalent cations out to the sides of the horizontally migrating waste liquid plumes. The complicated nature of the cation exchange distribution at borehole C5923 is shown in Figure 5.4.

Figure 5.3. Water-Extractable Nitrate, Sodium, Technetium-99, and Uranium in Sediments from Borehole C5923
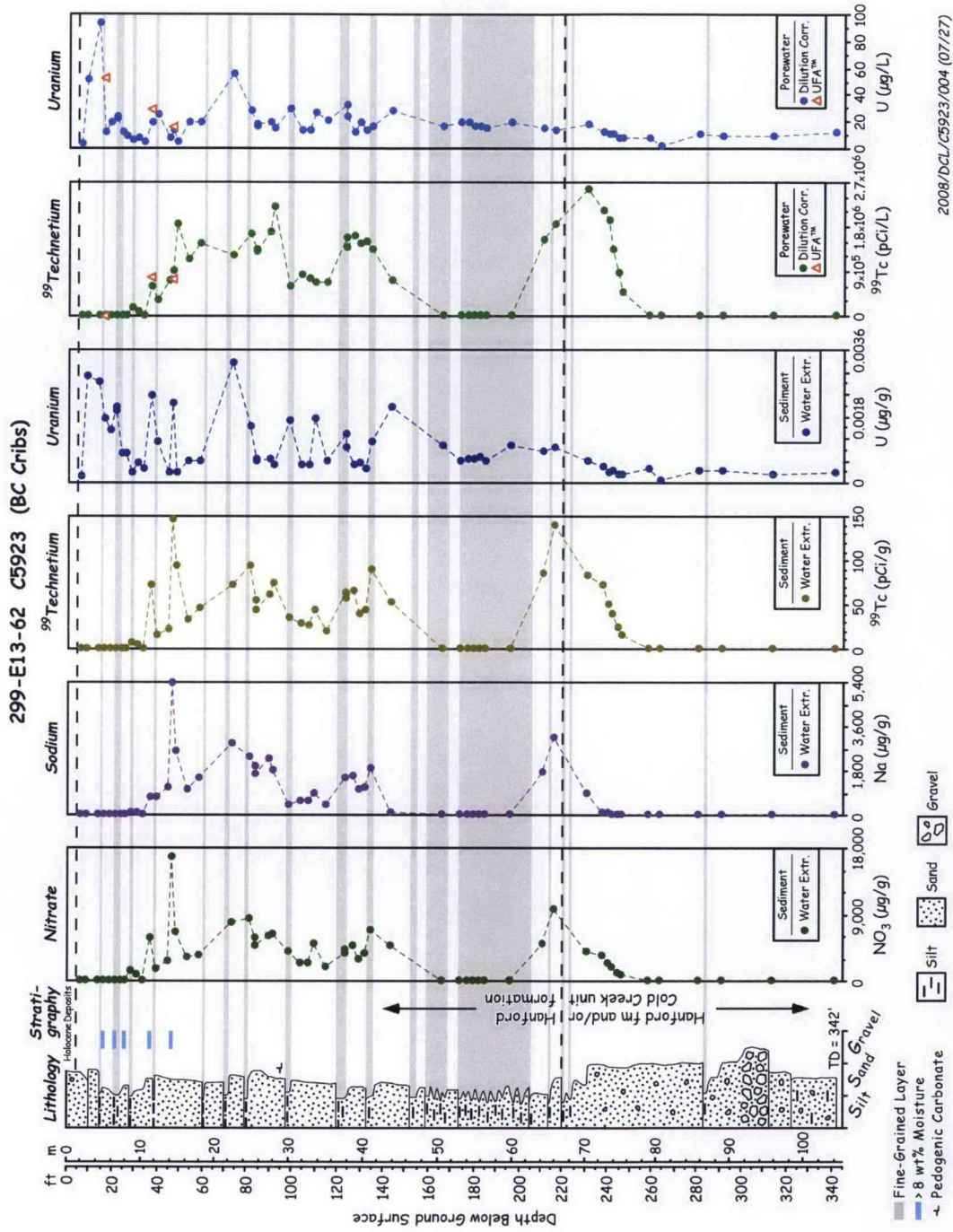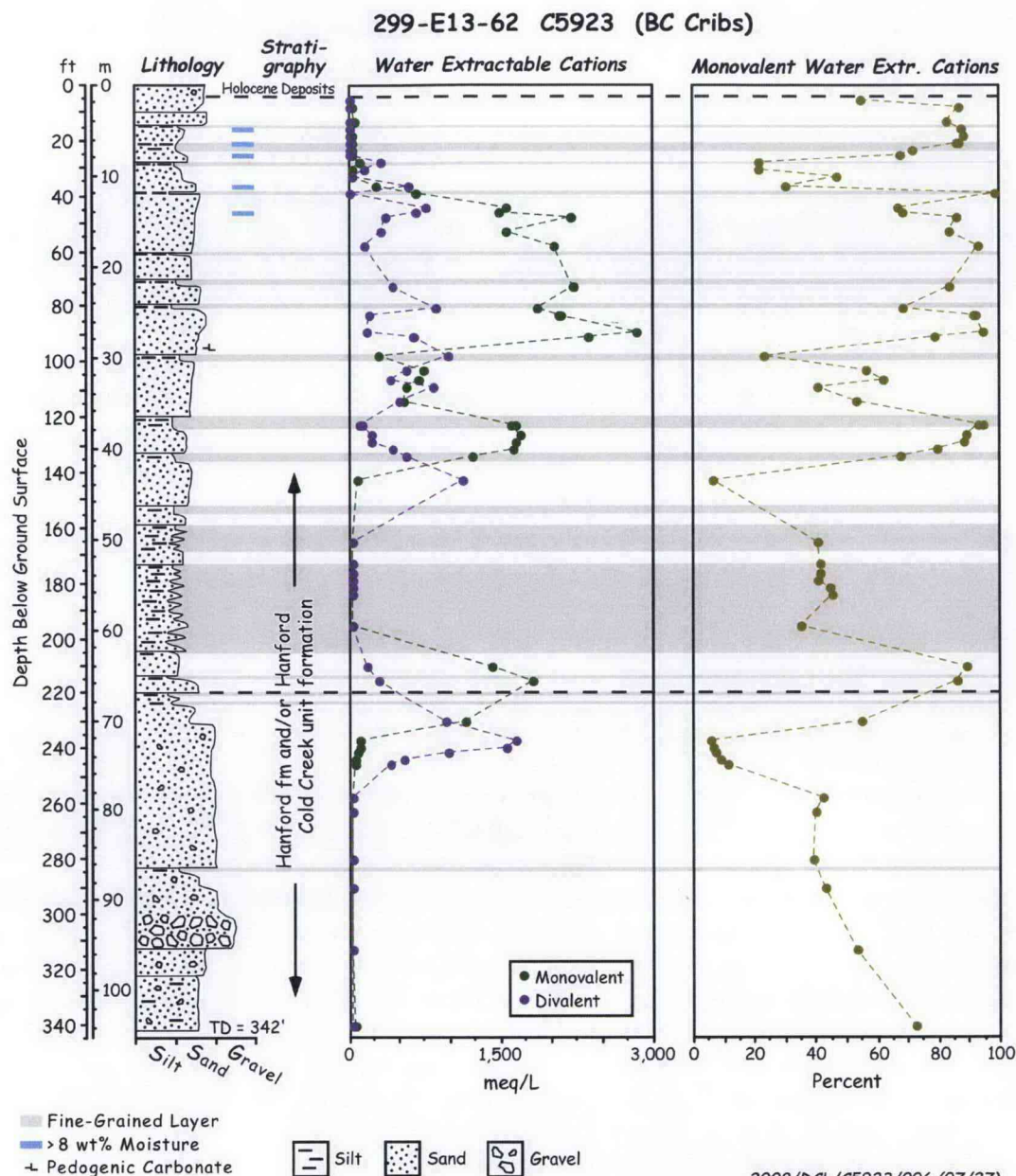
Figure 5.4. Distribution of Water Extractable Mono- and Di-valent Cations in Borehole C5923 Sediments

The anion and cation pore-water data suggest that waste fluids have descended down at least to 242 ft bgs at borehole C5923. The leading edge of sodium plumes generally lags behind the leading edge of the more mobile nitrate, so based on data in Table 5.4, the nitrate data suggest that the waste liquids descended to depths below 246 ft bgs, but perhaps not beyond 258 ft bgs. The difference between the maximum extent of the sodium and nitrate distributions is caused by the ion exchange reactions wherein sodium is adsorbed on sediment surface cation exchange sites and is somewhat retarded in its descent with the waste fluids.

Table 5.7 shows the same water-extract major cation data converted to pore-water concentrations where we used the simplifying assumption that adding de-ionized water to field moist sediment does not significantly dissolve solids and minerals; rather, it only dilutes and promotes the separation of the extant small volume of pore fluid. For highly contaminated vadose zone pore water, this assumption is fairly valid, but for slightly or uncontaminated pore water, the de-ionized water does dissolve some mildly soluble salts and thus over-estimates the true pore-water concentrations. Figure 5.5 shows the calculated pore-water EC and ionic strength for the pore water in sediments from borehole C5923 plotted along with the reciprocal of inverted field data to show a qualitative representation of the shapes of the depth distributions of these parameters. More discussion on correlating pore-water chemical composition with soil resistivity is found in Sections 5.2 and 5.3.

As part of the characterization of the water extracts, other chemical species such as aluminum, silicon, iron, manganese, zinc, and trace constituents such as arsenic, boron, barium, beryllium, bismuth, cadmium, cobalt, chromium, copper, lithium, molybdenum, nickel, lead, selenium, thallium, vanadium, titanium, and zirconium were measured. However, considering that their concentrations were generally low to non-detectable, the data are not presented in this ERC ground-truthing document. Table 5.5 compares the measurements of phosphorous and sulfur (reported as phosphate and sulfate) that were performed using the ICP-OES to corroborate the direct measurement of the anions phosphate and sulfate using the IC. The data from the two independent measurements compared well.

The only potential radiological COCs that were measurable in the water extracts were technetium-99 and uranium, and their concentrations on both a per gram of sediment basis and as pore-water concentrations are listed in Table 5.8. The technetium-99 data show elevated technetium-99 water-extract concentrations occurring in a complicated vertical profile from 28 to 245.5 ft bgs. There appear to be two thick lobes to the distribution (28 to 143 ft bgs and 210 to 245.5 ft bgs). Within the lobes are local maxima at 36.8, 45.5, 86.5, 90.5, 134.3, and 215.5 ft bgs. The deepest penetration of significant technetium-99 occurs at the same place as the significantly elevated nitrate at 245.5 ft bgs. These two mobile contaminants are often found to travel and distribute in the vadose zone in a similar pattern. Elevated water-extractable concentrations of uranium are found both shallow in the vadose zone from 8 to 20.5 ft bgs and deeper from 36.8 to 39.3, 73 to 80.5, and 134 to 143 ft bgs. The more significant water-leachable uranium concentrations are from 8 to 13, at 36 and at 73 ft bgs. This suggests that uranium is less mobile than the technetium-99 and nitrate. Figure 5.3 shows the calculated pore-water concentration of water-extractable technetium-99 and uranium as a function of depth.

Table 5.8 also lists the total ionic strength of the calculated pore waters in the vadose zone profile at C5923. Of all the pore-water parameters, the total ionic strength should correlate best with the soil-resistivity data, which are influenced by the total dissolved salt content in the sediment. The total ionic strength correlations with the field and laboratory resistivity measurements for borehole C5923 are discussed in sections 5.2 and 5.3 of this report. A qualitative view of the distribution of the pore water and field resistivity data is shown in Figure 5.5. The distribution of pore water EC and ionic strength at C5923 is more irregular and penetrates deeper than at C4191 placed through B-26 trench. Considering that twice as much water was disposed of to the two nearest cribs, B-16 and B-17, and four other cribs are quite close, one might expect deeper penetration at C5923 than at C4191. The peak ionic strengths at C5923 are somewhat higher, 2.5 to 3.5 M, in the more concentrated lobe of the plume from 44 to 90 ft bgs than at C4191, which had a peak ionic strength of 2 to 2.3 M near 91 ft bgs. Two other localized peak ionic strengths are found at C5923 at 132 ft bgs (2.36 M) and from 215 to 237 ft bgs (2.6 M). At C4191, there are two local maxima in ionic strength at 101 ft bgs (1.6 M) and at 131 ft bgs (1.4 M). The total

mass of salt disposed of in the vicinity of borehole C5923 is at least twice as large as the mass disposed of to the B-26 trench, so finding more residual salt in the pore water at C5923 might be expected; however, considering that the volume of liquid disposed of near C5923 was also twice as high as the volume disposed of at C4191, perhaps the concentration of the pore water at C5923 should be quite similar to the pore water below C4191 instead of showing more saline conditions.

Table 5.6. Water Extractable Cations in Borehole C5923 Sediments (µg/g dry soil)

HEIS #	mid depth	Ca	Mg	Sr	Na	K
	ft bgs	µg/g soil	µg/g soil	µg/g soil	µg/g soil	µg/g soil
B1T740	5.5	6.98E+00	1.74E+00	8.34E-03	1.04E+01	5.62E+00
B1T741	8	4.32E+00	1.09E+00	(8.04E-03)	4.43E+01	2.55E+00
B1T743	13	4.45E+00	1.24E+00	(2.59E-03)	3.39E+01	3.28E+00
B1T744	15.5	3.91E+00	9.68E-01	(6.91E-03)	4.26E+01	3.08E+00
B1T745	18	2.78E+00	5.65E-01	(1.24E-02)	2.99E+01	2.59E+00
B1T746	20.5	5.01E+00	8.00E-01	(3.72E-03)	4.07E+01	3.73E+00
B1T816	20.5	4.34E+00	7.66E-01	(6.05E-03)	3.81E+01	3.48E+00
B1T747	23	7.92E+00	1.25E+00	5.13E-03	2.67E+01	3.92E+00
B1T748	25.5	1.07E+01	1.71E+00	1.41E-02	2.93E+01	4.69E+00
B1T749	28	2.47E+02	3.80E+01	9.13E-01	8.85E+01	1.86E+01
B1T750	30.5	1.60E+02	2.92E+01	6.63E-01	5.54E+01	1.67E+01
B1T751	33	2.77E+01	5.49E+00	1.00E-01	3.18E+01	8.37E+00
B1T825	36.8	1.16E+03	1.87E+02	5.28E+00	7.18E+02	4.45E+01
B1T826	39.3	6.49E+00	1.58E+00	1.62E-02	6.88E+02	8.01E+00
B1T828	44.3	4.23E+02	3.62E+01	1.25E+00	1.09E+03	2.38E+01
B1T752	45.5	1.85E+03	2.06E+02	7.26E+00	5.40E+03	8.59E+01
B1T753	48	2.77E+02	5.08E+01	1.40E+00	2.56E+03	2.98E+01
B1T755	53	1.39E+02	2.93E+01	8.89E-01	1.05E+03	1.12E+01
B1T757	58	7.17E+01	1.31E+01	5.07E-01	1.47E+03	1.24E+01
B1T763	73	3.21E+02	1.10E+02	2.21E+00	2.94E+03	3.74E+01
B1T766	80.5	6.41E+02	1.97E+02	5.28E+00	2.37E+03	4.51E+01
B1T767	83	8.78E+01	4.12E+01	9.17E-01	1.96E+03	2.64E+01
B1T817	83	7.14E+01	3.19E+01	7.56E-01	1.62E+03	2.31E+01
B1T985	89.3	4.60E+01	4.00E+01	4.15E-01	2.29E+03	3.11E+01
B1T768	90.5	2.76E+02	1.02E+02	2.38E+00	1.83E+03	3.89E+01
B1T771	98	7.27E+02	2.41E+02	4.22E+00	3.75E+02	2.52E+01
B1T773	103	2.54E+02	7.70E+01	1.77E+00	5.53E+02	2.14E+01
B1T9K9	106.8	1.89E+02	6.94E+01	1.31E+00	5.64E+02	2.25E+01
B1T9L0	109.3	7.44E+02	2.12E+02	4.82E+00	8.30E+02	3.53E+01
B1T9L1	114.3	1.87E+02	6.88E+01	1.13E+00	3.76E+02	1.70E+01
B1T777	123	4.30E+01	2.10E+01	3.70E-01	1.51E+03	1.80E+01
B1T818	123	5.53E+01	2.42E+01	5.02E-01	1.50E+03	2.29E+01
B1T9L2	126.8	9.58E+01	4.62E+01	8.29E-01	1.58E+03	2.43E+01
B1T9L3	129.3	6.77E+01	2.89E+01	5.76E-01	1.00E+03	2.11E+01

Table 5.6 (contd)

HEIS #	mid depth	Ca	Mg	Sr	Na	K
	ft bgs	µg/g soil	µg/g soil	µg/g soil	µg/g soil	µg/g soil
B1T9L4	131.8	1.52E+02	6.00E+01	1.17E+00	**1.09E+03**	2.25E+01
B1T9L5	134.3	4.94E+02	1.70E+02	3.78E+00	**1.85E+03**	**3.80E+01**
B1T781	143	**1.20E+03**	**2.90E+02**	**6.00E+00**	1.12E+02	2.49E+01
B1T790	165.5	2.15E+01	8.70E+00	9.25E-02	2.34E+01	7.69E+00
B1T793	173	1.38E+01	4.68E+00	7.37E-02	1.54E+01	3.87E+00
B1T9L6	176.8	1.45E+01	4.56E+00	7.82E-02	1.58E+01	3.65E+00
B1T9L7	179.3	1.58E+01	5.00E+00	8.26E-02	1.66E+01	3.58E+00
B1T9L8	181.8	1.43E+01	5.07E+00	5.05E-02	1.82E+01	4.85E+00
B1T9L9	184.3	1.36E+01	4.67E+00	7.19E-02	1.72E+01	4.75E+00
B1T798	195.5	2.39E+01	9.21E+00	9.34E-02	2.08E+01	6.06E+00
B1T7B4	210.5	1.19E+02	4.59E+01	9.28E-01	**1.76E+03**	2.57E+01
B1T7B6	215.5	2.97E+02	9.59E+01	2.54E+00	**3.17E+03**	5.24E+01
B1T7C2	230.5	4.24E+02	1.17E+02	3.15E+00	8.37E+02	3.17E+01
B1T9K6	236.8	**8.26E+02**	**1.63E+02**	**4.31E+00**	5.46E+01	2.96E+01
B1T9K7	239.3	6.31E+02	1.13E+02	**3.59E+00**	4.84E+01	2.89E+01
B1T9K8	241.8	4.20E+02	9.08E+01	2.19E+00	3.58E+01	2.11E+01
B1T824	244.3	2.18E+02	5.84E+01	1.07E+00	2.69E+01	1.53E+01
B1T7C4	245.5	1.75E+02	4.99E+01	8.89E-01	2.92E+01	1.55E+01
B1T7C9	258	1.48E+01	4.90E+00	4.81E-02	1.61E+01	5.15E+00
B1T7D1	263	1.60E+01	5.28E+00	8.14E-02	1.55E+01	5.53E+00
B1T7D8	280.5	1.36E+01	4.61E+00	5.02E-02	1.24E+01	5.10E+00
B1T7F2	290.5	1.58E+01	5.24E+00	5.60E-02	1.76E+01	6.12E+00
B1T7H1	313	8.53E+00	2.57E+00	2.03E-02	1.38E+01	5.06E+00
B1T7J2	340.5	6.30E+00	1.80E+00	1.59E-02	2.33E+01	7.45E+00
B1V530	344	5.99E+00	1.91E+00	<5.6E-02	3.86E+01	9.32E+00
B1V531	346.5	3.94E+00	1.31E+00	<5.6E-02	2.26E+01	4.94E+00
B1V532	349	1.96E+00	0.84E+00	<5.6E-02	2.06E+01	4.59E+00
B1V533	351.5	4.95E+00	1.45E+00	<5.6E-02	1.55E+01	4.71E+00

(a) Bold red values are elevated concentrations for given constituent.
(b) Bold blue values are lower than natural background for a given constituent.
(c) Parentheses signify values below level of quantitation but considered valid for this work.

Table 5.7. Water-Extractable Cations as Pore Water Concentrations in Borehole C5923 Sediments (mg/L)

HEIS #	mid depth	Ca	Mg	Sr	Na	K
	ft bgs	mg/L	mg/L	mg/L	mg/L	mg/L
B1T740	5.5	9.57E+01	2.39E+01	1.14E-01	1.43E+02	7.70E+01
B1T741	8	7.59E+01	1.92E+01	(1.41E-01)	7.78E+02	4.49E+01
B1T743	13	1.51E+02	4.23E+01	(8.80E-02)	1.15E+03	1.12E+02
B1T744	15.5	2.73E+01	6.76E+00	(4.82E-02)	2.97E+02	2.15E+01
B1T745	18	3.65E+01	7.42E+00	(1.62E-01)	3.92E+02	3.40E+01
B1T746	20.5	5.61E+01	8.95E+00	(4.16E-02)	4.56E+02	4.17E+01
B1T816	20.5	4.76E+01	8.40E+00	(6.64E-02)	4.18E+02	3.81E+01
B1T747	23	1.11E+02	1.76E+01	7.20E-02	3.75E+02	5.49E+01
B1T748	25.5	1.16E+02	1.85E+01	1.52E-01	3.17E+02	5.07E+01
B1T749	28	5.11E+03	7.86E+02	1.89E+01	1.83E+03	3.84E+02
B1T750	30.5	2.13E+03	3.89E+02	8.83E+00	7.38E+02	2.23E+02
B1T751	33	3.66E+02	7.25E+01	1.32E+00	4.21E+02	1.11E+02
B1T825	36.8	9.51E+03	1.53E+03	4.31E+01	5.87E+03	3.63E+02
B1T826	39.3	1.43E+02	3.47E+01	3.57E-01	1.52E+04	1.76E+02
B1T828	44.3	1.36E+04	1.16E+03	4.00E+01	3.50E+04	7.64E+02
B1T752	45.5	1.15E+04	1.28E+03	4.53E+01	3.37E+04	5.36E+02
B1T753	48	5.41E+03	9.95E+02	2.73E+01	5.00E+04	5.83E+02
B1T755	53	4.72E+03	9.94E+02	3.01E+01	3.55E+04	3.80E+02
B1T757	58	2.26E+03	4.12E+02	1.60E+01	4.63E+04	3.90E+02
B1T763	73	5.54E+03	1.89E+03	3.81E+01	5.06E+04	6.44E+02
B1T766	80.5	1.14E+04	3.50E+03	9.38E+01	4.22E+04	8.02E+02
B1T767	83	2.14E+03	1.00E+03	2.23E+01	4.77E+04	6.42E+02
B1T817	83	2.09E+03	9.33E+02	2.21E+01	4.74E+04	6.76E+02
B1T985	89.3	1.29E+03	1.13E+03	1.17E+01	6.46E+04	8.77E+02
B1T768	90.5	8.04E+03	2.98E+03	6.94E+01	5.33E+04	1.13E+03
B1T771	98	1.27E+04	4.22E+03	7.39E+01	6.57E+03	4.43E+02
B1T773	103	7.58E+03	2.30E+03	5.28E+01	1.65E+04	6.39E+02
B1T9K9	106.8	5.16E+03	1.89E+03	3.58E+01	1.54E+04	6.13E+02
B1T9L0	109.3	1.13E+04	3.22E+03	7.33E+01	1.26E+04	5.36E+02
B1T9L1	114.3	6.24E+03	2.30E+03	3.79E+01	1.26E+04	5.70E+02
B1T777	123	1.06E+03	5.17E+02	9.12E+00	3.73E+04	4.43E+02
B1T818	123	1.35E+03	5.89E+02	1.22E+01	3.65E+04	5.58E+02
B1T9L2	126.8	2.33E+03	1.12E+03	2.02E+01	3.85E+04	5.92E+02
B1T9L3	129.3	2.53E+03	1.08E+03	2.15E+01	3.75E+04	7.86E+02
B1T9L4	131.8	5.17E+03	2.03E+03	3.97E+01	3.70E+04	7.64E+02
B1T9L5	134.3	7.34E+03	2.52E+03	5.62E+01	2.75E+04	5.65E+02
B1T781	143	1.61E+04	3.87E+03	8.01E+01	1.49E+03	3.32E+02
B1T790	165.5	3.44E+02	1.39E+02	1.48E+00	3.75E+02	1.23E+02

Table 5.7 (contd)

HEIS #	mid depth	Ca	Mg	Sr	Na	K
	ft bgs	mg/L	mg/L	mg/L	mg/L	mg/L
B1T793	173	4.68E+02	1.59E+02	2.50E+00	5.22E+02	1.31E+02
B1T9L6	176.8	4.61E+02	1.45E+02	2.49E+00	5.03E+02	1.16E+02
B1T9L7	179.3	3.99E+02	1.26E+02	2.09E+00	4.19E+02	9.04E+01
B1T9L8	181.8	3.39E+02	1.20E+02	1.20E+00	4.30E+02	1.15E+02
B1T9L9	184.3	3.44E+02	1.19E+02	1.82E+00	4.38E+02	1.21E+02
B1T798	195.5	4.61E+02	1.77E+02	1.80E+00	4.01E+02	1.17E+02
B1T7B4	210.5	2.16E+03	8.33E+02	1.68E+01	3.19E+04	4.67E+02
B1T7B6	215.5	3.89E+03	1.25E+03	3.33E+01	4.14E+04	6.85E+02
B1T7C2	230.5	1.32E+04	3.64E+03	9.77E+01	2.60E+04	9.83E+02
B1T9K6	236.8	2.48E+04	4.90E+03	1.30E+02	1.64E+03	8.89E+02
B1T9K7	239.3	2.38E+04	4.26E+03	1.35E+02	1.83E+03	1.09E+03
B1T9K8	241.8	1.46E+04	3.16E+03	7.63E+01	1.25E+03	7.35E+02
B1T824	244.3	7.74E+03	2.07E+03	3.79E+01	9.54E+02	5.43E+02
B1T7C4	245.5	5.67E+03	1.62E+03	2.88E+01	9.44E+02	5.02E+02
B1T7C9	258	3.17E+02	1.05E+02	1.03E+00	3.44E+02	1.10E+02
B1T7D1	263	3.39E+02	1.12E+02	1.72E+00	3.29E+02	1.17E+02
B1T7D8	280.5	4.22E+02	1.43E+02	1.56E+00	3.85E+02	1.59E+02
B1T7F2	290.5	4.45E+02	1.47E+02	1.58E+00	4.96E+02	1.72E+02
B1T7H1	313	3.51E+02	1.06E+02	8.35E-01	5.66E+02	2.08E+02
B1T7J2	340.5	3.08E+02	8.78E+01	7.77E-01	1.14E+03	3.64E+02
B1V530	344	4.87E+02	1.55E+02	<4.23E-00	3.13E+03	7.58E+02
B1V531	346.5	1.32E+02	4.38E+01	<1.74E-00	7.56E+02	1.65E+02
B1V532	349	3.64E+01	1.56E+01	<0.97E+00	3.83E+02	8.53E+01
B1V533	351.5	3.75E+01	1.10E+01	<0.4E+00	1.17E+02	3.57E+01

(a) Parentheses signify values below level of quantitation but considered valid for this work.
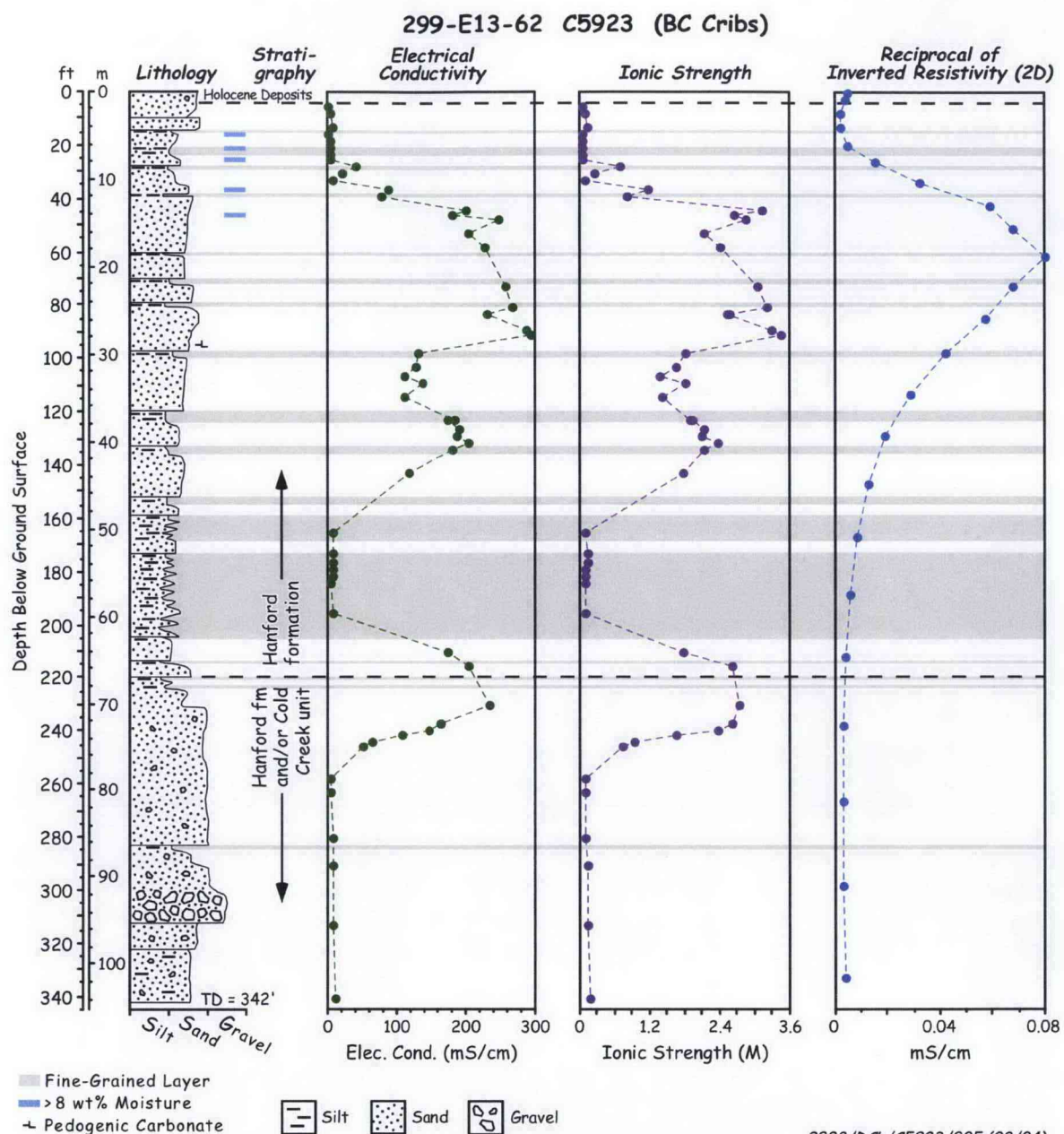
Figure 5.5. Pore Water Electrical Conductivity, Calculated Ionic Strength, and Reciprocal of Inverted Field Soil Resistivity Data for C5923 Borehole

Table 5.8. Water-Extractable Radionuclides and Pore Water Total Ionic Strength

HEIS #	mid depth	Technetium-99	U	Technetium-99	U	PW Ionic Strength
	ft bgs	pCi/g	µg/g	pCi/L	µg/L	M
B1T740	5.5	<0.424	<5.64E-04	<1.80E+03	<2.55E+00	0.03
B1T741	8	<0.424	**2.90E-03**	<1.69E+03	5.10E+01	0.07
B1T743	13	<0.424	**2.71E-03**	<4.17E+03	9.23E+01	0.11
B1T744	15.5	<0.424	1.73E-03	<9.20E+02	1.20E+01	0.02
B1T745	18	<0.424	1.41E-03	<1.59E+03	1.85E+01	0.03
B1T746	20.5	<0.424	2.04E-03	<1.54E+03	2.28E+01	0.04
B1T816	20.5	<0.424	1.94E-03	<1.52E+03	2.12E+01	0.04
B1T747	23	<0.424	8.13E-04	<2.16E+03	1.14E+01	0.04
B1T748	25.5	<0.424	7.62E-04	<1.55E+03	8.24E+00	0.04
B1T749	28	7.23	<5.64E-04	1.494E+05	<5.66E+00	0.69
B1T750	30.5	4.82	<5.64E-04	6.410E+04	<7.18E+00	0.26
B1T751	33	0.59	<5.64E-04	7.791E+03	<4.97E+00	0.07
B1T825	36.8	**72.14**	**2.35E-03**	5.892E+05	1.92E+01	1.17
B1T826	39.3	14.37	1.12E-03	3.161E+05	2.47E+01	0.80
B1T828	44.3	22.65	2.44E-04	7.256E+05	7.82E+00	**3.13**
B1T752	45.5	**145.85**	2.14E-03	9.093E+05	1.34E+01	**2.63**
B1T753	48	**93.57**	<5.64E-04	1.831E+06	<4.71E+00	**2.86**
B1T755	53	33.80	<5.64E-04	1.145E+06	<1.88E+01	**2.12**
B1T757	58	46.71	5.90E-04	1.469E+06	1.86E+01	**2.38**
B1T763	73	**71.66**	**3.23E-03**	1.234E+06	5.57E+01	**3.03**
B1T766	80.5	**93.25**	1.54E-03	1.657E+06	2.74E+01	**3.22**
B1T767	83	54.08	6.38E-04	1.315E+06	1.55E+01	**2.55**
B1T817	83	43.86	5.88E-04	1.282E+06	1.72E+01	**2.52**
B1T985	89.3	60.15	6.52E-04	1.693E+06	1.84E+01	**3.29**
B1T768	90.5	**74.75**	<5.64E-04	2.178E+06	<1.43E+01	**3.46**
B1T771	98	34.30	1.67E-03	6.010E+05	2.93E+01	1.81
B1T773	103	28.10	<5.64E-04	8.383E+05	<1.36E+01	1.62
B1T9K9	106.8	26.88	<5.64E-04	7.320E+05	<1.29E+01	1.37
B1T9L0	109.3	44.54	1.75E-03	6.764E+05	2.66E+01	1.81
B1T9L1	114.3	20.13	5.96E-04	6.729E+05	1.99E+01	1.39
B1T777	123	63.31	1.31E-03	1.560E+06	3.22E+01	1.87
B1T818	123	56.88	9.40E-04	1.383E+06	2.29E+01	1.91
B1T9L2	126.8	66.03	<5.64E-04	1.606E+06	<1.16E+01	2.10
B1T9L3	129.3	38.65	<5.64E-04	1.441E+06	<1.89E+01	2.07
B1T9L4	131.8	44.29	<5.64E-04	1.501E+06	<1.28E+01	**2.36**
B1T9L5	134.3	**89.99**	1.12E-03	1.337E+06	1.67E+01	2.11
B1T781	143	51.68	2.06E-03	6.900E+05	2.75E+01	1.77
B1T790	165.5	0.44	9.96E-04	6.982E+03	1.60E+01	0.08

Table 5.8 (contd)

HEIS #	mid depth	Technetium-99	U	Technetium-99	U	PW Ionic Strength
	ft bgs	pCi/g	μg/g	pCi/L	μg/L	M
B1T793	173	<0.424	<5.64E-04	<7.52E+03	<1.89E+01	0.11
B1T9L6	176.8	<0.424	6.12E-04	<6.23E+03	1.95E+01	0.11
B1T9L7	179.3	<0.424	6.30E-04	<5.39E+03	1.59E+01	0.09
B1T9L8	181.8	<0.424	6.83E-04	<4.68E+03	1.62E+01	0.09
B1T9L9	184.3	<0.424	<5.64E-04	<5.72E+03	<1.41E+01	0.09
B1T798	195.5	0.43	9.91E-04	8.259E+03	1.91E+01	0.10
B1T7B4	210.5	85.09	8.23E-04	1.544E+06	1.49E+01	1.76
B1T7B6	215.5	**139.87**	9.58E-04	1.827E+06	1.25E+01	**2.61**
B1T7C2	230.5	82.53	<5.64E-04	2.560E+06	<1.74E+01	**2.71**
B1T9K6	236.8	71.19	<5.64E-04	2.137E+06	<1.22E+01	**2.62**
B1T9K7	239.3	50.81	<5.64E-04	1.916E+06	<1.04E+01	**2.38**
B1T9K8	241.8	38.88	<5.64E-04	1.354E+06	<1.06E+01	1.63
B1T824	244.3	24.16	<5.64E-04	8.562E+05	<6.89E+00	0.92
B1T7C4	245.5	14.71	<5.64E-04	4.759E+05	<7.04E+00	0.71
B1T7C9	258	0.55	<5.64E-04	1.178E+04	<8.04E+00	0.08
B1T7D1	263	<0.424	<5.64E-04	<7.56E+02	<1.36E+00	0.08
B1T7D8	280.5	<0.424	<5.64E-04	<6.10E+03	<9.95E+00	0.10
B1T7F2	290.5	<0.424	<5.64E-04	<4.93E+03	<8.33E+00	0.11
B1T7H1	313	<0.424	<5.64E-04	<4.92E+03	<9.28E+00	0.11
B1T7J2	340.5	<0.424	<5.64E-04	<6.69E+03	<1.18E+01	0.15
B1V530	344	<0.388	<5.61E-04	<32	<0.05	0.30
B1V531	346.5	<0.388	<5.61E-04	<13	<0.02	0.082
B1V532	349	<0.388	<5.61E-04	<7.2	<0.01	0.035
B1V533	351.5	<0.388	<5.61E-04	<3.0	<0.01	0.016

(a) <values = below level of quantitation.
(b) Red type = values above natural background and bold red are peak values in various lobes of vertical distribution.

5.1.4   8 M Nitric Acid Extractable Amounts of Selected Elements

The amount of material that was extractable from the C5923 vadose zone sediment into 8 M nitric acid is shown in Table 5.9 to Table 5.11. The 8-M nitric acid extraction is a protocol used by the U.S. Environmental Protection Agency to estimate the maximum concentrations of regulated metals in contaminated sediment that would be biologically available. Aliquots of sediment from borehole C5923 were subjected to the acid extraction to look for elevated quantities of selected constituents and radionuclides.

The acid extract data for grab samples from C5923 in general did not show higher values for constituents in the shallow depths (relative to known Hanford site background values) in contrast to shallow sediments from borehole C4191 sediments that received directly the waste disposed of to the 216-B-26 trench. The lack of inflated concentrations for selected elements in the acid-extracts from

C5923 sediments, excepting perhaps acid-extractable iron (shown in Table 5.10), in comparison to sediments from C4191 reflects that fact that C5923 is not within the footprint of any of the cribs. Most highly reactive constituents in the liquid waste stream disposed of at the BC Cribs and Trenches reacted very close to the facility's bottom so that a sludge layer with reactive metals and radionuclide oxides,

Table 5.9. Acid-Extractable Light Elements in Borehole C5923 Sediments (µg/g dry sediment)

Sample (HEIS ID)	Depth (ft bgs)	Na	Mg	Al	P	S	K	Ca	Ti
B1T744	15.5	<1070	4580	6570	1010	<236	1080	5440	959
B1T748	25.5	<1030	4890	7630	974	<228	1300	11300	883
B1T749	28.0	<959	3800	5420	946	<212	817	10200	907
B1T825	36.0	1050	4780	7090	749	<227	1300	14600	671
B1T752	45.5	3340	4260	6860	588	721	1240	9180	691
B1T757	58.0	1770	3770	5000	346	<213	991	8450	414
B1T763	73.0	3270	4720	5730	435	368	1110	9330	434
B1T766	80.5	2600	4440	5350	394	<215	1080	8730	433
B1T9L0	108.8	<1130	4630	6250	377	<221	1560	8510	513
B1T9L5	133.8	2180	4350	6240	451	<223	1810	7810	410
B1T781	143.0	<1020	4080	5070	499	<226	1150	8480	364
B1T798	195.5	<997	4110	6400	447	<221	1380	9220	652
B1T7B4	210.5	2230	3890	5980	388	<249	1490	7720	513
B1T7C2	230.5	1020	3980	5340	404	<216	1060	6640	482
B1T7D1	263.0	<990	3900	5780	458	<219	1260	6160	635
B1T7F2	290.5	<961	3480	5160	491	<212	988	5700	680
B1T7H1	313.0	<1030	3130	4580	446	<227	760	4420	602

Table 5.10. Acid-Extractable Heavy Elements in Borehole C5923 Sediments (µg/g dry sediment)

Sample (HEIS ID)	Depth (ft bgs)	V	Mn	Fe	Co	Sr	Zr	Hg
B1T744	15.5	27.4	359	20100	10.9	25.4	<20.3	<0.053
B1T748	25.5	30.3	477	21400	13.1	33.5	<19.6	<0.051
B1T749	28.0	30	407	18400	10.8	32.1	18.3	<0.048
B1T825	36.0	23.6	395	17400	11.1	48.8	<19.5	<0.051
B1T752	45.5	22.4	303	14700	8.64	37.4	<20.9	0.066
B1T757	58.0	9.73	235	9630	<7.49	28.6	<18.3	<0.048
B1T763	73.0	9.6	241	11400	<7.8	29.2	<19	<0.05
B1T766	80.5	9.14	237	10700	<7.56	32.1	<18.4	<0.048
B1T9L0	108.8	11.9	273	11700	<7.79	32.3	<19	<0.05
B1T9L5	133.8	12.1	255	10600	<7.85	33.9	<19.1	<0.05
B1T781	143.0	11	233	9670	<7.96	32.1	<19.4	<0.051
B1T798	195.5	17.2	268	12400	<7.77	34.8	<18.9	<0.05
B1T7B4	210.5	14.5	270	11000	<8.78	29.9	<21.4	<0.056
B1T7C2	230.5	13.6	241	10300	<7.62	31.3	<18.6	<0.049
B1T7D1	263.0	17.5	238	11800	<7.71	28.4	<18.8	<0.049
B1T7F2	290.5	19	249	13200	<7.48	25.7	<18.2	<0.048
B1T7H1	313.0	17.8	185	10100	<8.01	22.7	<19.5	<0.051

Table 5.11. Acid Extractable Content for RCRA Metals and Radionuclides in Borehole C5923 Sediments (units μg/g except Tc pCi/g)

Sample (HEIS ID)	Depth (ft bgs)	Cr	Cd	Pb	Tc 99	U 238
B1T744	15.5	(5.30E+00)[a]	7.24E-02	2.99E+00	2.02E+01	3.49E-01
B1T748	25.5	(5.77E+00)	7.18E-02	3.57E+00	2.00E+01	4.18E-01
B1T749	28.0	(4.41E+00)	6.98E-02	2.38E+00	2.90E+01	3.87E-01
B1T825	36.0	(5.78E+00)	7.98E-02	3.76E+00	7.80E+01	4.00E-01
B1T752	45.5	(4.58E-02)	1.26E-02	4.44E-03	8.22E+01	3.53E-01
B1T757	58.0	(7.41E+00)	7.17E-02	2.85E+00	6.64E+01	3.17E-01
B1T763	73.0	(8.28E+00)	5.78E-02	2.83E+00	7.91E+01	3.97E-01
B1T766	80.5	(8.01E+00)	6.34E-02	3.49E+00	1.08E+02	3.72E-01
B1T9L0	108.8	(9.23E+00)	6.96E-02	2.91E+00	4.65E+01	3.91E-01
B1T9L5	133.8	(1.05E+01)	7.91E-02	3.06E+00	9.78E+01	3.11E-01
B1T781	143.0	(9.39E+00)	7.21E-02	3.74E+00	6.16E+01	4.37E-01
B1T798	195.5	(8.63E+00)	6.18E-02	2.42E+00	1.97E+01	4.28E-01
B1T7B4	210.5	(7.64E+00)	5.77E-02	2.97E+00	9.41E+01	3.48E-01
B1T7C2	230.5	(9.46E+00)	5.45E-02	2.05E+00	1.05E+02	1.38E-01
B1T7D1	263.0	(8.28E+00)	5.78E-02	2.13E+00	1.43E+01	5.49E-01
B1T7F2	290.5	(7.81E+00)	5.50E-02	1.95E+00	2.34E+01	3.51E-01
B1T7H1	313.0	(6.57E+00)	5.58E-02	1.66E+00	2.11E+01	3.06E-01

(a) Parentheses signify values below level of quantitation but considered valid.

hydroxides, phosphates and maybe other insoluble salts are located within the footprint. The acid extract data for sediment samples from C5923 do not show any "waste laden" sludge signatures and the acid extract data are not of much relevancy to the ERC "ground-truthing" exercise. Further, as shown in Table 5.10, no measureable mercury was detected in any of the acid extracts. Similarly no elevated concentrations of other RCRA-regulated metals were found.

5.1.5 Radionuclide Content in Vadose Zone Sediment from C5923

Selected grab samples in zones that contained high salt content in the pore waters were directly counted for gamma radioactivity. One grab sample from borehole C5923 at 48 ft bgs contained very minor amounts of cesium-137 right at the detection limit of ~0.15 pCi/g. Based on the cesium-137 distribution at the C4191 borehole directly below the 216-26 trench footprint, we feel that this detection of 0.16 pCi/g cesium-137 at 48 ft bgs is more than likely counting uncertainties. The SG field logging performed by Stoller Inc. did detect a few pCi/g cesium-137 in the top few feet of sediment at borehole C5923 that is a more realistic finding for the cesium-137 distribution at borehole C5923. Table 5.12 shows that no other man-made gamma-emitting radionuclides were seen in the sediments from C5923. This contrasts with the very low activities in borehole C4191, which is deeper than the 216-B-26 bottom where some fission products were measured for several more feet into the sediments. This is similar to observations at other Hanford inactive disposal sites. The GEA of the selected grab samples from borehole C5923 did show background activities of natural potassium-40 and daughter products of natural uranium-238 and thorium-232.

Table 5.12. Man-Made Fission Product GEA Data (pCi/g sediment) for Grab Samples from C5923

HEIS #	mid depth ft bgs	Co-60 pCi/g	Sb-125 pCi/g	Cs-137 pCi/g	Eu-152 pCi/g	Eu-154 pCi/g	Eu-155 pCi/g
B1T741	8	<0.10	<0.35	<0.13	<0.44	<0.27	<0.42
B1T752	45.5	<0.08	<0.26	<0.09	<0.33	<0.19	<0.29
B1T753	48	<0.14	<0.47	0.16	<0.63	<0.36	<0.63
B1T754	50.5	<0.11	<0.38	<0.14	<0.44	<0.28	<0.45
B1T763	73	<0.14	<0.46	<0.16	<0.61	<0.36	<0.62
B1T771	98	<0.11	<0.39	<0.14	<0.49	<0.30	<0.49
B1T9L5	134.3	<0.15	<0.51	<0.18	<0.67	<0.41	<0.70
B1T781	143	<0.12	<0.37	<0.14	<0.53	<0.28	<0.46
B1T7B4	210.5	<0.13	<0.41	<0.15	<0.51	<0.32	<0.51
B1T7C2	230.5	<0.15	<0.50	<0.18	<0.65	<0.38	<0.65
B1T7D8	280.5	<0.09	<0.28	<0.10	<0.36	<0.22	<0.36

PNNL performed technetium-99 and uranium-238 analysis on the one-to-one sediment-to-water extracts and the sediment acid extracts. The uranium and technetium water-extractable contents were previously discussed above. PNNL also performed wet chemical separations on acid extracts of the grab samples shown in Table 5.13 to measure strontium-90 and nickel-63, two beta-emitting radionuclides that were found to be present in the shallow depths (right near the trench bottom) at C4191. The strontium-90 and nickel-63 analyses were all below detection limits for grab samples from C5923 as shown in Table 5.13. In contrast to the shallow sediments at C4191, which was emplaced directly through the footprint of the 216-B-26 trench, no strontium-90 or nickel-63 was found in the sediments obtained from borehole C5923. Considering that these radionuclides are quite immobile in the geochemical environment in Hanford's subsurface, given the nature of the waste stream disposed of at the BC Cribs and Trenches and the fact that borehole C5923 is several 10s of feet from crib footprints, it was expected that no detectable nickel-63 or strontium-90 would be found.

5.1.6 Groundwater Analysis of Sample Obtained Prior to Decommissioning Borehole C5923

At the completion of drilling C5923 in July 2008, one groundwater sample was obtained at a depth of 359.9 ft bgs before the lower portion of the borehole was decommissioned. The water table was 350.6 ft bgs in July 2008 or 395.4 ft elevation based on data found in Table 2.2. This elevation is in line with the decreasing water table trend shown in Figure 2.22 and approximately 7.5 ft above the pre-Hanford water table. The composition of the groundwater was determined by the Waste Sampling and Characterization Facility (WSCF) and other commercial analytical laboratories. The water sample was taken at a depth of 359.9 ft bgs, approximately 9 ft below the water table. The results are shown in Table 5.14.

The major cations and several of the major anions were not measured, so it is not possible to perform cation-anion balances or to compare the total groundwater composition to the regional water composition. However, based on the measured nitrate concentration, there is a hint that groundwater at this borehole contains a trace of the disposed scavenged bismuth phosphate waste stream. This differs from the

Table 5.13. Other Radionuclides Present in the C5923 Sediments

HEIS #	mid depth ft bgs	Ni-63 pCi/g	Sr-90 pCi/g
B1T744	15.5	<12.2	<48.6
B1T748	25.5	<11.8	<49.2
B1T749	28	<11	<47.6
B1T825	36.8	<11.7	<47.5
B1T752	45.5	<12.5	<49.2
B1T757	58	<11	<48.4
B1T763	73	<11.4	<49.2
B1T766	80.5	NA	<47.8
B1T9L0	109.3	<11.4	<48.8
B1T9L5	134.3	<11.5	<49.1
B1T781	143	NA	<49.4
B1T798	195.5	<11.4	<49.3
B1T7B4	210.5	<12.9	<55.6
B1T7C2	230.5	<11.2	<49.3
B1T7D1	263	<11.3	<49.1
B1T7F2	290.5	<11	<48.2
B1T7H1	313	<11.7	<52.2

Table 5.14. Groundwater Composition at Water Table at C5923 in July 2008

7/15/2008		Water Table 350.6 ft bgs		Sampled at 359.9 ft bgs	
	Units	Value		Units	Value
pH Measurement		8.12	Iron	µg/L	<54.5
Specific Conductance	mS/cm	1.196	Lead	µg/L	<45
Total organic carbon	µg/L	--	Magnesium	mg/L	--
Alkalinity	mg/L	--	Manganese	µg/L	406±2
Chloride	mg/L	--	Nickel	µg/L	<4
Cyanide	µg/L	--	Potassium	mg/L	--
Fluoride	mg/L	0.32±0.02	Sodium	mg/L	--
Nitrate	mg/L	9.34±0.18	Thallium	µg/L	<37
Nitrite	mg/L	0.21±0.02	Vanadium	µg/L	<12
Sulfate	mg/L	--	Zinc	µg/L	<9
Phosphate	mg/L	--	Technetium-99	pCi/L	<5.9
Aluminum	µg/L	--	Tritium	pCi/L	<270
Antimony	µg/L	<56	Uranium	µg/L	2.18±0.07
Arsenic	µg/L	<78	Sr-90	pCi/L	<0.9
Cadmium	µg/L	<4	Cs-137	pCi/L	--
Calcium	mg/L	--	I-129	pCi/L	<0.828
Chromium	µg/L	<13	Se-79	pCi/L	<2

(--) = not analyzed; (<) = value below sample quantification limit

analysis of the vadose zone pore waters from the deepest portion of the core, which show no detectable water-extractable nitrate. However, detectable water-extractable nitrate and technetium-99 in the vadose zone sediments at borehole C5923 are present as deep as 290 and 260 ft bgs, respectively, which is a much deeper penetration of water-extractable mobile and major contaminants than was found at borehole C4191 directly through the foot print of the 216-B-26 trench (too be discussed in Section 8). There is no detectable technetium-99 or other mobile radionuclides in the groundwater obtained in July 2008 from borehole C5923 (A). Neither the slightly-elevated nitrate nor the non-detectable technetium-99 suggest that groundwater currently below the BC Cribs and Trenches area contains concentrations above drinking water standards for these two risk drivers. A review of past groundwater monitoring reports starting from July 1956 through June 1966 (see Appendix C for details) show only intermittent detection of gross beta (mainly ruthenium-106) and nitrate in monitoring wells surrounding the BC Cribs and Trenches. The active disposal period into the cribs and trenches was 1956 through 1957.

5.2 Field Electrical-Resistivity Results at Borehole C5923 (A)

Based on the descriptions provided in Section 4.1, the pole-pole resistivity data at BC Cribs and Trenches has been shown to be of sufficient quality to develop empirical models that relate the geochemistry and field soil-resistivity data. The instrument and environment noise was observed to be low such that a majority of the field measurements could be retained for HRR, 2D inversion, and 3D inversion processing. Additionally, variability in target strength was observed in all processing methods, allowing more complex analyses to be performed.

Empirical model development was conducted with several key geochemical parameters to test which parameter has the highest correlation to the soil resistivity as measured in the field. Several parameters suggest direct causation, such as ionic strength or pore-water EC. Other models, including correlation of soil resistivity with pore-water technetium-99 concentration, were developed to explore indirect causation. Clearly, the pore-water concentration of technetium-99 is too low to produce a target if it were the sole analyte. However, it is known that technetium-99 and nitrate have very similar transport mechanisms. The empirical model may be used to understand the distribution of technetium-99 at the BC Cribs and Trenches site if the correlations for technetium-99 and resistivity are similar among the different boreholes and the disposal ratio of nitrate to technetium-99 was constant among the individual waste sites.

Issues regarding how best to scale the borehole and surface-based data for developing empirical relationships are the subject of an intense academic debate. Later sections explore and propose methodologies to handle correlating the volume-averaging information (surface-based resistivity) against the discrete sample data (borehole). One particular issue is that the borehole information is collected at a much finer interval than the surface-based data, and thus the true subsurface complexity is not fully detailed by surface-based surveys.

5.2.1 HRR at Borehole C5923 (A)

Figure 5.6 shows the HRR apparent-resistivity results for FY05-Line 4. For reference, features such as trench and crib locations are shown on the figure. The figure shows two low-resistivity features close to the surface that correlate to the location of the cribs in the northeast portion of the site and trenches in the north central portion. A large and deep low-resistivity anomaly is located between the cribs and trenches, which is a false anomaly due to the superposition of the two plumes, and a deep low-resistivity

layer (another conductive plume or water table). East of the cribs, the resistivity goes to background conditions over a very short distance.

To facilitate empirical model development, each of the new boreholes was placed along a resistivity line. Borehole C5923 (A) was placed 153 m from the eastern edge of FY05-Line 4. At Borehole C5923 (A), the resistivity data show a clear low-resistivity target at approximately 20 to 40 meters bgs. Above and below the target, resistivity increases, isolating the target. Variability can be seen in the target zone, as identified by the solid contour lines. The data also appear to be free from cultural interferences such as pipes and tanks known to exist in the area.

Equation 4-7 (Chapter 4) was used as the plotting algorithm to obtain the depth estimates of the apparent resistivity values shown in Figure 5.6, with coefficients of u=(3.97, 22.4, 3.97). These coefficients were based on the least-squares fitting of target depth using co-located resistivity data from FY04-Line 1 and borehole C4191 (see Rucker and Fink 2007). Figure 5.7 shows the extracted resistivity profiles for the HRR, 2D-inverted, and 3D-inverted data collected at Borehole C5923 (A). The markers plotted along the vertical profiles represent the edge of the model cells and thus give an indication of the volume over which the electrical resistivity is either measured (HRR) or calculated (2D and 3D). Depending on how the numerical models were formulated, the cell size either grows with depth (as in the 3D inverted data), decreases with depth (as in HRR), or stays the same over the entire depth interval (as in the 2D inverted). Regardless of the analysis method used, the volumetric measurement that represents electrical resistivity still must be considered as a point estimate in order to compare directly with the borehole geochemistry data.
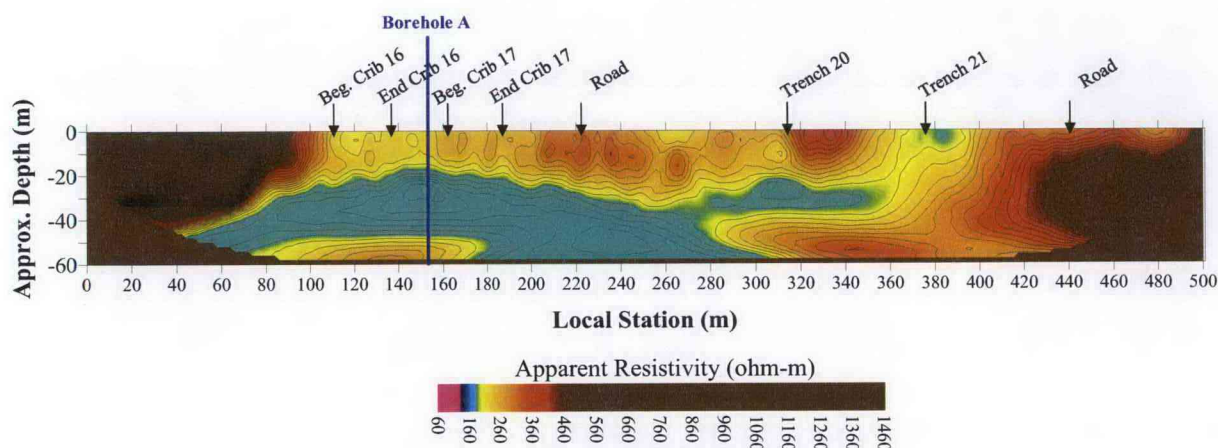
Figure 5.6. HRR Results of FY05-Line 4
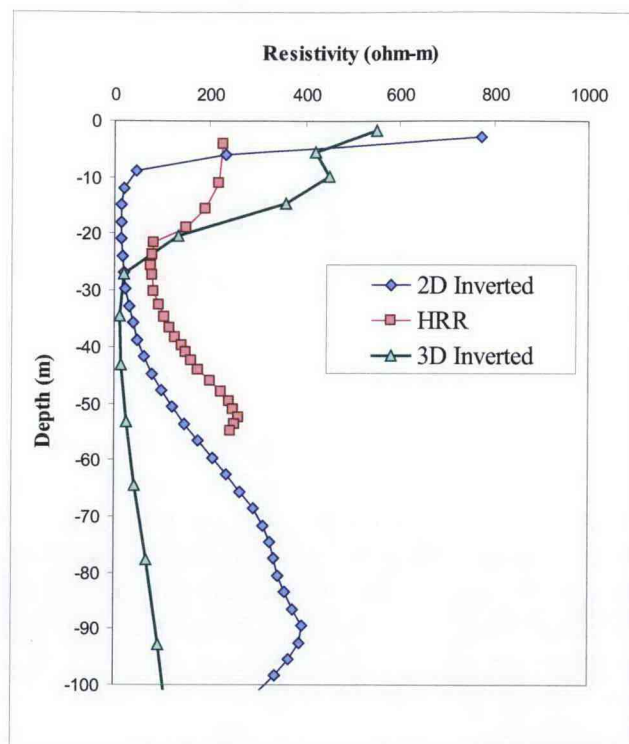
Figure 5.7. Vertical Profiles of HRR, 2D Inverted, and 3D Inverted Resistivity Data at the Location of Borehole C5923 (A)

The individual geochemical species in Borehole C5923 (A) were sampled at a much higher spatial frequency and at different depths than the field-acquired apparent-resistivity data. To calculate correlations and develop the empirical models, the measured (field) geophysical data were re-sampled at the soil sampling depths with linear interpolation. The other option included re-sampling geochemistry data to match the depths of the geophysical data. This second option was deemed inappropriate due to the high spatial variability of the geochemical data compared to the geophysical data. Additionally, the geophysical data were not extrapolated to depths beyond that calculated by HRR, and comparisons were only performed to depths of approximately 54 m (177 ft) bgs.

Figure 5.8 shows the results of comparing the pore-water EC and HRR at Borehole C5923 (A). The plot on the left displays the profile of HRR and EC; the plot on the right shows the scatter of co-located EC and HRR data. Qualitatively, the data show a good inverse correlation. As the pore-water EC increases, the apparent soil resistivity decreases. Quantitatively, the scatter plot shows the linear regression model used to relate the HRR and EC, with an $R^2=0.588$. Five data values, circled in both plots, demonstrate the limitations of surface-based geophysics. That is, small-scaled variability is averaged out by the field resistivity due to the volume-averaging electrical measurements. Additionally, Day-Lewis and Singha (2008) explained that conventional geochemical measurements preferentially sample from the mobile domain (pore space where fluid moves freely), and soil electrical resistivity is sensitive to the electrolytic solute in both the mobile and immobile domains. These differences in measurement domains would cause some of the variances observed in the scatter plot.

It should be noted that slightly different coefficients for the HRR plotting could be used to gain better correlation with the geochemical data. The profile data of Figure 5.8 shows that the peak target values in the HRR data are lower in elevation than those of the geochemistry. Changing the last plotting coefficient from 3.97 to 0 increases the correlation to 0.673. However, the coefficients from Rucker and Fink (2007) are used here for consistency.
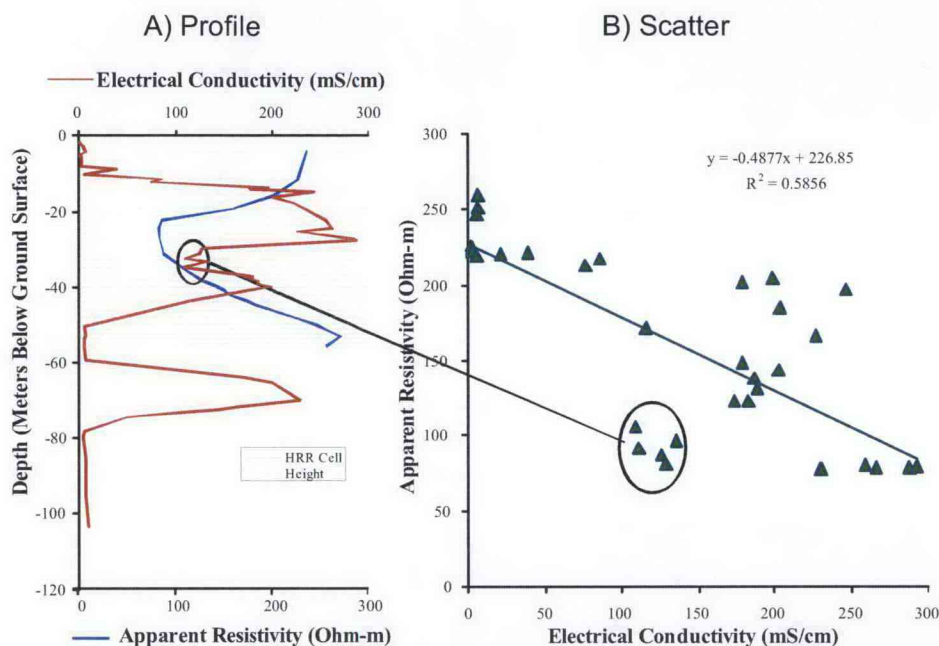
Figure 5.8. Profile and Scatter Plots for HRR and Pore-Water EC at Borehole C5923 (A)

The deepest HRR measurements show a slight decreasing trend in resistivity. The decrease could be the result of the high EC layer at 70 m depth. Unfortunately, the field resistivity data were not acquired deep enough to image this conductive layer. The plotting routine for HRR optimized the depth-plotting coefficients based on a target within the top 45 m. As will be shown later, the shallow depth limitation of the HRR plotting routine does not affect the capability of the 2D or 3D inversion models to image down to the water table.

The scaling issues of large volume (and volume averaging) measurements for HRR and small-volume measurements of pore-water EC prevent the creation of more complex petrophysical models that relate the two measurements. As an example of the scaling, cell boundaries for the HRR algorithm are shown as gray lines through the profile plot (see left hand graphic in Figure 5.8); the cells are much larger than the sampling domain for the geochemistry. Many geochemical samples could comprise one HRR reading. Based on this mismatch in scales between the two types of measurements, the HRR and geochemistry are related through simple linear regression. Other more complex petrophysical models include the Archie's Equation (Archie 1942) for clean sands and Waxman-Smits (Waxman and Smits 1968) for more complex shaley sands.

Figure 5.9 through Figure 5.11 show the vertical profile and scatter plots for the C5923 vadose zone pore-water ionic strength and nitrate and technetium-99 concentrations, respectively. The ionic strength is the most appropriate variable to use for comparison since it accounts for all ionic species. However,

the nitrate concentration appears to have the best correlation with the HRR data, with a R^2 value of 0.639. The technetium-99 concentration has the worst correlation with HRR data with a R^2 value of 0.54.
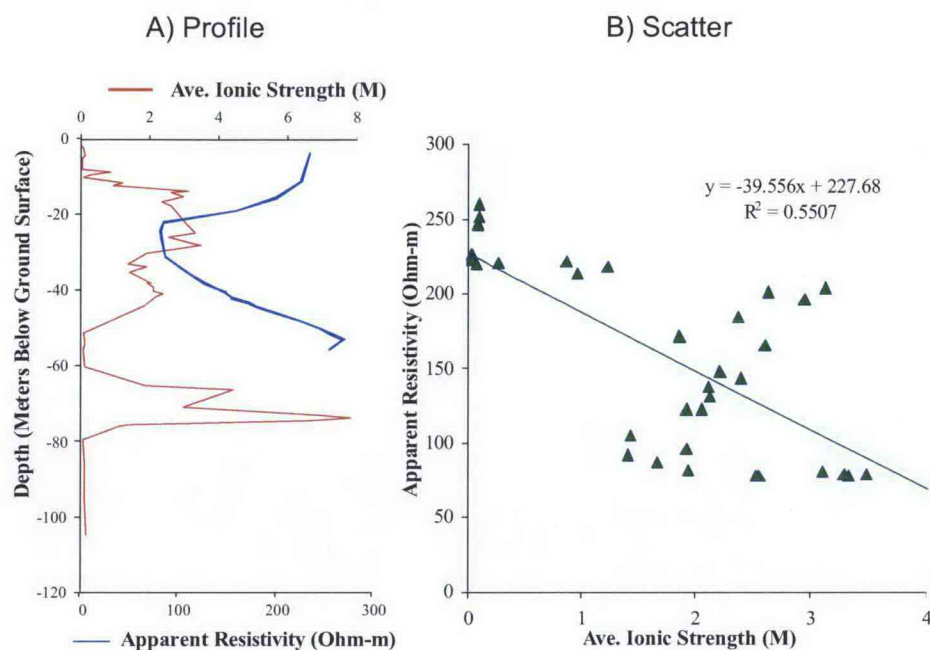
Figure 5.9. Profile and Scatter Plots for HRR and Ionic Strength at Borehole C5923 (A)
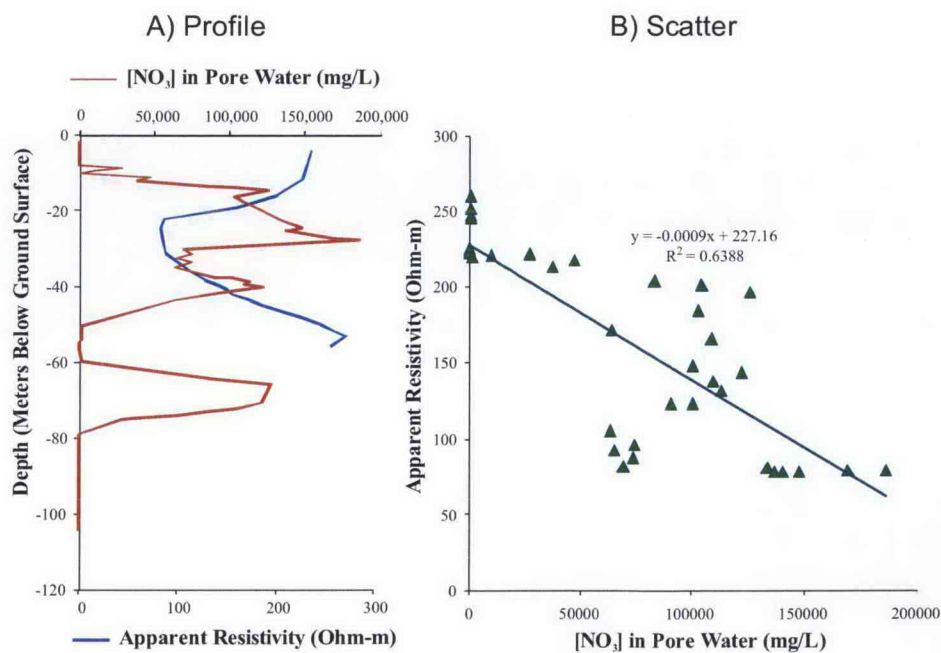
Figure 5.10. Profile and Scatter Plots for HRR and Nitrate Concentration at Borehole C5923 (A)
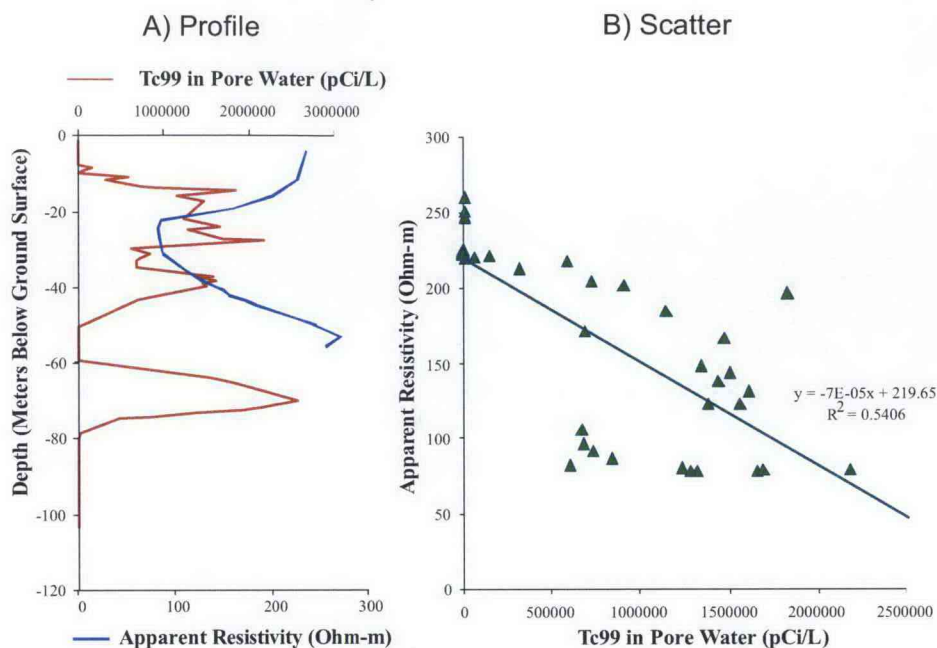
A) Profile   B) Scatter

Figure 5.11. Profile and Scatter Plots for HRR and Technetium-99 Concentration at Borehole C5923 (A)

5.2.2   2D Inversion at Borehole C5923 (A)

Figure 5.12 shows the inversion results for FY05-Line 4. For reference, features such as trench and crib locations are shown on the figure. The inversion was completed in three iterations using the smooth model inversion with a final root mean square error of 5.88%. At Borehole C5923 (A), the resistivity model shows a clear low-resistivity target at approximately 8 to 50 meters bgs (Figure 5.7). Above and below the target, resistivity increases, isolating the target. Variability can be seen in the target zone, as identified by the solid contour lines. Other low-resistivity features in the plot include the plume beneath Trench 216-B-20 and the deep anomaly between the trenches and cribs.
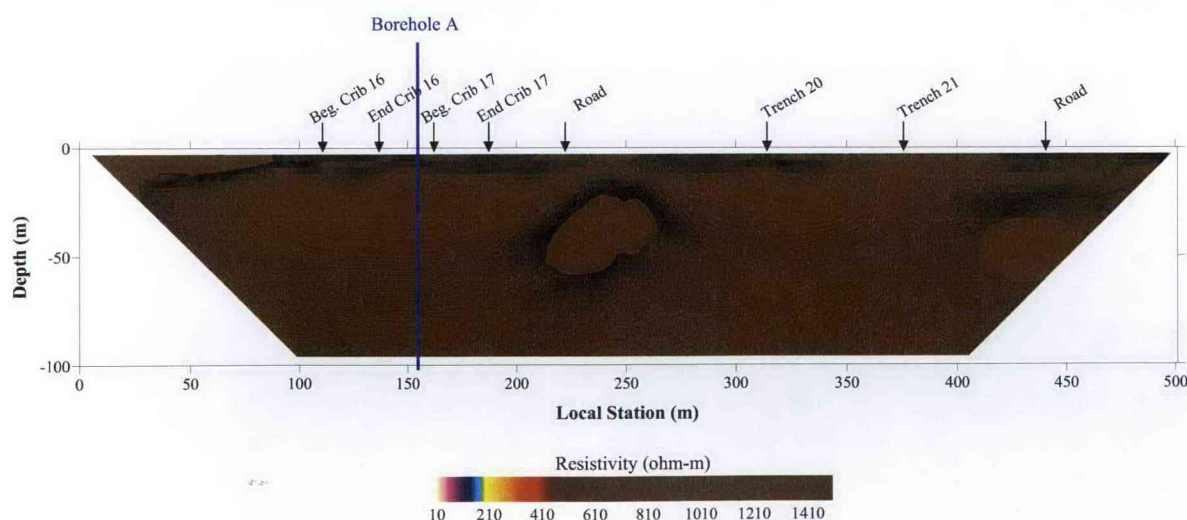
Figure 5.12. 2D Inversion Results of FY05-Line 4

5.33

The pore-water EC from Borehole C5923 (A) and 2D inverted-resistivity data were evaluated at co-located positions. The profile in Figure 5.13 shows that the resistivity begins to decrease at higher elevation than the geochemistry data, likely causing the poor match seen in the scatter plot on the right. The scatter plot was developed using two strategies. The first strategy used all the data to formulate a linear regression model and correlation coefficient (red regression line). The second, per Rucker and Fink (2007), used only those resistivity data that were sensitive to changing EC values (green regression line), which is the upper 50 m. Oldenburg and Li (1999) discussed the problem of sensitivity with depth using surface-based electrical resistivity. That is, the sensitivity of electrical resistivity in model cells deep in the section is much lower than the sensitivity of resistivity in cells closer to the surface. Therefore, preferentially picking the region that is most sensitive for correlation analysis shows how the electrical-resistivity data could be used for estimating geochemical parameters in the very near surface. Conversely, it demonstrates the low reliability of very deep resistivity measurements acquired below a low-resistivity anomaly. The focus of the upper 50 m for the sensitive region also allows a comparison with the HRR regression values.
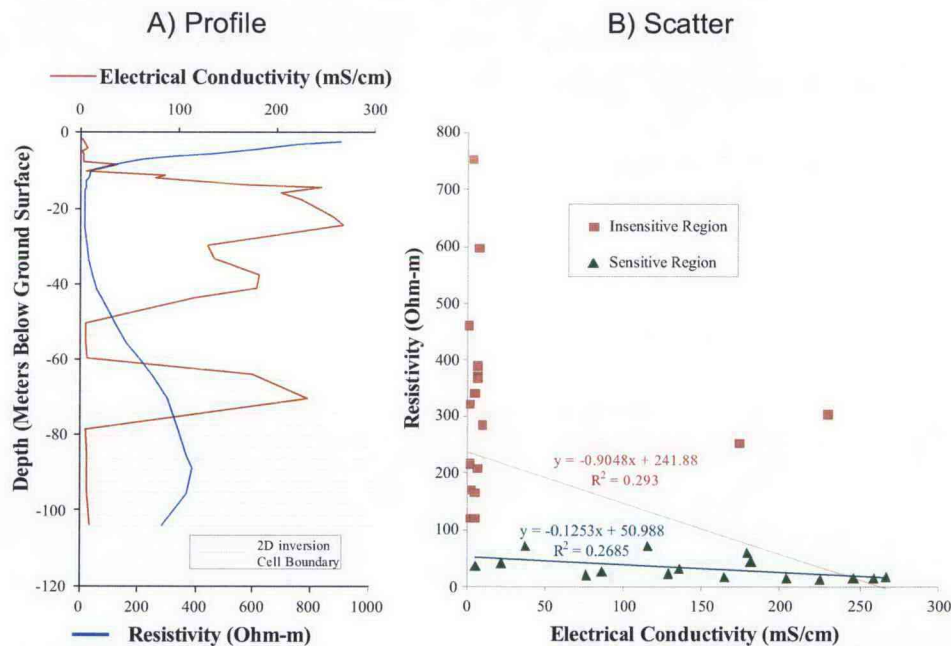
Figure 5.13. Profile and Scatter Plots for 2D Inversion and Pore-Water EC at Borehole C5923 (A)

In general, the regression of Figure 5.14 shows a poor fit due to 1) the high scatter and the insensitivity of the soil resistivity to the small-scale variability in pore-water EC and 2) the elevation mismatch of the targets. The issue of small-scale variability could be minimized by acquiring a lower number of samples in the borehole or averaging the borehole data over the cell volume of the electrical-resistivity model cell. As an example of model cell size, the profile within Figure 5.14 shows the cell boundaries used in the inversion model. When the EC is averaged over the 2D inversion model cell domain, which reduces the data count from 58 to 28, the correlation coefficient increases from 0.269 to 0.340 for the most sensitive region (upper 50 m).

The issue of elevation accuracy for target identification in resistivity inversion results has been identified by several authors. Zhou et al. (2000) showed that estimated depths to the top of sink holes from inversion results ranged in error between 0 and 10 m, with an average depth error of 2.4 m. The differences in target elevation interpreted from boreholes and surface soil electrical resistivity may be due to out-of-plane effects (Bentley and Gharibi 2004) or to constraints imposed during the inversion to obtain a "unique" solution. For the BC Cribs and Trenches problem, a portion of the low-resistivity zone may be at a higher elevation adjacent to FY05-Line 4, causing the out-of-plane effects and an apparent upward shift in the modeled position of the low-resistivity zone on FY05-Line 4. Constraints used in the inversion program to obtain unique solutions (such as smoothness) could also cause a mismatch in target location. As shown in Figure 5.15, a 3.4-m downward shift of the model results improves the correlation with Borehole C5923 (A) geochemistry data and accounts for possible out-of-plane effects. The correlation coefficient increases for the most sensitive measurements from 0.214 to 0.514 due to the 3.4 m downward shift.

Another large elevation mismatch occurs with the high EC layer at 70 m. The HRR plot (see, for example, Figure 5.6) shows the decreasing resistivity trend to begin at about 50 m and the inversion model places it at approximately 90 m. This elevation mismatch is causing the large scatter in the regression analysis, decreasing the goodness of fit for all data (in red).
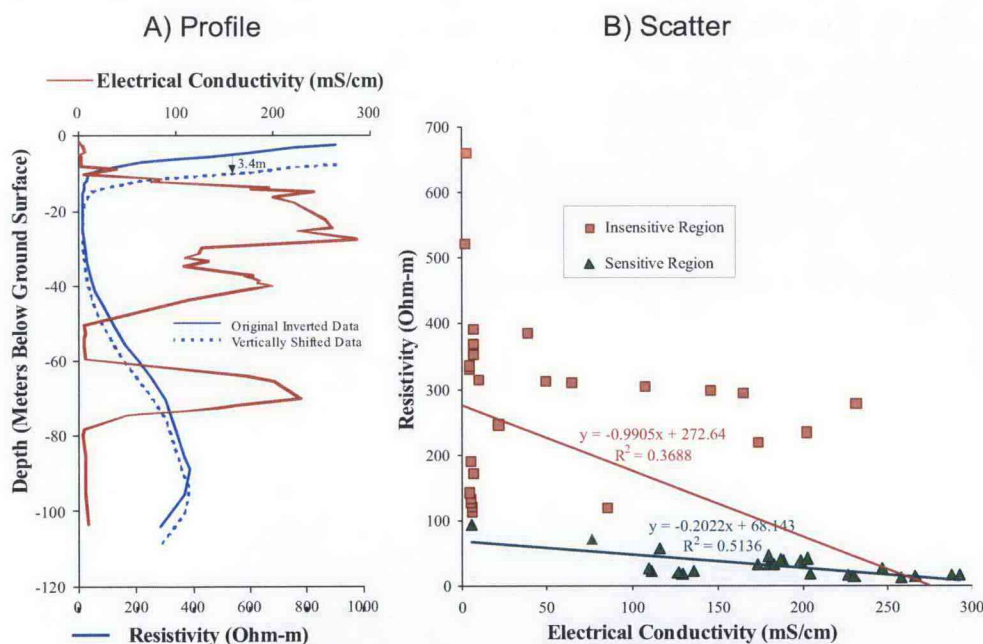
Figure 5.14. Profile and Scatter Plots for 2D Inversion and Pore-Water EC at Borehole C5923 (A), with Inversion Elevations Shifted by 3.4 m

Figure 5.16 shows the linear regression correlations between the 2D model data and borehole data of ionic strength, nitrate concentration, and technetium-99 concentration. The scatter plot was created with data after a shift in elevation of 3.4 m (deeper). Again, the technetium-99 shows the worst correlation, and the EC regression of Figure 5.15 demonstrates the best correlation with 2D inverted resistivity.

5.2.3   3D Inversion at Borehole C5923 (A)

The 3D inversion results for model domain 3 (see Figure 4.13 for model domains) are shown in Figure 5.17. The figure is focused on the vicinity near Borehole C5923 (A) by showing vertical slices of contoured soil resistivity values. The figure shows a low-resistivity anomaly beneath all of the cribs, with the profile of extracted data shown in Figure 5.7. Compared to the HRR and 2D inversion, the 3D inversion shows the elevation of the target to be the deepest.

The regression and profile data for EC in Borehole C5923 (A) and 3D inversion results are shown in Figure 5.18. The profile data show that the target in the original inversion results at Borehole C5923 (A) does not match well to the geochemistry target. The inversion results indicate that the target is deeper than the geochemistry. To account for the apparent offset, the 3D inverted-resistivity data were shifted by 5 m upwards to match target depths with geochemistry.

The scatter and regression in Figure 5.18B shows a poor goodness of fit when considering all data. The data, however, appear to be of two populations that include a shallow and deep set. Separate regression analyses were run on these individual populations, and the shallow data alone appear to have a much better correlation. The shallow data are those with a depth of 0 to 50 m bgs. When the resistivity data are shifted by 5 m upwards, the correlation is even better, as demonstrated in Figure 5.18C. Considering that the 3D inversion accounts for out-of-plane effects, the apparent shift in resistivity data relative to borehole geochemistry can only be explained by the numeric implementation of the mathematics and the use of smoothing and dampening constraints.
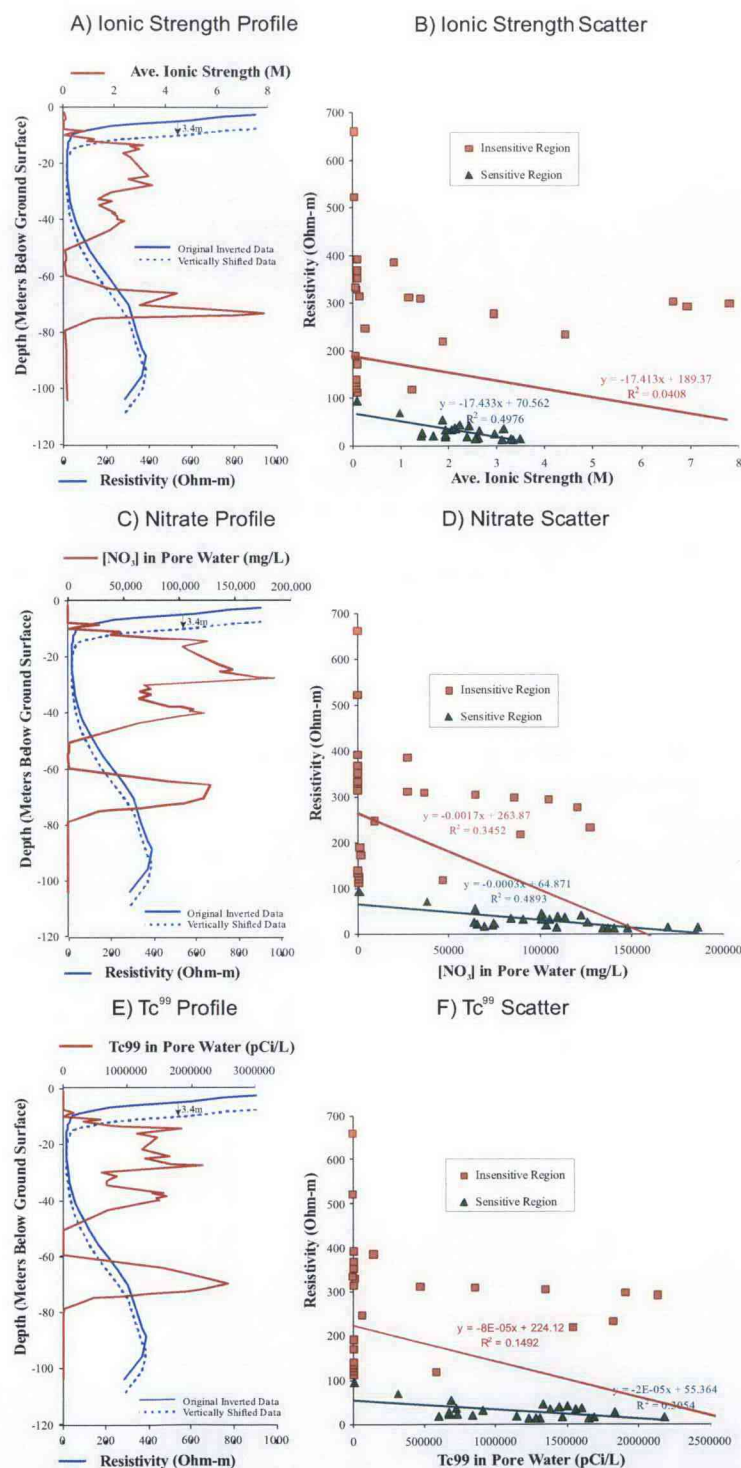
Figure 5.15. Profile and Scatter Plots of Geochemistry Data and 2D Inversion Results for Borehole C5923 (A), Including Ionic Strength, Nitrate Concentration, and Technetium-99 Concentration
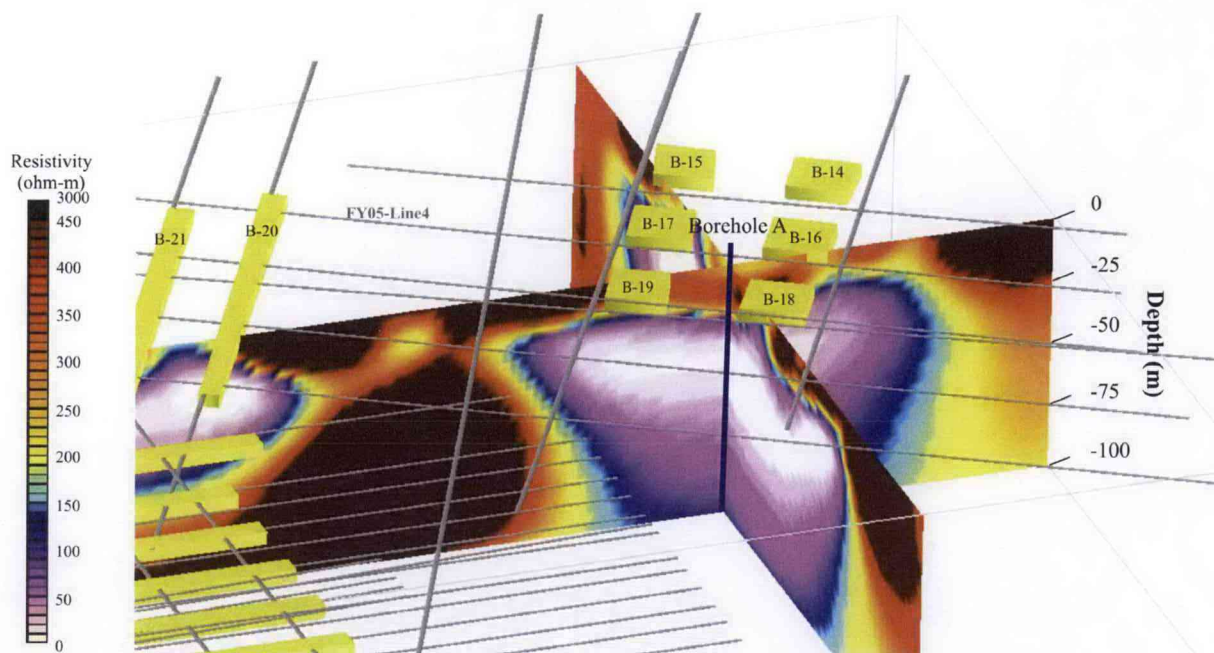
Figure 5.16. 3D Inversion Results of Model Domain 3 of the BC Cribs Site

Figure 5.18 shows the profile and scatter with regression for borehole C5923 vadose zone pore-water ionic strength, nitrate, and technetium-99 concentrations. The scatter plots were created with data after a shift of 5 m (upward) in elevation. Unexpectedly, the ionic strength shows the worst correlation, whereas the nitrate concentration shows the best correlation with 3D inverted resistivity.

A) Profile

B) Scatter

C) Scatter of Shifted Data
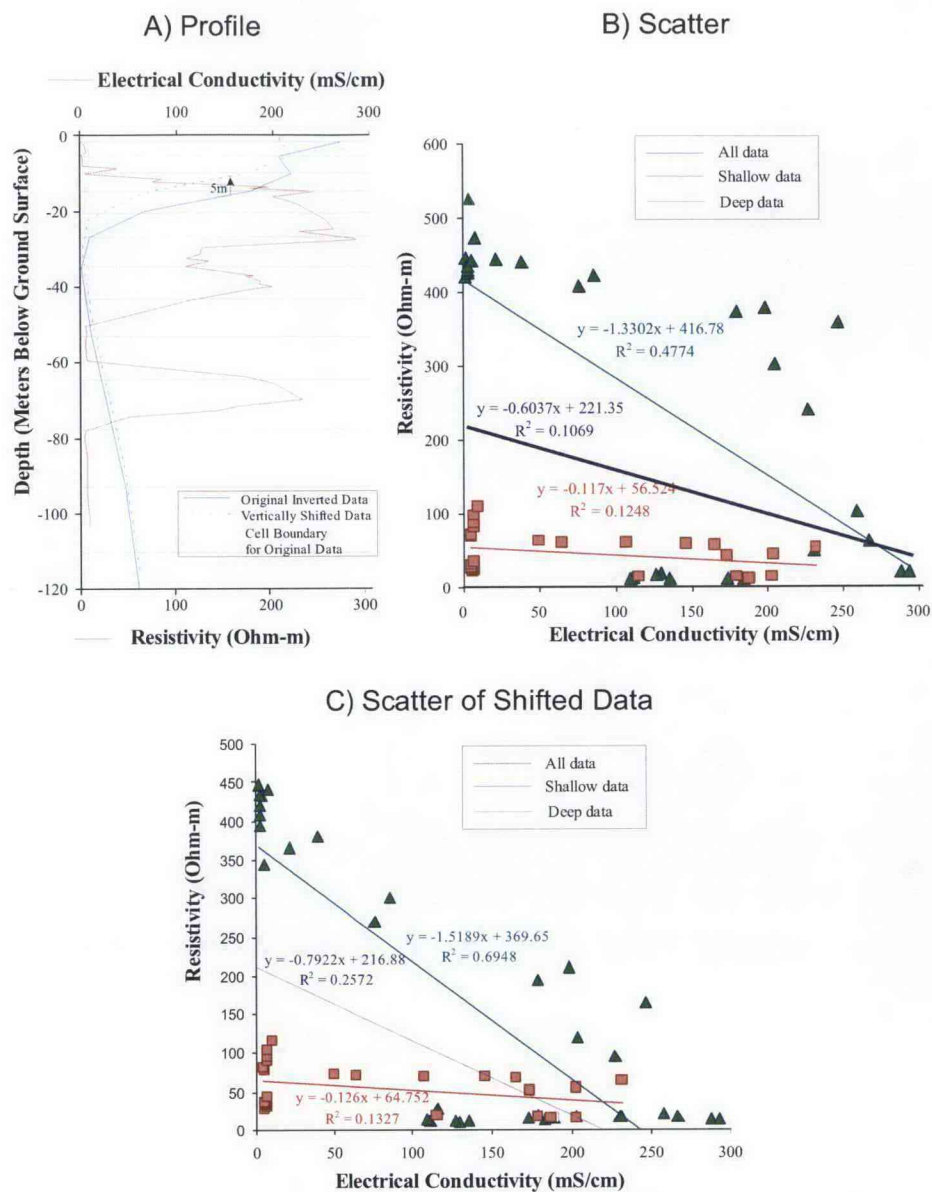
Figure 5.17. Profile and Scatter Plots for 3D Inversion and Pore-Water EC at Borehole C5923 (A)

A) Profile data with and without 5-m shift in resistivity elevation, B) scatter and regression of deep, shallow, and all data with no shift in resistivity, C) scatter and regression of deep, shallow, and all data with 5-m elevation shift in resistivity.
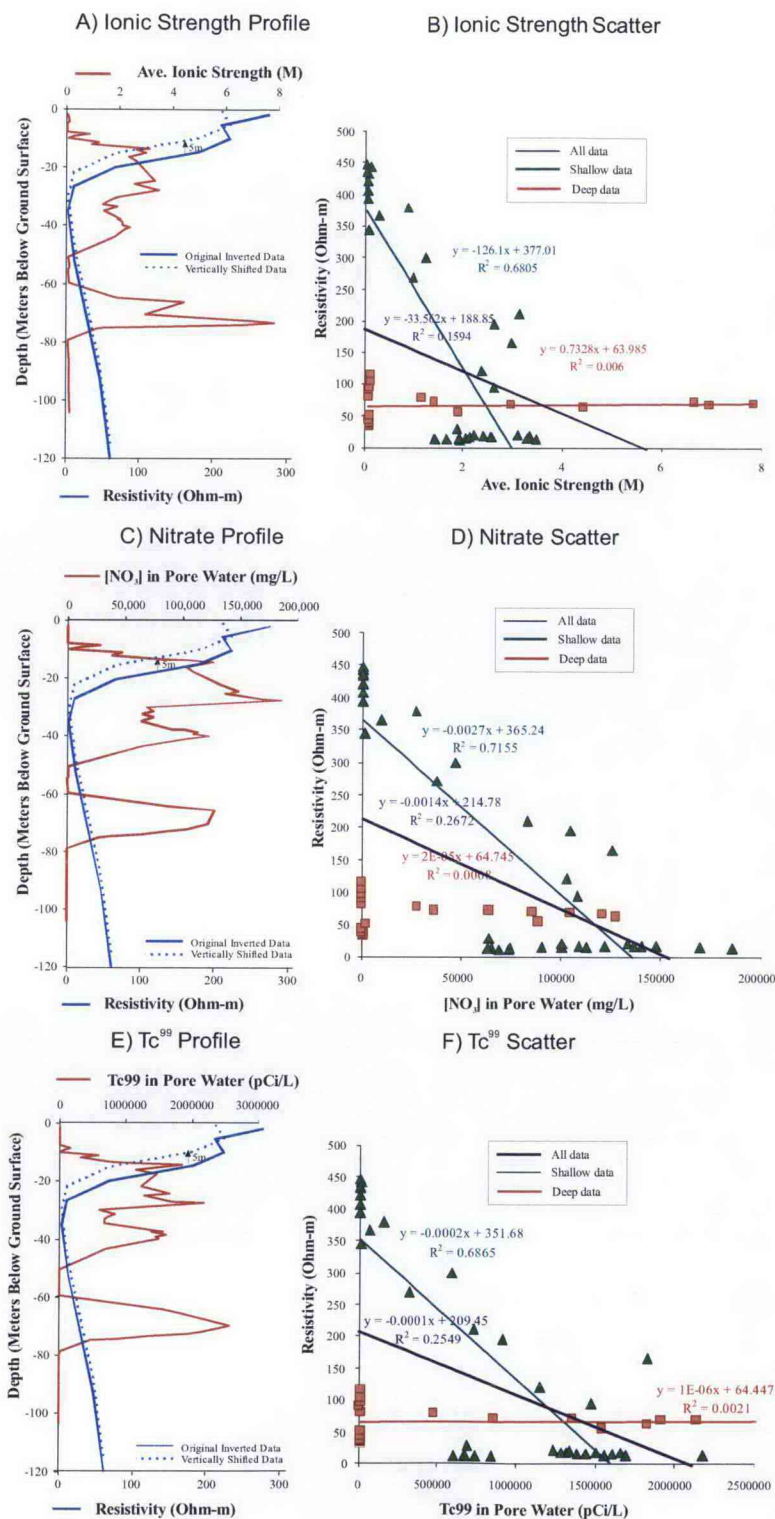
Figure 5.18. Profile and Scatter Plots of Geochemistry Data and 3D Inversion Results for Borehole C5923 (A), Including Ionic Strength, Nitrate Concentration, and Technetium-99 Concentration

5.3 Laboratory Geophysical Results at Borehole A (C5923)

5.3.1 Laboratory Measured Geo-Hydrological Parameters

5.3.1.1 Particle Size Distribution of Sediments in Borehole C5923 (A)

Particle-size data for 20 selected grab samples were converted into size-fraction percent by weight, and the percent by weight passing each sieve was plotted as a curve on a semi-logarithmic scale to describe the C5923 vadose zone sediment size distribution for selected depths. The resulting data represent the percentage of particles retained and passing through each sieve. Laser particle-size analyses were used to characterize the < #230 fraction and to quantify silt and clay content. The percentage of each size fraction was used to determine texture according to the USDA classification and the Unified Soil Classification System (USCS) specified by ASTM D 2487 (ASTM 2000). The particle-size moments of the distributions, a range of cumulative percentile values (the grain size at which a specified percentage of the grains are coarser, e.g., d_{16}, d_{50}, d_{85}) and the related coefficients, e.g., coefficient of uniformity, C_u, and coefficient of curvature, C_c, c, were calculated from the grain-size distributions using the methods described by Folk (1980). In order to compare different sediments, grain-size distributions are often described by their deviation from a prescribed ideal distribution. Geometric scaling is usually employed to place equal emphasis on small differences in fine particles and larger differences in coarse particles. The logarithmic Udden–Wentworth grade scale (Udden 1914; Wentworth 1922) in which the boundaries between successive size classes differ by a factor of two is most often used.

Figure 5.19 is a plot of the size-distribution curves for 20 grab samples that were analyzed. Particle-size analysis of Borehole C5923 (A) samples yielded USDA textures ranging from sand to silt loam (Table 5.15). The clay content ranged from less than 1% to 12%. The silt content ranged from 2% to 11%, whereas the sand content ranged from 38% to 94%. The coarse fraction ranged from 0 to 50% whereas the percentage of fines (< #230 sieve) ranged from 3.4 to 17%. A dry sieving approach, rather than wet sieving, was adopted to minimize waste generation. However, dry sieving is known to cause an over estimation of the coarse fraction, especially in sediments with high-fines content, as the fines can aggregate into sand and fine pebble-sized particles. Nevertheless, using LDS to characterize the < #230 (< 63 µm) fraction produced data of very high quality that showed good continuity with dry-sieve measurements. The < 63 µm content ranged from 3.45 to 20.56 percent with a mean of 10.34 percent.

The particle-size data were used to calculate parameters that will be used for establishing correlations with physicochemical and hydrophysical properties. Figure 5.20 shows a plot of effective particle diameter, d_e, as a function of textural components, including mud (silt plus clay) mass fraction. The effective diameter is derived from the d_{10} value. The relationship to mud content is important as dry sieving typically does not separate silt and clay portions, but quantifies only their sum. As can be expected, the effective diameter decreases with increasing clay content. The same is true for silt, although the relationship is not as strong. The effective diameter increases exponentially with sand content. The relationship to mud content is also quite strong, especially if the two high-silt outliers are removed.

PSDs, particularly of sands and silts, have considerable practical value. Both theory and experiments have shown that permeability (air and water), surface area, and surface electrical conductance are strongly related to the effective particle diameter. These data are needed to develop constitutive properties for fate

and transport models, which are needed to design appropriate remedies and for translating resistivity measurements into data that can be used to initialize such models.

Table 5.15. Textural Composition and Particle-Size Statistics for Borehole C5923 (A) Samples

HEIS	Depth (ft)	USCS Texture	USDA Classification				USCS Classification				D_5	D_{10}	D_{16}	D_{30}	D_{50}	D_{60}	D_{75}	D_{84}	D_{95}	Effective Grain Diameter (mm)	Geometric Mean Diameter (mm)	Sorting Index	C_c	C_u
			% Clay	% Silt	% Sand	% Gravel	% Clay	% Silt	% Sand	% Gravel														
BIT741	8.0	Silty sand	2.05	7.81	78.59	11.54	2.88	10.37	82.78	3.96	0.016	0.051	0.096	0.208	0.421	0.579	0.985	1.505	3.966	0.078	0.627	0.185	1.470	11.343
BIT743	13.0	Poorly graded sand	1.13	2.09	93.96	2.83	1.41	2.55	95.93	0.10	0.110	0.254	0.374	0.557	0.755	0.855	1.044	1.217	1.713	0.206	0.582	0.368	1.431	3.367
BIT744	15.5	Silty sand	3.93	11.35	76.88	7.84	5.26	14.49	77.68	2.56	0.004	0.023	0.054	0.138	0.299	0.418	0.718	1.098	2.855	0.058	0.715	0.165	1.967	17.958
BIT752	45.5	Silty sand	1.66	10.15	83.65	4.53	2.50	14.68	81.50	1.31	0.017	0.041	0.070	0.135	0.250	0.331	0.532	0.779	1.866	0.074	0.776	0.219	1.331	8.005
BIT753	48.0	Poorly-graded sand w/ silt	1.31	4.62	92.28	1.79	1.79	6.48	91.50	0.23	0.039	0.092	0.142	0.235	0.359	0.433	0.587	0.746	1.283	0.098	0.750	0.308	1.388	4.708
BIT754	50.5	Poorly graded sand	0.96	2.74	93.41	2.89	1.27	3.63	94.82	0.27	0.077	0.163	0.239	0.371	0.538	0.632	0.825	1.016	1.626	0.134	0.661	0.333	1.339	3.885
BIT763	73.0	Well-graded sand w/ silt	2.60	5.12	90.35	1.94	3.27	6.45	90.10	0.19	0.019	0.079	0.148	0.277	0.434	0.521	0.693	0.862	1.396	0.104	0.716	0.304	1.873	6.634
BIT771	98.0	Silty sand	2.00	8.55	89.19	0.26	2.76	13.04	84.18	0.03	0.018	0.047	0.076	0.128	0.193	0.231	0.307	0.384	0.633	0.067	0.860	0.315	1.497	4.899
BIT9L5	134.3	Silty sand	1.73	7.88	90.39	0.00	2.32	14.91	82.76	0.00	0.024	0.052	0.072	0.098	0.120	0.130	0.148	0.163	0.200	0.141	0.921	0.412	1.413	2.522
BIT778	135.5	Poorly-graded sand w/silt	1.04	5.80	92.39	0.78	1.50	9.08	89.32	0.10	0.036	0.071	0.104	0.165	0.248	0.298	0.404	0.514	0.891	0.239	0.818	0.314	1.282	4.174
BIT779	138.0	Silty sand	3.33	6.84	88.71	1.12	4.20	8.79	86.90	0.12	0.009	0.049	0.101	0.202	0.328	0.398	0.538	0.675	1.116	0.063	0.775	0.290	2.108	8.199
BIT781	143.0	Silty sand	2.21	9.42	88.36	0.01	3.00	15.57	81.43	0.00	0.016	0.043	0.067	0.104	0.144	0.165	0.203	0.238	0.338	0.053	0.902	0.358	1.548	3.863
BIT789	163.0	Silty sand	3.68	6.13	89.12	1.07	4.53	7.59	87.81	0.08	0.007	0.052	0.116	0.240	0.385	0.461	0.607	0.746	1.169	0.337	0.750	0.299	2.407	8.856
BIT790	165.5	Silty sand	4.05	9.50	86.34	0.12	5.13	13.06	81.80	0.01	0.005	0.029	0.064	0.127	0.200	0.238	0.310	0.378	0.583	0.045	0.862	0.307	2.312	8.082
BIT7B4	210.5	Silty sand	2.34	8.05	89.18	0.42	3.14	11.63	85.18	0.05	0.015	0.048	0.081	0.143	0.223	0.267	0.359	0.451	0.751	0.069	0.840	0.306	1.617	5.623
BIT7B6	215.5	Silty sand	1.03	10.36	88.16	0.44	1.63	17.85	80.45	0.07	0.024	0.045	0.065	0.103	0.158	0.192	0.266	0.346	0.631	0.190	0.877	0.304	1.231	4.266
BIT7C2	230.5	Silty sand	5.72	8.62	85.05	0.61	6.92	10.67	82.36	0.05	0.001	0.020	0.063	0.164	0.287	0.351	0.473	0.589	0.941	0.038	0.805	0.267	3.926	17.976
BIT7C9	258.0	Silty sand w/gravel	1.99	7.98	65.15	24.60	2.89	10.14	74.40	12.30	0.016	0.050	0.102	0.258	0.636	0.970	1.986	3.548	13.518	0.070	0.372	0.110	1.372	19.315
BIT7D8	280.5	Silty sand w/gravel	6.75	4.69	38.70	49.87	7.63	4.91	67.46	19.99	0.000	0.026	0.185	0.862	1.992	2.661	4.054	5.492	10.480	0.037	0.170	0.165	10.803	102.831
BIT7F2	290.5	Silty sand	2.78	7.54	79.20	10.47	3.69	9.63	83.54	3.13	0.011	0.047	0.098	0.223	0.444	0.599	0.979	1.438	3.427	0.063	0.633	0.196	1.751	12.640
BIT7H2	315.5	Silty sand	2.55	5.62	65.70	26.08	3.31	6.80	79.39	10.44	0.016	0.073	0.160	0.395	0.855	1.200	2.097	3.257	8.829	0.085	0.373	0.163	1.770	16.338
BIT7H7	328.0	Silty sand	11.95	4.65	38.35	45.06	12.89	4.71	79.83	2.57	0.000	0.000	0.038	0.734	1.799	2.193	2.759	3.178	4.164	0.026	0.314	0.169	1685.761	15055.760
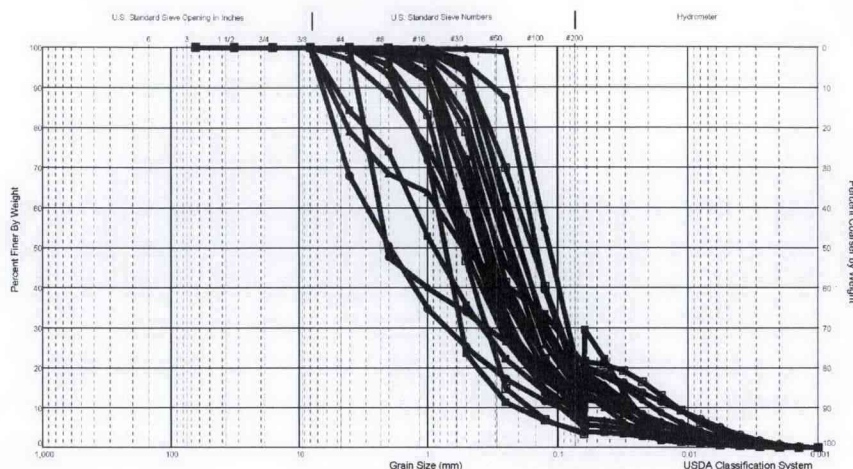
Figure 5.19. PSD Curves from Borehole C5923 (A) Showing Range of Textures
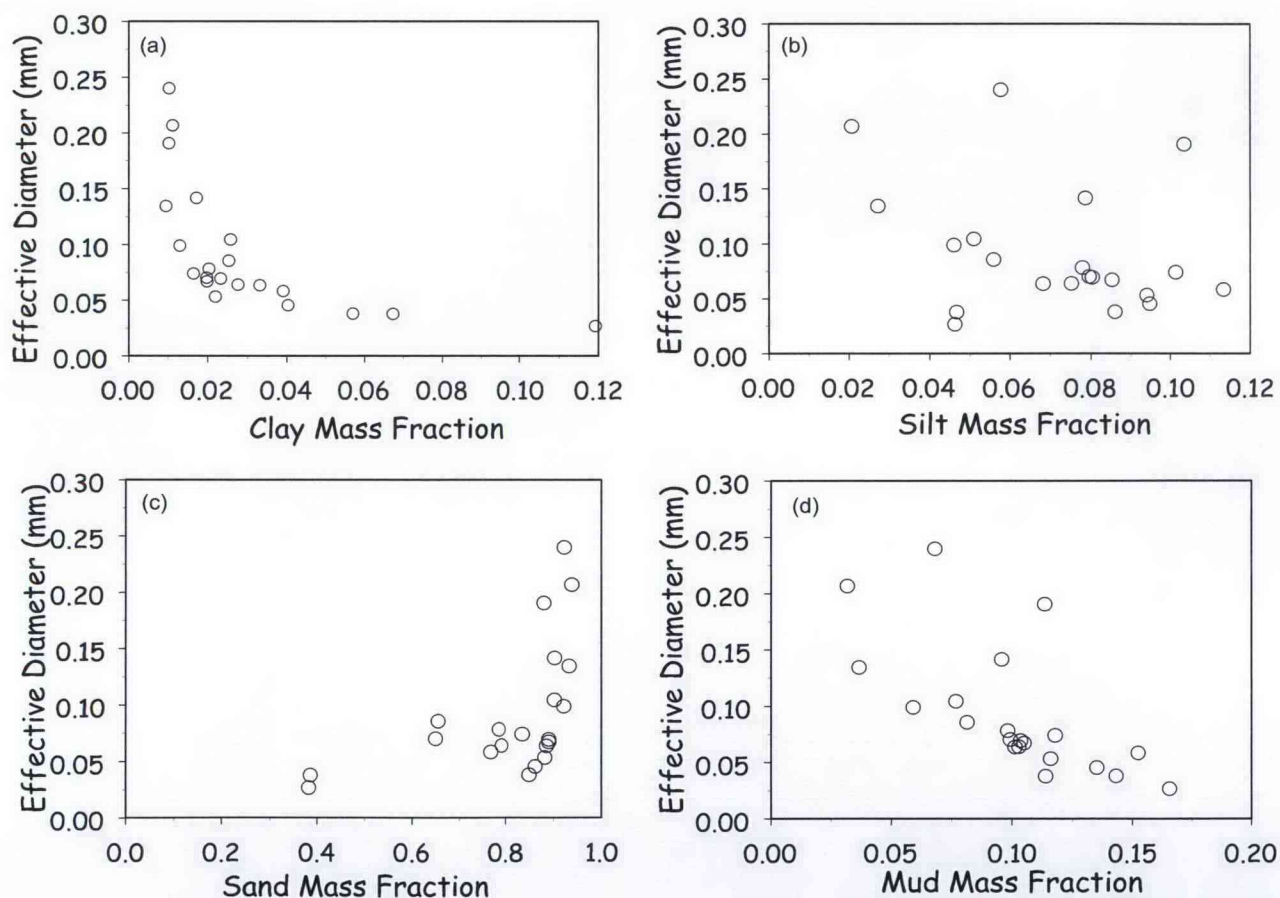
Figure 5.20. The Dependence of Effective Particle Diameter on Textural Components, (a) Clay Content, (b) Silt Content, (c) Sand Content, and (d) Mud Content (fraction passing the #230 sieve consisting of silt and clay)

5.3.1.2   Particle-Size Distribution of Sediments in Borehole C5924 (B)

Owing to the level of contaminants in Borehole C5923 (A), efforts to further characterize the grain-size distributions were focused on Borehole C5923 (B). In these analyses, 12 samples were separated into size fractions based on the logarithmic Udden–Wentworth grade scale (Udden 1914; Wentworth 1922). The mass of soil retained in each sieve was used to calculate the class weight in each particle-size class. The sediments passing the #230 siver were used to calculate the content of fines. Figure 5.21 shows a histogram of the geometric grain size of the sediments from borehole C5924 (B), and Table 5.16 shows the grain-size frequency for these samples. The fines content (passing the #230 sieve) ranged from 1.39 to 10.83 percent with a mean of 5.04 percent. These sediments were considerably coarser than those from Borehole 5923 (A) where fines content rangeD from 3.45 to 20.56 percent with a mean of 10.34 percent. The mode of the PSDs for C5924 (B) occur at the #60 and #120 sieve sizes except for sample B1T7D8 for which the mode occurs at the #10 sieve size. Characterization of these size classes using gamma energy analysis to measure the natural potassium-40, uranium, and thorium forms the basis for estimating grain-size distributions from borehole gamma logs that is further discussed in Section 5.3.2.5.
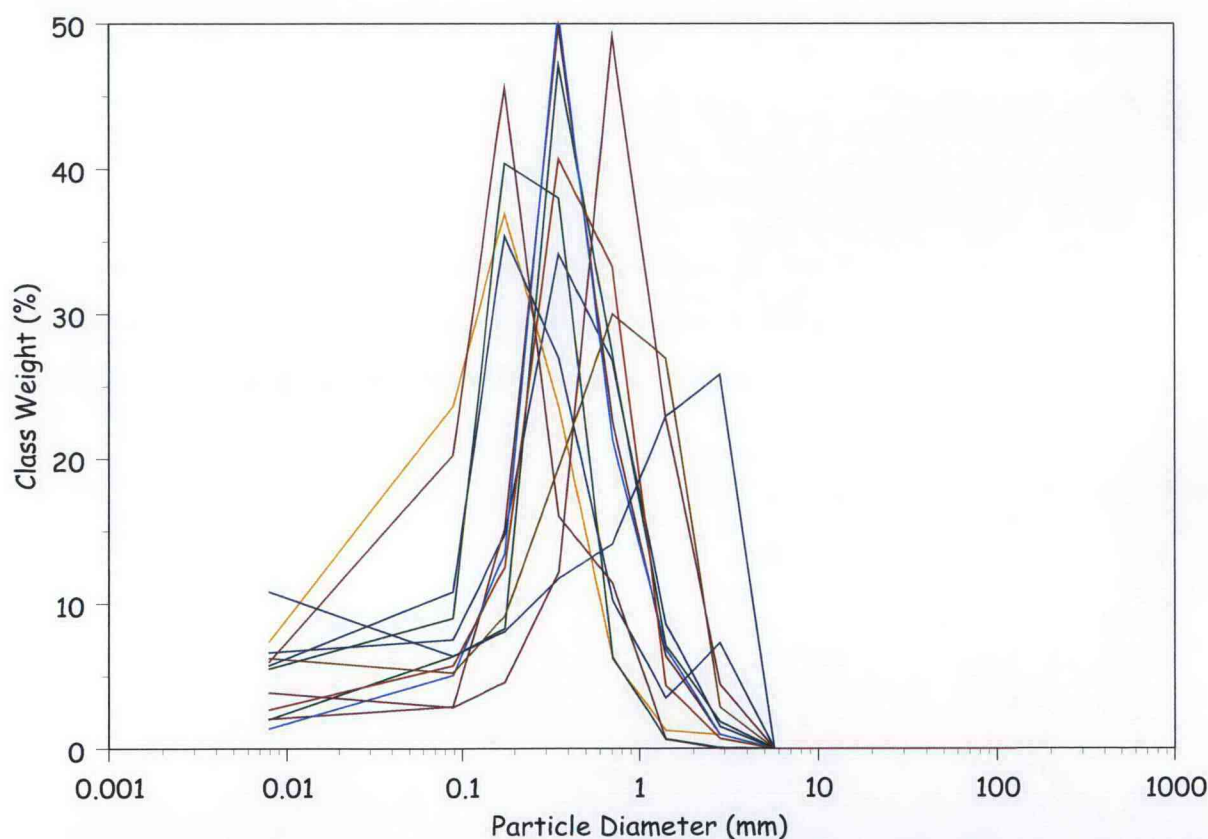
Figure 5.21.   Grain-Size Frequency Histograms for Sediments from Borehole 5924 (B), Analyzed by Dry Sieving and Laser Granulometery. Grain diameter is plotted as a geometric size scale.

Table 5.16. Grain Size Frequency for Borehole C5924 (B) Analyzed by Sieving and Laser Diffraction (> #230)

Size Terms		d_g (mm)	Sieve Size	Class Weight (gm)											
				BIT6D9	BIT6F0	BIT6F4	BIT6F6	BIT6F7	BIT6H1	BIT6H2	BIT6H5	BIT6H6	BIT6J0	BIT7D8	BIT743
Gravel	Cobble	128.000	2-1/2"	0.00	0.00	0.00	0.00	0.00	0.00	0.00	0.00	0.00	0.00	0.00	0.00
	very coarse	45.255	1-1/4"	0.00	0.00	0.00	0.00	0.00	0.00	0.00	0.00	0.00	0.00	0.00	0.00
	Coarse	22.627	5/8"	0.00	0.00	0.00	0.00	0.00	0.00	0.00	0.00	0.00	0.00	0.00	0.00
	Medium	11.314	5/16"	0.00	0.00	0.00	0.00	0.00	0.00	0.00	0.00	0.00	0.00	0.00	0.00
	Fine	5.657	#5	0.00	0.00	0.00	0.00	0.00	0.00	0.00	0.00	0.00	0.00	0.00	0.00
	very fine	2.828	#10	1.52	0.96	1.86	0.97	0.96	2.86	0.70	7.31	0.00	0.07	25.84	4.44
Sand	very coarse	1.414	#18	8.61	6.40	7.13	1.27	6.87	26.97	4.35	3.50	0.65	0.66	22.94	22.83
	Coarse	0.707	#35	26.76	22.64	27.19	6.20	21.38	30.03	33.27	10.26	11.43	6.33	14.15	49.18
	Medium	0.354	#60	34.15	49.83	47.15	23.61	50.88	19.47	40.70	26.97	16.05	38.03	11.77	12.22
	Fine	0.177	#120	14.79	15.19	8.29	36.92	13.45	9.17	12.53	35.39	45.58	40.40	8.09	4.58
	very fine	0.088	#230	7.53	2.91	6.37	23.62	5.06	5.25	5.74	10.83	20.25	9.00	6.39	2.87
Mud		0.008	<#230	6.64	2.07	2.03	7.42	1.39	6.25	2.70	5.75	6.03	5.52	10.83	3.87

5.3.1.3 Porosity and Bulk Density of Intact Cores from Borehole C5923 (A)

Dry-bulk densities were determined by oven drying the core samples following completion of the saturated hydraulic conductivity. Sediments were dried for 24 hrs at 105°C, and the dry weight was determined. A summary of measured dry-bulk densities of complementary porosity estimates on core samples from Borehole C5923 (A) is presented in Table 5.17.

Table 5.17. Summary of Hydro-Physical Properties for Core Samples from Borehole C5923 (A)

HEIS	Z_{top} (ft)	Z_{bot} (ft)	Z_{mid} (ft)	Core Wet Wt. (gm)	Core Dry Wt. (gm)	Dry Bulk Density (gm/cm³)	Porosity (cm³/cm³)	Saturated Water Content (cm³/cm³)
B1T7J3-2	38.0	38.5	38.25	2071.90	1583.17	1.481	0.4535	0.3978
B1T7J4-2	38.5	39.0	38.75	2349.80	1695.10	1.586	0.4149	0.3648
B1T7J5-2	41.0	41.5	41.25	2271.10	2111.42	1.975	0.2712	0.2178
B1T7J6-2	43.5	44.0	43.75	2349.30	1754.69	1.641	0.3943	0.3015
B1T7J7-2	86.0	86.5	86.25	2123.90	1596.06	1.542	0.4310	0.3078
B1T7J8-2	88.5	89.0	88.75	2168.50	1708.79	1.598	0.4102	0.3275
B1T7J9-2	106.0	106.5	106.25	2058.00	1698.44	1.677	0.3810	0.3009
B1T7K0-2	108.5	109.0	108.75	2265.40	1643.53	1.623	0.4010	0.3095
B1T7K1-2	126.0	126.5	126.25	1933.00	1730.64	1.877	0.3073	0.2199
B1T7K2-2	129.0	129.5	129.25	2240.00	1702.91	1.781	0.3426	0.2393
B1T7K3-2	131.0	131.5	131.25	2155.70	1770.71	1.711	0.3688	0.2787
B1T7K4-2	133.5	134.0	133.75	2195.30	1874.67	1.754	0.3529	0.2710
B1T7K5-2	176.0	176.5	176.25	2018.50	1738.29	1.736	0.3593	0.2781
B1T7K6-2	178.5	179.0	178.75	1904.50	1746.73	1.706	0.3704	0.3060
B1T7K7-2	181.0	181.5	181.25	2188.00	1988.70	1.900	0.2987	0.2196
B1T7K8-2	183.5	184.0	183.75	2330.00	1583.17	1.481	0.4535	0.3978
B1T7K9-2	236.0	236.5	236.25	2267.90	1695.10	1.586	0.4149	0.3648
B1T7L0-2	238.5	239.0	238.75	2263.90	2111.42	1.975	0.2712	0.2178
B1T7L1-2	241.0	241.5	241.25	2196.40	1754.69	1.641	0.3943	0.3015
B1T7L2-3	243.0	243.5	243.25	2243.80	1596.06	1.542	0.4310	0.3078

Dry bulk density, ρ_b, is used to establish the density-volume relationship of soils and sediments, especially porosity. The mean and standard error derived from Borehole C5923 (A) samples shown in Table 5.17 was 1.71 ± 0.035 Mg/m³. This result is slightly higher than the typical 1.5 to 1.6 Mg/m³ observed in Hanford formation sediments and may be a reflection of drilling techniques and handling of the samples after collection. Soil compaction can have a strong impact on porosity, permeability to air and water, and electrical properties.

Particle density, ρ_s, is also widely use for establishing the density-volume relationship of soils. It is typically used in the calculation of porosity. Measurements of ρ_s were made on the < 2 mm fraction of six samples from Borehole C5924 (B) using the pycnometer method (Blake and Hartge 1986a; ASTM 2006c). These measurements gave a mean and standard error of 2.72 ± 0.007 Mg/m³. A ρ_s > 2.65 Mg/m³ for Hanford sediments is not surprising. The widely used value of 2.65 Mg/m³ corresponds to the specific gravity of quartz. However, many silicate and nonsilicate minerals present in Hanford sediments, such as feldspars, micas, and kaolinite, exhibit densities ranging from 2.3 to 3.0 Mg/m³ whereas the density of

iron-containing minerals like hematite and goethite, also present in Hanford sediments, often exceeds 3.3 Mg/m^3. The particle density of a bulk soil is therefore a weighted average that depends on mineral composition and is calculated using a mass weighted mean of all the particles.

Porosity (ϕ) is the volume of voids in a sample (the air- and liquid-filled volume) divided by the total volume of the sample and was calculated from the bulk density and particle density as $\phi = 1 - \rho_b / \rho_s$. The particle density for a given parent material is generally invariant in space, so changes in the porosity are typically due to changes in ρ_b. Estimates of porosity derived from bulk density and particle density measurements ranged from 0.2710 to 0.4535 m^3/m^3 with a mean and standard error of 0.3705 ± 0.013 m^3/m^3. These values are consistent with what can be expected for fine- to coarse-sands of the Hanford formation. Saturated water contents ranged from 0.2178 to 0.3978 m^3/m^3 with a mean and standard error of 0.2983 ± 0.0135 m^3/m^3. Although the saturated water content is often assumed to be equivalent to the porosity, the results for the C5923 (A) cores show significant differences between the calculated total porosity and measured saturated water content. The difference between porosity and saturated water content is typically attributed to air entrapment. Although there are few published reports for Hanford sediments, a value of 10 to 15% is commonly reported in the literature. Table 5.17 shows differences between porosity and saturated water contents ranging from 0.05 to 0.1233 m^3/m^3 with a mean and standard error of 0.08 ± 0.005 m^3/m^3.

5.3.1.4 Specific Surface Area of Vadose Sediments from Borehole C5923 (A)

The specific surface-area data for selected grab samples from C5923 (A) are shown in Table 5.18, whereas Figure 5.22 shows the dependence of SSA on textural components taken from Table 5.15. In general, SSA should increase with increasing clay and silt content and decrease with sand content. Similarly, SSA should decrease with increasing effective particle diameter. For the characterization of coarse sediments, which generally have small surface areas, the traditional nitrogen adsorption BET technique is not considered sufficiently accurate. For maximum accuracy for coarse grained sediments, krypton gas at liquid nitrogen temperature or gas flow techniques are better choices for measuring low surface area samples, because of lower krypton gas saturation pressure than nitrogen gas.

Most of the sediment samples collected at between 45 and 143 and 215 to 230 ft bgs showed much higher SSA after the washing steps to remove pore-water salts that precipitated while drying the sediments for SSA measurement (Table 5.18). This indicated that the high sodium nitrate porewater precipitates impacted both measurements of SSA and CEC. None of the plots of measured SSA shown in Figure 5.22 have the expected relationships. Generally, SSA increases with increasing clay and silt contents and decreases with effective grain size. Instead, the plots show very poor correlation with textural components and size statistics, as exemplified in the plot against effective diameter. An explanation for the very poor correlations has not been found. Another option to estimate SSA for these low-surface-area samples would be to estimate SSA from the measured grain-size distributions. SSAs were calculated according to Bear (1988)

$$SSA_c = \frac{6.0}{\rho_s} \sum \frac{c_i}{d_i} + \frac{2}{\rho_s z} \tag{5.1}$$

where SSA_c = calculated SSA in m²/g
  ρ_s = particle density
  c_i = mass fraction of the ith spherical particle (sand and silt assumed to be spherical)
  d_i = diameter of the ith particle.

The contribution of the clay component is calculated with the second term in Eq. (5.1) in which z is the thickness of the clay platelet. The estimated platelet thicknesses for montmorrilionite and illite are 10^{-9} and 10^{-11} m respectively.

The calculated SSA, SSAc, ranged from 16.84 to 98.47 m²/g. Figure 5.22 shows a monotonic increase in SSAc with increasing clay content. The relationship with silt is less well defined whereas SSAc decreases with increasing sand content as would be expected (Figure 5.22). A plot of SSAc versus mud content (silt plus clay) also shows an increase in SSAc with increasing mud as would be expected. The SSA is most often used in predicting the sorption behavior of reactive contaminants. Of greater importance to this project is its relationship to the gas permeability and the surface electrical conductance of porous media. The gas adsorption isotherm derived during measurement of the surface area can also be used to extend the water-retention function to dry conditions.

Table 5.18. SSA and CEC for Borehole C5923 (A) Vadose Zone Sediments

		2nd run (with washing)		1st run (without washing)	
HEIS #	Depth (ft)	SSA (m²/g)	CEC (meq/100 g)	SSA (m²/g)	CEC (meq/100 g)
BIT741	8	10.1 ± 0.04	9.28 ± 0.95	11.9 ± 0.06	11.21 ± 0.65
BIT743	13	9.08 ± 0.04	7.27 ± 0.65	11.8 ± 0.05	9.25 ± 0.75
BIT744	15.5	10.0 ± 0.05	7.14 ± 0.70	13.1 ± 0.06	9.73 ± 0.33
BIT752	45.5	9.61 ± 0.04	8.58 ± 1.39	2.21 ± 0.01	32.67 ± 2.02
BIT753	48	4.05 ± 0.02	5.65 ± 0.14	0.878 ± 0.01	18.39 ± 0.35
BIT754	50.5	3.69 ± 0.02	7.10± 1.23	1.88 ± 0.01	14.55 ± 0.27
BIT763	73	3.50 ± 0.01	6.22± 0.75	0.855 ± 0.004	22.25 ± 0.43
BIT771	98	5.32 ± 0.02	7.10 ± 0.66	1.01 ± 0.003	15.60 ± 0.13
BIT9L5	134.3	4.11 ± 0.02	7.84 ± 0.22	0.997 ± 0.003	19.54 ± 0.38
BIT781	143	2.62 ± 0.02	7.53 ± 0.06	1.12 ± 0.004	15.35 ± 0.83
BIT789	163	3.22 ± 0.02	6.61 ± 0.07	4.13 ± 0.02	8.06 ± 0.12
BIT790	165.5	3.76 ± 0.02	6.59 ± 0.18	3.53 ± 0.02	8.19 ± 0.06
BIT7B4	210.5	2.67 ± 0.01	8.00 ± 0.15	1.65 ± 0.01	17.21 ± 0.16
BIT7B6	215.5	4.39 ± 0.02	7.63± 0.20	1.08 ± 0.005	23.21 ± 0.20
BIT7C2	230.5	3.53 ± 0.01	6.91 ± 0.15	1.59 ± 0.01	15.37 ± 0.28
BIT7C9	258	5.53 ± 0.02	7.47 ± 0.71	8.14 ± 0.02	9.46 ± 0.46
BIT7D8	280.5	10.1 ± 0.02	9.00 ± 0.08	10.8 ± 0.03	10.35 ± 0.38
BIT7F2	290.5	5.83 ± 0.03	7.69 ± 0.08	8.85 ± 0.03	9.76 ± 0.42
BIT7H2	315.5	6.13 ± 0.02	6.27 ± 0.23	6.01 ± 0.02	8.17 ± 0.12
BIT7H7	328	2.32 ± 0.01	3.23 ± 0.36	2.35 ± 0.01	5.44 ± 0.20
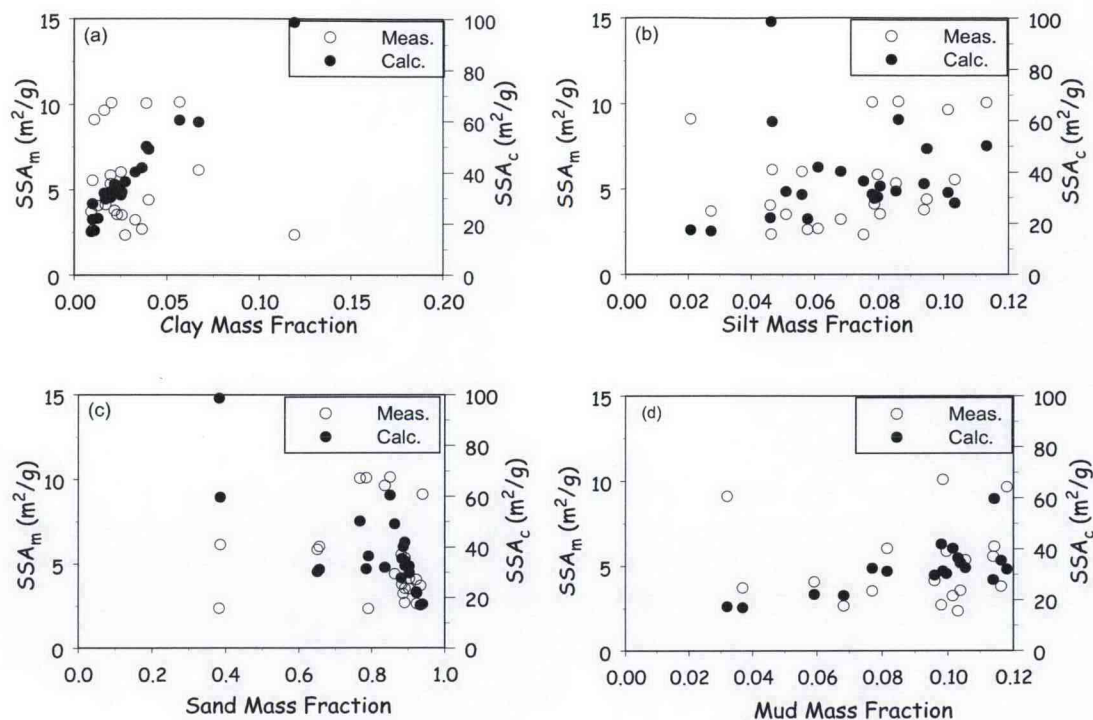
Figure 5.22. Measured (left axis) and Calculated (right axis) SSA as a Function of Texture for Borehole C5923 (A) Sediment

5.3.1.5 Cation Exchange Capacity of Vadose Zone Sediments from Borehole C5923 (A)

The CEC values of the pre-rinsed sediments and not-rinsed sediments from Borehole C5923 (A) are also shown in Table 5.18. Rinsed sediments usually show low CEC values compared to those from sediments without rinsing. The CEC data for the unrinsed sediments was biased high in depth regions where high sodium nitrate concentrations existed in the pore waters (between 45 and 143 and 215 to 230 ft bgs). Based on the exchangeable sodium data for the rinsed sediments, the values reported in Table 5.18 for the rinsed sediments in the zone of maximum sodium nitrate porewater concentration exist (46 to 73 and 210 to 216 ft bgs) may still be biased high by between 0.2 to 0.4 meq/100 g, despite the three rinse steps used to remove the salts. However, we have elected to use the measured values on the rinsed sediments and looked at the correlation of both CEC and SSA to each other and to the textural composition of the sediments as shown in Table 5.15. The correlations are shown in the XY scatter plots in Figure 5.23.
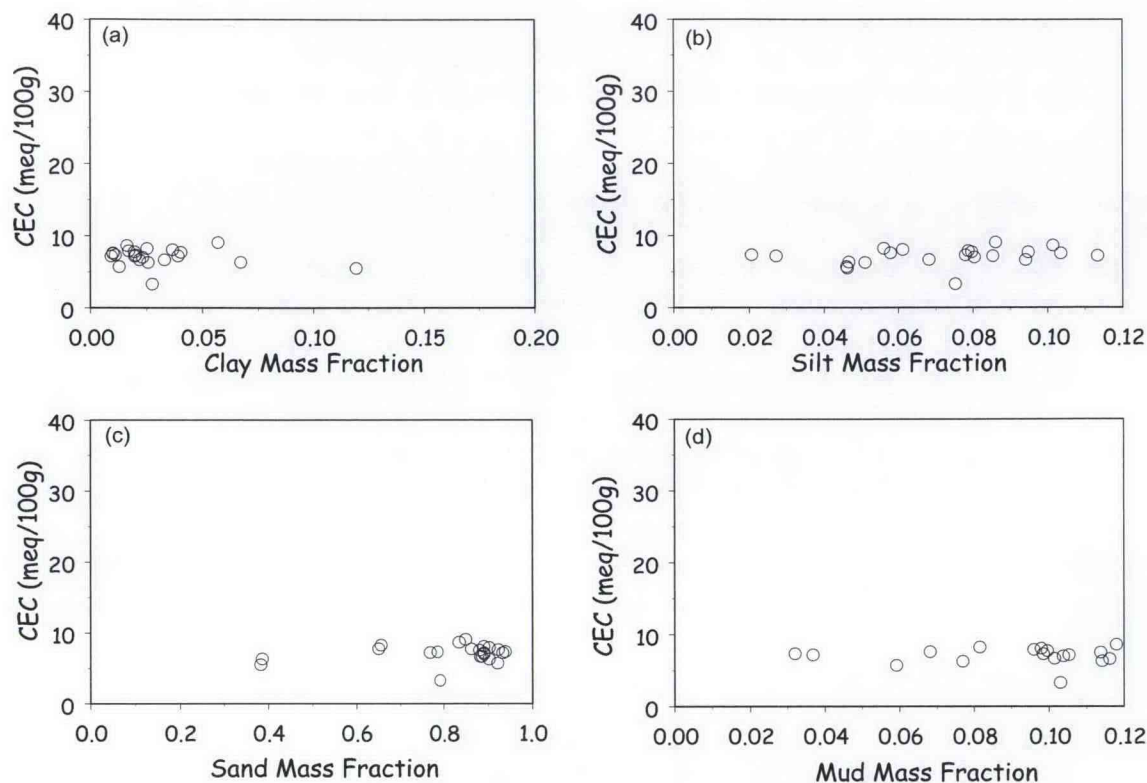
Figure 5.23. Measured CEC as a Function of Soil Textural Parameters for Borehole C5923 (A) Sediments

The CEC ranged from 3.23 meq/100 g to 9.28 meq/100 g. The mean value for the sediments measured was 7.16 meq/100 g., which is quite low. Plots of CEC as a function of textural parameters fail to show meaningful relationships with clay content, silt, mud, or sand (Figure 5.23). In fact, the relationships are somewhat counter intuitive in that the lower the clay content, the larger the CEC. Unlike the surface areas, the correlations of CEC with silt and mud content (Figure 5.23b and d) are no better and show essentially the same lack of trend. This observation is not consistent with the relationships observed for other Hanford sediments. The CEC correlation with effective particle diameter (not plotted) also shows a lot of scatter, but does follow the correct inverse relationship where the CEC increases as mean particle diameter decreases.

A plausible explanation for the observation that the CEC correlation with the clay and sand content is opposite to the physically meaningful relationship is not available. We do not believe that residual sodium nitrate salts that were not washed out after the three rinses are causing enough bias to yield the counterintuitive relationship.

5.3.1.6 Saturated Hydraulic Conductivity

Table 5.19 contains the saturated hydraulic conductivity data obtained from selected intact cores from Borehole C5923 (A). Figure 5.24 shows example plots of discharge versus hydraulic head for four C5923 core samples. The two samples, B1TJ4-2 and B1TJ8-2, represent two extremes in hydraulic

conductivity, 0.62 cm/hr and 126.99 cm/hr, respectively, found at borehole C5923. Samples B1TJ6-2 and B1TK2-2 showed more intermediate values, 35.57 cm/hr and 2.05 cm/hr, respectively. Discharge versus hydraulic head for all of the samples showed the expected linear response for heads between 10 and 30 m with a few requiring heads of over 80 cm to collect useful data in a reasonable time period. One sample, B1T7K4-2, produced no discharge and was removed from the test. These data were used to calculate saturated hydraulic conductivity as described in Section 3.3.13.

The mean K_s and standard deviation for each sample are summarized in Table 5.19. These values were compared to published values of K_s, which are included in Table 5.19 as a reference. Figure 5.25 shows a plot of Ks versus depth, compared to effective grain diameter (Figure 5.25a) and mud mass fraction (Figure 5.25b). K_s is perhaps one of the most variable hydraulic parameters with reported coefficients of variation of 100%. Nevertheless, comparison with published values of similar soils is a useful exercise in determining whether the measured values are reasonable. The high degree of correlation between discharge and head and the similarity to published values for similar soils suggest that these C5923 sediment data are of good quality.

Table 5.19. Saturated Hydraulic Conductivity for Borehole C5923 (A) Sediment Cores

Sample	Z_{top} (ft)	Z_{bot} (ft)	Z_{mid} (ft)	Reps.	K_s(cm/s)	Std. Error	K_s(ft/d)	Std. Error	K_s(cm/hr)	Std. Error	Reference Values of K_s (cm/hr)
B1T7J3-2	38.0	38.5	38.3	3	0.000783	2.80E-06	2.2205823	0.007942	2.82	0.010085	Sandy Loam
B1T7J4-2	38.5	39.0	38.8	3	0.000173	1.14E-06	0.4899727	0.003233	0.62	0.004105	Silt Loam
B1T7J5-2	41.0	41.5	41.3	3	0.001363	4.78E-06	3.8633363	0.013559	4.91	0.017218	Loamy sand
B1T7J6-2	43.5	44.0	43.8	3	0.009881	0.000553	28.012642	1.568338	35.57	1.991541	Sand
B1T7J7-2	86.0	86.5	86.3	3	0.004452	0.000237	12.620126	0.673127	16.03	0.854765	Sand
B1T7J8-2	88.5	89.0	88.8	3	0.00484	4.92E-05	13.722112	0.139369	17.42	0.176977	Sand
B1T7J9-2	106.0	106.5	106.3	3	0.006605	0.000153	18.725086	0.434098	23.78	0.551235	Sand
B1T7L3-2	112.5	115.0	113.8	3	0.008441	0.000312	23.929242	0.885411	30.39	1.124331	Sand
B1T7K1-2	126.0	126.5	126.3	3	0.001439	2.15E-05	4.0804802	0.060971	5.18	0.077424	Loam sand
B1T7K2-2	129.0	129.5	129.3	3	0.001415	5.33E-05	4.0113429	0.150973	5.09	0.191711	Loamy sand
B1T7K3-2	131.0	131.5	131.3	3	0.003083	4.94E-05	8.7405798	0.140042	11.1	0.177831	Sand
B1T7K4-2	133.5	134.0	133.8	3	NA	NA	NA	NA	NA	NA	NA
B1T7K5-2	176.0	176.5	176.3	3	0.001248	3.03E-05	3.53714	0.085778	4.49	0.108925	Loamy Sand
B1T7K6-2	178.5	179.0	178.8	3	0.000543	2.22E-05	1.5393317	0.063014	1.95	0.080018	Loam
B1T7K7-2	181.0	181.5	181.3	3	0.000667	2.91E-05	1.8900968	0.08264	2.4	0.104939	Sandy loam
B1T7J8-2	183.5	184.0	183.8	3	0.035251	0.001021	99.937869	2.895002	126.91	3.676193	Coarse Sand
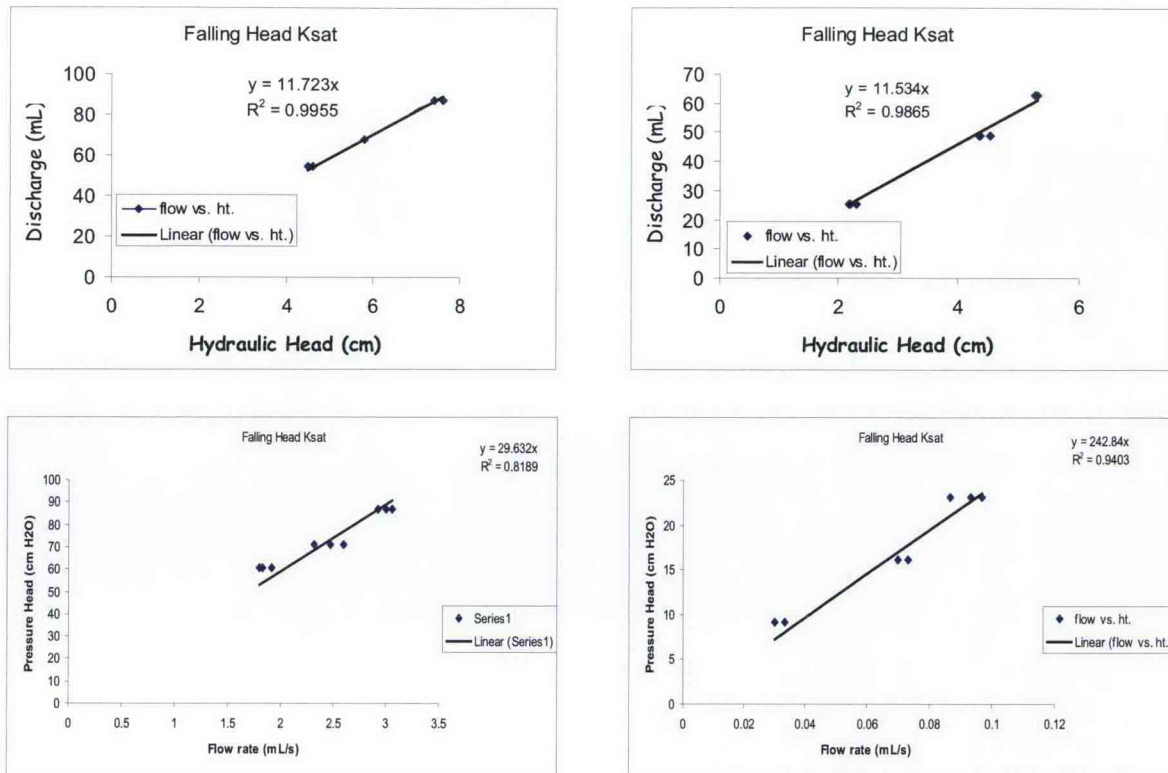
Figure 5.24. Plots of Discharge Versus Hydraulic Head for Borehole C5923 (A) Core Samples, (a) Core B1TJ4-2, and (b) B1TJ8-2, (c) B1TJ6-2, and (d) B1TK2-2
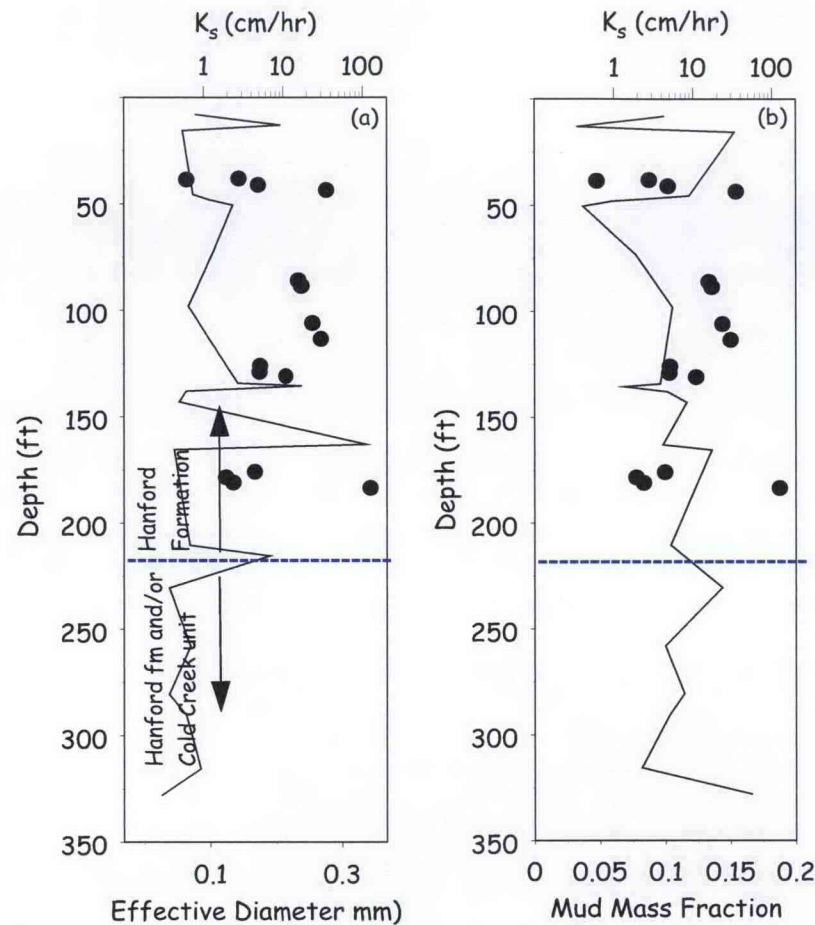
Figure 5.25. Plots of Saturated Hydraulic Conductivity for Borehole C5923 (A) Core Samples, (a) K_s Compared to Effective Diameter from PSDs, (b) K_s Compared to Mud (silt plus clay) Mass Fraction

5.3.1.7   Air Permeability

Table 5.20 presents a summary of the air permeability for core samples from Borehole C5923 (A). Although the procedure usually calls for drying of the sample, air permeability was measured at the antecedent moisture to gain insight into air permeability under field conditions. Such information is critical to the design and operation of the soil desiccation systems that may be used at the site. The values presented in Table 5.20 represent the intrinsic air permeability, k_a. Whereas the soil's hydraulic conductivity depends on properties of both the soil matrix and moving fluid, the soil permeability is a function of the soil's pore-space characteristics, that is, porosity, pore-size distribution, pore shape, pore tortuosity, and connectivity. The intrinsic air permeability is therefore a measure of the average cross-sectional area of the pores conducting air and has dimensions of m^2. An air-permeability value equivalent to the saturated hydraulic conductivity can be calculated as shown in Equation 5.2 following Table 5.20.

Table 5.20. Air Permeability at Antecedent Soil Water Content for Borehole C5923 (A) Samples

HEIS ID	Depth (ft)			Intrinsic Air Permeability	Air Permeability
	Top	Bot	Zmid	k (m^2)	cm/hr
B1T7J3-2	35	37	36	NA	
B1T7J3-3	35	37	36	4.19E-12	0.0813
B1T7J4-3	35	37	36	4.03E-13	0.0078
B1T7J5-2	40	42	41	NA	
B1T7J5-3	40	42	41	1.55E-11	0.3009
B1T7J6-2	43	45	44	1.21E-10	2.3539
B1T7J6-3	43	45	44	3.95E-12	0.0767
B1T7J7-2	85	88	86.5	3.74E-11	0.7255
B1T7J7-3	85	88	86.5	3.26E-11	0.6326
B1T7J8-3	88	90	89	4.39E-11	0.8517
B1T7J8-2	88	90	89	5.70E-12	0.1106
B1T7J9-2	105	108	106.5	1.12E-11	0.2179
B1T7J9-3	105	108	106.5	3.40E-11	0.6607
B1T7K0-3	108	110	109	1.53E-11	0.2976
B1T7K0-2	108	110	109	NA	
B1T7L3-3	113	115	114	5.94E-11	1.1537
B1T7L3-2	113	115	114	1.44E-11	0.2796
B1T7K1-3	125	128	126.5	1.40E-11	0.2711
B1T7K1-2	125	128	126.5	1.88E-12	0.0366
B1T7K2-3	128	130	129	1.55E-11	0.3001
B1T7K2-2	128	130	129	NA	
B1T7K3-3	130	133	131.5	3.54E-11	0.6870
B1T7K3-2	130	133	131.5	2.44E-12	0.0474
B1T7K4-3	133	135	134	1.32E-11	0.2567
B1T7K4-2	133	135	134	7.02E-13	0.0136
B1T7K5-2	175	177	176	6.18E-12	0.1201
B1T7K5-3	175	177	176	2.61E-11	0.5070
B1T7K6-2	178	180	179	2.46E-12	0.0477
B1T7K6-3	178	180	179	1.79E-11	0.3483
B1T7K7-3	180	183	181.5	2.54E-12	0.0493
B1T7K7-2	180	183	181.5	1.18E-12	0.0229
B1T7K8-3	183	185	184	1.34E-11	0.2611
B1T7K8-2	183	185	184	NA	
B1T7K9-3	235	238	236.5	5.22E-11	1.0134
B1T7K9-2	235	238	236.5	2.80E-11	0.5437
B1T7L0-2	238	240	239	5.22E-11	1.0134
B1T7L0-3	238	240	239	7.90E-11	1.5347
B1T7L1-3	240	243	241.5	8.30E-11	1.6126
B1T7L1-2	240	243	241.5	1.73E-10	3.3643
B1T7L2-3	243	245	244	1.33E-11	0.2592
B1T7L2-2	243	245	244	2.94E-11	0.5704

$$K_a = \kappa_a \frac{\rho_a g}{\mu} \qquad (5.2)$$

where K_a =   pneumatic conductivity

      ρ_a =   density of air

      g =   acceleration due to gravity

      μ =   dynamic viscosity of air.

The intrinsic air permeability ranged from 4×10^{-13} m^2 to 1.73×10^{-10} m^2 with a mean value of 2.95×10^{-11} m^2. The pneumatic conductivity ranged from 0.0078 cm/hr to 3.36 cm/hr with a mean value of 0.57 cm/hr.

Saturated hydraulic conductivity and air conductivity show similar trends with depth and a similar relation to texture parameters (see Figure 5.26). Samples that showed a high antecedent moisture were typically finer in texture and showed low conductivities for both air and water whereas coarser, drier samples showed high conductivities for both air and water. A striking difference, however, is the large difference in absolute values for air and water conductivities. Such differences can be expected to increase from cores to the undisturbed field conditions. Tuli et al. (2005) reported large differences between disturbed and undisturbed samples, suggesting a large impact of soil structure and pore-space characteristics on air flow. They reported that the permeability of both fluid phases (air and water) was greatly reduced for the disturbed samples, especially for soil air permeability, due to its greater dependency on soil aggregation and structure. An even more important observation was that regardless of soil disturbance, the tortuosity–connectivity parameter (l) for the water permeability and air permeability functions were different. Our measurements of air permeability were not made at dry conditions, but the larger differences between air permeability and water permeability suggest that such a discrepancy might indeed exist. This would indicate a need to move away from the general practice of using the same parameter value for both the air and water phase permeabilities. Nonetheless, these data provide an important benchmark against which field measurements of air permeability for desiccation treatability testing can be compared.
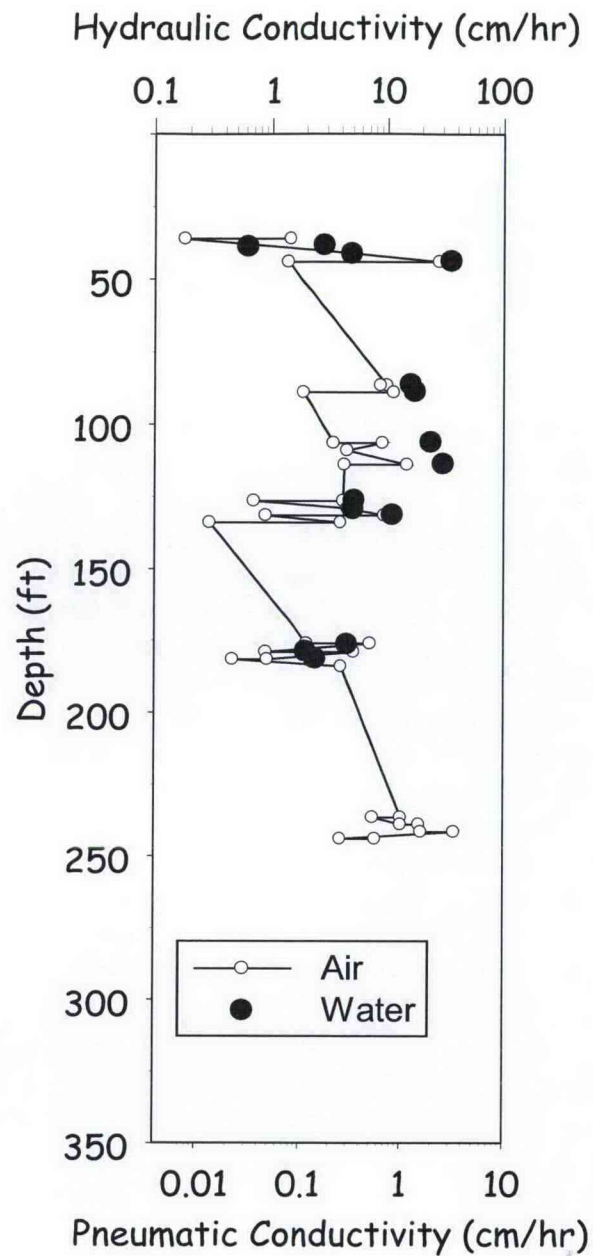
Figure 5.26. Plots of Air Conductivity at the Antecedent Moisture Content and Saturated Hydraulic Conductivity for Borehole C5923 (A) Core Samples

5.3.2   Laboratory Electrical Results for Borehole C5923 (A)

Resistivity measurements were made on all undisturbed cores and many repacked grab samples. The results of these measurements are summarized in Table 5.21. The resistivity ranged from 2.38 ohm-m to 13,909 ohm-m (Ωm) whereas the injection current ranged from 1 to 100 mA. Overall, repeatability was quite good with the standard deviation (σ) of five replicate measurements generally falling between 0 and

5%. A small fraction of samples that showed somewhat higher values of σ was typically coarse with low moisture content. Data quality was also assessed by calculating the reciprocity from measurements in which the current and potential electrodes were reversed. Ideally, measurements made with an electrode configuration must show full reciprocity. In other words, reciprocal measurements in which the current and potential electrodes are reversed should have the same apparent resistivity. In general, reciprocal measurements showed a reciprocity of between 5%, which is considered good, and 1%, which is considered very good. A dataset with 1% reciprocity represents the ideal dataset.

Of the total number of samples, there were 12 samples on which no resistivity measurements could be made with the MiniSting® (AGI-Advanced Geosciences, Inc., Austin, Texas) resistivity meter. These samples appeared too resistive to inject current into the sample. Even after sequentially reducing the injected current from 100 mA down to 1 mA, it was impossible to determine the resistivity. In general, these samples were coarse textured and very low in moisture.

Table 5.21. Summary of Laboratory MiniSting Resistivity Measurements on Borehole C5923 (A) Samples

Type	HEIS #	Z_{top} (ft)	Z_{bot} (ft)	Z_{mid} (ft)	V/I (W)	σ (%)	I (mA)	ρ (Ohm-m)
Grab	B1T740	5.00	6.00	5.50	3767.80	12.30	5.00	977.74
Grab	B1T741	7.50	8.50	8.00	4340.00	0.20	5.00	1126.20
Grab	B1T742	10.00	11.00	10.50	14377.00	0.70	2.00	3730.90
Grab	B1T743	12.50	13.50	13.00	35630.00	1.00	1.00	9245.90
Grab	B1T744	15.00	16.00	15.50	1930.90	0.10	10.00	501.06
Grab	B1T745	17.50	18.50	18.00	5932.40	0.00	5.00	1539.40
Grab	B1T746	20.00	21.00	20.50	2273.09	0.00	10.00	591.23
Grab	B1T747	22.50	23.50	23.00	3641.90	0.00	2.00	945.04
Grab	B1T748	25.00	26.00	25.50	2970.30	0.20	10.00	770.79
Grab	B1T749	27.50	28.50	28.00	1697.50	0.30	10.00	440.50
Grab	B1T750	30.00	31.00	30.50	917.08	0.00	10.00	237.98
Grab	B1T751	32.50	33.50	33.00	2713.50	0.10	10.00	704.14
Grab	B1T825	36.50	37.00	36.75	100.59	47.40	2.00	26.10
Core	**B1T7J3-3**	**38.00**	**38.50**	**38.25**	**111.36**	**0.00**	**5.00**	**34.99**
Core	**B1T7J3-2**	**38.50**	**39.00**	**38.75**	**56.80**	**0.10**	**100.00**	**17.84**
Grab	B1T826	39.00	39.50	39.25	1405.10	0.00	10.00	364.62
Core	**B1T7J5-3**	**40.50**	**41.00**	**40.75**	**11.81**	**0.40**	**5.00**	**3.71**
Core	**B1T7J5-2**	**41.00**	**41.50**	**41.25**	**141.41**	**0.10**	**100.00**	**44.43**
Grab	B1T827	41.50	42.00	41.75	N/A	N/A	N/A	N/A
Core	**B1T7J6-3**	**43.00**	**43.50**	**43.25**	**7.57**	**0.20**	**100.00**	**2.38**
Core	**B1T7J6-2**	**43.50**	**44.00**	**43.75**	**102.68**	**0.00**	**5.00**	**32.26**
Grab	B1T828	44.00	44.50	44.25	945.58	0.10	10.00	245.37
Grab	B1T752	45.00	46.00	45.50	67.27	0.00	10.00	17.46
Grab	B1T753	47.50	48.50	48.00	298.71	0.50	10.00	77.51
Grab	B1T754	50.00	51.00	50.50	962.98	0.20	10.00	249.89

Table 5.21 (Contd)

Type	HEIS #	Z_{top} (ft)	Z_{bot} (ft)	Z_{mid} (ft)	V/I (W)	σ (%)	I (mA)	ρ (Ohm-m)
Grab	B1T755	52.50	53.50	53.00	1096.40	0.10	10.00	284.50
Grab	B1T756	55.00	56.00	55.50	N/A	N/A	N/A	N/A
Grab	B1T757	57.50	58.50	58.00	722.49	1.10	10.00	187.48
Grab	B1T758	60.00	61.00	60.50	788.01	2.70	10.00	204.49
Grab	B1T759	62.50	63.50	63.00	2238.30	0.80	10.00	580.82
Grab	B1T760	65.00	66.00	65.50	1186.00	0.10	10.00	307.77
Grab	B1T761	67.50	68.50	68.00	539.08	0.30	10.00	139.89
Grab	B1T762	70.00	71.00	70.50	471.45	0.00	10.00	122.34
Grab	B1T763	72.50	73.50	73.00	109.84	16.20	10.00	28.50
Grab	B1T764	75.00	76.00	75.50	1654.60	0.10	10.00	429.37
Grab	B1T765	77.50	78.50	78.00	619.85	0.20	10.00	160.85
Grab	B1T766	80.00	81.00	80.50	79.49	0.00	10.00	20.63
Grab	B1T817	82.50	83.50	83.00	775.56	0.00	10.00	201.25
Core	**B1T7J7-3**	**85.50**	**86.00**	**85.75**	**129.81**	**0.00**	**5.00**	**40.78**
Core	**B1T7J7-2**	**86.00**	**86.50**	**86.25**	**141.41**	**0.10**	**100.00**	**44.43**
Grab	B1T829	86.50	87.00	86.75	645.13	0.00	10.00	167.41
Core	**B1T7J8-3**	**88.00**	**88.50**	**88.25**	**101.87**	**0.00**	**5.00**	**32.00**
Core	**B1T7J8-2**	**88.50**	**89.00**	**88.75**	**78.42**	**0.20**	**100.00**	**24.64**
Grab	B1T985	89.00	89.50	89.25	752.27	0.10	10.00	195.21
Grab	B1T768	90.00	91.00	90.50	465.32	0.20	10.00	120.75
Grab	B1T769	92.50	93.50	93.00	1307.00	0.00	5.00	339.16
Grab	B1T770	95.00	96.00	95.50	2251.70	0.50	10.00	584.31
Grab	B1T771	97.50	98.50	98.00	292.45	3.10	10.00	75.89
Grab	B1T772	100.00	101.00	100.50	155.36	0.20	10.00	40.32
Grab	B1T773	102.50	103.50	103.00	1460.50	0.20	10.00	378.98
Core	**B1T7J9-3**	**105.50**	**106.00**	**105.75**	**207.45**	**0.10**	**5.00**	**65.17**
Core	**B1T7J9-2**	**106.00**	**106.50**	**106.25**	**246.67**	**0.00**	**20.00**	**77.49**
Grab	B1T9K9	106.50	107.00	106.75	1090.20	0.00	10.00	282.89
Core	**B1T7K0-3**	**108.00**	**108.50**	**108.25**	**233.49**	**0.00**	**5.00**	**73.35**
Core	**B1T7K0-2**	**108.50**	**109.00**	**108.75**	**41.69**	**0.00**	**20.00**	**13.10**
Grab	B1T9L0	109.00	109.50	109.25	300.73	0.00	10.00	78.04
Core	**B1T7L3-3**	**113.00**	**113.50**	**113.25**	**149.48**	**0.40**	**10.00**	**46.96**
Core	**B1T7L3-2**	**113.50**	**114.00**	**113.75**	**424.23**	**0.00**	**10.00**	**133.27**
Grab	B1T9L1	114.00	114.50	114.25	918.82	0.10	10.00	238.43
Grab	B1T774	115.00	116.00	115.50	1499.80	0.50	10.00	389.19
Grab	B1T775	117.50	118.50	118.00	N/A	N/A	N/A	N/A
Grab	B1T776	120.00	121.00	120.50	1443.30	0.80	10.00	374.54
Grab	B1T777	122.50	123.50	123.00	257.63	52.70	2.00	66.85
Core	**B1T7K1-3**	**125.50**	**126.00**	**125.75**	**164.35**	**0.20**	**5.00**	**51.63**
Core	**B1T7K1-2**	**126.00**	**126.50**	**126.25**	**95.71**	**0.10**	**20.00**	**30.07**
Grab	B1T9L2	126.50	127.00	126.75	418.94	0.20	10.00	108.71
Grab	B1T9L3	129.00	129.50	129.25	1210.00	3.30	10.00	314.00

Table 5.21 (Contd)

Type	HEIS #	Z_{top} (ft)	Z_{bot} (ft)	Z_{mid} (ft)	V/I (W)	σ (%)	I (mA)	ρ (Ohm-m)
Core	**B1T7K3-3**	**130.50**	**131.00**	**130.75**	**147.02**	**0.10**	**5.00**	**46.19**
Core	**B1T7K3-2**	**131.00**	**131.50**	**131.25**	**183.19**	**0.00**	**10.00**	**57.55**
Grab	B1T9L4	131.50	132.00	131.75	N/A	N/A	N/A	N/A
Core	**B1T7K4-3**	**133.00**	**133.50**	**133.25**	**334.71**	**0.00**	**5.00**	**105.15**
Core	**B1T7K4-2**	**133.50**	**134.00**	**133.75**	**36.81**	**0.00**	**10.00**	**11.56**
Grab	B1T9L5	134.00	134.50	134.25	311.90	1.10	10.00	80.94
Grab	B1T778	135.00	136.00	135.50	164.16	0.10	10.00	42.60
Grab	B1T779	137.50	138.50	138.00	293.07	0.20	10.00	76.05
Grab	B1T780	140.00	141.00	140.50	1056.60	21.80	2.00	274.18
Grab	B1T781	142.50	143.50	143.00	242.23	0.10	10.00	62.86
Grab	B1T782	145.00	146.00	145.50	890.88	12.20	1.00	231.18
Grab	B1T783	147.50	148.50	148.00	836.86	4.70	10.00	217.16
Grab	B1T784	150.00	151.00	150.50	2757.00	0.30	5.00	715.42
Grab	B1T785	152.50	153.50	153.00	19790.00	1.60	1.00	5135.40
Grab	B1T786	155.00	156.00	155.50	4798.80	5.60	2.00	1245.30
Grab	B1T787	157.50	158.50	158.00	3267.50	1.00	5.00	847.90
Grab	B1T788	160.00	161.00	160.50	6883.20	2.00	2.00	1786.20
Grab	B1T789	162.50	163.50	163.00	26938.00	47.80	1.00	6990.30
Grab	B1T790	165.00	166.00	165.50	5907.80	1.70	5.00	1533.10
Grab	B1T791	167.50	168.50	168.00	393.39	0.00	10.00	102.08
Grab	B1T792	170.00	171.00	170.50	34359.00	0.20	2.00	8916.00
Grab	B1T793	172.50	173.50	173.00	20635.00	8.00	1.00	5354.60
Core	**B1T7K5-3**	**175.50**	**176.00**	**175.75**	**4945.20**	**0.00**	**5.00**	**1553.60**
Core	**B1T7K5-2**	**176.00**	**176.50**	**176.25**	**4915.50**	**0.10**	**1.00**	**1544.30**
Grab	B1T9L6	176.50	177.00	176.75	22115.00	0.20	2.00	5738.90
Core	**B1T7K6-3**	**178.00**	**178.50**	**178.25**	**3093.90**	**0.00**	**5.00**	**971.97**
Core	**B1T7K6-2**	**178.50**	**179.00**	**178.75**	**3352.20**	**0.20**	**2.00**	**1053.10**
Grab	B1T9L7	179.00	179.50	179.25	15435.00	1.30	1.00	4005.20
Core	**B1T7K7-3**	**181.00**	**181.50**	**181.25**	**1758.70**	**0.00**	**5.00**	**552.51**
Core	**B1T7K7-2**	**181.50**	**181.50**	**181.50**	**1622.50**	**0.00**	**10.00**	**509.72**
Grab	B1T9L8	181.50	182.00	181.75	19852.00	0.00	1.00	5151.40
Core	**B1T7K8-3**	**183.00**	**183.50**	**183.25**	**N/A**	**N/A**	**N/A**	**N/A**
Core	**B1T7K8-2**	**183.50**	**184.00**	**183.75**	**1642.00**	**0.00**	**10.00**	**515.85**
Grab	B1T9L9	184.00	184.50	184.25	20839.00	0.10	2.00	5407.60
Grab	B1T794	185.00	186.00	185.50	12225.00	0.50	2.00	3172.30
Grab	B1T795	187.50	188.50	188.00	11101.00	0.10	2.00	2880.70
Grab	B1T796	190.00	191.00	190.50	13411.00	3.80	2.00	3480.20
Grab	B1T819	190.00	191.00	190.50	14391.00	0.30	2.00	3734.40
Grab	B1T797	192.50	193.50	193.00	2471.80	3.60	10.00	641.41
Grab	B1T798	195.00	196.00	195.50	11679.00	1.50	2.00	3030.70
Grab	B1T799	197.50	198.50	198.00	22197.00	4.10	2.00	5760.10
Grab	B1T7B0	200.00	201.00	200.50	4180.20	0.10	5.00	1084.70

Table 5.21 (Contd)

Type	HEIS #	Z_{top} (ft)	Z_{bot} (ft)	Z_{mid} (ft)	V/I (W)	σ (%)	I (mA)	ρ (Ohm-m)
Grab	B1T7B1	202.50	203.50	203.00	3181.60	0.20	10.00	825.62
Grab	B1T7B2	205.00	206.00	205.50	3460.90	0.00	5.00	898.08
Grab	B1T820	205.00	206.00	205.50	3255.40	0.00	5.00	844.75
Grab	B1T7B3	207.50	208.50	208.00	1314.70	0.20	10.00	341.15
Grab	B1T7B4	210.00	211.00	210.50	364.03	0.10	10.00	94.47
Grab	B1T7B5	212.50	213.50	213.00	350.72	0.00	10.00	91.01
Grab	B1T7B6	215.00	216.00	215.50	88.42	0.10	10.00	22.95
Grab	B1T7B7	217.50	218.50	218.00	677.12	0.20	10.00	175.71
Grab	B1T7B8	220.00	221.00	220.50	1053.20	0.40	10.00	273.31
Grab	B1T7B9	222.50	223.50	223.00	424.32	0.00	5.00	110.11
Grab	B1T7C0	225.00	226.00	225.50	550.88	0.10	10.00	142.95
Grab	B1T7C1	227.50	228.50	228.00	710.69	16.60	2.00	184.42
Grab	B1T7C2	230.00	231.00	230.50	628.91	0.00	10.00	163.20
Grab	B1T7C3	232.50	233.50	233.00	1737.90	0.10	10.00	450.98
Core	**B1T7K9-3**	**235.50**	**236.00**	**235.75**	**217.72**	**0.00**	**10.00**	**68.40**
Core	**B1T7K9-2**	**236.00**	**236.50**	**236.25**	**175.91**	**0.10**	**10.00**	**55.26**
Grab	B1T9K6	236.50	237.00	236.75	2212.20	7.10	10.00	574.07
Core	**B1T7L0-3**	**238.00**	**238.50**	**238.25**	**N/A**	**N/A**	**N/A**	**N/A**
Core	**B1T7L0-2**	**238.50**	**239.00**	**238.75**	**197.32**	**0.00**	**10.00**	**61.99**
Grab	B1T9K7	239.00	239.50	239.25	2165.50	0.00	10.00	561.94
Core	**B1T7L1-3**	**240.50**	**241.00**	**240.75**	**286.23**	**0.00**	**10.00**	**89.92**
Core	**B1T7L1-2**	**241.00**	**241.50**	**241.25**	**213.43**	**0.10**	**10.00**	**67.05**
Grab	B1T9K8	241.50	242.00	241.75	2473.60	3.20	10.00	641.88
Core	**B1T7L2-3**	**243.00**	**243.50**	**243.25**	**361.38**	**0.00**	**5.00**	**113.53**
Core	**B1T7L2-2**	**243.50**	**244.00**	**243.75**	**406.77**	**3.90**	**1.00**	**127.79**
Grab	B1T824	244.00	244.50	244.25	4607.60	0.00	10.00	1195.60
Grab	B1T7C4	245.00	246.00	245.50	3493.40	0.70	5.00	906.51
Grab	B1T7C5	247.50	248.50	248.00	3501.20	0.10	10.00	908.54
Grab	B1T7C6	250.00	251.00	250.50	20034.00	0.50	2.00	5198.70
Grab	B1T7C8	252.50	253.50	253.00	38572.00	0.40	1.00	10009.00
Grab	B1T7C7	255.00	256.00	255.50	11213.00	0.30	2.00	2909.80
Grab	B1T7C9	257.50	258.50	258.00	13426.00	0.20	1.00	3483.90
Grab	B1T7D0	260.00	261.00	260.50	28417.00	2.90	1.00	7374.20
Grab	B1T7D1	262.50	263.50	263.00	12168.00	0.20	2.00	3157.50
Grab	B1T7D2	265.00	266.00	265.50	44637.00	2.00	1.00	11583.00
Grab	B1T7D3	267.50	268.50	268.00	25208.00	0.80	1.00	6541.50
Grab	B1T7D4	270.00	271.00	270.50	22240.00	6.50	2.00	5771.10
Grab	B1T7D5	272.50	273.50	273.00	28127.00	3.20	1.00	7298.80
Grab	B1T7D6	275.00	276.00	275.50	20945.00	0.10	2.00	5435.00
Grab	B1T7D7	277.50	278.50	278.00	53599.00	12.80	1.00	13909.00
Grab	B1T7D8	280.00	281.00	280.50	32300.00	0.20	1.00	8381.70
Grab	B1T7D9	282.50	283.50	283.00	N/A	N/A	N/A	N/A

Table 5.21 (Contd)

Type	HEIS #	Z_{top} (ft)	Z_{bot} (ft)	Z_{mid} (ft)	V/I (W)	σ (%)	I (mA)	ρ (Ohm-m)
Grab	B1T7F0	285.00	286.00	285.50	39543.00	0.80	1.00	10261.00
Grab	B1T7F1	287.50	288.50	288.00	32565.00	6.20	1.00	8450.60
Grab	B1T7F2	290.00	291.00	290.50	11060.00	2.40	2.00	2870.00
Grab	B1T7F3	292.50	293.50	293.00	20464.00	0.00	1.00	5310.40
Grab	B1T7F4	295.00	296.00	295.50	51541.00	0.10	1.00	13375.00
Grab	B1T7F5	297.50	298.50	298.00	34688.00	0.90	1.00	9001.30
Grab	B1T7F6	300.00	301.00	300.50	37640.00	0.00	1.00	9767.30
Grab	B1T7F7	302.50	303.50	303.00	53326.00	1.90	1.00	13838.00
Grab	B1T7F8	305.00	306.00	305.50	38879.00	0.20	1.00	10089.00
Grab	B1T7F9	307.50	308.50	308.00	33352.00	6.20	1.00	8654.60
Grab	B1T7H0	310.00	311.00	310.50	41038.00	5.20	1.00	10649.00
Grab	B1T7H1	312.50	313.50	313.00	49692.00	3.00	1.00	12895.00
Grab	B1T7H2	315.00	316.00	315.50	40213.00	0.20	1.00	10435.00
Grab	B1T7H3	317.50	318.50	318.00	N/A	N/A	N/A	N/A
Grab	B1T7H4	320.00	321.00	320.50	30189.00	0.10	1.00	7833.80
Grab	B1T7H5	322.50	323.50	323.00	32308.00	0.10	1.00	8383.80
Grab	B1T7H6	325.00	326.00	325.50	50499.00	0.70	1.00	13104.00
Grab	B1T7H7	327.50	328.50	328.00	N/A	N/A	N/A	N/A
Grab	B1T823	330.00	331.00	330.50	51564.00	0.30	1.00	13381.00
Grab	B1T7H9	332.50	333.50	333.00	47976.00	7.10	1.00	12450.00
Grab	B1T7J0	335.00	336.00	335.50	N/A	N/A	N/A	N/A
Grab	B1T7J1	337.50	338.50	338.00	N/A	N/A	N/A	N/A
Grab	B1T7J2	340.00	342.00	341.00	42405.00	2.60	1.00	11004.00
Grab	B1T984	341.00	342.00	341.50	N/A	N/A	N/A	N/A
Grab	B1V530	343.50	344.50	344.00	N/A	N/A	N/A	N/A
Grab	B1V531	346.00	347.00	346.50	N/A	N/A	N/A	N/A
Grab	B1V532	348.50	349.50	349.00	N/A	N/A	N/A	N/A
Grab	B1V533	351.00	352.00	351.50	N/A	N/A	N/A	N/A

-N/A resistivity measurements not possible due to high electrode contact resistance limiting current injection.
-Grab samples packed into a 2-in ID × 6-in long resistivity cell to a mean density of 1.6 gm/cm^3.
-Bolded text for emphasis on minimally disturbed core liners.

5.3.2.1 Profile of Laboratory-Measured Soil Electrical Resistivity

Figure 5.27 shows semi-log plots of the measured bulk-resistivity for all the samples analyzed and the resistivity separated by sample type for Borehole C5923 (A). Figure 5.27a shows a single plot of all resistivity values whereas Figure 5.27b separates resistivity into values measured on the cores and those measured on the grab samples. The resistivity profile shows essentially two scales of spatial variability, one at a relatively small scale and the other at a much larger scale. The small-scale variation in resistivity persists over the entire profile and is most likely associated with small-scale changes in texture and the effect of the equilibrium moisture content. These small-scale lithologic changes correlate well with the location of fine-textured layers as identified on the geologist's log (see Appendix A) and are known to

affect the distribution of contaminants. Thus, these variations in texture and moisture content have a compounding effect on soil resistivity. Finally, the resistivity profile provides some insight into the locations of fine-textured layers and their impact on contaminant distribution.

The moist fine-grained layers typically exhibit relatively low resistivity because of water content and solute concentration that are higher than those in adjacent coarser materials. The top 15 ft of sediments in borehole C5923 appears to be quite resistive with resistivity values ranging from around 1000 Ohm-m to 9000 Ohm-m. The resistivity shows a sharp decline to around 700 Ohm-m between 15 and 33 ft bgs after which it decreases to a mean value of around 150 Ohm-m between 33 and 150 ft bgs. However, there are several instances where resistivity dropped below this value and provided a potentially strong target for detection. Strong targets occur between 40 and 60 ft, between 75 and 125 ft, and between 200 and 250 ft bgs (Figure 5.27), with the strongest target centered between 40 and 60 ft. In this zone, the measured bulk resistivity decreased sharply to less than 10 Ohm-m. Given the proximity to the surface, this response is likely due to the combined effects of high moisture, from natural recharge, and high pore-water ionic strength from the past liquid-waste discharges. Measured resistivity values from 75 to 150 ft bgs are also significantly less than the background resistivity of native pore waters and sediments, suggesting the presence of electrolytic contaminants. The small-scale variations in soil texture in this zone are likely acting as localized capillary breaks that would have been penetrated under large fluxes of water but would subsequently limit the downward migration of contaminants because of low hydraulic conductivities at the antecedent moisture. Another zone of low resistivity is evident between 200 and 250 ft with a mean resistivity of around 200 Ohm-m. Based on the geologist's logs, the 220 ft-depth is assumed to be the contact between the Hanford formation and Cold Creek unit and represents a major change in texture to coarser sediments. Under current recharge conditions, it is unlikely that there is a large accumulation of moisture at this depth. These resistivity values are again significantly lower than those expected for native coarse-textured sediments. Thus, the sharp decline in resistivity is most likely due to an accumulation of contaminants at or near the contact between these two sedimentary units.
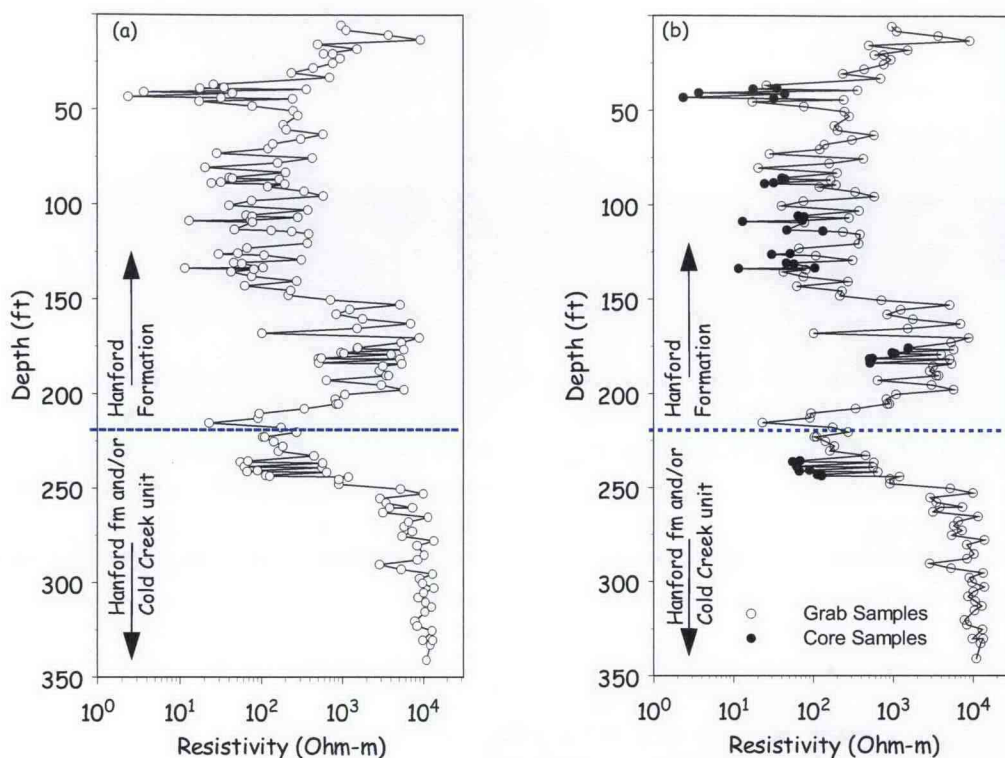
Figure 5.27. Semi-Log Plot of Vertical Resistivity Profile at the Location of Borehole C5923 (A), (a) Resistivity on all Samples, and (b) Resistivity Separated by Sample Type. Measurements were made on core and grab samples using a Mini-Sting resistivity meter with a 2" Wenner Array.

Most of the vertical resistivity variability is in the Hanford formation, above the 220-ft depth. Below this depth, small-scale fluctuations decrease dramatically, suggesting a more homogeneous distribution of texture and therefore less variation in moisture. The soil-resistivity profile is therefore interpreted to describe a pattern of contamination that can be attributed to the downward migration of waste fluids disposed of to the neighboring cribs. Owing to the low-resistivity values at depth (e.g., 250 ft), it can be surmised that waste fluids penetrated at least to this depth. This is consistent with the pore-water chemical analyses and the volume of water discharged at the neighboring cribs. Although the resistivity profile alone is insufficient to determine whether contaminants entered the groundwater, this profile provides some indication of the depth to which the most concentrated nitrate waste migrated. However, not all of the small-scale fluctuation is due to small-scale lithologic differences. Figure 5.27b shows that core-measured resistivities were generally lower than those measured on adjacent repacked grab samples. This discrepancy may be due to two factors: 1) differences in bulk density and packing arrangement between the less-disturbed cores and repacked samples and 2) possible differences in moisture content between the two samples. Although efforts were made to pack the grab samples to representative densities, it is essentially impossible to reproduce the packing arrangement and density of the cores. Further, there is always some small loss of water from the grab samples when they are being examined and/or processed in the dry laboratory atmosphere.

Electrical conductivity is strongly dependent on the formation factor, which is essentially the inverse of the tortuosity factor. A repacked sample with a smaller tortuosity factor, hence a larger formation factor, would give rise to a more resistive medium under equivalent moisture contents and salt concentrations. While the cores remained capped and sealed between sampling and measurement, the grab samples were opened for sub-sampling to conduct chemical analyses, which would have made them susceptible to moisture loss. Lower moisture contents in the core would contribute to a larger bulk resistivity.

5.3.2.2   Relationship Between Apparent Bulk Resistivity and Pore-water Chemistry

Figure 5.28 compares the laboratory-measured soil resistivity profile with the calculated concentration of nitrate (dilution corrected 1:1 sediment to de-ionized water extracts). The trend in the pore-water nitrate profile is consistent with that observed in the laboratory soil resistivity profile. The nitrate concentration gradually increases from the surface down to about 25 ft bgs after which it shows a sharp increase and reaches a peak at around 45 ft bgs. Although the resistivity data show a lot more small-scale fluctuations than the nitrate data, the trends are quite consistent with resistivity decreasing as nitrate concentration increases. The nitrate concentration starts to decline from around 140 ft bgs to reach a minimum at 175 ft bgs whereas resistivity increases in the same interval. The nitrate plume is at least bimodal (if not tri-modal) with the deepest peak occurring at or near the interface between the Hanford and Cold Creek units. The soil resistivity shows a sharp decline in the same interval after which it increases to background levels from about 250 ft bgs to the bottom of the borehole. Even though there is measurable nitrate at depths beyond 250 ft, the sediments were quite dry, and resistivity measurements, when possible, were quite high, on the order of 10 k Ohm-m. The high correlation between pore-water nitrate concentration and measured soil resistivity suggests that these data could be combined to allow inferences of spatial distribution of nitrate concentrations, or resistivity response, at the site.

Figure 5.29 shows a similar plot for pore-water ^{99}Tc concentration as a function of depth. The concentration of ^{99}Tc required to generate a decrease in the apparent resistivity is quite large, and as such, resistivity cannot be used to detect technetium-99. However, as seen in Figure 5.29b, the relationship between the resistivity and technetium-99 profiles is quite good and essentially mimics that of pore-water nitrate. Because technetium-99 mobility is similar to nitrate mobility, the correlation between technetium-99 and laboratory-measured apparent resistivity is actually caused by the nitrate in the pore water. Figure 5.30 shows the plot for pore-water total ionic strength, which theoretically best represents the electrical conductance properties of the pore water. The inverse relationship between the laboratory measured bulk resistivity and total ionic strength is equally strong, as might be expected.
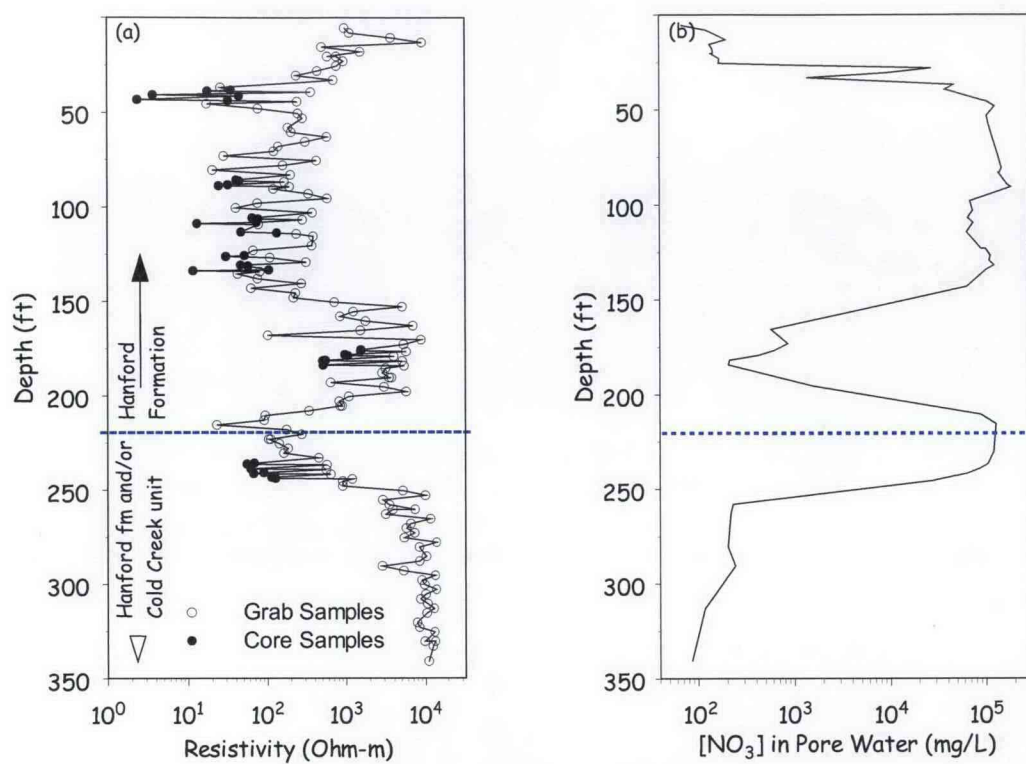
Figure 5.28. Semi-Log Plot of Vertical Resistivity Profile at the Location of Borehole C5923 (A), (a) Resistivity and (b) Pore Water Nitrate Concentration Extracted from Grab Samples
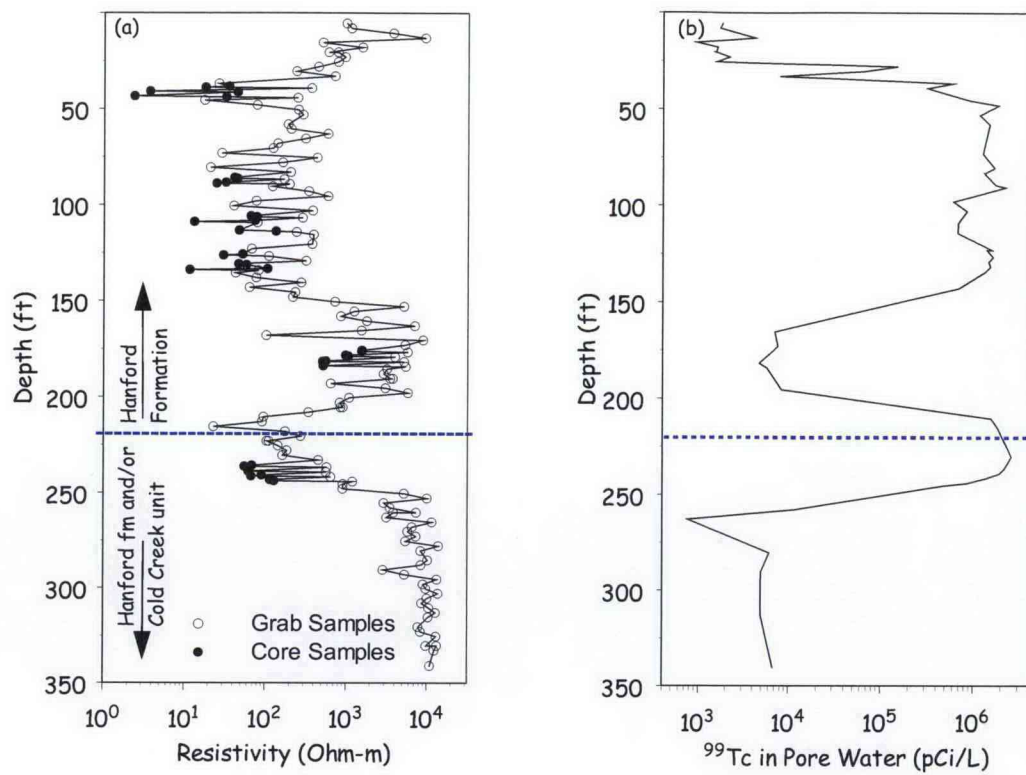
Figure 5.29. Semi-Log Plot of Vertical Resistivity Profile at the Location of Borehole C5923 (A), (a) Apparent Resistivity, and (b) Pore Water Technetium-99 Concentration Extracted from Grab Samples
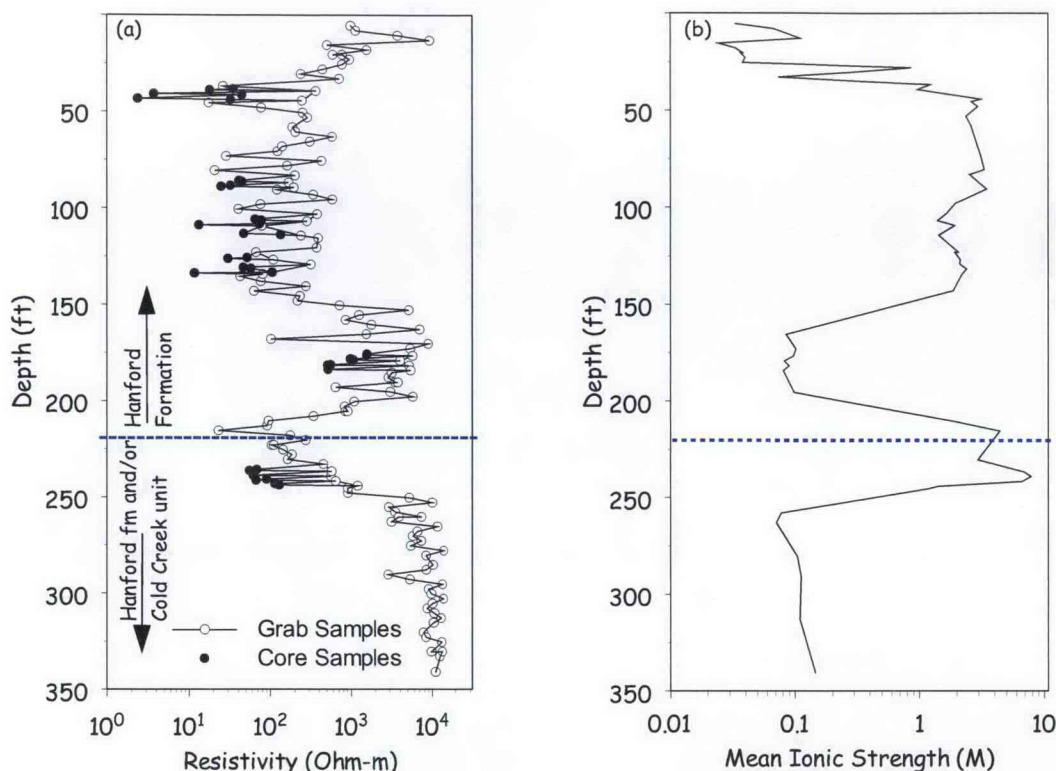
Figure 5.30. Semi-Log Plot of Vertical Resistivity Profile at the Location of Borehole C5923 (A), (a) Apparent Resistivity, and (b) Mean Ionic Strength Measured on Water Extracts from Grab Samples

5.3.2.3 The Relationship Between Laboratory-Measured and Field Resistivity

Comparisons of laboratory-measured resistivity to pore-water chemistry show good agreement. Of more importance to the overall objectives is the relationship between the laboratory-measured resistivity and the apparent resistivity derived from inversion of field resistivity surveys. Surface resistivity surveys conducted at the BC Cribs and Trenches site have been used to generate 2D soil resistivity profiles that intersect the location of Borehole C5923 (A). Figure 5.31 compares the laboratory-measured soil resistivity profiles with those derived from the interpolation of the field data. The most striking difference is the absence of small-scale detail in the inverted profiles from the field survey.

By the nature of the measurements, laboratory-measured resistivity reflects changes in lithology, the impacts of varying soil moisture, and other factors that influence resistivity at the scale of such heterogeneities.
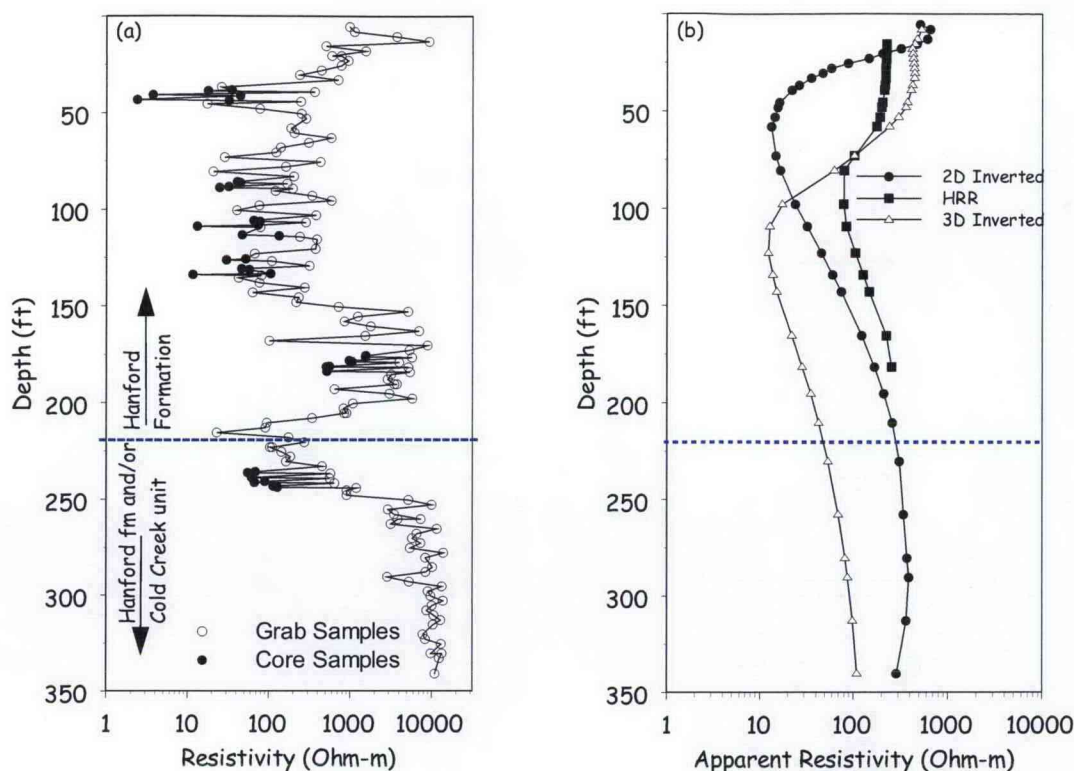
Figure 5.31. Profiles of Resistivity for Borehole C5923 (A), (a) Obtained from D.C. Resistivity Measurements on Borehole C5923 (A) Grab and Core Samples, (b) HRR, 2D Inverted, and 3D Inverted

Although surface-based field resistivity measurements reflect a pattern that is consistent with the distribution of contaminants in the subsurface, the vertical resistivity profiles extracted from the inversion-profile models only capture the shallowest low-resistivity zone or some average of the upper two lobes of the actual plume. Furthermore, the location of the low apparent resistivity feature appears to be dependent on the method of analysis. The HRR analysis indicates that the low-resistivity zone should occur between approximately 60 and 125 ft bgs, with a decrease in resistivity consistent with the bulk-average obtained from the MiniSting measurements on the grab samples and minimally disturbed cores. The 2D inverted profile of the field-survey data appears to focus on the zone of lowest measured resistivity near 40-ft bgs, though it predicts this lowest zone to occur closer to the 50- to 60-ft depth range. The 3D inverted profile of the field survey data suggests a much deeper low-resistivity zone centered near 125 ft bgs. The maximum penetration depth of the HHR profile (depth to which the field measurements interrogate) was around 175 ft bgs for the field survey conditions used in the vicinity of borehole C5923. The low-resistivity zone found by inverting the field data occurs around 60 ft bgs for the 2D analysis and 100 to 110 ft bgs for the 3D analysis, compared to between 40 and 50 ft bgs based on laboratory measurements of soil resistivity and calculated pore-water compositions from 1:1 sediment-water extracts.

The 2D inverted profile as modeled extends to the depth of the borehole and captures the initial decline in resistivity from near-surface conditions as well the first low-resistivity zone. The first low-resistivity zone is fairly accurately modeled and is centered around 50 to 60 ft bgs, an offset of 5 to 10 ft from the actual highest concentration of pore-water solute concentration. However, below this depth, there is a monotonic increase in resistivity until around 275 ft bgs, after which resistivity declines slightly. The inflection point between the shallow low-resistivity zone and the deeper high-resistivity zone occurs near 125 to 135 ft bgs, which is 20 to 30 ft higher in elevation from where the borehole-measured data (MiniSting, ionic-strength, nitrate, etc) mark the basal terminus of the upper salt plume. The 2D inverted profile of the field survey data, however, completely misses the deeper portions of the salt plume that exhibits another localized maxima located near the interface between the Hanford formation and the Cold Creek unit.

The 3D inverted profile of the field survey data also shows a decline in resistivity as the depth increases, but the first low-resistivity zone is pushed downward relative to the HRR and 2D profiles. The 3D inversion locates the first peak of the plume at a depth of about 110 ft bgs, compared to 45 ft bgs based on laboratory measurements. The low-resistivity zone from the 3D inversion extends from about 75 ft to about 150 ft bgs and appears to coincide with the low-resistivity zone observed between 75 and 125 ft bgs. However, this profile also misses the deeper low-resistivity plume present in the C5923 borehole sediments at the transition from the Hanford formation to the Cold Creek unit at 220 ft. The inverted-resistivity calculated values also appear to be about an order of magnitude smaller than those measured in the laboratory. However, this can be expected, given the difference between the scale of laboratory observation and the scale of the inverse model.

The comparison of the resistivity profile derived from the laboratory measurements with the surface survey data is an essential part of the "ground-truthing" (verification) process and is needed to resolve the issues of non-uniqueness often associated with the interpretation of surface surveys. However, for a variety of reasons, such a comparison is not a trivial task. For one, the vertical resistivity profile derived from the laboratory-measured resistivities is made up of relatively dense, equi-spaced measurements on a linear depth scale, whereas vertical resistivity profiles obtained during electrode expansion in the typical surface-based field resistivity surveys are equi-spaced on a logarithmic scale to reflect the increase in volume averaging that occurs as the electrode arrays are expanded to allow obtaining measurements from greater depths (Pal 1991). Inherently, these two data sets will have different levels of accuracy and detail along the vertical axis, and because the field resistivity survey curve is characterized by averaging, there is a substantial loss of information with depth. The laboratory resistivity profile contains far more vertical spatial detail than can be retrieved from a resistivity field survey, and the difference in scales of observation must be first resolved. Although a given subsurface contaminant (resistivity) distribution will give rise to a unique resistivity survey curve at the surface, the retrieval of stratigraphic information from the inversion of the observed field survey curve is nearly impossible given all the geologic, physical, and geochemical variables that influence the resistivity response.

5.3.2.4   Resolution of Electrical-Resistivity Measurements from the Surface

The resolution of electrical-resistivity measurements taken solely from the ground surface is hampered partly due to observational limitations, partly due to interpretational limitations, and partly due to the subsurface resistivity heterogeneities that combine to limit the uniqueness of inversions. Observational limitations arise from the physical limitations of the surface survey methods. The

electrical-resistivity method uses a pair of electrodes to pass current through a heterogeneous distribution of "resistive" soil particles while measuring the voltage drop over an adjacent pair of electrodes. When applied strictly from the ground surface, the voltage drop is measured through large volumes of the subsurface. As the distance between the voltage-measurement electrode and current-injection electrode pairs increases, the volume of soil over which the measurements are made increases. The consequence is a measured apparent-resistivity distribution that becomes smooth relative to the individual layers that comprise the earth.

Many have described the consequence of smoothing using electrical digital filter theory (Koefoed, 1970; Ghosh, 1971; Das and Verma, 1980; O'Neill and Merrick, 1984). Applied in this way, a resistivity kernel function, which is dependent on layer parameters (resistivity and thickness of each layer), is convolved with a function comprising the Bessel function of the first kind of order zero (J_o). Das and Kerma (1984) showed that apparent resistivity (ρ_a) for the pole-pole electrode arrangement is represented by

$$\rho_a(x) = \int_{-\infty}^{\infty} T(y)\left[-J_o\left(e^{x-y}\right)e^{x-y}\right]dy \tag{5.3}$$

where x = ln (r)
r = transmitter and receiver electrode separation distance for the pole-pole array
y = ln (1/λ)
λ = dummy variable of integration
$T(y)$ = input function of layer parameters and kernel function

and the terms in brackets represent the filter function.

Koefoed (1976) demonstrated that the first part of Eq. 5.3, the input function T, can be computed from a stacking process (or superposition since linearity is assumed) of layers beginning from the bottom-most layer and moving upwards through the profile to the earth's surface. The second part of Eq. 5.3, the filter function involving the Bessel function, was tabulated by Koefoed et al. (1972). The filter function was represented by a discrete 61-point digital filter. Other sized filters were also tabulated by O'Neill and Merrick (1984). An example of the filter function for the pole-pole array is shown in Figure 5.32. The filter is similar to a sinc function (i.e., sin [(x)/x]), which acts as a low-pass filter. That is, high-frequency components are removed, leaving only low-frequency components. High-frequency components are those that have variability over a very short distance.

The convolution of the input function with the filter function produces a 1D apparent-resistivity function. To demonstrate the process and resolution of surface-based electrical resistivity, the laboratory-based resistivity data acquired from MiniSting were convolved with the filter function to produce an "expected" apparent resistivity. To begin, Figure 5.33 shows the MiniSting resistivity data with an averaged resistivity function simulating the laboratory data. The original data (see Table 5.21) set contains 160 measurements, after removing duplicates. To actually implement the filtering, however, the number of resistivity layers in the measured profile has to be less than half the size of the filter. The averaging procedure of the MiniSting data involved discretizing layers along logical breaks in continuity and calculating the resulting
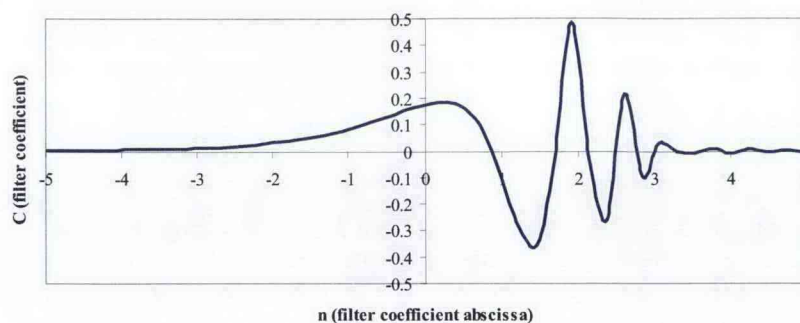
Figure 5.32. Example Pole-Pole Filter for Determining Apparent-Resistivity Values of a Layered Earth Using Digital Filter Theory
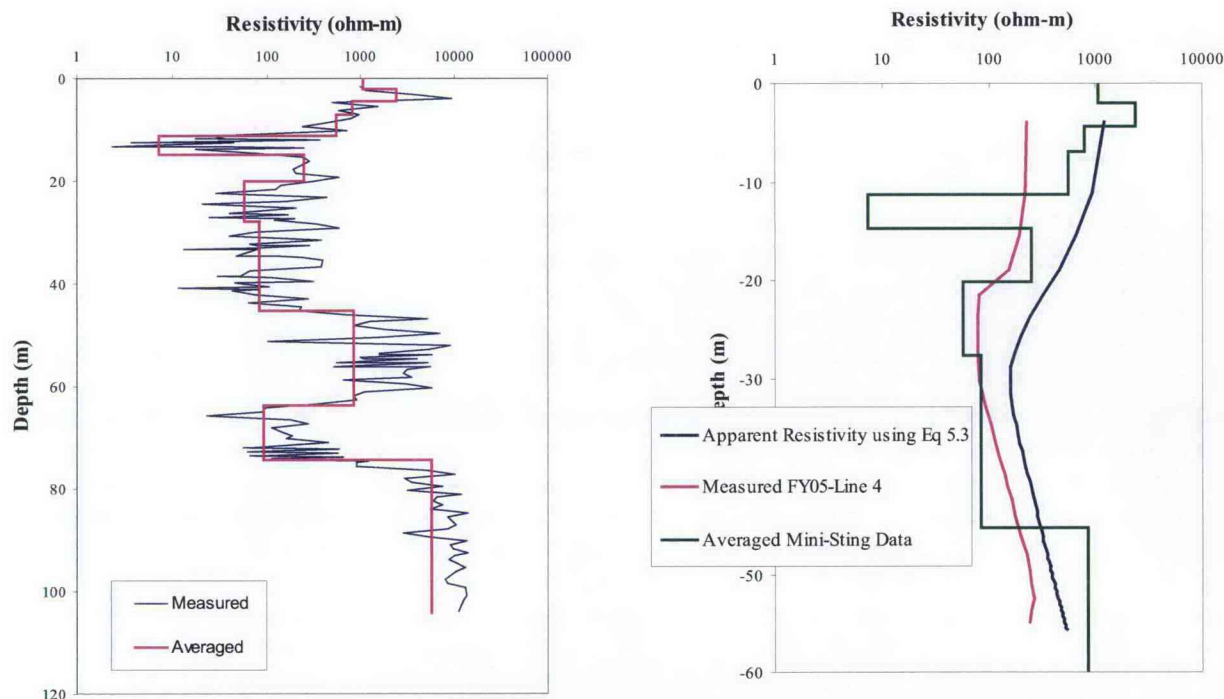

Figure 5.33. Reanalysis of MiniSting Data from Borehole 5923(A), (a) Data Averaged by Discretizing Layers Along Logical Breaks in Continuity and Calculating the Resulting Resistivity Values Within the Layer Using a Parallel Resistor Model and (b) D Filtering of Averaged MiniSting Data

resistivity values within the layer using a parallel resistor model. The parallel resistor model tends to favor the lower resistivity layers. The result, as shown in Figure 5.33a, is an 11-layer model.

The input function, T, used the averaged 11-layer MiniSting data for calculating the expected apparent resistivity. Figure 5.33b shows the results of the convolution. The MiniSting apparent-resistivity data were plotted using the HRR algorithm to allow direct comparison with apparent resistivity

acquired in the field (Line 4 from FY05—see Section 5.2 for more details) directly over Borehole 5923(A). The comparison between laboratory-derived apparent resistivity and field-measured resistivity is very similar in shape but not in values. The laboratory-derived apparent resistivity is approximately 2 to 5 times that of the field-measured apparent resistivity. This difference could be caused by either or both of two phenomena (a) out-of-plane effects from the field measured data or (b) laboratory measurement bias.

The resolution of the technique can clearly be seen in the resulting apparent-resistivity function. The 3.5-m-thick layer of very low resistivity centered at about 15 m bgs was not observed in either of the apparent-resistivity profiles. There does exist a low apparent-resistivity bump in both laboratory and field measurements. The low values observed in the apparent resistivity are likely due to the moderately low MiniSting resistivity between 20 and 45 m bgs. These results bode well for the quality of field-acquired data as they produce theoretically defensible results. It may limit, however, the expectations of the methodology in general because of the problems arising from the so-called electrical equivalence of middle layers and its effect on surface resistivity measurements.

The effects of the electrical equivalence of middle layers have been discussed at length in the literature (Maillet 1947; Koefoed 1979; van Overmeeren 1989; Zohdy 1989). In fact, it has been shown that resolving the resistivity, ρ_i, of the ith layer in either a bowl-shaped (i.e., $\rho_{i-1} > \rho_i < \rho_{i+1}$) or ascending-type ($\rho_{i-1} < \rho_i < \rho_{i+1}$) profile is next to impossible. Different combinations of layer thicknesses (h_i) and resistivities (ρ_i,) will be electrically equivalent provided the longitudinal conductance ($h_i\sigma_i = h_i/\rho_i$, where σ_i is the electrical conductivity of ith layer) remains unchanged (Pal 1991). In the case of bell-shaped ($\rho_{i-1} < \rho_i < \rho_{i+1}$) and descending-type ($\rho_{i-1} > \rho_i > \rho_{i+1}$) sounding curves, the equivalent middle-layer parameters will be such that the transverse resistance ($h_i\rho_i$) remains constant. In addition, thin layers having finite resistivities occurring deep in the profile, such as the deep low-resistivity layer in C5923, will tend to be suppressed in the surface resistivity curves.

Nonetheless, lithostratigraphy is rarely used to constrain the inversion or interpretation of the field resistivity measurements, and as such, they do no not reflect any of the heterogeneity observed at the site. This is not a reflection of the quality of the data, but more so, a reflection of the analysis. Commercially available software routinely used to invert 2D apparent-resistivity data can be classified into two groups: 1) those based on smooth inversion algorithms and 2) those based on block inversion algorithms. Smooth inversion is a cell-based inversion whereas polygons are employed to define layers and/or bodies of equal resistivity in block inversion (Olayinka and Yaramanci 2000). Thus, the ability of these two inversion approaches to define the geometry of subsurface structures and their resistivity is significantly different. In a comparison of smooth and block inversion approaches, Olayinka and Yaramanci (2000) compared the 2D inversions for different geologic models (a vertical fault, a graben, and a horst) using a Wenner array. The results showed that the images obtained from smooth inversion, while useful in determining the geometry of the structures, were able to provide only guides to the true resistivity because of the smearing effects. By using a plane layer earth model as the starting model for the block inversion, the inversion more adequately represented the true subsurface geology in terms of both the geometry and the formation resistivity (Olayinka and Yaramanci 2000). An improved inversion model could incorporate the observed differences in soil type, water contents, and even changes in pore-water chemistry in a block inversion approach to allow better interpretation of near-surface geophysical field surveys.

To further illustrate the limitations of the analysis method, the resistivity profile data from the laboratory measurements on C5923 sediments were used to investigate the effects of inhomogeneities on the predicted surface resistivity profile. In the first instance, a Walsh filter was used to obtain an "upscaled" resistivity profile to observe how and why the small-scale information in the profile is progressively lost with depth in going from the laboratory-measured profile to the field-measured survey

curves. This approach is motivated by the fact that the resistivity layering in the laboratory-measured profile mimics a horizontally-layered Earth, suggesting that it can be better described by a discrete rather than continuous curve. A number of authors have shown that the retrieval of layers from continuously recorded logs can therefore be easily accomplished using Walsh sequence analysis (Lanning and Johnson 1983; Pal 1991; Maiti and Tiwari 2005). Walsh sequence analysis is similar to Fourier frequency analysis and is based on the decomposition of a given space series into a number of component functions (Harmuth 1972: Beauchamp 1975). The difference between the two analyses is that the component functions of Walsh sequence analysis are rectangular and discontinuous whereas they are continuous sinusoids in Fourier frequency analysis. The sequence is defined as one-half the number of times the function crosses zero (i.e., the baseline) within the interval of time or space within which that function is defined, in this case over the depth of the profile. In Walsh domain filtering, coefficients can only take values of 0 or 1. Details on the Walsh sequence analysis and its application can be found in the cited works above. A MATLAB program was developed to perform the analysis using the laboratory-measured resistivity data from C5923 sediments.

Perhaps one limitation of the Walsh sequence analysis is that it is well-defined only for signals of N samples, where N is an integer power of 2 (i.e., $y=2^N$). Consequently, the step width of any discrete signal resulting from sequence filtering is also a power of 2. The number of samples analyzed from C5923 was 160 (N=7.322), so data were re-sampled to create a data set for N=8, i.e., 256 data points. Figure 5.34a shows a plot of the interpolated resistivity profile from Borehole C5923 (A) normalized between 0.0 and 1.0 over the sampling interval. Figure 5.34b shows the Walsh low-pass representation of the resistivity profile with the calculated boundaries between resistivity zones. These zones can then be used to calculate an upscaled or bulk average resistivity for comparison with the resistivity sounding or for input into a forward model to predict a sounding (e.g., surface-based field survey).

In practice, for a given desired step width or "minimum resolvable layer thickness (MRLT)," there is no reason not to include all sequence components that are compatible with it. Therefore, the only low-pass sequence filters of practical interest are those with a cutoff sequence equal to one less than a power of 2. For boundary identification, a Walsh check value of 0.07 was assigned by trial and error to produce reasonable and stable results. A correction to the depth of a boundary is indicated by Equation 5.4 (Lanning and Johnson, 1983; Maiti and Tiwari, 2005):

$$B_i = W_i \pm 0.5 \Delta sw \qquad (5.4)$$

where B_i is true location of the ith boundary; W_i is the depth detected by the Walsh method; and Δsw is the step width of the low-pass version of the resistivity log. For the second low-pass operation, relative energy build up is shifted, depending on the true position of the boundary. Hence, to obtain the true position of the boundary, two sets of zone boundaries can be averaged as a final estimate

$$B_i = W_i' \pm 0.5 \Delta sw \qquad (5.5)$$

where W_i' is the final i^{th} boundary detected by the Walsh method, which leads to an increase of resolution by a factor of 2 using two low-pass examples.
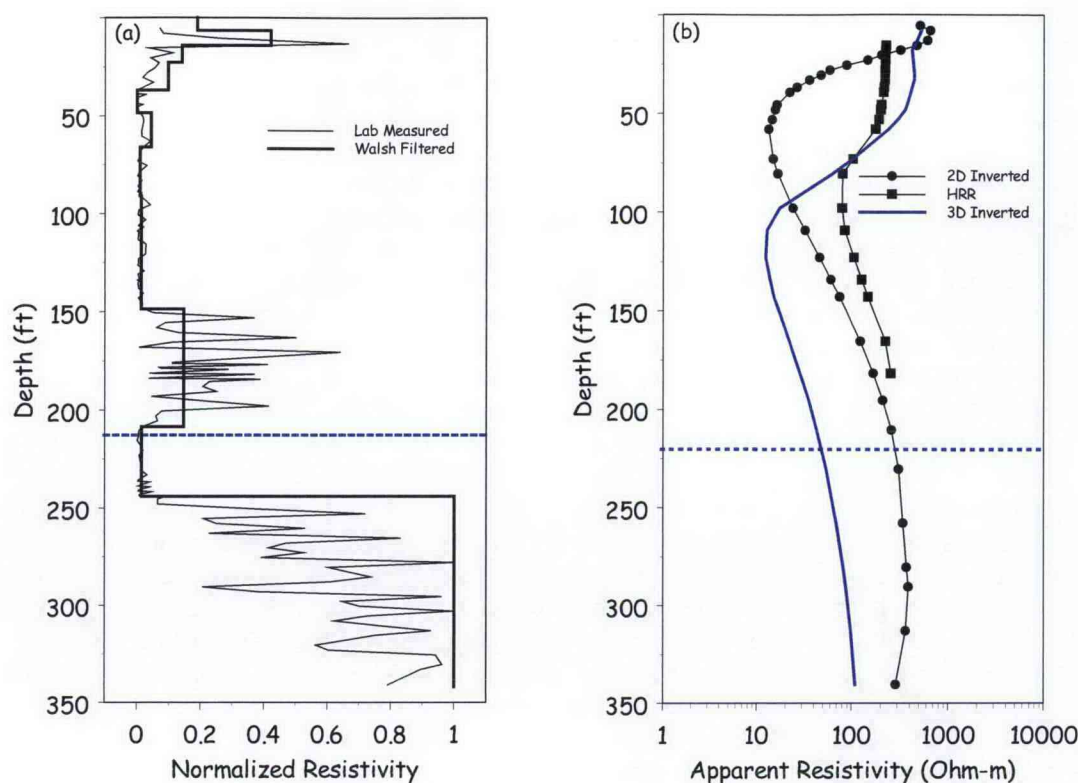
Figure 5.34. Comparison of Resistivity Profile and Sounding Curves from Borehole C5923 (A)
(a) Resistivity Normalized Between 0.0 and 1.0 over the Depth Interval and a Walsh Low-
Pass Representation of the Resistivity Profile Showing the Calculated Boundaries
Between Resistivity Zones, (b) Resistivity Soundings from HRR, 2D Inverted, and 3D
Inverted

The Walsh low-pass filtering approach clearly shows a series of step functions that coincide quite
well with the relatively sharp boundaries between resistivity zones. The resulting step width of 1.3 ft
(based on interpolating 340 ft over 256 intervals) defines the maximum resolvable layer thickness over
the profile. The step width is a function of the cut-off sequence used in the Walsh low-pass filtering
operation and is therefore adjustable. This width was adjusted to minimize the discrepancy between
boundary picks and obvious resistivity changes. These boundaries can then be used to calculate the bulk
resistivity for more direct comparison with resistivity soundings. The similarity between the Walsh
boundaries shown in Figure 5.34 and those derived from simple "eyeballing" of the zones in Figure 5.33
is quite remarkable.

In the second approach, the laboratory-measured resistivity profile was used as input to a forward
resistivity model to simulate a hypothetical surface-based resistivity field survey while taking into
consideration the inhomogeneities in resistivity and water content to define the starting model. The
model uses a solution to the Poisson's equation to predict subsurface resistivity distributions and field
surveys that would be observed with different electrode configurations (Pidlisecky et al. 2007). The
laboratory-measured resistivities were projected onto a solution grid and assumed to represent a layered
earth with each layer extending to the boundary. The model domain extended 500 m in the horizontal
direction and 105 m in the vertical. For the simulation of the surface resistivity survey, we assumed a

100-electrode system with spacing of 5 m. The simulation assumed a Wenner configuration and an injection current of 1 A. Figure 5.35 shows a plot of the simulated pseudosection.
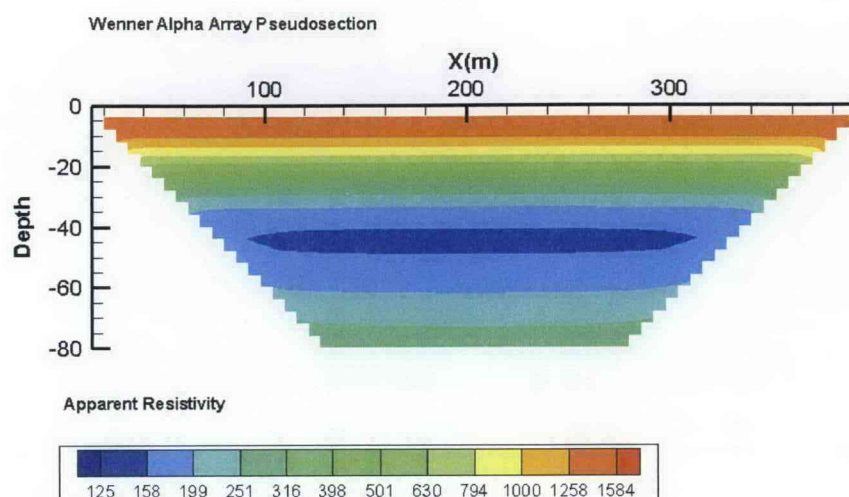

Figure 5.35. The Apparent-Resistivity Pseudosection (a rectangular prism) from a Simulated 2D Wenner Imaging Survey over the C5923 Borehole. The input resistivity model is based on the lab-measured resistivity profile.

Figure 5.36 shows that the pseudosection can be strongly distorted from the actual location and geometry of the original structure, such as shown in Figure 5.31.a. The pseudosection is merely a graphical representation of the apparent resistivity and gives only a very approximate picture of the true subsurface resistivity distribution. Essentially all of the small-scale information from the vertical resistivity profile is lost, suggesting that retrieval of fine-scale stratigraphic information from the inversion of the observed sounding curve would be essentially impossible. Nevertheless, the values of apparent resistivity within the top-most resistive and low-conductivity zones are within the range of the laboratory measurements.

Figure 5.36b shows a resistivity profile extracted from the pseudosection at the midpoint of the domain. The predicted apparent resistivities are in good agreement with those reported for the field measurements (see Rucker and Benecke 2006). The simulated field profile shows a peak resistivity of 1670 Ohm-m, which compares well with the block-averaged value for that zone. The lowest resistivity is observed around the 100-ft depth, which is consistent with lab and field observations. Below this depth, the curve shows a monotonic increase in resistivity with no evidence of the deeper solute front actually observed in the sediments at C5923. Again, these results are consistent with the results of the field survey.
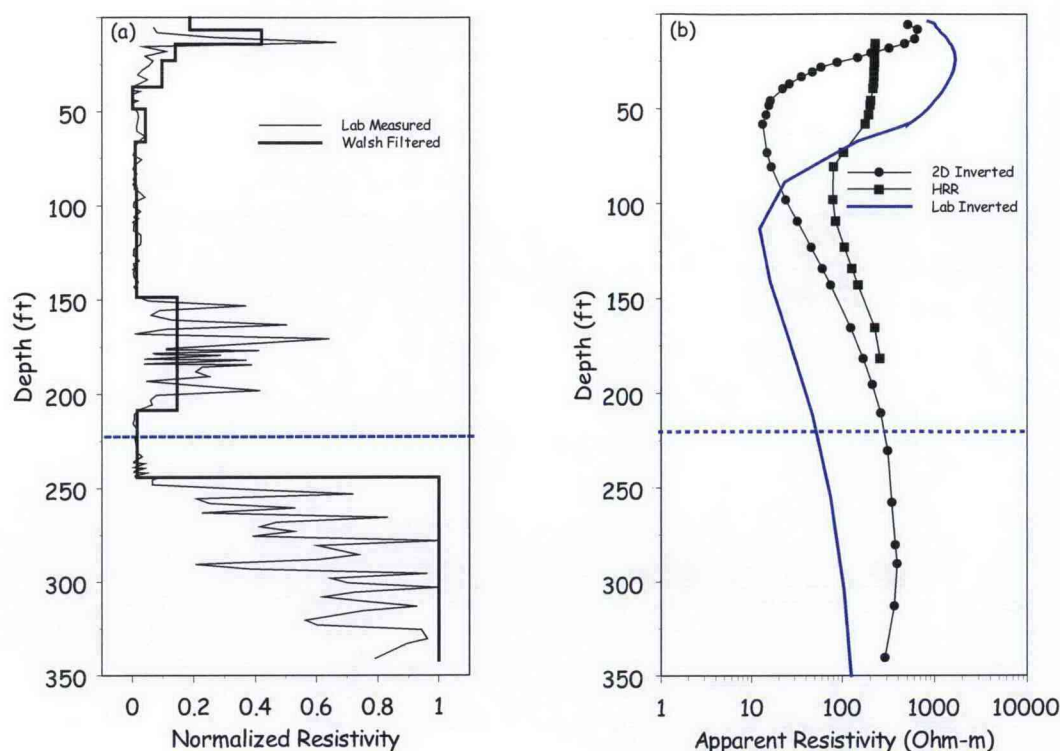
Figure 5.36. Comparison of Resistivity Profile and Sounding Curves from Borehole C5923 (A)
(a) Resistivity Normalized Between 0.0 and 1.0 over the Depth Interval and a Walsh Low-
Pass Representation of the Resistivity Profile Showing the Calculated Boundaries
Between Resistivity Zones, (b) Resistivity Profiles from HRR, 2D Inversion of Field Data,
and 3D Inversion of Field Data Compared to a Profile Derived from the Inversion of a
Simulated Survey Using the Laboratory-Measured Profile as the Starting Mode

More importantly, these results highlight a very important point that the laboratory-measured profile
and field surveys are inherently different and capture different levels of detail. Even with a model that
considers observed inhomogeneities in bulk resistivity, it was essentially impossible to reproduce the
laboratory-measured distribution used as the initial condition. It is therefore unlikely that inversion, with
unresolved issues of non-uniqueness and the electrical equivalence of middle layers, can ever produce the
same profile as that derived from the laboratory resistivity measurements on the intact cores and grab
samples or one that explicitly matches the resistivity derived from the pore-water chemistry.

5.3.2.5 The Relationship between the Soil Electrical Resistivity Profile and Borehole Logs

A priori knowledge of the stratification in resistivity would minimize the problem of interpreting
resistivity soundings (e.g. Flathe, 1976) but such information is typically not available. Different
lithologic units may also have similar resistivities. These features cannot be distinguished from each
other based on resistivity alone. For example, a hyper-saline zone at depth and a wet clay/silt layer could
be equally conductive. Additional information such as hydrophysical properties (e.g. water content, clay

content, PSD, SSA, CEC, or borehole natural gamma (potassium-40, uranium-238, and thorium-232) [KUT] logs) would be required to differentiate why the field sounding looks as measured. Another option could be to use multimodal investigations in the field. For example, a fine-textured conductive layer would have a different induced polarization signature than a layer whose low resistivity was due only to ionic (pore water) constituents. Water content/porosity measurements and γ-ray spectroscopy, used to quantify the natural isotopes ^{40}K, ^{238}U, and ^{232}Th, have the potential to provide the required information. *A priori* lithologic data are often limited to geologist's logs whereas borehole SG logs are typically collected on every new borehole installed at the Hanford site, although they are rarely used to constrain lithology. Figure 5.37 compares the laboratory-measured resistivity and calculated electrical conductivity profiles with the normalized total gamma ($I_{GR} = (\gamma - \gamma_{min})/(\gamma_{max} - \gamma_{min})$ from Borehole C5923 (A). The total gamma response is due to the presence of potassium-40, uranium-238, and thorium-232, all of which are known to show a strong dependence on lithology. In general, I_{GR} appears to be inversely proportional to resistivity and therefore directly proportional to electrical conductivity. The normalized total gamma, I_{GR}, shows essentially five main zones or facies, 0-50 ft, 50 – 100 ft, 100- 150 ft, 150 -235 ft and > 235 ft. The low in I_{GR} at 20 ft bgs coincides with the high-resistivity (low conductivity) anomaly at the same depth. The I_{GR} in the 0-50 ft zone shows the lowest values but increases sharply around 50 ft. The sharp change in I_{GR} around 50 ft bgs coincides with the low-resistivity zone (highest conductivity) at the same depth. Beyond this depth, there is a general increase in soil electrical resistivity and a decline in I_{GR} to a minimum around 235 ft bgs. These data suggest that the distribution of the salt plume is controlled by the lithology with major differences in resistivity coinciding with major changes in I_{GR}, which result from the lithologic differences. The minimum in I_{GR} is most likely the true location of the contact between the Hanford formation and the Cold Creek Units. The negative correlation between soil electrical resistivity and I_{GR} is caused by the dependence of the gamma response on lithology.

It is known that a significant part of sediment ^{238}U and ^{232}Th is bound in dark-colored, ferromagnetic minerals in the parent materials for siliclastic sediments (Kogan et al. 1969). This implies that the gamma-ray activities of Hanford formation sands should be a function of the grain size and particle density. Owing to the depositional environment, ^{40}K is uniformly spread throughout the principal rock-forming minerals, such as quartz and feldspar and sediments with the same parent materials, suggesting that similar grain sizes from different locations should show similar ^{40}K activities. Elevated ^{40}K activity levels can also be indicative of increased clay content. Figure 5.38 compares the trend in the resistivity from the laboratory measurements on C5923 sediments with that of the ^{40}K from the KUT measurements. The similarity between the ^{40}K and I_{GR} profiles is expected because the ^{40}K is the largest contributor to I_{GR} in these sediments. These logs can therefore be used to identify the major architectural elements and dominant facies in the formation. Differences in gamma-ray activity from the natural distribution of radionuclides may therefore have some application in constraining the inversion model and in the interpretation of results. However, the challenge is to relate gamma-ray spectra to useful parameters, such as grain size statistics, which are beyond this project's work scope.

Figure 5.39 compares the normalized total gamma, I_{GR}, with laboratory measured soil resistivity with the geometric mean grain diameter and sorting index derived from grain-size distribution curves. Figure 5.39b essentially shows a coarsening upward in texture to the 250-ft depth, after which the particle size remains relatively constant. The sorting index shows a similar pattern with a high degree of sorting deep in the profile and a decrease towards the surface. Again the transitions between the different facies are evident and appear consistent with the gamma log and measured laboratory soil resistivity. More importantly, grain-size distributions and nuclear logs, such as gamma-ray, porosity, and density, will not

be affected by the high ionic strengths in the pore waters observed at this site (and other waste sites where there are no long-lived gamma emitters remaining in the sediment profile) and as such can be used as unbiased indicators of the lithologic changes. Closer to the footprints of inactive disposal facilities the total gamma logs may require subtraction of the gamma activity of cesium-137 and cobalt-60 and perhaps actinides as well as compensation for Bremmstrahlung diffuse radiation from strontium-90. Based on these relationships, the following approximate values of soil resistivity can be assigned to the different Hanford BC Cribs and Trenches site facies; silt/clay: 20 to 100 Ohm-m; fine sand: 300 to 2,000 Ohm-m; coarse/dry sand: 3,000 to 10,000 Ohm-m.
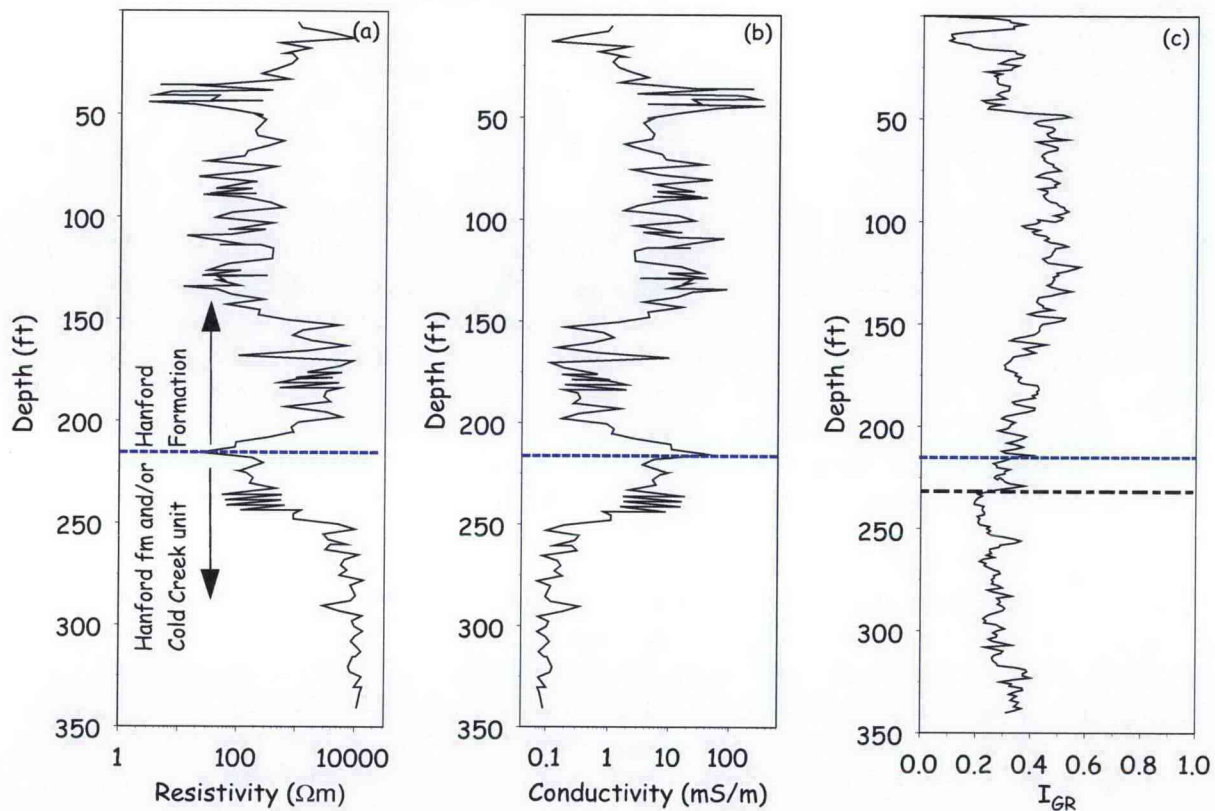
Figure 5.37. The Relationship Between Resistivity and SG Logs at Borehole C5923 (A), (a) Resistivity Based on Laboratory Measurements and (b) Electrical Conductivity Calculated from Resistivity, and (c) Normalized Total Gamma. The blue dotted line shows the location of the Hanford formation-Cold Creek contact based on geologist's logs whereas the black dashed line shows the contact based on scaled total gamma log.
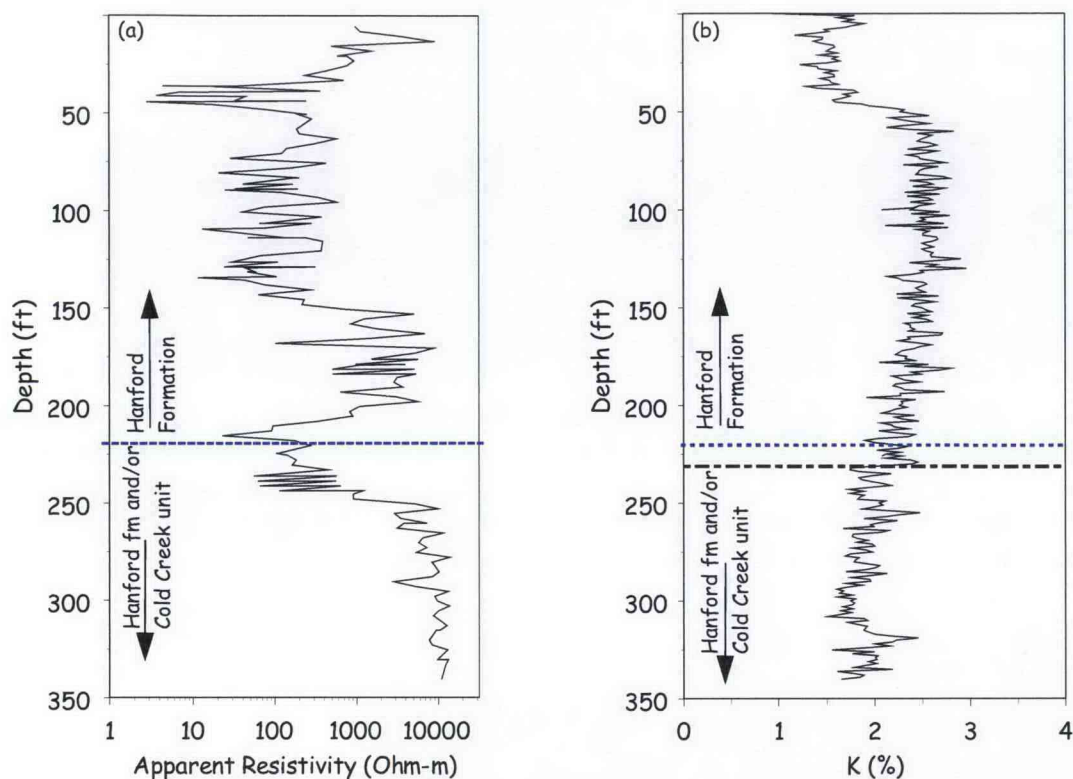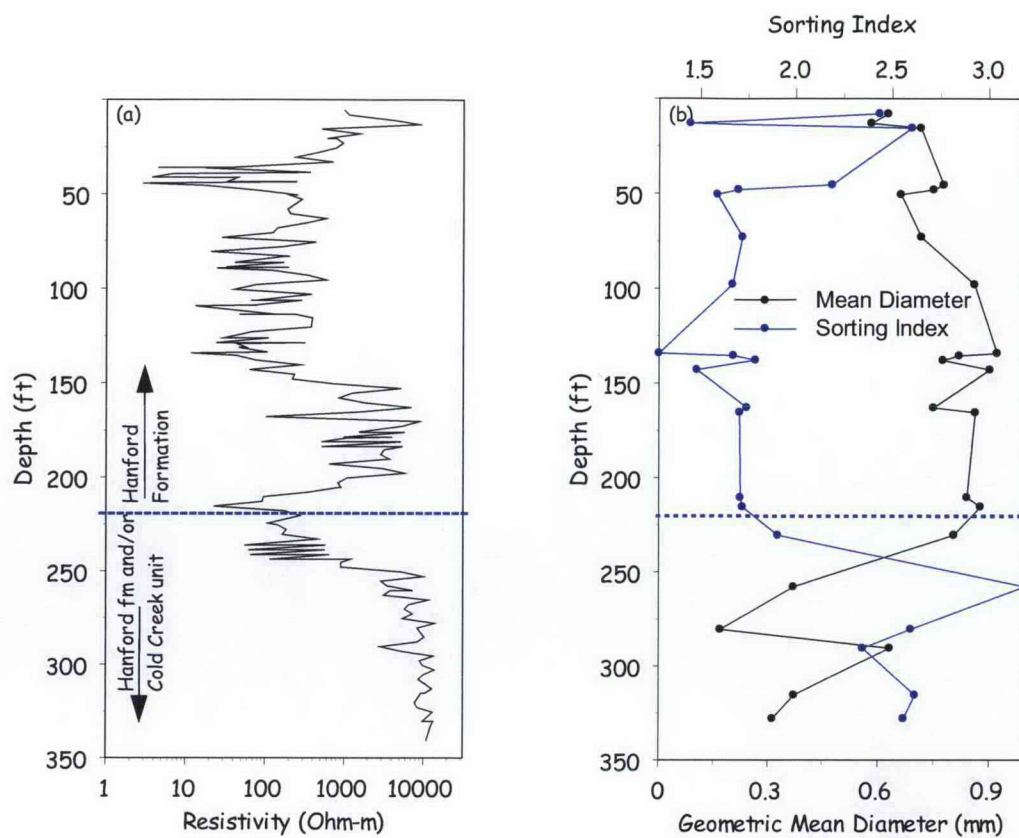
Figure 5.38. The Relationship Between Resistivity and SG Potassium-40 Logs at Borehole C5923 (A), (a) Apparent Resistivity Based on Laboratory Measurements and (b) Total Potassium Distribution Versus Depth from ^{40}K log. The blue dotted line shows the location of the Hanford formation-Cold Creek contact based on geologist's logs whereas the black dashed line shows the contact based on scaled %K.

Figure 5.39. Relationship Between (a) Laboratory-Measured Resistivity and (b) Grain Size Distribution Indicators, Including the Geometric Mean Diameter and the Sorting Index

5.3.2.6 The Relationship Between the Laboratory Measured Soil Electrical Resistivity Profile and Laboratory Measured PSD, SA, and CEC

CEC and SSA were measured on select grab samples from Borehole C5923 (A). Figure 5.40a shows a plot of CEC whereas Figure 5.40b shows a plot of SSA as functions of depth. CEC ranged from 3.23 to 9.28 meq/g with a mean and standard error of 7.16 ± 0.276 meq/100 g. The SSA ranged from 2.32 to 10.1 m^2/g with a mean and standard error of 5.48 ± 0.586 m^2/g.

As shown in Figure 5.40, results were separated into high ionic strength (high salinity) and low ionic strength (low salinity) samples. At low ionic strengths, the CEC can be accurately estimated from the total soil extractable cations. However, in saline sediments, accurate determination of the CEC requires prewashing to remove soluble salts in the pore water. All of the samples were washed three times before analyses. CEC results after washing show significant differences between samples that were initially high in salinity and those that were initially low. For initially low ionic strength samples, the CEC ranged from 3.23 to 9.28 with a mean of 7.06 ± 0.48 meq/100 g. For initially high ionic strength samples, the CEC ranged from 5.65 to 8.58 with a mean 7.26 ± 0.27 meq/100. The SSA for initially low ionic strength samples ranged from 2.32 to 10.1 m^2/g with a mean of 6.61 ± 0.87 m^2/g. However, the initially high ionic

strength samples ranged from 2.69 to 9.61 m^2/g with a mean of 4.35 ± 0.06 m^2/g. The means are significantly different.

Both CEC and SSA showed some variation with depth. To better understand these variations, results were analyzed to identify any dependence on lithology. As shown earlier, two major lithologic units have been identified at the site; the Hanford formation and Cold Creek unit with the contact occurring around 220 ft bgs. Analytical results were separated into measurements made in the 0- to 220-ft range and the > 220-ft depth. Analysis of SSA data showed a range of mean and standard error of 5.44 ± 0.721 m^2/g in the 0- to 220-ft interval and 5.572 ± 1.09 m^2/g in the > 220-ft depth interval. These results are not significantly different. A similar analysis of the CEC measurements show a mean and standard error of 7.32 ± 0.235 meq/100 g in the 0- to 220-ft interval and 6.76 ± 0.798 meq/100 g in the > 220-ft interval, which are statistically different.

Relationship Between CEC, SSA, and Water Content

The variation in CEC and SSA with depth has been shown to follow the variations in sediment texture, particularly the abundance of fines. If vertical variations in CEC and SSA are due entirely to lithologic variations, then these values should show a strong correlation to water content, textural composition, and grain-size moments. Figure 5.41 shows depth profiles of CEC and SSA compared to water content for borehole C5923. Both CEC (Figure 5.41a) and SSA (Figure 5.41b) show their highest values on the 0- to 50-ft interval where moisture content was highest. Both CEC and SSA appear to roughly follow the trend in water content. There is a progressive decrease in water content with depth from the 0- to 50-ft zone, and this trend is accompanied by a general decrease in CEC (Figure 5.40a) and SSA (Figure 5.40b). To better understand the relationship, water content was regressed on CEC and SSA (Figure 5.42). Ideally, one would expect a positive correlation between water content, CEC, and SSA. Under equilibrium conditions, finer textured soils would tend to have higher CECs and SSAs because of higher clay contents and also would retain more water. Although Figure 5.42a shows a general increase in water content with CEC, the correlation is not very strong and has limited predictive capability. Figure 5.42b shows a slight increase in water content with increasing SSA but the relationship is not strong enough to be used for predictive purposes. Figure 5.43 shows plots of CEC versus soil texture parameters.

The lack of correlation between water content and CEC or SSA is an indication that most of the water may not be adsorbed by clay interlayer sites but may be retained by some other means. To further investigate these relationships, or lack thereof, CEC was regressed on soil textural parameters derived from PSDs. Figure 5.43 shows plots of CEC as a function of sand, silt, and mud mass fractions, and the Fredle index. Owing to the low clay content, clay and silt mass fractions were summed and reported as a mud mass fraction. The Fredle index is computed from the cumulative probability d-values as the ratio of the mean diameter to the sorting index. Ideally, CEC should decrease as sand mass fraction increases.
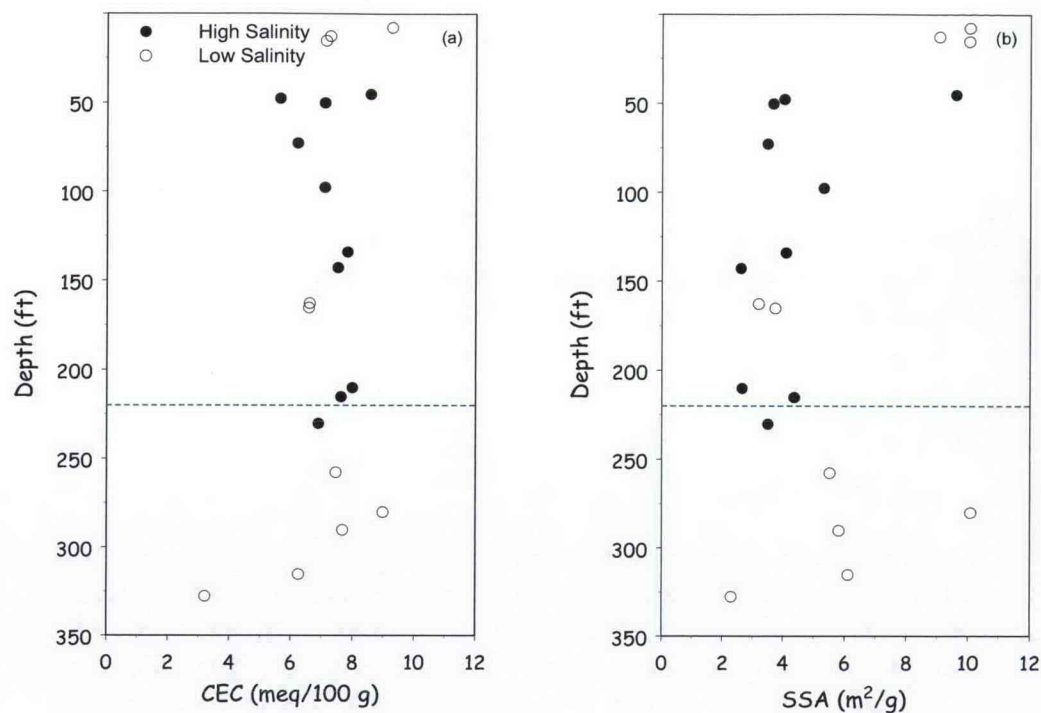
Figure 5.40. The Variation in CEC and SA with Depth at Borehole C5923 (A), (a) CEC, and (b) SSA
Results Are Further Separated by Pre-Wash Ionic Strength. The dotted line shows the
location of the Hanford formation-Cold Creek contact based on geologist's logs.
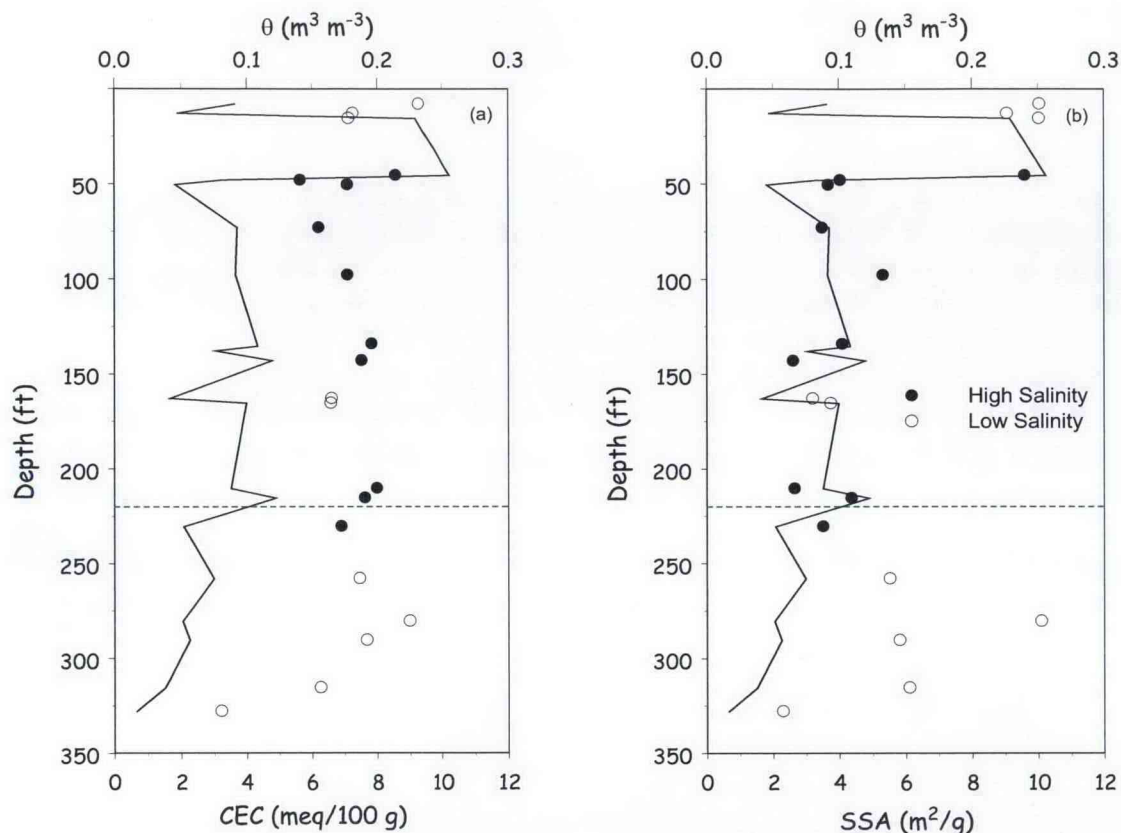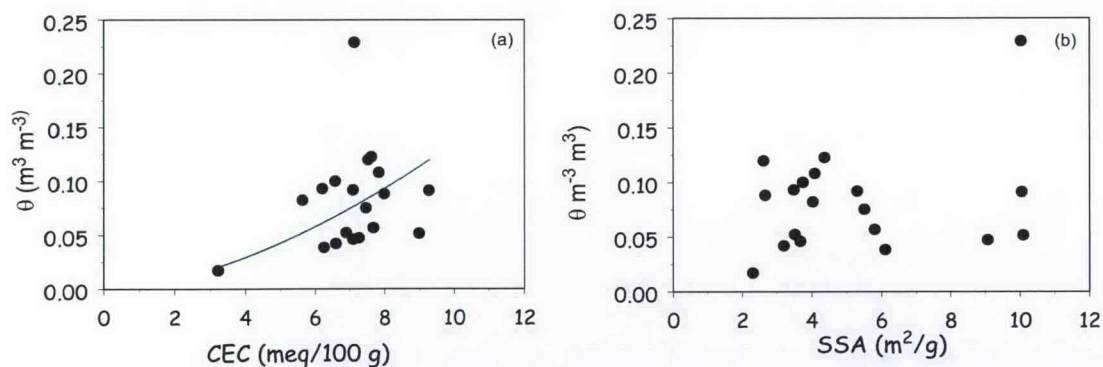
Figure 5.41. The Variation in CEC and SSA with Depth at Borehole C5923 (A) and the Relation to Water Content (a) CEC, and (b) SSA. Results are further separated by pre-wash ionic strength. The dotted line shows the location of the Hanford formation-Cold Creek contact based on geologist's logs.

Figure 5.42. The Relationship Between Water Content and (a) CEC, (b) SSA Based on Measurements on Borehole C5923 (A)

However, as shown in Figure 5.43, there is no obvious relationship. This can be expected, given that the sediments contain a large amount sand and the generally low CEC of these materials. Figure 5.43b shows a general increase in CEC with silt mass fraction, although there appears to be two populations, one showing the expected increase and the other showing a decrease. The same relationship is apparent

for the mud mass fraction and the Fredle index. The decrease in CEC with increasing Fredle index is due to the increase in the index as mean diameter increases. The reason for the apparent separation into two populations is uncertain but could be related to pore-water salinity.

Figure 5.44 shows a similar plot of SSA as a function of sand, silt, and mud mass fractions, and the Fredle index. Typically, the SSA should decrease with increasing mean particle diameter. Thus, the SSA should decrease with increasing sand fraction and increase with increasing silt, clay, or mud fraction. Owing to the low clay content, the range of SSA was quite small, and relationships to textural parameters are less apparent. However, the range of SSA observed for these sediments falls in the range of 9 to 12 m^2/g observed for Hanford formation sediments (Ward et al. 2008). Figure 5.45 shows a plot of measured SSA versus measured CEC. In general, there is an increase in SSA with increasing CEC, although the correlation is not very strong. The existence of such a relationship yet with poor correlation with grain size statistics suggests that the relationship is being influenced by some other mechanism.
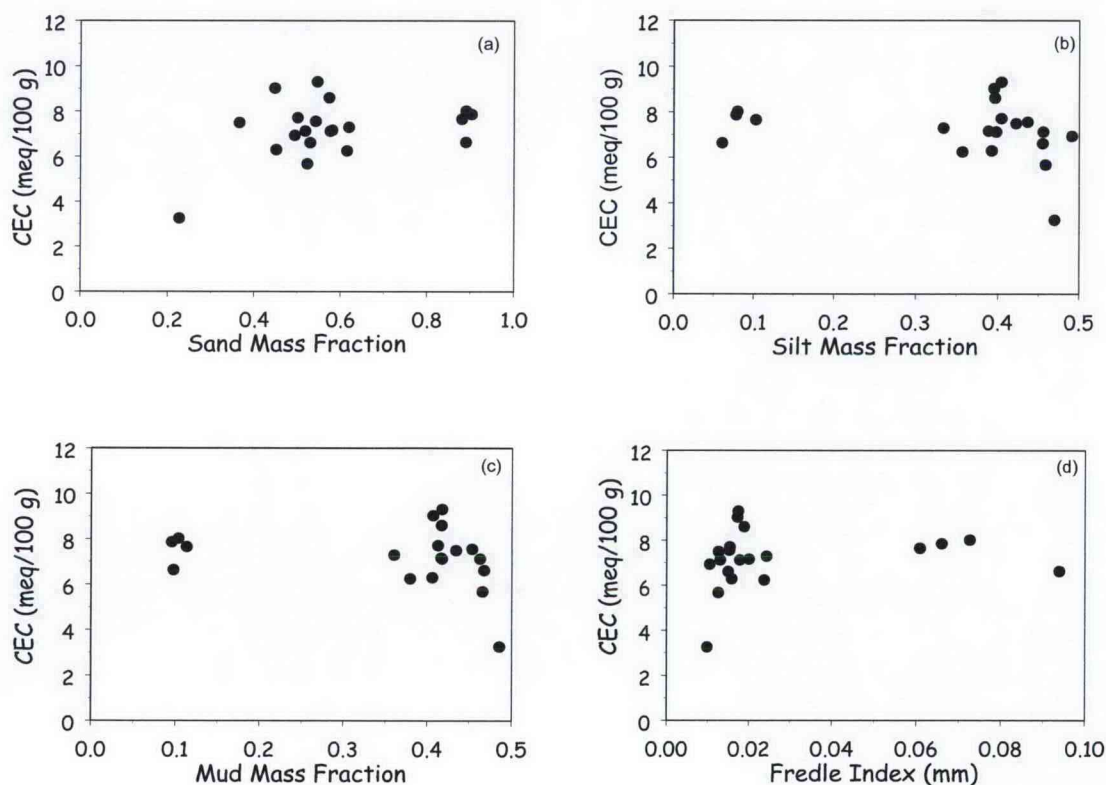

Figure 5.43. The Relationship Between CEC and Soil Textural Parameters (s) Sand Mass Fraction, (b) Silt Mass Fraction, (c) Mud, and (d) the Fredle index, Calculated as the Ratio of the Mean Diameter to the Sorting Index
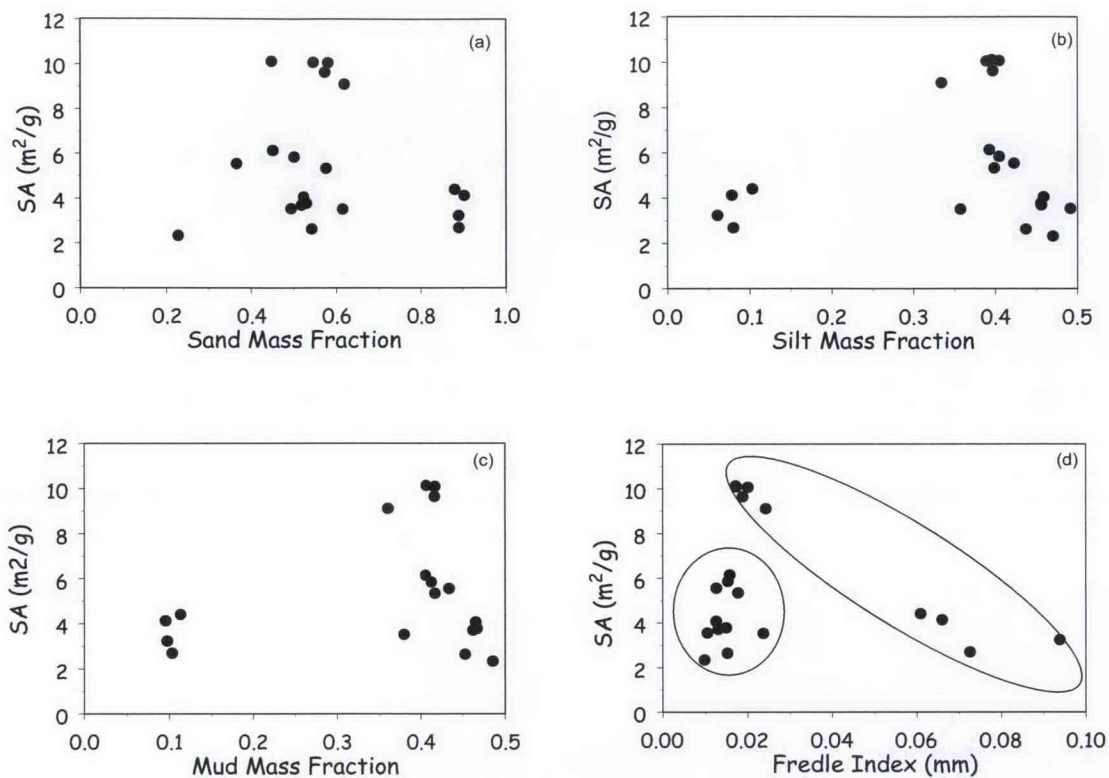
Figure 5.44. The Relationship Between SSA and Soil Textural Parameters (s) Sand Mass Fraction, (b) Silt Mass Fraction, (c) Mud, and (d) the Fredle index, Calculated as the Ratio of the Mean Diameter to the Sorting Index
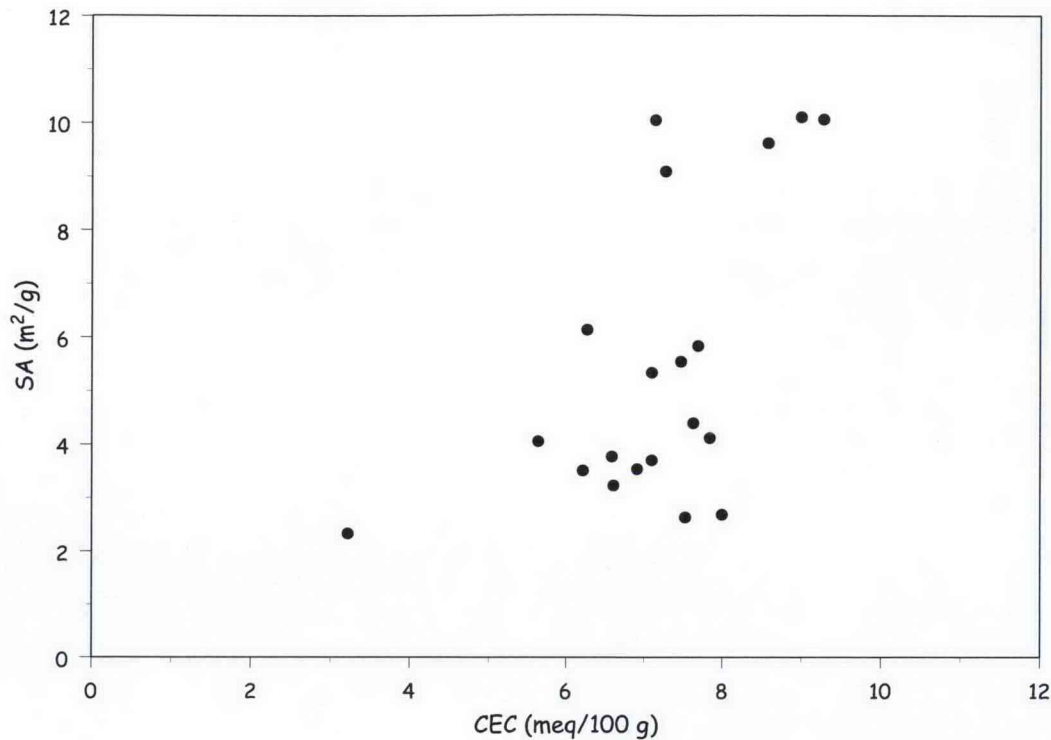
Figure 5.45. The Relationship Between SSA and CEC for Borehole C5923 (A)

Relationship Between CEC, SSA and Electrical Conductivity

Both the CEC and SSA data show significant variation with the grain-size data but do show a somewhat stronger cross correlation (Figure 5.45). Putting aside this large scatter in any of the correlations shown in Figures 5.43 through 5.45, there is slight indication of an inverse correlation between SSA and the laboratory-measured soil resistivity (Figure 5.46b). However, there appears to be no relationship between CEC and laboratory-measured soil resistivity (Figure 5.46a). This is not surprising as the bulk resistivity or its inverse conductivity is dominated by the pore fluids with very little contribution from individual grain-surface conductivity. This observation has important implications on the choice of model used to invert the field or laboratory soil resistivity data. There are several models, ranging from those based on Archies Law to more sophisticated models that account for particle surface conductivity. These data obtained in the laboratory using the sediments from borehole C5923 (A) suggest that Archie's law, developed for clean sandstones and applicable when clay content is close to zero, may suffice for the BC Cribs and Trenches site.